UNIVERSITÉ DU LUXEMBOURG

PhD-FSTM-2025-135

The Faculty of Science, Technology and Medicine

Universitat de les Illes Balears

Faculty of Science

DISSERTATION

Defence held on 08/12/2025 in Luxembourg to obtain the degree of

DOCTEUR DE L'UNIVERSITÉ DU LUXEMBOURG EN PHYSIQUE

AND

DOCTOR OF THE UNIVERSITY OF THE BALEARIC ISLANDS IN PHYSICS

by

Daniele Di Miceli

Born on 5 December 1996 in Segrate (Italy)

TRANSPORT PROPERTIES AND INDUCED SUPERCONDUCTIVITY IN MAGNETIC TOPOLOGICAL INSULATORS

Dissertation defence committee

Dr Jan Lagerwall, Chairman
Professor, Université du Luxembourg

Dr Ludger Wirtz, Vice Chairman
Professor, Université du Luxembourg

Dr Alessandro De Martino
Senior Lecturer, City St George's, University of London

Dr Dario Bercioux
Professor, Donostia International Physics Center

Dr Javier Osca
Assistant Lecturer, Universitat de les Illes Balears

Doctoral Programme in Physics
Doctoral Thesis
2025

Transport properties and induced superconductivity in magnetic topological insulators

Daniele Di Miceli

Supervisor: *Prof. Dr. Llorenç Serra*
Supervisor: *Prof. Dr. Thomas Schmidt*
Tutor: *Prof. Dr. Rosa Lopez*

Doctor of the University of Luxembourg
Doctor of the University of the Balearic Islands

Abstract

This thesis is devoted to the theoretical investigation of magnetic topological insulator–superconductor heterostructures as a promising platform for realizing topological superconductivity and zero-energy Majorana modes. We first review the physics of three-dimensional topological insulators in the Bi_2Se_3 family and discuss the possible two- and three-dimensional topological phases they can achieve in the presence of a net magnetization. By including the effect of a mean-field superconducting pairing induced via proximity to a conventional superconductor, we analyze the emergence of two- and one-dimensional topological superconducting regimes that support zero-energy Majorana states at their boundaries.

To identify experimental signatures of topological superconductivity, we study electronic transport in a normal–superconductor–normal (NSN) junction on a magnetic topological insulator slab, where only the central region is proximitized. Solving the scattering problem within the Blonder–Tinkham–Klapwijk (BTK) formalism, we compute reflection and transmission amplitudes across the junction for different topological superconducting phases in the central sector, and extract the conductance signals associated with distinct Majorana modes. Particular emphasis is placed on the conductance behavior under an asymmetrically distributed bias between the left and right leads of the junction.

Finally, we adopt a perturbative approach to obtain the leading-order correction to the anomalous Green's function, enabling us to evaluate the induced pairing correlations in a thin film of magnetic topological insulator. By solving the equation of motion for the unperturbed system, we obtain a general expression for the anomalous propagator and analyze a limiting case in which a closed-form analytical solution is possible. The induced superconducting order parameter is subsequently classified according to its spin and momentum symmetries, with particular emphasis on the role of magnetization in shaping these properties.

Resumen

Esta tesis está dedicada a la investigación teórica de heteroestructuras formadas por aislantes topológicos magnéticos y superconductores, consideradas como una plataforma prometedora para la realización de la superconductividad topológica y de modos de Majorana de energía nula. En primer lugar, revisamos la física de los aislantes topológicos tridimensionales de la familia Bi_2Se_3 y discutimos las posibles fases topológicas bidimensionales y tridimensionales que pueden surgir en presencia de una magnetización neta. Al incluir el efecto de un acoplamiento superconductor de campo medio inducido por proximidad a un superconductor convencional, analizamos la aparición de regímenes de superconductividad topológica unidimensional y bidimensional que soportan estados de Majorana de energía nula en sus fronteras.

Con el fin de identificar marcas experimentales de la superconductividad topológica, estudiamos el transporte electrónico en una unión normal–superconductor–normal (NSN) sobre una lámina de aislante topológico magnético, donde únicamente la región central está proximizada. Resolviendo el problema de dispersión dentro del formalismo de Blonder–Tinkham–Klapwijk (BTK), calculamos las amplitudes de reflexión y transmisión a través de la unión para distintas fases superconductoras topológicas en la región central, y extraemos las señales de conductancia asociadas a modos de Majorana distintos. Se presta especial atención al comportamiento de la conductancia bajo un voltage distribuido asimétricamente entre los electrodos izquierdo y derecho de la unión.

Finalmente, adoptamos un enfoque perturbativo para obtener la corrección de primer orden de la función de Green anómala, lo que nos permite evaluar las correlaciones de apareamiento inducidas en una película delgada de aislante topológico magnético. Al resolver la ecuación de movimiento para el sistema no perturbado, obtenemos una expresión general para el propagador anómalo y analizamos un caso límite en el que es posible una solución analítica en forma cerrada. El parámetro de orden superconductor inducido se clasifica posteriormente de acuerdo con sus simetrías en espín y momento, con especial énfasis en el papel de la magnetización en la modificación de dichas propiedades.

Resum

Aquesta tesi està dedicada a la investigació teòrica d'heteroestructures formades per aïllants topològics magnètics i superconductors, considerades com una plataforma prometedora per a la realització de la superconductivitat topològica i de modes de Majorana d'energia nul · la. En primer lloc, revisem la física dels aïllants topològics tridimensionals de la família Bi_2Se_3 i discutim les possibles fases topològiques bidimensionals i tridimensionals que poden aparèixer en presència d'una magnetització neta. En incloure l'efecte d'un acoblament superconductor de camp mitjà induït per proximitat amb un superconductor convencional, analitzem l'aparició de règims de superconductivitat topològica unidimensional i bidimensional que sustenten estats de Majorana d'energia nul · la a les seves vores.

Amb l'objectiu d'identificar signatures experimentals de la superconductivitat topològica, estudiem el transport electrònic en una unió normal–superconductor–normal (NSN) sobre una làmina d'aïllant topològic magnètic, on només la regió central està proximitzada. Resolent el problema de dispersió dins del formalisme de Blonder–Tinkham–Klapwijk (BTK), calculem les amplituds de reflexió i transmissió a través de la unió per a diferents fases superconductores topològiques en la regió central, i en traiem els senyals de conductància associats a modes de Majorana diferenciats. Es presta una atenció especial al comportament de la conductància sota un biaix de potencial distribuït asimètricament entre els elèctrodes esquerre i dret de la unió.

Finalment, adoptem un enfocament perturbatiu per obtenir la correcció de primer ordre de la funció de Green anòmala, cosa que ens permet avaluar les correlacions d'aparellament induïdes en una pel · lícula prima d'aïllant topològic magnètic. En resoldre l'equació de moviment per al sistema no pertorbat, obtenim una expressió general per al propagador anòmal i analitzem un cas límit en què és possible una solució analítica en forma tancada. El paràmetre d'ordre superconductor induït es classifica posteriorment d'acord amb les seves simetries d'espín i moment, amb especial èmfasi en el paper de la magnetització en la modificació d'aquestes propietats.

Zesummefaassung

An dëser Dissertatioun gi magnéitesch topologesch Isolator-Supraleedungs Heterostrukturen theoretesch analyséiert. Dës Systemer stellen eng villverspriechend Plattform duer, fir topologesch Superleedung an Nullenergie-Majorana-Zoustänn z'erreechen. Als éischt gëtt d'Physik vun dräidimensionalen topologeschen Isolatoren aus der Bi_2Se_3 -Famill ënnersicht, an et gëtt diskutéiert, wéi eng méiglech zwee- an dräidimensional topologesch Phase si an der Präsenz vun enger Net-Magnetiséierung unhuele kënnen. Duerch den Afloss vun enger mëttelwäerteger, duerch Proximitéit induzéierter Supraleedungskopplung, entstinn zwee- an eendimensional topologesch Supraleedungsregimer, déi Nullenergie-Majorana-Zoustänn un hire Grenzen hunn.

Fir experimentell Signature vun topologescher Supraleedung z'identifizéieren, gëtt den elektroneschen Transport an enger normal–supraleedungs–normal (NSN)-Jonctioun, op engem magnéiteschen topologeschen Isolator ënnersicht, wou nëmmen déi mëttelst Regioun proximiséiert ass. Duerch d'Léisung vum Streeproblem am Kader vum Blonder–Tinkham–Klapwijk (BTK)-Formalismus ginn d'Reflexiouns- an Transmissiouns-Amplituden iwwer d'Jonctioun fir verschidden topologesch Supraleedungsphase berechent, an d'Leedungssignaler, déi mat ënnerschiddleche Majorana-Zoustänn verbonne sinn, ginn extrahéiert. Besonnesch Opmierksamkeet gëtt dem Verhale vun der Leedung ënnert enger asymmetresch verdeelter Spannung tëscht de lénksen an de rietse Leedungen vun de Jonctioune geschenkt.

Zum Schluss gëtt eng perturbativ Approche ugeholl, fir d'Haaptuerdnungskorrektur vun der anomaler green'scher Funktioun ze bestëmmen, wat et erméiglecht, déi induzéiert Paarungskorrelatiounen an engem dënne Film vun engem magnéiteschen topologeschen Isolator ze bewäerten. Duerch d'Léise vun der Beweegungsgläichung fir deen ongestéierte System gëtt een allgemengen Ausdrock fir den ongewéinlechen Propagator hiergeleet, an e Grenzfall analyséiert, an deem eng genau analytesch Léisung méiglech ass. Déi induzéiert supraleedend Uerdnungsparameter ginn duerno no hirer Spin- a Momentum-Symmetrie klassifizéiert, mat engem besonnesche Fokus op d'Roll vun der Magnetiséierung beim Forme vun dëse Charakteristiken.

Acknowledgments

I spent much of the time of this PhD thinking about quitting. Reaching the end would not have been possible without the people around me.

First and foremost, I would like to thank my supervisors, Llorenç and Thomas, for the opportunity they gave me. Llorenç, I owe you my deepest gratitude for your genuine interest and support at every level—both professional and personal—which you have shown me since the very first moment. Thomas, thank you for the freedom to explore that you always granted me, and for your understanding support when I needed it most. I count myself lucky for the friendly and open relationship I have shared with both of you. Your constant encouragement and appreciation of my work have been crucial in achieving whatever results I was able to obtain. For all this, I am deeply thankful.

I am grateful to all the colleagues from the MAGMA project, especially Edi, Kristof, and Julian, for their constructive feedback, help, and invaluable contributions to my research.

A sincere thanks to all the people who, at different stages, have walked with me through parts of this journey.

I am thankful to all the people in the TMQS group, especially Chen, Endo, and Vlad, for the nice moments we spent together. An even bigger thank you to Edi, for all the help and support—at work and beyond—during the last year of my PhD. I owe it to you that I was able to finish my last project. Many thanks also to all the nice people I met in Luxembourg for the good times we shared. A special thanks to Laura for our runs together—I am glad we were both late that day.

Un enorme gracias a toda la gente de Palma, especialmente a los compañeros del IFISC. Un abrazo fuerte para Pruden, Marta y Ana: si mi estancia en España ha sido positiva, os lo debo principalmente a vosotros. Gracias por incluirme desde el primer momento, especialmente cuando aún no sabía hablar castellano. Pase lo que pase en el futuro, siempre estaréis en mi corazón. Os quiero mucho.

I can't forget the people I met during my many visits to Siegen over these years, especially Kati and Gabriel. I hope our paths will cross again in the future.

Impossibile citare tutte le persone che in questi anni mi hanno supportato da lontano e che ho continuato a sentire vicine, nonostante tutto.

Un grande grazie a tutti gli amici in Italia. Grazie per l'entusiasmo e l'affetto con cui mi avete accolto a ogni rientro: avete reso difficili le mie partenze e facili i ritorni. Grazie per esserci sempre e per farmi sentire che, nonostante il tempo e la distanza, nulla sia davvero cambiato.

Un enorme grazie alla mia famiglia, per non farmi mai mancare il loro affetto e il loro sostegno, e per la forza con cui mi avete accompagnato nei momenti più difficili di questo percorso. Non sarei mai potuto diventare la persona che sono senza di voi. Grazie.

Infine, il mio ringraziamento più grande non può che andare a Bea. Scusami per tutto ciò che abbiamo dovuto sopportare in questi anni e grazie per averne condiviso il peso con me.

List of Publications

Main Publications

1. *Proximity–induced superconductivity in magnetic topological insulator films*
   D. Di Miceli, E. Zsurka, K. Moors, L. Serra, and T. L. Schmidt
   arXiv:2512.03797 (2025)

2. *Quantum-anomalous-Hall current patterns and interference in thin slabs of chiral topological superconductors*
   D. Di Miceli and L. Serra
   Scientific Reports **13**, 19955 (2023)

3. *Conductance asymmetry in proximitized magnetic topological-insulator junctions with Majorana modes*
   D. Di Miceli, E. Zsurka, J. Legendre, K. Moors, T. L. Schmidt, and L. Serra
   Phys. Rev. B **108**, 035424 (2023)

Other Publications

1. *Optimizing proximitized magnetic topological insulator nanoribbons for Majorana bound states*
   E. Zsurka, D. Di Miceli, J. Legendre, L. Serra, D. Grützmacher, T. L. Schmidt, and K. Moors
   Phys. Rev. B **112**, 094504 (2025)

2. *Low-energy modeling of three-dimensional topological-insulator nanostructures*
   E. Zsurka, C. Wang, J. Legendre, D. Di Miceli, L. Serra, D. Grützmacher, T. L. Schmidt, P. Rüßmann, and K. Moors
   Phys. Rev. Materials **8**, 084204 (2024)

3. *Topological properties of finite-size heterostructures of magnetic topological insulators and superconductors*
   J. Legendre, E. Zsurka, D. Di Miceli, L. Serra, K. Moors, and T. L. Schmidt
   Phys. Rev. B **110**, 075426 (2024)

Contents

List of Acronyms

ABS Andreev bound state.

BCS Bardeen–Cooper–Schrieffer.

BdG Bogoliubov–de Gennes.

BHZ Bernevig–Hughes–Zhang.

BTK Blonder–Tinkham–Klapwijk.

BZ Brillouin zone.

CAR crossed Andreev reflection.

MBS Majorana bound state.

MCPS Majorana chiral propagating state.

MTI magnetic topological insulator.

NS normal–superconductor.

NSN normal–superconductor–normal.

PHS particle–hole symmetry.

QAH quantum anomalous Hall.

QH quantum Hall.

QL quintuple layer.

QSH quantum spin Hall.

SC superconductor.

SOC spin–orbit coupling.

TI topological insulator.

TRIM time–reversal invariant momenta.

TRS time–reversal symmetry.

TSC topological superconductor.

Introduction

Symmetry and topology are two of the most important principles in physics, lying at the very heart of our modern theoretical understanding of physical systems [1]. Symmetry refers to a transformation—such as a spatial translation, rotation, or time reversal—under which a system remains invariant. The fundamental connection between symmetries and conservation laws was rigorously established by Emmy Noether's theorem, a cornerstone of twentieth-century mathematical physics [2, 3]. For each continuous symmetry of a physical system, there corresponds a conserved quantity: translational invariance yields momentum conservation, rotational invariance implies conservation of angular momentum, and time-translational invariance leads to energy conservation [4, 5].

In contrast, topology classifies phases of matter based on global, quantized invariants that remain unchanged under smooth deformations of system parameters. While traditional condensed matter phases are distinguished by symmetry breaking and local order parameters, topologically nontrivial phases may share identical local symmetries yet differ profoundly in their global properties [6–8]. This topological framework has led to the discovery of exotic phases in insulators and superconductors that are distinguished from the conventional ones by a nontrivial bulk band topology. Moreover, due to the bulk–boundary correspondence, a topologically nontrivial phase is characterized by the emergence of gapless states localized at the boundaries of the system, giving rise to a variety of remarkable transport phenomena.

The first nontrivial insulating phase to be discovered was the integer quantum Hall (QH) state, which occurs in two-dimensional electron systems under a strong perpendicular magnetic field. In analogy with the classical Hall effect, electrons whose motion is driven by an external electric field experience a transverse deflection, resulting in a finite Hall conductance. However, unlike its classical counterpart, the Hall conductance in the QH regime is quantized in integer multiples of e^2/h with an extraordinary precision of one part in 10^9, reflecting its topological origin [9–11]. Within the topological framework, the quantized conductance is related to a nonzero topological invariant—the Chern number—and arises from the presence of gapless chiral edge states, which carry current along the boundaries while the bulk remains gapped and insulating [12, 13].

It did not take long for a generalization of the QH effect to emerge. Building on the same topological principles, the quantum anomalous Hall (QAH) effect was predicted to arise without an external magnetic field, relying instead on intrinsic magnetic order to break time-reversal symmetry [14–16]. Subsequently, the quantum spin Hall (QSH) state was proposed as its time-reversal-symmetric analog, effectively comprising two QH systems—one per spin species—with equal and op-

posite bulk invariants that overall preserve time-reversal symmetry. In this regime, the chiral edge modes become helical, with electrons of opposite spin propagating in opposite directions along the same edge [17–22]. Extending this paradigm to three dimensions lead to three-dimensional topological insulators (TIs), where spin-filtered one-dimensional channels are replaced by two-dimensional surface Dirac cones exhibiting robust spin-momentum locking [23–26].

Since the topological classification applies to gapped phases, it naturally extends to superconductors where the energy spectrum of single quasiparticles is fully gapped. In this context, one- and two-dimensional topological superconductors (TSCs) have been predicted, attracting even more research interest [27]. Their nontrivial bulk band topology enforces the emergence of gapless boundary modes protected by intrinsic particle–hole symmetry, which at zero energy correspond to Majorana quasiparticles—fermionic excitations that are their own antiparticles [28–30]. These exotic states are particularly appealing in the context of topological quantum computation, since the nonlocal encoding of qubits in Majorana modes provides intrinsic protection against local perturbations and disorder [31–34].

In this landscape, topological insulators of the Bi_2Se_3 family have emerged as a versatile platform for engineering a variety of symmetry-protected topological phases, owing to their time-reversal symmetry–protected surface states featuring Dirac-like dispersion and spin–momentum locking [35, 36]. When confined into a thin film geometry, hybridization between the Dirac cones in the top and bottom surfaces opens a gap in the energy spectrum, making the Dirac fermions massive [37]. If the resulting gapped surface states retain a nontrivial band topology, the system realizes an effective quantum spin Hall phase. In contrast, breaking time-reversal symmetry through magnetic doping can drive the system into the quantum anomalous Hall regime [38–40].

Hybrid heterostructures composed of magnetically doped topological insulators and conventional s-wave superconductors (SCs) can also realize different classes of topological superconductors depending on symmetry and geometry [28–30]. Inducing superconducting correlations in the QAH regime provides a natural setting for the chiral topological superconductor—the superconducting analog of the quantum Hall state—characterized by chiral Majorana edge modes with linear, gapless dispersion [41–44]. In contrast, when the system is confined into a narrow nanoribbon geometry such that the QAH edge states hybridize, the proximitized magnetic topological insulator (MTI) is expected to realize a one-dimensional topological superconductor, hosting localized Majorana bound states at its ends [45–47].

Goal and Motivation

In this thesis, we explore the interplay between magnetism, topology, and superconductivity in MTI–SC hybrid structures, where distinct forms of topological superconductivity can emerge [41, 42, 45, 46]. The motivation for investigating the physics of such hybrid systems is twofold, as proximitized MTIs lie at the crossroads of fundamental research and technological innovation. From an applied perspective, they provide a solid-state environment in which Majorana quasiparticles can be engineered and manipulated. These zero-energy modes exhibit non-Abelian ex-

change statistics and allow quantum information to be encoded nonlocally in pairs of Majorana states localized at different ends of a topological nanowire, ensuring robustness against local perturbations and decoherence [31–34]. At the same time, the coexistence and interplay of magnetism, topology, and superconductivity is intrinsically fascinating from a fundamental condensed matter viewpoint. It gives rise to unconventional superconducting phases with exotic properties, such as chiral superconductivity, anomalous Josephson effects, and topological phase transitions with no analog in conventional materials [28, 30, 48, 49].

The main goal of this thesis is to develop a theoretical framework for understanding and modeling proximitized MTIs, with the aim of supporting and complementing ongoing experimental efforts. This objective is pursued along two complementary directions. On the one hand, we perform numerical simulations of transport in normal–superconductor–normal (NSN) junctions, aiming to characterize topological superconducting phases that host Majorana modes through their electrical response, and to identify experimentally accessible signatures of nontrivial topology. On the other hand, we develop a second-quantized perturbative framework to describe the proximity effect in a MTI thin film, which enables us to derive the induced superconducting order parameter with its full spin, momentum, and spatial structure, and to analyze its dependence on magnetization, film thickness, and all the microscopic parameters of the Hamiltonian. Together, these two approaches provide a coherent picture of how superconductivity emerges in proximitized MTIs and how its topological properties can be probed in realistic device geometries.

Structure of the Thesis

The thesis is structured as follows. In Part I, we present the theoretical foundations of topology in condensed matter physics, with particular emphasis on the nontrivial insulating states realized in compounds of the Bi_2Se_3 family. In Section 1.1, we review the fundamental concepts of topological band theory for gapped Hamiltonians, introducing the Chern number and the $\mathbb{Z}_2$ index as the invariants characterizing two-dimensional systems with and without time-reversal symmetry, respectively. In Section 1.1.3, we present the generalized classification of topological phases within the framework of the "periodic table" of gapped systems, which systematically organizes free-fermion Hamiltonians according to their symmetry class and spatial dimension. In Section 1.2, we turn to the physics of three-dimensional TIs of the Bi_2Se_3 family, which can host distinct topological phases both in extended three-dimensional systems and in confined lower-dimensional geometries. To describe them, we introduce low-energy continuum Hamiltonians that serve as effective models for the three- and two-dimensional cases, respectively.

In Chapter 2, we extend the first-quantized effective description to proximitized MTIs, incorporating the mean-field induced pairing within the Bogoliubov–de Gennes framework. In Section 2.2, we discuss the physics of a two-dimensional proximitized MTI thin film, which can host the chiral topological SC phase characterized by the emergence of linear, gapless Majorana modes propagating along the edges. In Section 2.3, we examine the regime where the film width is reduced and the system is confined to an effective one-dimensional nanowire. In this limit, a distinct TSC

phase can be realized by tuning magnetization and chemical potential, giving rise to localized zero-energy Majorana bound states at the ends of finite-length wires.

Part II is devoted to the study of transport in double NSN junctions composed of normal (N) and proximitized (S) thin films of MTI. The transport problem is formulated within the Landauer–Büttiker framework for phase-coherent transport in multiterminal conductors. In Section 3.1, we derive the expression for the differential conductance using the Blonder–Tinkham–Klapwijk formalism, which accounts for Andreev reflection at the normal–superconductor interfaces. In Section 3.1.1, we outline the complex band-structure approach employed to compute the scattering amplitudes that characterize transport through the junction.

Two original results are presented in the following sections. In Section 3.2, we investigate the conductance under asymmetric voltage drops applied on the two sides of the junction, for a total bias below the surface gap of the proximitized MTI. We show that in topological phases hosting Majorana modes, the conductance acquires an antisymmetric profile as a function of the bias-splitting parameter, reflecting equal scattering processes at the two interfaces. In Section 3.3, we discuss high-bias transport signatures of the chiral TSC, in condition of symmetric bias splitting. We identify a regime of large oscillations in the total differential conductance, arising from the interference of co-propagating chiral modes associated with the emergence of Majorana states.

In Part III, we develop a second-quantized framework to describe the induced superconducting correlations in MTI–SC hybrid structures within the Green's function formalism, with the goal of obtaining explicit expressions for the induced pairing as a function of the film thickness, the magnetization, and all the microscopic Hamiltonian parameters. In Chapter 4, we introduce the second-quantized Hamiltonian of the MTI–SC heterostructure, together with the corresponding Green's function formalism, which describes the propagation of single quasiparticles and Cooper pairs. In Section 4.3, we derive the perturbative corrections to the normal and anomalous Green's functions in the magnetic topological insulator, treating the tunneling as a perturbation on the unperturbed ground states of the decoupled materials.

In Chapter 5, we derive and solve the equations of motion for the unperturbed Green's functions of the two separated materials. We first consider the SC, where the normal and anomalous propagators are coupled via the Gor'kov equations. We then derive and solve the equation of motion for the normal MTI Green's function in real space, obtaining both a general solution—valid for arbitrary magnetization, energy, and Hamiltonian parameters—and a closed-form analytical expression, valid in the limit of vanishing in-plane momentum and restricted to the topological surface states confined at the film interfaces.

Chapter 6 presents original results on induced superconductivity in thin films of MTI compounds from the Bi_2Se_3 family. In Section 6.1, we begin by evaluating the perturbative correction to the anomalous Green's function in the magnetic topological insulator, building on the results for the unperturbed propagators obtained in Chapter 5. We analyze the effect of magnetization on the pairing amplitude and the spatial profile of the induced SC correlations, deriving an explicit expression for the decay length in an analytically tractable limit. In Section 6.2, we address the spin symmetry of the induced order parameter, decomposing it into singlet and triplet components, and showing that increasing magnetization enhances the weight

of spin-polarized pairing channels, consistently with the polarization of the proximitized surface states. In Section 6.3, we turn to the momentum-space structure of the order parameter and connect it to the topology of the proximitized MTI thin film. By projecting onto circular harmonics, we resolve the pairing components with different in-plane angular momentum, and demonstrate that strong magnetization drives the system into a chiral TSC phase with p-wave pairing.

Finally, the last chapter summarizes the main results of this work and presents the conclusions of the thesis.

Part I

Topological Matter

Chapter 1

Topological Insulators

Overview

The concept of topology has become central to modern condensed matter physics, providing a unifying framework to classify phases of matter beyond the conventional paradigm of symmetry breaking. This perspective has not only deepened our theoretical understanding but has also led to the prediction and experimental realization of novel materials with exotic transport properties. Among the most promising materials are three-dimensional topological insulators, which can host distinct nontrivial states in both two- and three-dimensional geometries and are particularly significant in view of their potential applications in future quantum technologies.

This chapter provides the theoretical background required for the thesis and is structured as follows. In Section 1.1 we review the principles of topological band theory, introducing the main topological invariants, and discussing the periodic table of topological insulators and superconductors, which systematically classifies all gapped free-fermion Hamiltonians based on symmetry constraints and spatial dimensionality. In Section 1.2, we introduce the three-dimensional topological insulators of the Bi_2Se_3 family, which play a central role in this thesis. We analyze their topological features and the associated boundary states in effective three- and two-dimensional geometries, presenting the minimal effective Hamiltonian models that captures the low-energy physics of these materials.

1.1 Topological Band Theory

Topology is concerned with those properties of geometric objects that are invariant under continuous deformations. These deformations, also known as topological transformations or homeomorphisms, establish a one-to-one, continuous, and invertible mapping between the points of two spaces [6, 7, 50]. Objects that are related through such a transformation are said to be topologically equivalent and are characterized by a discrete invariant, the genus, which counts the number of holes in a three-dimensional shape as shown in Fig. 1.1.

The genus is defined through the Gauss–Bonnet theorem, which states that the

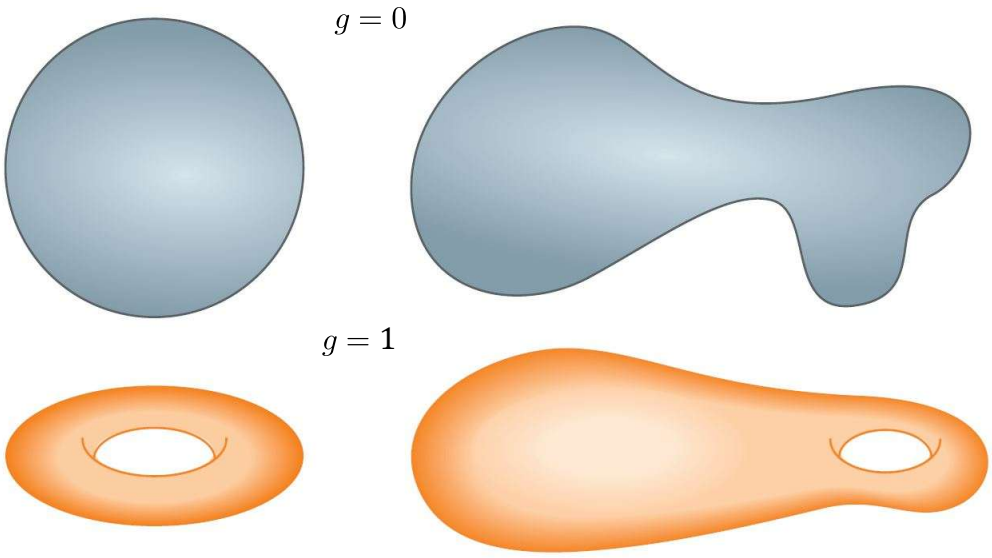

Figure 1.1: Distinct topological surfaces characterized by a different value of the topological invariant g, the genus. Adapted from [8].

integral of the Gaussian curvature K over the surface S of an object is quantized

$$\frac{1}{2\pi}\int_S K \,\mathrm{d}A = n\,, \tag{1.1}$$

where $n \in \mathbb{N}$ is an integer related to the genus through $n = 2(1-g)$. The remarkable implication of the Gauss–Bonnet theorem is that the genus is a global property that cannot be changed by a local or smooth deformation, being independent of the local curvature of the surface [51, 52].

The same conceptual framework extends naturally to condensed matter systems: two gapped Hamiltonians describing insulating phases are topologically equivalent if they can be continuously deformed one into each other without closing the energy gap [23, 24]. In this context, distinct classes of Hamiltonians are characterized by discrete topological invariants, in the same way as the genus classifies topologically distinct surfaces in geometry. The quantization of the topological invariants underlies the phenomenon of the *topological protection*: as long as the bulk energy gap remains open, continuous deformations of the Hamiltonian leave the topological invariant unchanged, and thus preserve the global physical properties of the system. A change in the topological state can only occur via a quantum phase transition, during which the energy gap closes and the topological invariant undergoes a discontinuous change [53, 54]. The topological classification framework allows for a systematic distinction between qualitatively different quantum phases and their associated transitions, each characterized by different types of topological invariants depending on the symmetries and dimensionality of a given system.

One of the most profound consequences of the topological classification of gapped systems is the bulk–boundary correspondence, which asserts the existence of gapless boundary states at interfaces where the topological invariant changes [55–57]. Indeed, at the interfaces between distinct topological phases, the discrete change of the invariant requires a local closing of the energy gap to smoothly interpolate between the two phases, in accordance with the classification of gapped Hamiltonians.

Since the vacuum is topologically equivalent to a trivial insulator, the boundary of a nontrivial topological phase must host such a transition, resulting in the emergence of zero-energy states localized at the boundary. These modes are protected by the same symmetries that enforce the nontrivial bulk topology and give rise to exotic transport phenomena [58].

1.1.1 Chern Invariant

The Chern invariant is an integer-valued topological index that characterizes two-dimensional systems with broken time–reversal symmetry (TRS) [59–61]. Consider a Hamiltonian H that depends on time t through a set of parameters $\mathbf{R}(t) = (R_1(t), R_2(t), \ldots, R_D(t))$:

$$H(t) \equiv H[\mathbf{R}(t)]\,, \tag{1.2}$$

where $\mathbf{R}(t)$ is a vector in a D-dimensional parameter space, not necessarily related to the spatial dimension of the physical system. For each $\mathbf{R}(t)$, we denote by $|n(t)\rangle \equiv |n(\mathbf{R}(t))\rangle$ the n-th orthonormal eigenstates of $H(t)$:

$$H(t)\,|n(t)\rangle = \varepsilon_n(t)\,|n(t)\rangle\ . \tag{1.3}$$

Suppose the Hamiltonian is slowly varied by changing $\mathbf{R}(t)$ adiabatically along a path in parameter space. If the system is initially in the n-th eigenstate

$$|\psi(t=0)\rangle = |n(t=0)\rangle\ , \tag{1.4}$$

then the adiabatic theorem ensures that the system will remain in the n-th eigenstate

$$|\psi(t)\rangle = C_n(t)\,|n(t)\rangle\ . \tag{1.5}$$

Because the time evolution is unitary, the coefficient $C_n(t)$ must be a pure phase factor. Without loss of generality, we can write

$$C_n(t) = \mathrm{e}^{\mathrm{i}\gamma_n(t)} \exp\left(-\frac{\mathrm{i}}{\hbar}\int_0^t \mathrm{d}t'\,\varepsilon_n(t')\right)\ , \tag{1.6}$$

where $\gamma_n(t)$ is the so-called Berry phase [62]. Taking the time derivative of Equation (1.5)

$$\frac{\mathrm{d}}{\mathrm{d}t}\,|\psi(t)\rangle = \dot{C}_n(t)\,|n(t)\rangle + C_n(t)\frac{\mathrm{d}}{\mathrm{d}t}\,|n(t)\rangle\ , \tag{1.7}$$

and inserting this into the time-dependent Schrödinger equation

$$\mathrm{i}\hbar\frac{\mathrm{d}}{\mathrm{d}t}\,|\psi(t)\rangle = H(t)\,|\psi(t)\rangle = \varepsilon_n(t)\,|\psi(t)\rangle\ , \tag{1.8}$$

we obtain

$$\dot{C}_n(t)\,|n(t)\rangle + C_n(t)\frac{\mathrm{d}}{\mathrm{d}t}\,|n(t)\rangle = -\frac{\mathrm{i}}{\hbar}\varepsilon_n(t)\,|\psi(t)\rangle\ . \tag{1.9}$$

Projecting the above equation onto $\langle n(t)|$ and taking the time-derivative of Equation (1.6) yields

$$\frac{\mathrm{d}}{\mathrm{d}t}\gamma_n(t) = \mathrm{i}\,\langle n(t)|\,\frac{\partial}{\partial t}\,|n(t)\rangle\ . \tag{1.10}$$

The time dependence of the energy eigenstate $|n(t)\rangle \equiv |n(\mathbf{R}(t))\rangle$ is entirely determined by time dependence of the parameters $\mathbf{R}(t)$

$$\frac{\mathrm{d}}{\mathrm{d}t}|n(\mathbf{R}(t))\rangle = \sum_{\mu} \frac{\partial |n(\mathbf{R}(t))\rangle}{\partial R_\mu} \frac{\mathrm{d}R_\mu}{\mathrm{d}t} = \nabla_{\mathbf{R}} |n(\mathbf{R})\rangle \cdot \dot{\mathbf{R}}(t)\,, \tag{1.11}$$

and therefore eq. (1.10) can be written as

$$\frac{\mathrm{d}}{\mathrm{d}t}\gamma_n(t) = \mathrm{i}\,\langle n(\mathbf{R})|\,\nabla_{\mathbf{R}}\,|n(\mathbf{R})\rangle \cdot \dot{\mathbf{R}}(t) = \mathcal{A}^n(\mathbf{R}(t)) \cdot \dot{\mathbf{R}}(t)\,, \tag{1.12}$$

where we introduced the Berry connection as

$$\mathcal{A}^n(\mathbf{R}) = \mathrm{i}\,\langle n(\mathbf{R})|\,\nabla_{\mathbf{R}}\,|n(\mathbf{R})\rangle\ . \tag{1.13}$$

Integrating over time, yields the total geometric phase accumulated along a path C in parameter space [59–62]

$$\gamma_n(t) = \int_0^t \mathcal{A}^n[\mathbf{R}(t')] \cdot \dot{\mathbf{R}}(t')\,\mathrm{d}t' = \int_C \mathcal{A}^n(\mathbf{R}) \cdot \mathrm{d}\mathbf{R}\,. \tag{1.14}$$

In a three-dimensional parameter space, we can introduce the Berry curvature as

$$\mathbf{\Omega}_n(\mathbf{R}) = \nabla_{\mathbf{R}} \times \mathcal{A}^n(\mathbf{R})\,, \tag{1.15}$$

and for a closed path that forms the boundary of a surface S, the closed-path Berry phase can thus be rewritten using Stokes' theorem as

$$\gamma_n = \int_{\partial S} \mathcal{A}^n(\mathbf{R}) \cdot \mathrm{d}\mathbf{R} = \int_S \mathrm{d}\mathbf{S} \cdot \mathbf{\Omega}_n(\mathbf{R})\,. \tag{1.16}$$

In crystalline solids, the relevant parameter space is the first Brillouin zone (BZ), and in momentum space the Berry connection takes the following form

$$\mathcal{A}^n(\mathbf{k}) = \mathrm{i}\,\langle u_{n\mathbf{k}}|\,\nabla_{\mathbf{k}}\,|u_{n\mathbf{k}}\rangle\ , \tag{1.17}$$

where $|u_{n\mathbf{k}}\rangle$ is the periodic part of the Bloch wavefunction for the n-th energy state with momentum $\mathbf{k}$. The associated Berry curvature is then given by

$$\mathbf{\Omega}_n(\mathbf{k}) = \nabla_{\mathbf{k}} \times \mathcal{A}^n(\mathbf{k})\,, \tag{1.18}$$

and the Berry phase acquired by adiabatic transport around a closed loop $C \equiv \partial S$ in momentum space is

$$\gamma_n = \oint_{\partial S} \mathcal{A}^n(\mathbf{k}) \cdot \mathrm{d}\mathbf{k} = \int_S \mathrm{d}\mathbf{S} \cdot \mathbf{\Omega}_n(\mathbf{k})\,. \tag{1.19}$$

In two-dimensional gapped phases, the above equation motivates the definition of the *Chern number*, which measures the flux of Berry curvature through the BZ [63]:

$$\mathcal{C}_n = \frac{1}{2\pi} \int_{\mathrm{BZ}} \mathrm{d}\mathbf{S} \cdot \mathbf{\Omega}_n(\mathbf{k})\,. \tag{1.20}$$

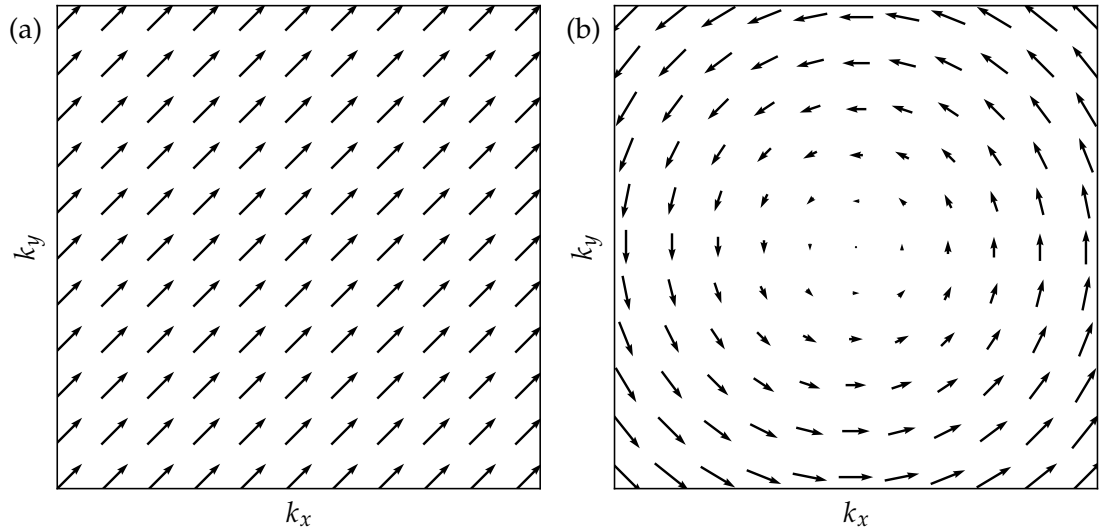

Figure 1.2: Schematic illustration of the Berry connection in a two-dimensional Brillouin zone for (a) a topologically trivial band with $\mathcal{C} = 0$ and (b) a topologically nontrivial band with $\mathcal{C} = 1$.

A nonzero Chern number implies a winding or self-rotation in the structure of the Berry connection in the Brillouin zone as illustrated in Fig. 1.2 for a two-dimensional system. This winding reflects the nontrivial topology of the bulk and is associated with a nonvanishing Chern number [8].

The physical meaning of the Chern number can be understood through the analogy between the Berry curvature and a magnetic field, which emerges naturally from the semiclassical dynamics of Bloch electrons. When a wave packet is formed from states within a single energy band, its center-of-mass dynamics is governed by the following semiclassical equations of motion [64]

$$\dot{\mathbf{r}} = \frac{1}{\hbar}\nabla_{\mathbf{k}}\,\varepsilon_n(\mathbf{k}) - \dot{\mathbf{k}} \times \boldsymbol{\Omega}_n(\mathbf{k})\,, \tag{1.21}$$

$$\hbar\dot{\mathbf{k}} = -e\mathbf{E} - e\dot{\mathbf{r}} \times \mathbf{B}(\mathbf{r})\,, \tag{1.22}$$

where $\varepsilon_n(\mathbf{k})$ is the band dispersion, $\mathbf{E}$ is the electric field, and $\mathbf{B}$ is the magnetic field. The first term $\nabla_{\mathbf{k}}\,\varepsilon_n(\mathbf{k})$ is the usual group velocity, while the second one $\dot{\mathbf{k}}\times\boldsymbol{\Omega}_n(\mathbf{k})$ is the Berry curvature correction, which acts like a Lorentz force in momentum space. In the absence of a real-space magnetic field, Equation (1.22) reduces to $\hbar\dot{\mathbf{k}} = -e\mathbf{E}$ and plugging it into Equation (1.21), we obtain [64]

$$\dot{\mathbf{r}} = \frac{1}{\hbar}\nabla_{\mathbf{k}}\,\varepsilon_n(\mathbf{k}) + \frac{e}{\hbar}\mathbf{E} \times \boldsymbol{\Omega}_n(\mathbf{k})\,, \tag{1.23}$$

which reveals that the wave packet experiences an additional velocity that is orthogonal to both the electric field $\mathbf{E}$ and the local Berry curvature $\boldsymbol{\Omega}_n(\mathbf{k})$.

The analogy between the Berry curvature and a magnetic field becomes particularly relevant when considering transport phenomena in two-dimensional electron systems. The total electric current is obtained by integrating the band velocity of

the electrons in Equation (1.23) over all the occupied states. For a completely filled state, the conventional group-velocity term vanishes upon integration over the BZ, while the anomalous velocity results in a net transverse current that directly reflects the nontrivial topology of the bulk bands [24, 55]

$$\mathbf{j} = -\frac{e^2}{\hbar} \sum_{n \in \mathrm{occ}} \int_{\mathrm{BZ}} \frac{\mathrm{d}^2\mathbf{k}}{(2\pi)^2}\, \mathbf{E} \times \mathbf{\Omega}_n(\mathbf{k})\,. \tag{1.24}$$

This expression is related to a quantized transverse conductivity [14, 65]

$$\sigma_{xy} = \frac{e^2}{h}\mathcal{C}\,, \tag{1.25}$$

where $\mathcal{C}$ is the total Chern number obtained by summing the first Chern invariant of all occupied bands

$$\mathcal{C} = \sum_{n \in \mathrm{occ}} \mathcal{C}_n\,. \tag{1.26}$$

Equation (1.25) establishes a direct correspondence between the macroscopic transport response and the topological properties of the Bloch wavefunctions defined over the BZ. The transverse deflection of charge carriers under an applied electric field thus closely resembles the classical Hall effect, with the Berry curvature playing the role of an effective magnetic field in momentum space. Consequently, a system characterized by a nonzero Chern number exhibits a quantized Hall conductance even in the absence of an external magnetic field and is referred to as a Chern insulator or integer QAH state [15, 55].

The quantization of the Hall conductance can also be understood within the framework of topological band theory through the bulk–boundary correspondence. At the interface between a Chern insulator and the vacuum—which is topologically equivalent to a trivial insulator—gapless edge states necessarily emerge to interpolate between the two distinct topological phases that require a local closing of the energy gap. Therefore, the Chern invariant counts the number of such chiral edge modes present at the boundaries of the system [14, 15, 55]. In sufficiently wide samples, these edge states propagate unidirectionally along the edges and are immune to elastic backscattering, as no counter-propagating states are available on the same edge. As a result, they enable ballistic transport that is exceptionally robust against disorder and imperfections, providing a natural explanation for the precise quantization of the transverse conductance. A sketch of the chiral edge state connecting valence and bulk bands in a Chern insulator and the corresponding electron channel in real space is shown in Figure 1.3.

1.1.2 The $\mathbb{Z}_2$ Topological Invariant

In time-reversal invariant systems, the Chern number identically vanishes due to the antisymmetric nature of the Berry curvature under time-reversal transformation. Therefore, the topological classification of band insulators in two dimensions requires the introduction of a new topological invariant, known as the $\mathbb{Z}_2$ invariant, which emerges naturally from the global structure of the occupied bands and generalizes the concept of topology to time-reversal symmetric Hamiltonians [19, 22, 24].

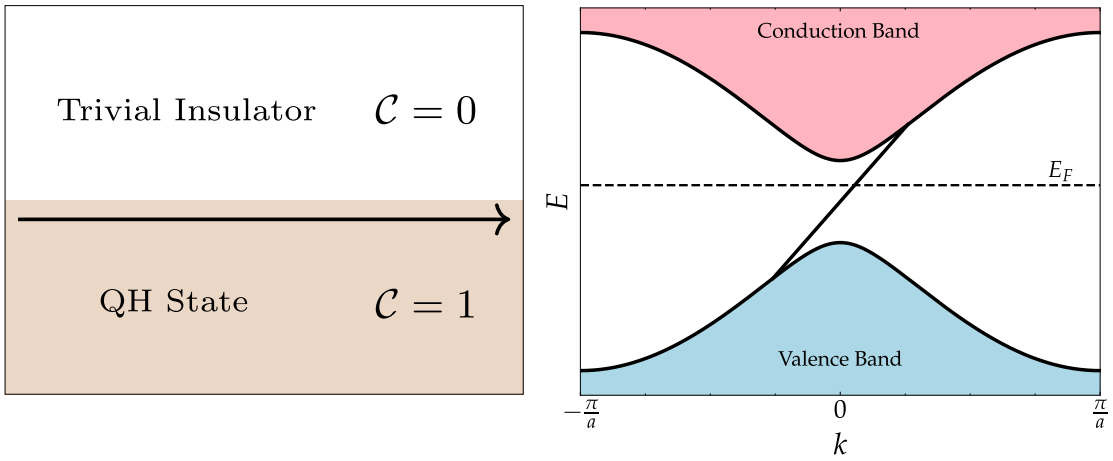

Figure 1.3: Bulk-boundary correspondence in the quantum Hall effect. Left: interface between a trivial insulator and a Chern insulator with $\mathcal{C} = 1$, hosting a chiral edge mode. Right: sketch of the band structure with a single edge state connecting valence and conduction bulk bands.

For spinful systems, TRS is represented by the antiunitary operator

$$\mathcal{T} = \mathrm{i}\sigma_y K\,, \tag{1.27}$$

where K denotes complex conjugation and σ_y is the Pauli matrix acting in spin space. For spin-1/2 particles, this operator satisfies $\mathcal{T}^2 = -1$, a property that leads to the fundamental constraint known as Kramers' theorem: all eigenstates of a time-reversal symmetric Hamiltonian must be at least twofold degenerate [66]. Indeed, assuming the existence of a non-degenerate eigenstate $|\chi\rangle$, one would have

$$\mathcal{T}\,|\chi\rangle = c\,|\chi\rangle\ , \tag{1.28}$$

for some complex number c. Applying $\mathcal{T}$ once more yields

$$\mathcal{T}^2\,|\chi\rangle = \mathcal{T}(c\,|\chi\rangle) = c^*\mathcal{T}\,|\chi\rangle = |c|^2\,|\chi\rangle\ . \tag{1.29}$$

However, this contradicts the identity $\mathcal{T}^2 = -1$, implying that $|\chi\rangle$ and $\mathcal{T}\,|\chi\rangle$ must be linearly independent and the eigenstates are thus degenerate.

In the absence of spin–orbit coupling (SOC), Kramers' degeneracy reduces to the trivial spin degeneracy between up and down states. In contrast, in the presence of spin-orbit interactions, the degeneracy acquires a nontrivial character and has important implications for the structure of the energy spectrum. In momentum space, TRS imposes that [24, 55]

$$\mathcal{T}H(\mathbf{k})\mathcal{T}^{-1} = H(-\mathbf{k})\,. \tag{1.30}$$

This implies that at the time–reversal invariant momenta (TRIM) in the Brillouin zone where $\mathbf{k}$ and $-\mathbf{k}$ correspond to the same momentum state, the energy eigenstates must appear in degenerate Kramers' pairs due to time-reversal invariance.

These high-symmetry points, which play a central role in the topological classification of band structures, are commonly referred to as Kramers' points. Although the Chern number vanishes in the presence of TRS, two-dimensional systems can still exhibit a distinct topological classification characterized by a $\mathbb{Z}_2$ invariant, which takes the values $\nu = 0$ or 1 [67]. The existence of these two topological classes can be understood through the bulk-boundary correspondence.

Consider a one-dimensional edge of a two-dimensional time-reversal invariant system. While the presence of edge-localized states generally depends on microscopic details at the boundary, Kramers' theorem ensures that any such states must be twofold degenerate at the TRIM $k_x = 0$ and $k_x = \pi/a$ in the one-dimensional edge BZ. The topological nature of the system is determined by how the edge-state branches connect between these two points. Specifically, the number of times the edge bands cross the Fermi energy can be either even or odd. If the number of Fermi-level crossings is even, the Hamiltonian can be smoothly deformed pushing the edge states into the bulk without breaking TRS, indicating a topologically trivial phase. In contrast, an odd number of crossings signals the presence of robust, symmetry-protected edge modes that cannot be eliminated without closing the bulk gap, thus characterizing a topologically nontrivial insulator. This distinction is captured by the bulk-boundary correspondence, which links the number N_K of edge states crossing the Fermi level to the change in the bulk $\mathbb{Z}_2$ invariant across the interface [24, 55]:

$$N_K = \Delta\nu \mod 2\,, \tag{1.31}$$

meaning that for $\nu = 1$ the system host a pair of helical edge states—two counter-propagating modes related by TRS. A sketch of the helical edge states crossing the bulk energy gap in a 2D system with $\nu = 1$ is shown in Figure 1.4. Since the system can be viewed as two copies of the QH state with opposite Chern numbers—one for each spin species—the two-dimensional time-reversal invariant topological insulator is referred to as a QSH insulator [17–19].

One formal definition of the $\mathbb{Z}_2$ invariant, analyzes the symmetry properties of Bloch wavefunctions at the special TRIM [22, 24, 67, 68]. In particular, one can introduce the so-called sewing matrix

$$w_{mn}(\mathbf{k}) = \langle u_m(\mathbf{k})|\mathcal{T}|u_n(-\mathbf{k})\rangle\,, \tag{1.32}$$

which encodes how the occupied Bloch states $|u_n(\mathbf{k})\rangle$ at momentum $\mathbf{k}$ are related to those at $-\mathbf{k}$ under the action of the time-reversal operator $\mathcal{T}$. At the TRIM points Λ_i, where $\mathbf{k} = -\mathbf{k} \mod \mathbf{G}$, the sewing matrix becomes antisymmetric due to Kramers' degeneracy, and satisfies

$$w^T(\Lambda_i) = -w(\Lambda_i)\,. \tag{1.33}$$

This antisymmetry allows one to define the Pfaffian $\mathrm{Pf}[w(\Lambda_i)]$, whose square yields the determinant of the matrix. The $\mathbb{Z}_2$ topological invariant ν can then be computed as

$$(-1)^\nu = \prod_i \frac{\sqrt{\det[w(\Lambda_i)]}}{\mathrm{Pf}[w(\Lambda_i)]}\,, \tag{1.34}$$

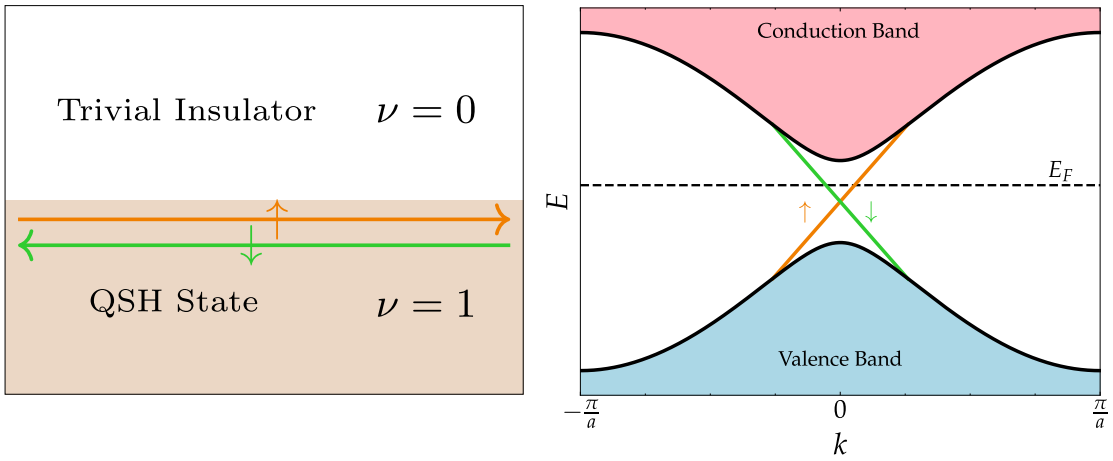

Figure 1.4: Bulk-boundary correspondence in the quantum spin Hall effect. Left: interface between a trivial insulator and a QSH state with $\nu = 1$, hosting a pair of helical edge channels. Right: sketch of the band structure with a pair of counter-propagating edge states connecting valence and conduction bulk bands.

where the product runs over all TRIMs in the Brillouin zone. The above definition can be easily extended from two to three dimensions by considering all the TRIM within the three-dimensional BZ.

The physical meaning of this formulation is that the sewing matrix encodes the global structure of the occupied states under TRS. Although Kramers' theorem guarantees that the states come in degenerate pairs, it does not determine the relative phases between the two partners. These phases therefore remain locally unconstrained in momentum space. The distinction between a trivial and a topological time-reversal-invariant state lies precisely in whether one can determine the relative phases between the Kramers pairs smoothly and globally across the BZ. The sewing matrix defined in Equation (1.32) encodes exactly this information: its antisymmetric form at the TRIMs reflects the Kramers constraint imposed by TRS, while its Pfaffian provides a compact measure of whether the two Kramers states can be consistently chosen without encountering a sign ambiguity. In this sense, the gauge-invariant quantity in Equation (1.34) detects a topological obstruction in the phase structure of the occupied bands: a product equal to -1 over all TRIMs signals that a globally smooth, time-reversal-symmetric gauge cannot be defined, corresponding to a nontrivial topological phase [24, 55].

1.1.3 Periodic Classification

The classification of topological phases in free-fermion systems is rooted in the interplay between symmetry and geometry, and can be generalized in the so-called periodic table of topological insulators and superconductors [69–71]. This framework generalizes the notion of topological invariants to all spatial dimensions and symmetry classes, providing a unified description of gapped topological phases. The classification is based on the presence or absence of three fundamental discrete symmetries: time-reversal symmetry $\mathcal{T}$, particle-hole symmetry $\mathcal{P}$, and chiral symmetry

defined as the combination $\mathcal{S} = \mathcal{T}\mathcal{P}$. The algebraic properties of these symmetry operators—specifically, whether they square to $+1$ or -1—determine in which symmetry class a given system belongs to. There are ten distinct classes which correspond directly to the Altland-Zirnbauer classification of random matrices [72]: their topological properties across spatial dimensions are summarized in Table 1.1.

	Symmetry			Dimension d							
	$\mathcal{T}$	$\mathcal{P}$	$\mathcal{S}$	1	2	3	4	5	6	7	8
A	0	0	0	0	$\mathbb{Z}$	0	$\mathbb{Z}$	0	$\mathbb{Z}$	0	$\mathbb{Z}$
AIII	0	0	1	$\mathbb{Z}$	0	$\mathbb{Z}$	0	$\mathbb{Z}$	0	$\mathbb{Z}$	0
AI	1	0	0	0	0	0	$\mathbb{Z}$	0	$\mathbb{Z}_2$	$\mathbb{Z}_2$	$\mathbb{Z}$
BDI	1	1	1	$\mathbb{Z}$	0	0	0	$\mathbb{Z}$	0	$\mathbb{Z}_2$	$\mathbb{Z}_2$
D	0	1	0	$\mathbb{Z}_2$	$\mathbb{Z}$	0	0	0	$\mathbb{Z}$	0	$\mathbb{Z}_2$
DIII	-1	1	1	$\mathbb{Z}_2$	$\mathbb{Z}_2$	$\mathbb{Z}$	0	0	0	$\mathbb{Z}$	0
AII	-1	0	0	0	$\mathbb{Z}_2$	$\mathbb{Z}_2$	$\mathbb{Z}$	0	0	0	$\mathbb{Z}$
CII	-1	-1	1	$\mathbb{Z}$	0	$\mathbb{Z}_2$	$\mathbb{Z}_2$	$\mathbb{Z}$	0	0	0
C	0	-1	0	0	$\mathbb{Z}$	0	$\mathbb{Z}_2$	$\mathbb{Z}_2$	$\mathbb{Z}$	0	0
CI	1	-1	1	0	0	$\mathbb{Z}$	0	$\mathbb{Z}_2$	$\mathbb{Z}_2$	$\mathbb{Z}$	0

Table 1.1: Topological classification of gapped free-fermion systems according to the Altland-Zirnbauer symmetry class and spatial dimension d. The first three columns indicate the presence (± 1) or absence (0) of time-reversal $\mathcal{T}$, particle-hole $\mathcal{P}$, and chiral and $\mathcal{S}$ symmetries, respectively. Each entry shows the type of topological invariant in that dimension: trivial (0), integer ($\mathbb{Z}$), or binary ($\mathbb{Z}_2$).

Each symmetry class admits a topological classification in every spatial dimension d, characterized by an associated topological invariant taking values in $\mathbb{Z}$, $\mathbb{Z}_2$, or 0 (trivial). The integer QH effect arises in class A, which lacks both time-reversal and particle-hole symmetry. In two dimensions $d = 2$, this class supports an integer-valued topological invariant, corresponding to the Chern number introduced in Section 1.1.1. In contrast, the QSH state belongs to class AII, defined by the absence of particle-hole symmetry and the presence of time-reversal symmetry with $\mathcal{T}^2 = -1$ for spinful electrons. In $d = 2$, this class admits a $\mathbb{Z}_2$ topological invariant that distinguishes the QSH phase from a trivial insulator, as discussed in Section 1.1.2. The same symmetry class also hosts three-dimensional topological insulators, which can be viewed as the natural extension of the QSH phase to $d = 3$. In both two- and three-dimensional cases, TRS protects the gapless helical edge or surface states, rendering them robust against nonmagnetic disorder and perturbations.

TSCs also arise naturally within this classification framework [28, 30]: since the single-particle excitation spectrum is gapped by the presence of superconducting pairing, the topology of the bulk wavefunction can be classified analogously to that of insulators, and is encompassed by the periodic table of topological phases. Moreover, since these systems are intrinsically particle-hole symmetric, the topological

boundary modes predicted by the bulk-boundary correspondence take the form of zero-energy Majorana quasiparticles—fermionic excitations that are their own antiparticles [29, 73, 74]. Most notably, systems in class D, which is defined by the presence of particle–hole symmetry (PHS) with $\mathcal{P}^2 = 1$ and the absence of both time-reversal and chiral symmetries, can host topological superconducting phases. In two dimensions ($d = 2$), this class supports an integer topological invariant $\mathbb{Z}$, analogous to the Chern number, which counts the number of chiral Majorana edge modes propagating along the boundary. This realizes a chiral topological superconductor, which serves as the superconducting analogue of the quantum Hall state [41, 42]. Instead, in one dimension ($d = 1$), class D admits a $\mathbb{Z}_2$ classification and captures the physics of the Kitaev chain, where the nontrivial phase supports localized Majorana zero modes at the ends of the system [45, 46, 75, 76]. If TRS is preserved, instead, the Hamiltonian falls into the symmetry class DIII and in two dimensions ($d = 2$) it is characterized by a $\mathbb{Z}_2$ invariant. The corresponding state is the superconducting counterpart of the QSH insulator and exhibit a pair of counterpropagating helical edge states related by time-reversal symmetry [42, 77, 78].

Three-dimensional topological insulators of the Bi_2Se_3 family are the main focus of the remainder of this chapter. These materials not only exhibit rich physical properties arising from their nontrivial bulk topology, but also serve as a versatile platform for engineering a variety of different topological phases. In particular, they can host the QAH phase in effectively two-dimensional geometries with magnetic doping, and give rise to one- and two-dimensional TSC states when brought into proximity with conventional s-wave superconductors.

1.2 Three-dimensional Topological Insulators

The classification of gapped free-fermion systems according to their dimensionality and fundamental symmetries discussed above provides a unifying framework for understanding topological phases of matter. Among the most prominent examples emerging from this periodic classification are the so-called three-dimensional TIs, which constitute the natural generalization of the QSH state to $d = 3$. Through the bulk-boundary correspondence, these systems are characterized by an insulating bulk and gapless Dirac-cone shaped surface states with spin and momentum locked to each other that generalize the QSH helical edge states in two-dimensions [23, 25, 35, 79].

According to Table 1.1, three-dimensional TIs belong to the symmetry class AII and they are spinful systems characterized by TRS with $\mathcal{T}^2 = -1$ and by the absence of both PHS and chiral symmetry. In three dimensions, it is possible to define a set of four $\mathbb{Z}_2$ indices $(\nu_0; \nu_1\nu_2\nu_3)$. A strong topological insulator corresponds to $\nu_0 = 1$ and it is characterized by an odd number of Dirac cones states on any surface—independently of the surface orientation—and it is robust against perturbations that do not break TRS. In contrast, a weak topological insulator has $\nu_0 = 0$ but at least one nonzero weak index $\nu_i = 1$, and it can be viewed as a stack of two-dimensional QSH layers. In this case, the presence of gapless surface states depends on the surface orientation, and such states can be removed by perturbations that

break translational symmetry, making weak TIs more sensitive to disorder than their strong counterparts [15, 55, 79].

In the following, we focus on the properties of materials of the Bi_2Se_3 family—namely bismuth selenide Bi_2Se_3, bismuth telluride Bi_2Te_3 and antimony telluride Sb_2Te_3. These materials are *strong* topological insulators characterized by robust surface states, consisting of a single Dirac cone at the high-symmetry point Γ in the BZ, located inside a large bulk gap that exceeds the thermal energy scale at room temperature [35, 36]. In recent years, they have attracted considerable attention, both as a platform for exploring the fundamental properties of topological matter and for their potential applications in areas ranging from spintronics to quantum computing, owing to their robust metallic surface states capable of supporting ballistic transport.

1.2.1 Crystal Structure

The materials of the Bi_2Se_3 family crystallize in a rhombohedral structure with space group $R\bar{3}m$, which can also be described in the equivalent hexagonal setting illustrated in Figure 1.5. The fundamental structural unit is the quintuple layer (QL), composed of five atomic planes stacked along the crystallographic c axis in the sequence Se1–Bi1–Se2–Bi1′–Se1′. Within a quintuple layer, adjacent atomic planes are strongly bonded, while neighboring QLs are weakly coupled through weak van der Waals bonding. Viewed along the z axis, the atoms in each layer form a triangular lattice, with successive layers occupying distinct A, B, and C positions in the hexagonal close-packed arrangement. This layered structure, combined with the atomic properties of the constituent atoms, gives rise to strong SOC, which plays a crucial role in the topological properties of the material [30, 35, 80, 81].

The bulk electronic structure of Bi_2Se_3 is characterized by a direct energy gap located at the $\Gamma = (0, 0, 0)$ point of the BZ. In the absence of SOC, the conduction and valence bands are mainly derived from the p_z orbitals of Bi and Se atoms, since they are energetically favourable over the $p_{x,y}$ ones due to the crystal-field splitting. In the atomic limit, these orbitals possess a well-defined parity under spatial inversion: states predominantly derived from Bi exhibit even (+) parity, whereas those originating from Se exhibit odd (−) parity. Inclusion of strong spin-orbit coupling mixes orbital and spin degrees of freedom of the strong SOC and induces a band inversion at Γ, whereby the conduction-band minimum and valence-band maximum exchange their parity character [35, 80]. This inversion is one of the hallmarks of the topologically non-trivial phase and leads, via the bulk-boundary correspondence, to the emergence of metallic surface states. First-principles calculations predict a bulk gap of approximately 300 meV in Bi_2Se_3, significantly larger than the thermal energy scale at room temperature $k_BT \approx 26$ meV, ensuring the robustness of the surface states against thermal excitations. The BZ and the bulk energy bands of Bi_2Se_3 are shown in Figure 1.6.

Assuming translational invariance in all spatial directions, the low-energy, long-wavelength physics in the vicinity of the Γ point can be described by an effective model constructed from the four relevant states with well-defined parity $\tau = \pm$ and

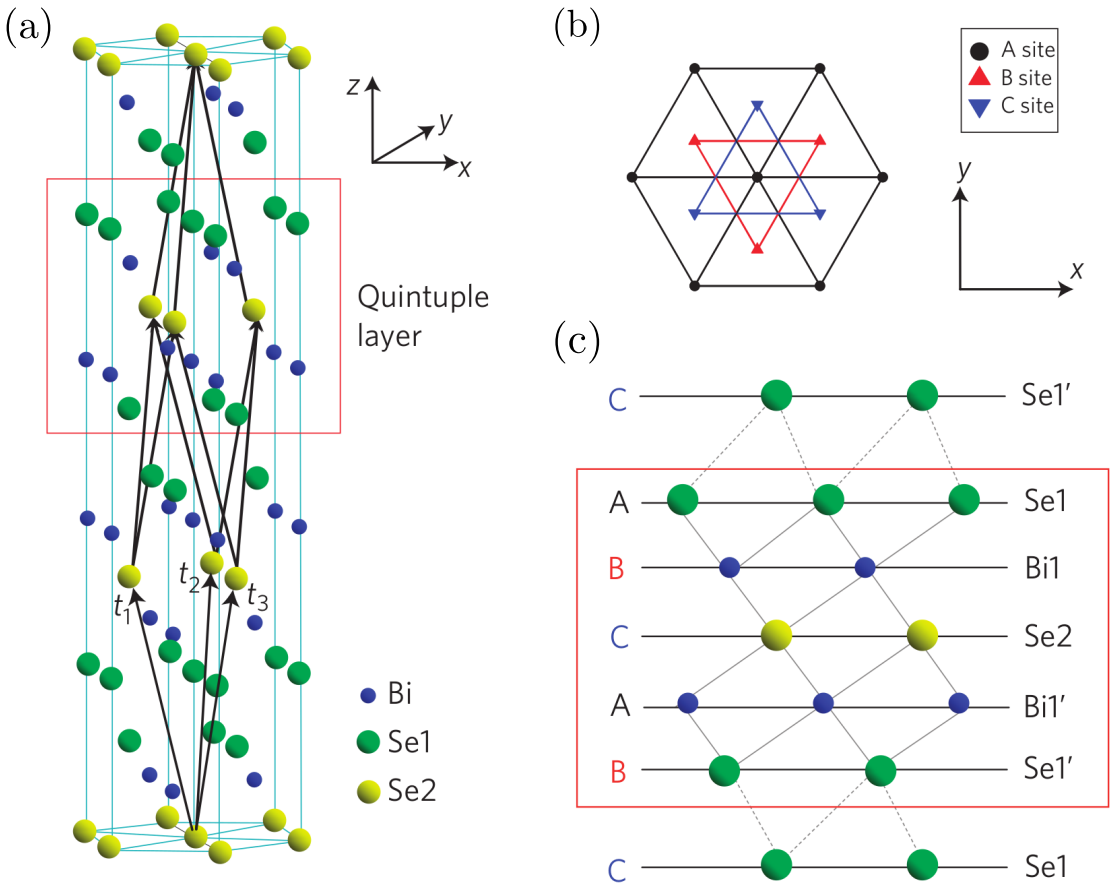

Figure 1.5: Crystal structure of Bi_2Se_3. (a) Side view of the rhombohedral unit cell, highlighting a quintuple layer consisting of Se1–Bi1–Se2–Bi1′–Se1′. The primitive lattice vectors $\mathbf{t}_1$, $\mathbf{t}_2$, and $\mathbf{t}_3$ are indicated. (b) Top view along the z axis, showing the triangular lattice within a quintuple layer, with A, B, and C sites marked. (c) Layer stacking sequence along the z direction. Adapted from Ref. [35].

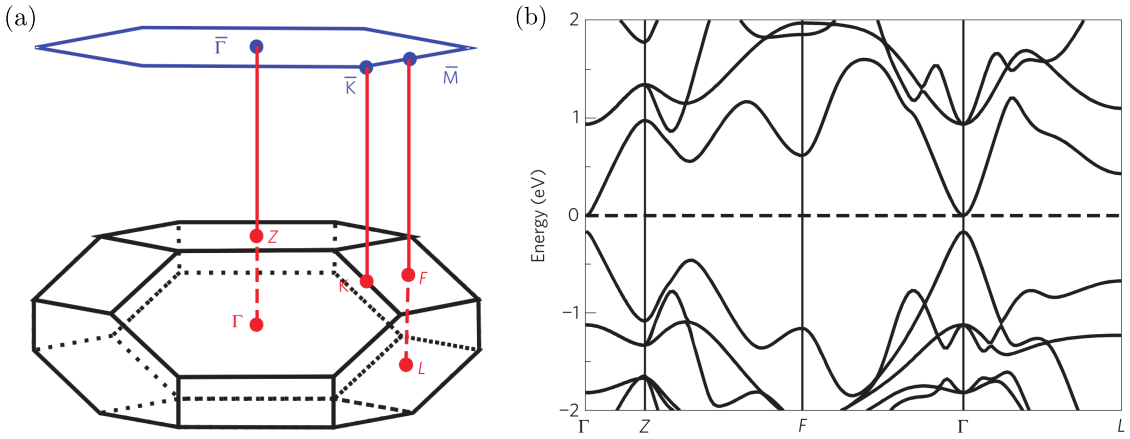

Figure 1.6: (a) Brillouin zone of Bi_2Se_3 in the hexagonal setting, indicating the high-symmetry points Γ, Z, F, K and L, together with their projections $\bar{\Gamma}$, $\bar{K}$, $\bar{M}$ onto the (111) surface BZ. (b) First-principles bulk band structure along high-symmetry directions. A direct gap is observed at the Γ point, where strong spin–orbit coupling induces a band inversion between the conduction and valence bands. The dashed horizontal line marks the Fermi level. Adapted from Ref. [35]

spin projection along the z axis $\sigma = \uparrow, \downarrow$. These states form the basis

$$\left\{ |\uparrow +\rangle, |\uparrow -\rangle, |\downarrow +\rangle, |\downarrow -\rangle \right\}, \tag{1.35}$$

which serves as the starting point for the $\mathbf{k}\cdot\mathbf{p}$ expansion and the construction of an effective 4×4 Hamiltonian near the $\Gamma = (0, 0, 0)$ point.

1.2.2 Three-Dimensional Bulk Model

The three-dimensional effective model for bulk TIs of the Bi_2Se_3 family can be obtained by imposing the constraints dictated by the relevant symmetries of the system. If a momentum-dependent Hamiltonian $H(\mathbf{k})$ is invariant under a symmetry operation g, it must satisfy [71, 82, 83]

$$D(g)^{-1} H\left(d_g(\mathbf{k})\right) D(g) = H(\mathbf{k}), \tag{1.36}$$

where $d_g(\mathbf{k})$ denotes the action of g in momentum space, and $D(g)$ is its representation in the Hilbert space of the chosen basis states. The relevant symmetries for the materials of the Bi_2Se_3 family follow from their rhombohedral crystal structure, classified by the space group $R\bar{3}m$. By excluding the lattice translations, one obtains the associated point group D_{3d}, containing the transformations that leave at least one point fixed. This set of symmetry operations consists of [35, 79, 80]:

(i) time-reversal symmetry $\mathcal{T}$, inherited from the non-magnetic character of the crystal;

(ii) inversion symmetry $\mathcal{I}$, with respect to the atomic plane containing the Se2 atoms;

(iii) threefold rotation symmetry $\mathcal{C}_3$ about the z axis.

Together, these symmetries impose important constraints on the form of the low-energy electronic Hamiltonian.

As already discussed in Equation (1.27), for spinful fermions TRS is represented by the operator

$$\mathcal{T} = \mathrm{i}\sigma_y K\,, \tag{1.37}$$

where $\sigma_{x,y,z}$ are Pauli matrices in spin space and K is complex conjugation. Its action on momentum is characterized by $d_{\mathcal{T}}(\mathbf{k}) = -\mathbf{k}$, and the symmetry constraint in Equation (1.36) reads as

$$-\mathrm{i}\sigma_y\, H^*(-\mathbf{k})\, \mathrm{i}\sigma_y = H(\mathbf{k})\,, \tag{1.38}$$

ensuring Kramers' degeneracy at all TRIMs in the Brillouin zone. Inversion symmetry acts only in orbital space, and it is represented as $\mathcal{I} = \tau_z$, where $\tau_{x,y,z}$ is a set of Pauli matrices acting in orbital space. Under the action of $\mathcal{I}$, the momentum is inverted $d_{\mathcal{T}}(\mathbf{k}) = -\mathbf{k}$, such that Equation (1.36) becomes

$$\tau_z\, H(-\mathbf{k})\, \tau_z = H(\mathbf{k})\,, \tag{1.39}$$

forcing the matrix elements that connect states of equal (opposite) parity to be even (odd) in momentum space. The three-fold rotation $\mathcal{C}_3$ around the z axis is represented by

$$\mathcal{C}_3 = \mathrm{e}^{\mathrm{i}\frac{\pi}{3}\sigma_z}\,, \tag{1.40}$$

and it acts on momentum rotating the in-plane momentum components k_x, k_y by $2\pi/3$ while leaving k_z unchanged

$$d_{\mathcal{C}_3}(\mathbf{k}) = \mathcal{R}_3\,\mathbf{k}\,, \qquad \text{where} \quad \mathcal{R}_3 = \begin{pmatrix} -\frac{1}{2} & \frac{\sqrt{3}}{2} & 0 \\ -\frac{\sqrt{3}}{2} & -\frac{1}{2} & 0 \\ 0 & 0 & 1 \end{pmatrix}. \tag{1.41}$$

The constraint in Equation (1.36) for the $\mathcal{C}_3$ rotational symmetry thus reads as

$$\mathrm{e}^{-\mathrm{i}\frac{\pi}{3}\sigma_z}\, H\left(d_{\mathcal{C}_3}(\mathbf{k})\right)\, \mathrm{e}^{\mathrm{i}\frac{\pi}{3}\sigma_z} = H(\mathbf{k})\,, \tag{1.42}$$

imposing the energy bands to be isotropic to leading order in the in-plane momentum, and allowing only combinations of $k_x \pm \mathrm{i}k_y$ in the linear terms.

Up to second order in momentum, the most general Hamiltonian $H(\mathbf{k})$ that satisfies the symmetry relations in Equations (1.38), (1.39) and (1.42), can be expressed in the basis of states of Equation (1.35) as [84]

$$h_{\mathrm{TI}}(\mathbf{k}) = \begin{pmatrix} a + b\,k_\parallel^2 + c\,k_z^2 & \gamma\,k_z & 0 & \beta\,(k_x - \mathrm{i}k_y) \\ \gamma^*\,k_z & a' + b'\,k_\parallel^2 + c'\,k_z^2 & \beta\,(k_x - \mathrm{i}k_y) & 0 \\ 0 & \beta^*\,(k_x + \mathrm{i}k_y) & a + b\,k_\parallel^2 + c\,k_z^2 & -\gamma^*\,k_z \\ \beta^*\,(k_x + \mathrm{i}k_y) & 0 & -\gamma\,k_z & a' + b'\,k_\parallel^2 + c'\,k_z^2 \end{pmatrix}, \tag{1.43}$$

where we defined the in-plane momentum as $k_\parallel^2 \equiv k_x^2 + k_y^2$. Let us define $C_0 \equiv (a + a')/2$, $M_0 \equiv (a - a')/2$, $D_1 \equiv (c + c')/2$, $D_2 \equiv (b + b')/2$, $B_1 \equiv -(c - c')/2$, $B_2 \equiv -(b - b')/2$, $A_1 \equiv \gamma$ and $A_2 \equiv \beta$ with $A_{1,2}$ assumed to be real. Then Equation (1.43) takes the following form [35, 79, 80, 84]

$$h_{\mathrm{TI}}(\mathbf{k}) = \varepsilon_0(\mathbf{k})\,\mathbb{I}_4 + \begin{pmatrix} M(\mathbf{k}) & A_1 k_z & 0 & A_2 k_- \\ A_1 k_z & -M(\mathbf{k}) & A_2 k_- & 0 \\ 0 & A_2 k_+ & M(\mathbf{k}) & -A_1 k_z \\ A_2 k_+ & 0 & -A_1 k_z & -M(\mathbf{k}) \end{pmatrix}, \tag{1.44}$$

where

$$\varepsilon_0(\mathbf{k}) \equiv C_0 + D_1 k_z^2 + D_2 k_\parallel^2\,, \qquad M(\mathbf{k}) \equiv M_0 - B_1 k_z^2 - B_2 k_\parallel^2\,, \tag{1.45}$$

and $k_\pm = k_x \pm \mathrm{i}k_y$. The Hamiltonian in Equation (1.44) constitutes the low-energy effective model for three-dimensional TIs of the Bi_2Se_3 family expanded around the $\Gamma = (0, 0, 0)$ point and expressed in the basis of states of Equation (1.35). Using a basis-independent notation, Equation (1.44) can finally be rewritten as

$$h_{\mathrm{TI}}(\mathbf{k}) = \varepsilon_0(\mathbf{k}) + A(\mathbf{k})\tau_x + M(\mathbf{k})\tau_z\,, \tag{1.46}$$

where we defined

$$A(\mathbf{k}) \equiv A_1 k_z \sigma_z + A_2\,(k_x \sigma_x + k_y \sigma_y)\,. \tag{1.47}$$

The material parameters, extracted by fitting the energy spectrum of Equation (1.46) to the *ab initio* band structures of the topological insulators of the Bi_2Se_3 family, are listed in Table 1.2.

	Bi_2Se_3	Bi_2Te_3	Sb_2Te_3
C_0 [eV]	−0.28	−0.014	0.10
D_1 [eV Å^2]	1.46	1.65	−6.48
D_2 [eV Å^2]	22.81	29.47	−4.26
A_1 [eV Å]	1.94	0.55	1.69
A_2 [eV Å]	4.33	4.40	3.89
M_0 [eV]	0.30	0.26	0.21
B_1 [eV Å^2]	6.00	4.62	19.32
B_2 [eV Å^2]	70.38	72.80	63.91

Table 1.2: Fitted parameters of the low-energy effective Hamiltonian for Bi_2Se_3, Bi_2Te_3 and Sb_2Te_3 taken from Ref. [81].

Physically, the parameter M_0 is related to the $\mathbf{k} = 0$ bulk gap and controls the band inversion at the Γ point, $B_{1,2}$ capture the effective masses of the conduction and valence bands along k_z and in-plane directions, respectively, and $D_{1,2}$ describe the particle-hole asymmetry in the energy spectrum via quadratic corrections. The parameter A_1 governs the linear coupling between opposite-parity states along k_z, and A_2 describes the linear in-plane coupling, enforced by $\mathcal{C}_3$ rotational symmetry

to appear in the combinations $k_\pm$. The system described by Equation (1.46) is an insulator for $|D_2| < |B_2|$ and a topologically nontrivial phase, characterized by the presence of surface states in the bulk gap, emerges when the band inversion parameters $B_{1,2}$ and the bulk gap M_0 have the same sign $M_0 \cdot B_{1,2} > 0$ [23, 79, 85].

The energy spectra for the various TI compounds of the Bi_2Se_3 family, obtained by discretization of the Hamiltonian in Equation (1.46) on a finite lattice along the z direction and imposing periodic boundary conditions along x and y, are presented in Figure 1.7. For all parameter sets corresponding to the different materials under consideration, the energy spectrum exhibit a pair of linear gapless modes traversing the bulk gap and connecting valence and conduction bands. These modes correspond to the topologically protected surface states, whose emergence in the nontrivial phase is a direct consequence of the bulk–boundary correspondence. While the present plots are obtained by fixing $k_y = 0$, the energy dispersion calculated in the full k_x, k_y plane would reveal the characteristic Dirac-cone shape of these topological boundary modes.

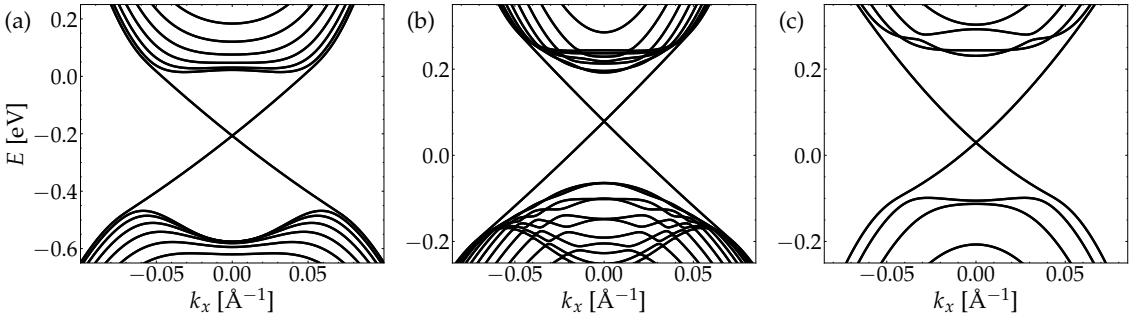

Figure 1.7: Energy spectra of (a) Bi_2Se_3, (b) Bi_2Te_3, and (c) Sb_2Te_3, obtained by discretizing the Hamiltonian in Equation (1.46) on a finite lattice with thickness $d = 100\,\text{Å}$ along the z direction, and periodic boundary conditions along x and y. The energy bands are shown as a function of k_x at fixed $k_y = 0$, using the material parameters listed in Table 1.2.

Magnetic Doping

While the materials of the Bi_2Se_3 family are intrinsically non-magnetic, a net magnetization can be induced by doping with magnetic elements such as chromium, vanadium, or manganese. The resulting magnetically doped TI is referred to as a *magnetic topological insulator* (MTI). Introducing such a spontaneous magnetization in proximity to the surfaces of a topological insulator breaks the time-reversal symmetry and substantially modifies the electronic structure, opening a gap in the surface spectrum and making the Dirac electrons massive [37, 38, 84].

The effect of a net magnetization can be incorporated into the low-energy theory through a Zeeman term of the form $\boldsymbol{\sigma} \cdot \boldsymbol{\Lambda}$, where $\boldsymbol{\Lambda} = (\Lambda_x, \Lambda_y, \Lambda_z)$ is the magnetization vector. In the following, we focus on the case of a MTI slab with in-plane dimensions much larger than its out-of-plane thickness d, and we consider a uniform magnetization oriented along the z axis. In this case, the three-dimensional slab of

magnetic TI can be modeled as [38]

$$\begin{aligned} h_{\mathrm{MTI}}(\mathbf{k}) &= h_{\mathrm{TI}}(\mathbf{k}) + \Lambda\sigma_z = \\ &= \varepsilon_0(\mathbf{k}) + A(\mathbf{k})\tau_x + M(\mathbf{k})\tau_z + \Lambda\sigma_z \,. \end{aligned} \tag{1.48}$$

The surface energy spectrum of Equation (1.48) near $\overline{\Gamma}$ for a slab with finite thickness $d = 100\,\text{Å}$ along the out-of-plane direction z and periodic boundary conditions in x and y is shown in Figure 1.8. The picture illustrates the difference between the gapless spectrum obtained in the presence of TRS with $\Lambda = 0$ and the massive Dirac-cone spectrum obtained for $\Lambda = 50$ meV.

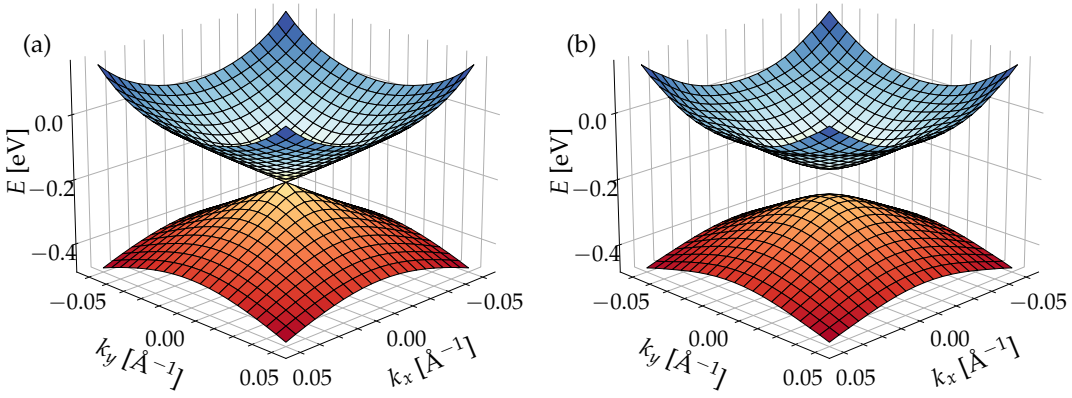

Figure 1.8: Surface state energy spectrum for Bi_2Se_3 plotted as a function of in-plane momentum k_x and k_y near the $\overline{\Gamma}$ point. The bands are obtained by discretizing the Hamiltonian in Equation (1.48) on a finite lattice with thickness $d = 100\,\text{Å}$ along the z direction, and periodic boundary conditions along x and y, using the material parameters listed in Table 1.2. Panel (a) shows a non-magnetic TI with $\Lambda = 0$, while panel (b) depict a MTI with $\Lambda = 50$ meV.

The out-of-plane spin polarization of the surface states of the MTI is also influenced by the presence of a finite magnetization. In the TRS-preserving case ($\Lambda = 0$), the states near the $\overline{\Gamma}$ point are equal superpositions of $\sigma =\uparrow$ and $\sigma =\downarrow$ components. When time-reversal symmetry is broken by a finite magnetization ($\Lambda \neq 0$), however, the states in the vicinity of the Dirac point acquire a net spin polarization, with opposite orientations for the conduction and valence surface bands [81].

Owing to the presence of topologically protected surface states that can be readily gapped by doping with magnetic elements, MTIs of the Bi_2Se_3 family have attracted considerable interest and emerged as a versatile platform for engineering other topological phases. First, when confined to two-dimensional geometries, a robust QAH state can be realized via magnetic doping, even in the absence of an external magnetic field [15, 39]. Second, when placed in proximity to a conventional superconductor, TIs provide a promising route for realizing topological superconductivity and Majorana modes [39, 41, 45]. The remainder of this chapter is devoted to the discussion of effective one- and two-dimensional models relevant to the description of magnetic topological insulators in confined geometries. Such effective models

will be subsequently used to investigate transport and superconducting properties in MTI-SC heterostructurs.

1.2.3 Two-Dimensional Surface Hamiltonian

We consider here a *thin film* of topological insulator, with finite thickness d along the z direction and translational invariance in the in-plane directions x and y. In the topologically nontrivial phase, gapless surface states appear at the two interfaces of the system, located at $z = 0$ and $z = d$. The low-energy dynamics of these modes can be captured by an effective two-dimensional Hamiltonian acting in the subspace of the surface states.

To construct such a model, we start from the three-dimensional MTI model and project it onto the subspace spanned by the two surface-localized eigenstates. The Hamiltonian in Equation (1.46) can be conveniently decomposed as [84]

$$h_{\mathrm{TI}}(k_x, k_y, k_z) = h_0(k_z) + h_{\parallel}(k_x, k_y)\,, \tag{1.49}$$

where the first term encodes the motion along z

$$h_0(k_z) = D_1 k_z^2 + \left(M_0 - B_1 k_z^2\right)\tau_z + A_1 k_z \tau_x \sigma_z\,, \tag{1.50}$$

and the second one contains the in-plane motion

$$h_{\parallel}(k_x, k_y) = C_0 + D_2 k_{\parallel}^2 - B_2 k_{\parallel}^2\,\tau_z + A_2(k_x\sigma_x + k_y\sigma_y)\tau_x\,. \tag{1.51}$$

Assuming $C_0 = 0$, which merely shifts the spectrum rigidly without affecting the underlying physics, the in-plane contribution vanishes at the $\overline{\Gamma}$ point, where $h_{\parallel} = 0$. At this high-symmetry point, the Hamiltonian therefore reduces to h_0 alone. Replacing $k_z \to -i\partial_z$ and imposing that the wavefunction vanishes at the boundaries $z = 0$ and $z = d$, one finds that the spectrum contains four low-energy eigenvalues well separated from the higher-energy states. Figure 1.9 shows the lowest eigenvalues E_n of the discretized energy spectrum of Equation (1.50), together with the corresponding probability densities $|\psi_n(z)|^2$.

Panel (a) illustrates that these four lowest eigenvalues are separated from the higher-energy modes by an energy gap of approximately 300 meV, while panel (b) shows that these modes are strongly localized near the two interfaces, since they correspond to the gapless boundary states of the topological phase. For the thickness considered here, the four lowest–energy modes exhibit identical probability–density profiles. In thinner slabs, however, hybridization between the top and bottom surfaces lifts this degeneracy, leading to different spatial profiles. In the absence of magnetization $\Lambda = 0$, time-reversal symmetry is preserved, and each mode is twofold degenerate due to Kramers' theorem. Without loss of generality, we denote their energies as $E_{\pm}$, and the corresponding eigenstates as φ_σ and χ_σ for $\sigma = \uparrow, \downarrow$.

Projecting the full three-dimensional Hamiltonian onto the basis of low-energy eigenstates of h_0

$$\left\{|\varphi_\uparrow\rangle\,, |\chi_\downarrow\rangle\,, |\varphi_\downarrow\rangle\,, |\chi_\uparrow\rangle\right\}, \tag{1.52}$$

we obtain a reduced model in the form of [35, 80, 84]

$$\tilde{h}_{\mathrm{2D}}(k_x, k_y) = \begin{pmatrix} h_+(k_x, k_y) & 0 \\ 0 & h_-^*(k_x, k_y) \end{pmatrix}. \tag{1.53}$$

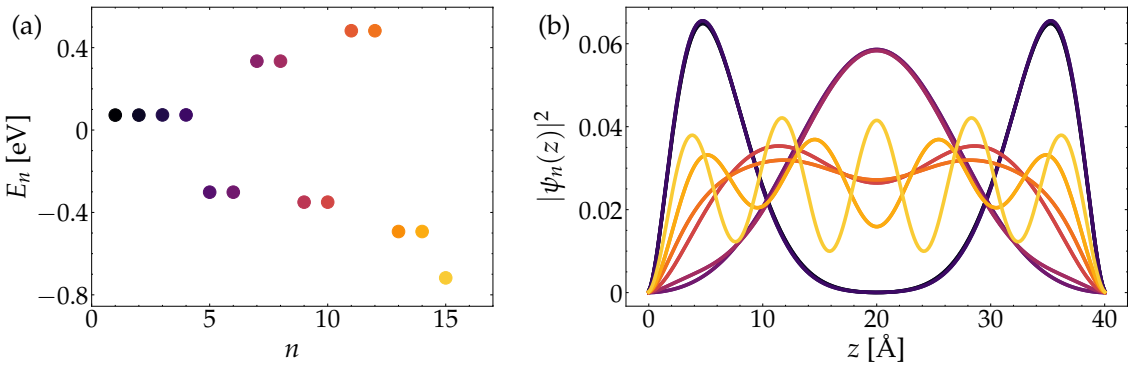

Figure 1.9: Discretized energy spectrum of Equation (1.50) computed using a finite lattice of thickness $d = 40\,\text{Å}$. Panel (a) presents the lowest-energy eigenvalues near the Dirac point, while panel (b) shows the probability densities $|\psi_n(z)|^2$ of the corresponding eigenstates. Eigenvalues and their associated probability densities are plotted using the same color. The plots were obtained using the material parameters of Bi_2Se_3 listed in Table 1.2.

Here, $h_\pm$ are two-dimensional Dirac Hamiltonians given by

$$h_\pm(k_x, k_y) \equiv -\mu - Dk_\parallel^2 + v_\text{F}\,(k_y\sigma_x - k_x\sigma_y) + \left(m_0 \pm \Lambda + m_1 k_\parallel^2\right)\sigma_z\,, \tag{1.54}$$

where v_F is the Fermi velocity and the parameter D characterizes the particle-hole asymmetry of the spectrum. The coefficients can be obtained from the material parameters of the three-dimensional Hamiltonian through [84]

$$\begin{aligned}
\mu &\equiv -\frac{E_- + E_+}{2} - C_0\,,\\
D &\equiv \frac{B_2}{2}\left(\langle\varphi_\uparrow|\tau_z|\varphi_\uparrow\rangle + \langle\chi_\uparrow|\tau_z|\chi_\uparrow\rangle\right) - D_2\,,\\
v_\text{F} &\equiv -\text{i}A_2\langle\varphi_\uparrow|\tau_x|\chi_\downarrow\rangle \in \mathbb{R}\,,\\
m_0 &\equiv \frac{E_- - E_+}{2}\,,\\
m_1 &\equiv -\frac{B_2}{2}\left(\langle\varphi_\uparrow|\tau_z|\varphi_\uparrow\rangle - \langle\chi_\uparrow|\tau_z|\chi_\uparrow\rangle\right)\,.
\end{aligned} \tag{1.55}$$

The values of the coefficients m_0, m_1, D, v_F for a thin film of Bi_2Se_3 are listed in Table 1.3 for several values of the film thickness d.

The eigenstates $|\varphi_\sigma\rangle$ and $|\chi_\sigma\rangle$ can be further combined to construct states $|t,\sigma\rangle$ and $|b,\sigma\rangle$ localized near the top and bottom surfaces of the thin film respectively. Explicitly, these states are given by

$$|t,\sigma\rangle = \frac{1}{\sqrt{2}}\left(|\varphi_\sigma\rangle + |\chi_\sigma\rangle\right)\,, \qquad |b,\sigma\rangle = \frac{1}{\sqrt{2}}\left(|\varphi_\sigma\rangle - |\chi_\sigma\rangle\right)\,. \tag{1.56}$$

The probability-density profiles of the surface-localized states $|t,\sigma\rangle$ and $|b,\sigma\rangle$ are shown in Figure 1.10 for a Bi_2Se_3 thin film of thickness $d = 40\,\text{Å}$. The states are

d [Å]	m_0 [eV]	m_1 [eV Å^2]	D [eV Å^2]	v_F [eV Å]
20	0.069	45.48	−17.35	4.09
30	−0.020	19.81	−12.64	4.06
40	−0.011	−2.82	−12.05	4.06
50	−0.0075	−4.29	−12.29	4.06
60	0.0012	−0.59	−12.24	4.06
70	0.00026	0.51	−12.24	4.06

Table 1.3: Values of the coefficients m_0, m_1, D, v_F for a TI slab ($\Lambda = 0$) with thickness between two and seven QLs. Above seven quintuple layers, m_0 and m_1 have negligible magnitudes and D and v_F become approximately constant. The values of the coefficients are taken from Ref. [84].

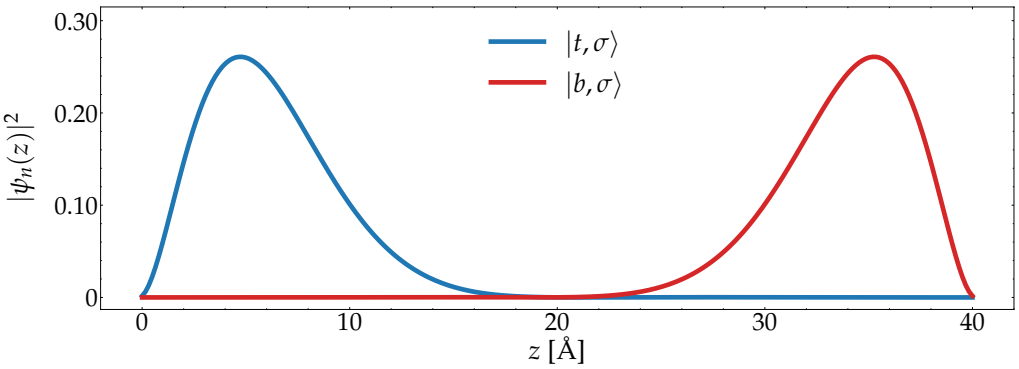

Figure 1.10: Probability density profiles $|\psi_n(z)|^2$ for the surface-localized basis states $|t,\sigma\rangle$ and $|b,\sigma\rangle$ obtained through Equation (1.56) for a Bi_2Se_3 thin film of thickness $d = 40$ Å. The eigenstates are normalized such that $\int \mathrm{d}z\, |\psi(z)|^2 = 1$.

exponentially confined near the top ($z = 0$) and bottom ($z = d$) interfaces, with localization lengths of approximately 10 Å.

In the basis of states

$$\left\{|t,\uparrow\rangle, |t,\downarrow\rangle, |b,\uparrow\rangle, |b,\downarrow\rangle\right\}, \tag{1.57}$$

where $\lambda = t, b$ labels the top and bottom interfaces of the thin film and $\sigma = \uparrow, \downarrow$ is the electron spin, the Hamiltonian in Equation (1.53) takes the form [44, 84]

$$h_{2\mathrm{D}}(k_x, k_y) = -\mu - Dk_\parallel^2 + v_\mathrm{F}\left(k_y\sigma_x - k_x\sigma_y\right)\lambda_z + \Lambda\sigma_z + m(k_x, k_y)\lambda_x\,, \tag{1.58}$$

where $m(k_x, k_y) = m_0 + m_1 k_\parallel^2$ and the Pauli matrices $\lambda_{x,y,z}$ and $\sigma_{x,y,z}$ act on the top/bottom layer and spin degrees of freedom, respectively. The energy band structure of a Bi_2Se_3 thin film described by Equation (1.58) is shown in Figure 1.11, illustrating the effect of confinement and finite magnetization on the surface spectrum. Here, we assumed an effective two-dimensional geometry with thickness $d = 40$ Å along z and infinite translational invariance along the in-plane directions x and y.

The asymmetry in the dispersion of the surface states above and below the Dirac point arises from a finite value of the parameter D, which accounts for electron–hole asymmetry in the system [81]. The figure illustrates that, even in the absence of

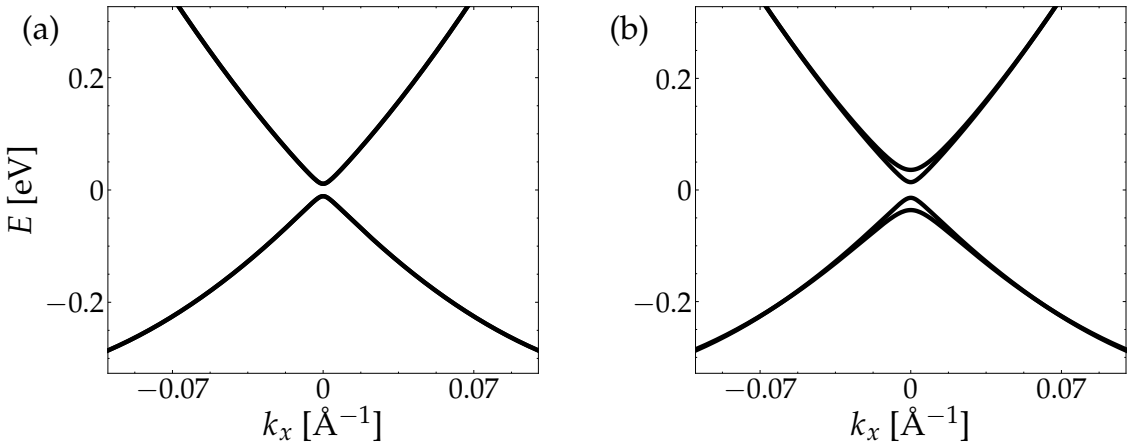

Figure 1.11: Energy dispersion of a Bi_2Se_3 thin film of thickness $d = 40\,\text{Å}$ along k_x with $k_y = 0$ described by Equation (1.58). The surface energy spectrum in (a) corresponds to a non-magnetic TI with $\Lambda = 0$, while that in (b) corresponds to a MTI with $\Lambda = 25$ meV. Both were obtained with the Hamiltonian parameters listed in Table 1.3.

magnetization, $\Lambda = 0$, the hybridization between top and bottom interfaces in a very thin film opens a finite-size gap m_0 in the surface energy spectrum, making the Dirac electrons massive. Furthermore, the presence of a finite Zeeman term lifts the degeneracy and opens a magnetic gap Λ [37, 38].

Quantum Anomalous Hall State

Omitting the particle–hole asymmetry term $Dk_\parallel^2$, the Hamiltonian in Equation (1.58) is equivalent to the four-band Bernevig–Hughes–Zhang (BHZ) model for two-dimensional QSH insulators, which has been shown to reproduce the behavior of the bulk Hamiltonian in Equation (1.46) in the thin-film limit [20, 86, 87]. In the absence of magnetic doping, it belongs to the unitary symmetry class AII, and its topological phase is characterized by a binary $\mathbb{Z}_2$ index. Conversely, when $\Lambda \neq 0$, TRS is broken and the system falls into the symmetry class A, whose topological properties are described by an integer-valued Chern number $\mathbb{Z}$. Physically, this implies that when a three-dimensional TI is confined to a two-dimensional slab geometry, such that only the topological surface states at the top and bottom interfaces remain, the effective 2D system can realize a trivial insulating phase, a QAH state, or a QSH insulator [39, 81, 84]. The state of the system is determined by the interplay between the surface gap m_0 and the magnetization Λ.

Within the low-energy model, topological phase transitions occur when the effective gap $m_0 \pm \Lambda$ changes sign. For $\Lambda = 0$, a sign reversal of m_0—for instance, when increasing the thickness from two to three quintuple layers (see Table 1.3)—marks the transition from a trivial insulator to a QSH insulator [81, 87]. For the case of finite magnetization $\Lambda \neq 0$, instead, the Chern number vanishes when $0 < |\Lambda| < |m_0|$, indicating that the system is in a trivial phase. Conversely, a sufficiently strong magnetic exchange term satisfying $|\Lambda| > |m_0|$ drives the system into a QAH phase [38–40, 84]. The energy spectrum of Equation (1.58) discretized over a finite lattice

with width $L_y = 5\,\mu$m along y and periodic boundary conditions along x is shown in Figure 1.12.

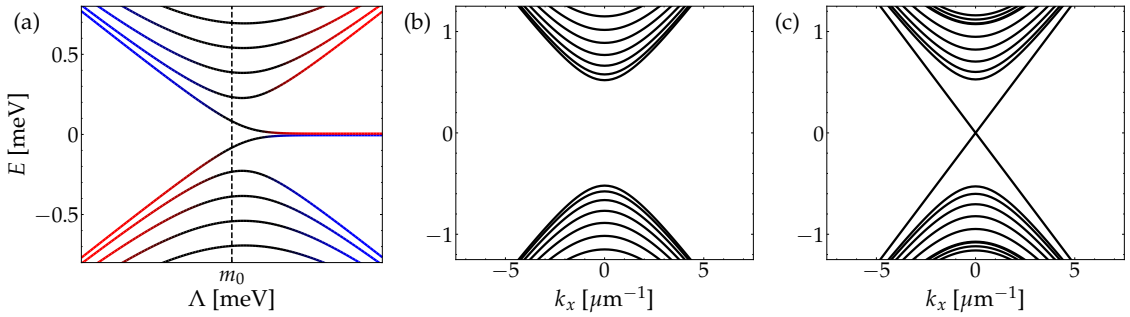

Figure 1.12: Energy spectrum of a thin film TI obtained by discretizing Equation (1.58) on a finite lattice with width $L_y = 5\,\mu$m along y and periodic boundary conditions along x. Panel (a) displays the $k_x = 0$ energy eigenvalues as a function of magnetization Λ, highlighting the closing and reopening of the surface gap at $\Lambda = m_0$. Red (blue) indicates spin-up (spin-down) polarized states as obtained from Equation (1.59). Panels (b)–(c) show the momentum-resolved spectrum near $k_x = 0$ for a trivial insulator with $\Lambda = 0.5\,$meV and for a QAH phase with $\Lambda = 1.5\,$meV, respectively. The remaining parameters were set to $m_0 = 1\,$meV, $m_1 = 0.001\,\text{meV}\mu\text{m}^2$, $v_F = 0.26\,\text{meV}\,\mu$m, and $D = 0$.

The figure illustrates the phase transition from a two-dimensional trivial insulator to the QAH state. Panel (a) shows that when the magnetization becomes sufficiently large to overcome the finite-size gap m_0, the $k_x = 0$ surface gap closes and subsequently reopens, with the emergence of spin polarized zero-energy states within the gap. These modes correspond to the topologically protected chiral edge states which characterize the unconventional transport properties of a QAH insulator and are responsible for the quantization of the transverse conductance. The colors represent states with opposite spin polarization along the z axis, obtained through the expectation value

$$\langle \sigma_z \rangle = \int \mathrm{d}z\, \psi^\dagger(z)\, \sigma_z\, \psi(z)\,. \tag{1.59}$$

The resulting spin polarization highlights that the order of valence and conduction bands is reverted when the bulk gap reopens. Panel (b) depicts the energy spectrum of a trivial insulator with $\mathcal{C} = 0$, whereas panel (c) shows that of a QAH insulator with $\mathcal{C} = 1$, characterized by a pair of gapless boundary modes crossing the surface gap, one per each edge of the system. The Chern number can be inferred via the bulk-boundary correspondence by counting the number of gapless linear edge states crossing the surface gap.

To illustrate that the gapless linear modes emerging within the surface gap in the QAH phase are the topologically protected edge states whose existence is guaranteed by the bulk-boundary correspondence, we discretize Equation (1.58) on a finite lattice of width $L_y = 1\,\mu$m along y, imposing periodic boundary conditions along x. The resulting discrete eigenvalues E_n of the lowest-energy states, together with their corresponding probability densities $\Psi_n(y)$, are shown in Figure 1.13.

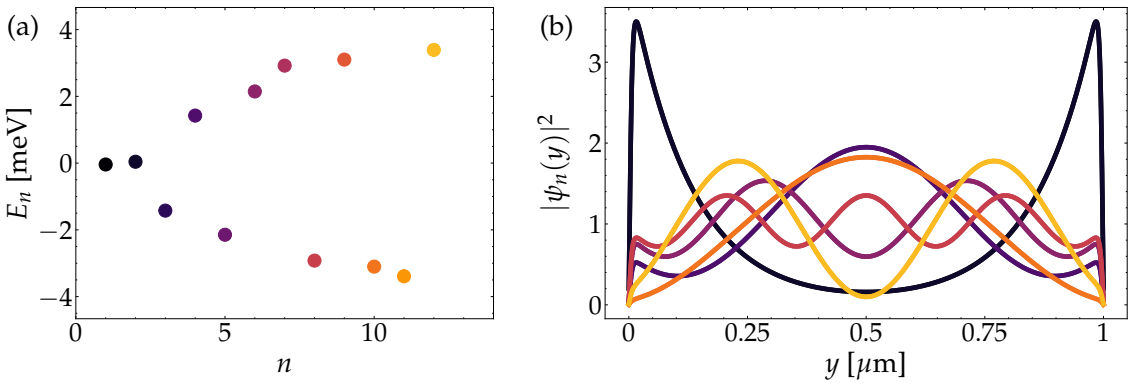

Figure 1.13: Discretized energy spectrum of Equation (1.58) obtained using a finite lattice of width $L_y = 1\,\mu$m along y and with periodic boundary conditions along x. Panel (a) shows the lowest-energy eigenvalues at the Dirac point $k_x = 0$, while panel (b) displays the corresponding probability densities $\psi_n(y)$. Eigenvalues and their associated probability densities are plotted using the same color. The remaining parameters were set to $m_0 = 1\,\text{meV}$, $m_1 = 0.001\,\text{meV}\mu\text{m}^2$, $v_F = 0.26\,\text{meV}\,\mu\text{m}$, $\mu = 0$ and $D = 0$.

Owing to topological protection, the two lowest-energy states appear exactly at zero energy and are localized near the system boundaries, with probability density peaks around $y = 0$ and $y = L_y$. It can be seen from the figure that, for the chosen parameters, they have a localization length of around ≈ 200 nm. In contrast, the higher-energy states display a finite probability density across the entire transverse section of the thin film and are therefore delocalized over the entire surface.

Summary

In this chapter, we developed the theoretical framework necessary to describe the low-energy physics of topological insulators of the Bi_2Se_3 family. We first introduced the main concepts of topological band theory, defining topological invariants such as the Chern number and the $\mathbb{Z}_2$ index, which classify two-dimensional systems according to the presence or absence of TRS. This formalism culminates in the periodic table of topological phases, which provides a systematic classification of gapped free-fermion Hamiltonians based on their symmetries and dimensionality.

We then turned to three-dimensional topological insulators of the Bi_2Se_3 family. After presenting their lattice and bulk band structure within the 3D $\mathbf{k}\cdot\mathbf{p}$ Hamiltonian near the Γ point, we showed how Dirac-like surface states emerge at the system boundaries as a consequence of the nontrivial topology. To capture the low-energy dynamics in thin-film geometries, we derived an effective two-dimensional model describing surface states localized at the top and bottom interfaces of the film. Special emphasis was placed on the role of magnetization, introduced via a Zeeman term, which gaps out the surface spectrum and drives a two-dimensional system into a QAH phase supporting chiral edge channels.

The effective Hamiltonians introduced in this chapter, namely Equations (1.46) and (1.58), will serve as the foundation for the following chapters. They will be

employed to model heterostructures formed by TIs and conventional superconductors, to analyze their transport properties, and to describe the induced pairing produced by proximity effect. In particular, when superconducting correlations are induced in the chiral edge channels of a magnetically doped TI thin film, the resulting two-dimensional QAH insulator provides the starting point for the realization of topological superconducting states, which are the focus of the next chapter.

Chapter 2

Topological Superconductivity

Overview

The topological band theory outlined in the first chapter applies to gapped Hamiltonians, encompassing both insulating and superconducting systems. While a variety of nontrivial insulating phases have been experimentally realized over the past decades, topological superconductivity has so far remained elusive. A particularly promising route toward engineering nontrivial SC states is represented by hybrid heterostructures consisting of thin films of MTIs in proximity to conventional superconductors. In such systems, the induced pairing can give rise to topological superconducting phases in both one- and two-dimensional geometries.

The emergence of topological superconductivity and Majorana quasiparticles in such hybrid systems is the focus of this chapter. In Section 2.1, we review the Bogoliubov–de Gennes framework and, building on the previous chapter, we introduce the proximitized Hamiltonians that describe induced pairing in three- and two-dimensional MTIs. In Section 2.2, we discuss the emergence of two-dimensional TSC states in thin films of proximitized topological insulators, characterized by propagating Majorana modes along the edges. Finally, in Section 2.3, we focus on effective one-dimensional MTI–SC nanowires, which can realize topological superconducting phases, that host zero-energy Majorana bound states localized at their ends.

2.1 Bogoliubov de Gennes Framework

The general ideas of topological band theory discussed in Section 1.1 can be straightforwardly extended from insulating to superconducting systems, since both are characterized by an energy gap for single particle excitations. In presence of translational invariance, a superconducting system can be described by the Hamiltonian [88–91]

$$H_{\mathrm{SC}} = \frac{1}{2} \sum_{\mathbf{k}} \Psi_{\mathbf{k}}^{\dagger} \, h_{\mathrm{BdG}}(\mathbf{k}) \, \Psi_{\mathbf{k}} \,, \tag{2.1}$$

which is expressed in the Nambu basis of electron and hole states

$$\Psi_{\mathbf{k}} = \begin{bmatrix} \psi_{\mathbf{k}} \\ \left(\psi^{\dagger}_{-\mathbf{k}}\right)^{T} \end{bmatrix} . \tag{2.2}$$

Here $\psi_{\mathbf{k}}$ denotes an n-component wavefunction in the single-particle basis describing the electron degrees of freedom, while $\psi^{\dagger}_{\mathbf{k}}$ corresponds to the hole parts, which can be seen as the absence of an electron in the corresponding state. In the second quantization formalism, $\psi_{\mathbf{k}}$ and $\psi^{\dagger}_{\mathbf{k}}$ are interpreted as annihilation and creation operators for electrons and holes, respectively. In this basis, the momentum-dependent Hamiltonian $h_{\mathrm{BdG}}(\mathbf{k})$ is given by [92, 93]

$$h_{\mathrm{BdG}}(\mathbf{k}) = \begin{pmatrix} h_0(\mathbf{k}) - \mu & \Delta_{\mathbf{k}} \\ \Delta^{\dagger}_{\mathbf{k}} & -h^{*}_0(-\mathbf{k}) + \mu \end{pmatrix} , \tag{2.3}$$

where h_0 is the normal-state Hamiltonian describing the non-proximitized system, and $\Delta_{\mathbf{k}}$ is the induced pairing. Equation (2.3) takes the name of Bogoliubov–de Gennes (BdG) Hamiltonian, and for $h_0(\mathbf{k}) = h^{*}_0(-\mathbf{k})$ it can be expressed as

$$h_{\mathrm{BdG}}(\mathbf{k}) = \Big[h_0(\mathbf{k}) - \mu\Big]\gamma_z + \Delta_{\mathrm{r}}(\mathbf{k})\gamma_x - \Delta_{\mathrm{i}}(\mathbf{k})\gamma_y \, , \tag{2.4}$$

where $\gamma_{x,y,z}$ are Pauli matrices acting in the Nambu space of electrons and hole, and we decomposed the pairing as

$$\Delta_{\mathbf{k}} = \Delta_{\mathrm{r}}(\mathbf{k}) + \mathrm{i}\Delta_{\mathrm{i}}(\mathbf{k}) \, . \tag{2.5}$$

In general, the BdG Hamiltonian can be diagonalized by introducing Bogoliubov quasiparticle operators, which are linear combinations of electron and hole ones [88, 92, 93]. An eigenstate $\Psi_{\mathbf{k},E}$ of the superconducting BdG Hamiltonian in Equation (2.3) with energy E

$$h_{\mathrm{BdG}}(\mathbf{k})\, \Psi_{\mathbf{k},E} = E\, \Psi_{\mathbf{k},E} \, , \tag{2.6}$$

can be expressed in the Nambu basis of Equation (2.2) as

$$\Psi_{\mathbf{k},E} = \begin{bmatrix} u_{\mathbf{k},E} \\ v_{\mathbf{k},E} \end{bmatrix} , \tag{2.7}$$

where $u_{\mathbf{k},E}$ and $v_{\mathbf{k},E}$ are complex amplitudes describing the electron and hole components of the wave function, respectively. The corresponding Bogoliubov operator, which creates a mixed electron–hole quasiparticle excitation in the superconducting condensate, is defined as

$$\Gamma_{\mathbf{k},E} = u^{*}_{\mathbf{k},E}\, \psi_{\mathbf{k}} + v^{*}_{\mathbf{k},E}\, \psi^{\dagger}_{-\mathbf{k}} \, . \tag{2.8}$$

For any normal-state Hamiltonian h_0, Equation (2.3) satisfies an intrinsic particle–hole symmetry [69, 70, 94]

$$\mathcal{P}\, h_{\mathrm{BdG}}(\mathbf{k})\, \mathcal{P}^{-1} = -h_{\mathrm{BdG}}(-\mathbf{k}), \tag{2.9}$$

where the particle–hole operator is defined as $\mathcal{P} = \gamma_x \mathcal{K}$ and acts reversing the quasiparticle momentum. In the absence of pairing, $\Delta_{\mathbf{k}} = 0$, the Hamiltonian trivially reduces to two copies of h_0 corresponding to the electron and hole sectors, which are related by PHS. A finite pairing $\Delta_{\mathbf{k}} \neq 0$ opens a gap in the band structure and couples particle and hole states. Nevertheless, the spectrum remains symmetric around zero energy. Indeed, applying Equation (2.9) to Equation (2.6) directly yields

$$h_{\mathrm{BdG}}(-\mathbf{k})\,\mathcal{P}\,\Psi_{\mathbf{k},E} = -E\,\mathcal{P}\,\Psi_{\mathbf{k},E}\,, \tag{2.10}$$

showing that every eigenstate at energy E and momentum $\mathbf{k}$ has a particle–hole related partner

$$\Psi_{-\mathbf{k},-E} = \mathcal{P}\,\Psi_{\mathbf{k},E}, \tag{2.11}$$

which is itself an eigenstate of the BdG Hamiltonian with energy $-E$ and momentum $-\mathbf{k}$. Physically, the two states are redundant, and the corresponding Bogoliubov operators satisfy [24]

$$\Gamma_{\mathbf{k},E} = \Gamma^{\dagger}_{-\mathbf{k},-E}\,, \tag{2.12}$$

meaning that creating a quasiparticle at energy $-E$ and momentum $-\mathbf{k}$ is equivalent to removing one at energy E and momentum $\mathbf{k}$. As an illustrative example of how the energy spectrum evolves, Figure 2.1 displays the energy bands of a free-electron model described by the normal-state Hamiltonian $h_0(\mathbf{k}) = |\mathbf{k}|^2$, together with the spectra obtained by diagonalizing the corresponding BdG Hamiltonian $h_{\mathrm{BdG}}(\mathbf{k})$ in the absence and in the presence of superconducting pairing.

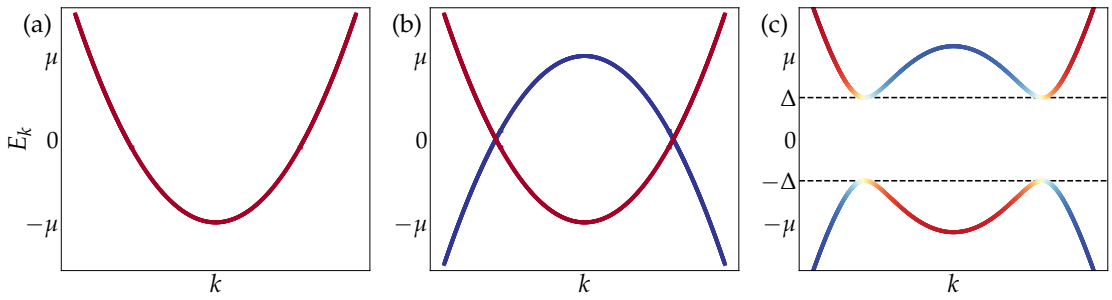

Figure 2.1: Energy spectrum of a free-electron system with parabolic dispersion, obtained from the normal-state Hamiltonian and from the corresponding BdG Hamiltonian in Equation (2.3). Panel (a)–(b) shows the normal-state spectrum obtained from h_0 and from the BdG Hamiltonian at $\Delta_{\mathbf{k}} = 0$, respectively. Panel (c) displays the Bogoliubov spectrum for a finite pairing amplitude $\Delta_{\mathbf{k}} \equiv \Delta \neq 0$, where an energy gap opens at the Fermi level coupling electron and hole branches. Red and blue denote electron-like and hole-like states, respectively, while yellow indicates mixed states.

From a topological perspective, the BdG Hamiltonian in Equation (2.3) can be classified according to the periodic table discussed in Section 1.1.3, and, depending on the underlying symmetries and dimensionality, may realize topologically nontrivial phases. Due to the bulk–boundary correspondence, such phases are characterized by gapless boundary excitations, which obey the constraint in Equation (2.12). At

zero energy and particle–hole invariant momenta $\mathbf{k} = -\mathbf{k}$ this reduces to [24]

$$\Gamma_0 = \Gamma_0^\dagger \,, \tag{2.13}$$

implying that an *unpaired* topologically protected zero-energy modes localized on one of the boundaries of the system realizes a quasiparticle excitation that is identical to its own antiparticle. Such zero-energy modes are therefore a realization of *Majorana* particles in condensed-matter systems [29, 73, 74, 95, 96].

2.1.1 Effective Model for Proximitized MTIs

Different topological superconducting phases with Majorana modes on the boundaries can be realized in thin films of MTIs by inducing a finite pairing via proximity to a conventional superconductor. Such hybrid systems are conveniently described within a low-energy BdG framework, based on the effective models introduced in Sections 1.2.2 and 1.2.3.

A three-dimensional proximitized MTI can be described within the BdG formalism, starting from the normal-state Hamiltonian $h_{3\mathrm{D}}$ introduced in Equation (1.48). Within this framework, the general BdG Hamiltonian of Equation (2.3) takes the explicit form [97, 98]

$$h_{3\mathrm{D}}^{\mathrm{BdG}}(\mathbf{k}) = \begin{pmatrix} h_{3\mathrm{D}}(\mathbf{k}) & \mathrm{i}\,\Delta\sigma_y \\ -\mathrm{i}\,\Delta^*\sigma_y & -h_{3\mathrm{D}}^*(-\mathbf{k}) \end{pmatrix} , \tag{2.14}$$

which is expressed in the Nambu basis of Equation (2.2) and where Δ denotes a momentum-independent *scalar* pairing potential. An equivalent formulation can be obtained by adopting an alternative Nambu basis, defined as [99]

$$\Psi_{\mathbf{k}} = \begin{bmatrix} \psi_{\mathbf{k}} \\ -\mathrm{i}\,\sigma_y \left(\psi_{-\mathbf{k}}^\dagger\right)^T \end{bmatrix} , \tag{2.15}$$

in which the hole components correspond to time-reversed electron operators. Within this basis, the three-dimensional BdG Hamiltonian takes the form [99, 100]

$$h_{3\mathrm{D}}^{\mathrm{BdG}}(\mathbf{k}) = \begin{pmatrix} h_{3\mathrm{D}}(\mathbf{k}) & \Delta \\ \Delta^* & -\sigma_y\, h_{3\mathrm{D}}^*(-\mathbf{k})\, \sigma_y \end{pmatrix} . \tag{2.16}$$

For simplicity, we consider here a conventional s-wave spin-singlet pairing, that is proportional to the identity in orbital space [98]. For generality, Equation (2.14) can be expressed in terms of Pauli matrices as

$$\begin{aligned} h_{3\mathrm{D}}^{\mathrm{BdG}}(\mathbf{k}) = {} & \Big[\varepsilon_0(\mathbf{k}) + M(\mathbf{k})\tau_z + \Lambda\sigma_z + A_2 k_y \sigma_y\Big]\gamma_z \\ & + \left(A_1 k_z \sigma_z + A_2 k_x \sigma_x\right)\gamma_0 \\ & - \mathrm{Re}\,(\Delta)\,\sigma_y\gamma_y - \mathrm{Im}\,(\Delta)\,\sigma_y\gamma_x \,, \end{aligned} \tag{2.17}$$

where $\sigma_{x,y,z}$ act on the spin subspace, $\tau_{x,y,z}$ on the orbital (parity) sector, and $\gamma_{x,y,z}$ on the Nambu particle–hole space, with γ_0 denoting the corresponding identity matrix. The terms entering the Hamiltonian are defined in Equations (1.45) and (1.47).

In a similar way, an induced pairing can be incorporated into the low-energy model $h_{2\mathrm{D}}$ introduced in Equation (1.58), which captures the physics of the topological surface states on the top and bottom interfaces of an effective two-dimensional MTI thin film. The corresponding BdG Hamiltonian, obtained from the general expression in Equation (2.3), becomes [42, 44, 101, 102]

$$h_{2\mathrm{D}}^{\mathrm{BdG}}(k_x,k_y)=\begin{pmatrix} h_{2\mathrm{D}}(k_x,k_y) & \Delta \\ \Delta^\dagger & -h_{2\mathrm{D}}^*(-k_x,-k_y)\end{pmatrix}, \qquad \Delta=\begin{pmatrix}\Delta_1 & 0\\ 0 & \Delta_2\end{pmatrix}\mathrm{i}\sigma_y\,, \tag{2.18}$$

where Δ_1 and Δ_2 are the pairing potential induced into the top and bottom surfaces of the thin film, respectively. By defining $\Delta_\pm \equiv \frac{1}{2}(\Delta_1 \pm \Delta_2)$, it is possible to express Equation (2.18) in terms of Pauli matrices as

$$\begin{aligned} h_{2\mathrm{D}}^{\mathrm{BdG}}(k_x,k_y) = {} & \Big[-(\mu + Dk_\parallel^2) + m(k_x,k_y)\lambda_x + \Lambda\sigma_z\Big]\gamma_z \\ & + v_F\left(k_y\sigma_x\lambda_z\gamma_0 - k_x\sigma_y\lambda_z\gamma_z\right) \\ & - \mathrm{Re}\,\left(\Delta_+ + \Delta_-\lambda_z\right)\sigma_y\gamma_y - \mathrm{Im}\,\left(\Delta_+ + \Delta_-\lambda_z\right)\sigma_y\gamma_x\,, \end{aligned} \tag{2.19}$$

where $\sigma_{x,y,z}$ act on the spin subspace, $\lambda_{x,y,z}$ on the top/bottom layer subspace, and $\gamma_{x,y,z}$ on the Nambu space of particles and holes, with γ_0 denoting the corresponding identity matrix.

When TRS is broken by a finite magnetization $\Lambda \neq 0$, the BdG Hamiltonians in Equations (2.17) and (2.19) belong to symmetry class D [69, 70], featuring particle–hole symmetry alone with $\mathcal{P}^2 = +1$. According to Table 1.1, in two dimensions ($d = 2$), their bulk topology is characterized by an integer invariant, analogous to the Chern number, which counts the chiral edge modes propagating along the boundary of a finite system. This phase is the superconducting analog of the QH state and is commonly referred to as a *chiral* topological superconductor [41, 42, 103].

Although the physical time-reversal symmetry is broken by the Zeeman coupling, the Hamiltonians admit a time-reversal-like transformation that remains preserved even in the presence of a finite magnetization. As a result, the system can be also classified in terms of time-reversal-like, particle–hole, and chiral symmetries, and falls within the BDI symmetry class [46, 69, 70]. Therefore, in one dimension ($d = 1$), the corresponding band topology is characterized by an integer invariant $N_{\mathrm{BDI}} \in \mathbb{Z}$, which counts the number of zero-energy bound states localized at the wire ends, identified as Majorana bound states (MBSs). In this sense, the proximitized one-dimensional QAH state effectively realizes a 1D p-wave SC [76, 104, 105].

2.2 Chiral Topological Superconductor

We begin by discussing the physical properties of a two-dimensional proximitized system described by the effective 2D Hamiltonian in Equation (2.19). Equivalent results can also be derived from the three-dimensional model of Equation (2.17), provided that the system thickness d along the out-of-plane z direction remains much smaller than the in-plane dimensions $L_{x,y}$.

For the special case $\mu = 0$, $D = 0$, and $\Delta_1 = -\Delta_2$ the Hamiltonian can be rewritten as the sum of four independent massive Dirac Hamiltonians [84]

$$h_{\mathrm{2D}}^{\mathrm{BdG}}(k_x, k_y) = \sum_{\eta=\pm} \sum_{\kappa=\pm} \chi^{\dagger}_{\mathbf{k},\,\eta\kappa}\, h_{\eta\kappa}(k_x, k_y)\, \chi_{\mathbf{k},\,\eta\kappa}\,, \tag{2.20}$$

where

$$h_{\eta\kappa}(k_x, k_y) = v_F\,(k_y\sigma_x - \kappa k_x\sigma_y) + m_{\eta\kappa}(k_x, k_y)\sigma_z\,. \tag{2.21}$$

The mass terms in each Dirac Hamiltonian have all the same general form

$$m_{\eta\kappa}(k_x, k_y) = m_{0,\,\eta\kappa} + m_{1,\,\eta\kappa}k_{\parallel}^2 \tag{2.22}$$

where

$$m_{0,\,\eta\kappa} = \kappa\Lambda + \eta\kappa m_0 + |\Delta|, \qquad m_{1,\,\eta\kappa} = \eta\kappa m_1. \tag{2.23}$$

The topology of the Hamiltonian in Equation (2.20) is characterized by an integer invariant $\mathcal{N}$, which is the analogue of the Chern invariant in superconducting systems and takes the name of BdG Chern number. Since the Hamiltonian is a sum of independent massive Dirac Hamiltonians, the BdG Chern number can be computed as the sum of the winding numbers $\mathcal{N}_{\eta\kappa}$ associated with each of the independent Hamiltonians $h_{\eta\kappa}$ [84]:

$$\mathcal{N} = \sum_{\eta,\kappa} \mathcal{N}_{\eta\kappa}\,. \tag{2.24}$$

Topological phase transitions take place when the Chern invariant $\mathcal{N}_{\eta\kappa}$ associated with one of the Dirac Hamiltonians changes its value, which occurs with the closing of the energy gap $2m_{0,\,\eta\kappa}$ at the $\overline{\Gamma}$ point. Consequently, the corresponding phase boundaries are determined by the condition

$$|\Delta| = \pm\Big(\Lambda \pm m_0\Big)\,. \tag{2.25}$$

The Chern number associated with each Hamiltonian $h_{\eta\kappa}(k_x, k_y)$ depends only on the sign of the mass term: the system is in a trivial phase for $m_{0,\,\eta\kappa} > 0$, while a negative mass $m_{0,\,\eta\kappa} < 0$ drives the system into a topological phase with $\mathcal{N}_{\eta\kappa} = \pm 1$, yielding the following condition for each Dirac Hamiltonian

$$|\Delta| \leq -\kappa\Lambda + \eta\kappa m_0\,. \tag{2.26}$$

Taking into account that the Chern numbers $\mathcal{N}_{\eta\kappa}$ acquire opposite values for opposite orientations of the magnetization, the full phase diagram can be easily determined in the (Λ, Δ) parameter space. The phase diagram a 2D proximitized MTI thin film with $m_0 > 0$, $\mu = 0$, and $\Delta_1 = -\Delta_2 = \Delta$ is shown in Figure 2.2.

In the absence of induced pairing $\Delta = 0$, the system undergoes a phase transition from the $\mathcal{C} = 0$ trivial insulating phase to the $\mathcal{C} = \pm 1$ quantum anomalous Hall state when $\Lambda = m_0$. Within the BdG formalism, this phase is characterized by $\mathcal{N} = \pm 2$ due to the doubling of degrees of freedom introduced by the Nambu basis. For a finite pairing $\Delta \neq 0$, this phase is adiabatically connected to a $\mathcal{N} = \pm 2$ superconductor, which corresponds to a proximitized QAH state. Importantly, however, in the presence of an induced pairing, the transition between the trivial SC phase with $\mathcal{N} = 0$ and the proximitized QAH phase with $\mathcal{N} = \pm 2$ must always

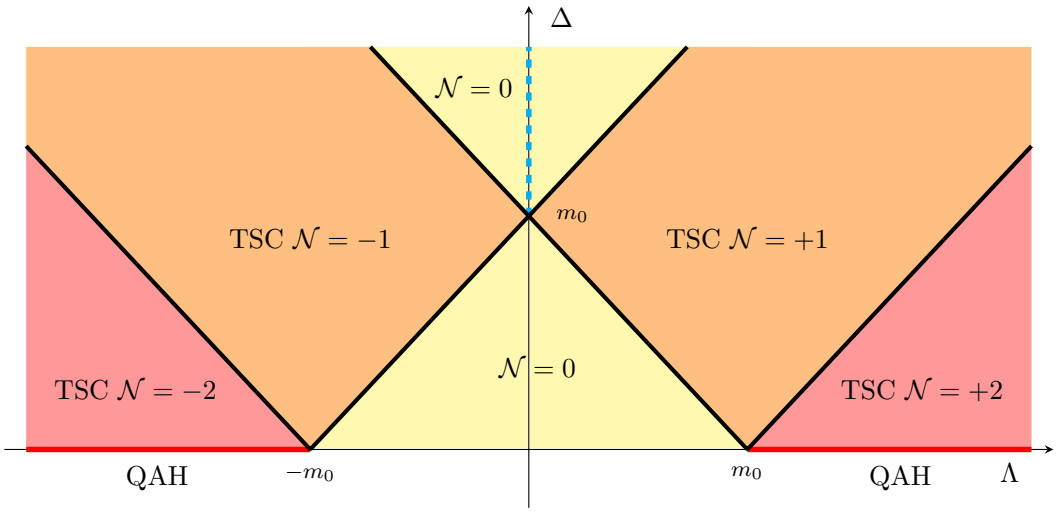

Figure 2.2: Phase diagram of the MTI-SC heterostructure as a function of magnetization Λ and induced pairing for $\mu = 0$ and $\Delta_1 = -\Delta_2 = \Delta$. Different colors indicate distinct topological phases characterized by different values of the BdG Chern number $\mathcal{N}$. The red lines mark the non-proximitized QAH phase at $\Delta = 0$, while the blue dashed one indicates the helical TSC, analogous to a proximitized QSH system. Adapted from Ref. [84].

pass through an intermediate region in which the system realizes a chiral TSC with $\mathcal{N} = \pm 1$. It is worth stressing that the $\mathcal{N} = 1$ phase emerges only when the induced pairing amplitudes at the top and bottom surfaces are unequal, $\Delta_1 \neq \Delta_2$. In contrast, if the superconducting proximity effect is symmetric on both interfaces, the system undergoes a direct transition between the trivial phase ($\mathcal{N} = 0$) and the $\mathcal{N} = 2$ superconductor [41, 42, 84].

2.2.1 Majorana Chiral Propagating States

An intuitive picture of the emergence of the chiral TSC phase near the transition between the QAH and the normal insulator can be obtained by considering the evolution of the edge states. According to the bulk–boundary correspondence, the BdG Chern number $\mathcal{N}$ in a superconductor equals the number of gapless zero-energy edge modes which cross the bulk energy gap and connect valence and conduction bands in a two-dimensional system with finite width [24]. The energy spectra of a proximitized MTI thin film in the different TSC phases with $\mathcal{N} = 0, 1, 2$ corresponding to different sectors of the above phase diagram are shown in Figure 2.3. The energy bands are obtained by discretizing Equation (2.19) on a finite lattice of width $L_y = 1\,\mu$m along the y direction and with periodic boundary conditions along x.

The energy eigenvalues at $k_x = 0$ are displayed in panel (a) as a function of the magnetization Λ and for chemical potential $\mu = 0$. The colors distinguish electron and hole states, quantified by the expectation value

$$\langle \gamma_z \rangle = \int \mathrm{d}y \, \Psi^\dagger_{k_x}(y) \, \gamma_z \, \Psi_{k_x}(y) \,, \tag{2.27}$$

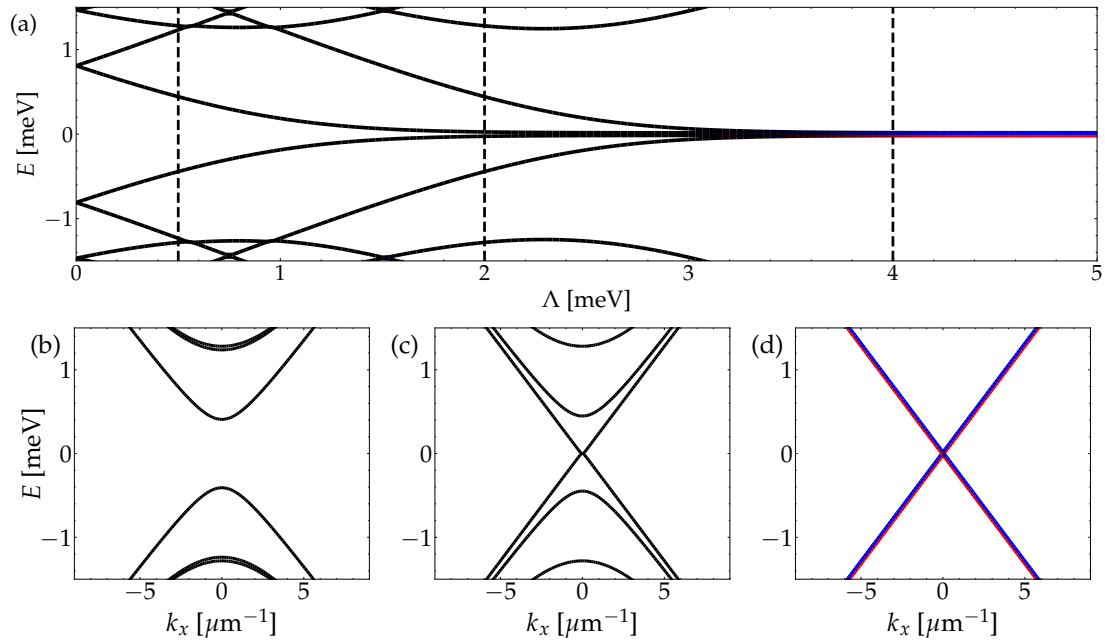

Figure 2.3: Energy spectrum of a proximitized MTI thin film, obtained by discretizing Equation (2.19) on a finite lattice of width $L_y = 1\,\mu$m along the y direction and with periodic boundary conditions along x. (a) Lowest-energy spectrum at $k_x = 0$ as a function of the magnetization Λ. Panels (b)–(d) show the corresponding band dispersions at the representative values of Λ marked by the dashed lines in panel (a): (b) $\mathcal{N} = 0$ trivial superconductor at $\Lambda = 0.5$ meV, (c) $\mathcal{N} = 1$ chiral TSC at $\Lambda = 2$ meV, and (d) $\mathcal{N} = 2$ proximitized QAH state at $\Lambda = 4$ meV. The Hamiltonian parameters are $m_0 = 1$ meV, $m_1 = 0.001$ meVμm^2, $v_F = 0.26$ meVμm, $\mu = 0$, $D = 0$, and we assumed an induced pairing $\Delta_1 = 1.5$ meV and $\Delta_2 = 0$. Red and blue colors denote electron- and hole-like states, respectively, as obtained from Equation (2.27).

whereas black corresponds to states with an equal mixture of electron and hole components. For the chosen parameters, the gap closes around $\Lambda \approx 1.5$ meV and $\Lambda \approx 3$ meV, where the topological phase transitions occur with the emergence of linear gapless edge states within the surface gap. Panel (b) shows the energy spectrum of a trivial SC phase with $\mathcal{N} = 0$, characterized by a finite energy gap at the $\overline{\Gamma}$ point. Increasing the magnetization drives the system into the $\mathcal{N} = 1$ chiral TSC depicted in panel (c), which hosts a gapless boundary mode on each edge. At zero energy, due to particle–hole symmetry, this *single* edge state satisfies the Majorana condition in Equation (2.13) and is therefore called a Majorana chiral propagating state (MCPS) [41–43, 84]. A further increase of the magnetization leads the system into the $\mathcal{N} = 2$ TSC shown in panel (d), characterized by a *pair* of particle–hole symmetric edge states on each boundary. This phase is the superconducting analog of a QAH insulator [41], to which it is adiabatically connected in the limit $\Delta = 0$. The edge localization of the low-energy states is illustrated by the transverse probability density profiles $|\psi_n(y)|^2$ of the corresponding eigenstates, which is shown Figure 2.4 for the four lowest-energy eigenstates at $k_x = 0$ in the three representative cases under consideration.

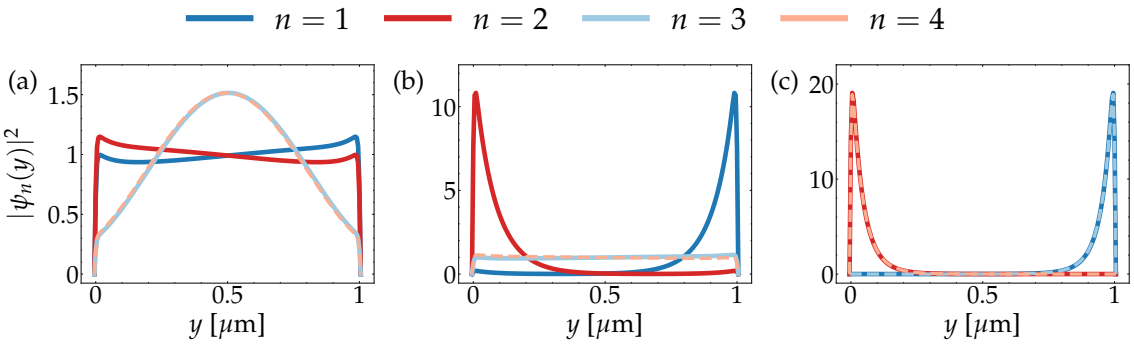

Figure 2.4: Transverse probability density profiles $|\psi_n(y)|^2$ for the first four eigenstates of Equation (2.19) at $k_x = 0$, discretized on a finite lattice of width $L_y = 1$ μm and periodic boundary conditions along x. The three panels correspond to the three different topological superconducting phases with (a) $\Lambda = 0.5$ meV, (b) $\Lambda = 2$ meV, and (c) $\Lambda = 4$ meV, whose energy spectrum is shown in Figure 2.3. At large magnetizatization blue (red) states are localized at the right (left) edge. The induced pairing and all other Hamiltonian parameters are chosen consistently.

In the $\mathcal{N} = 0$ trivial SC phase shown in panel (a), the four lowest-energy states are delocalized over the entire transverse section of the MTI thin film. Increasing the magnetization progressively pushes the two lowest-energy eigenstates toward the boundaries of the system, until they fully separate from the bulk continuum once the system enters the $\mathcal{N} = 1$ chiral TSC phase. In this regime, the probability density is localized at the edges $y = 0$ and $y = L_y$, and decays exponentially in the bulk, as illustrated in panel (b). A further increase of the magnetization drives two additional states toward the boundaries, until the system transitions to the $\mathcal{N} = 2$ phase shown in panel (c), where a pair of particle–hole symmetric edge states is localized on each side of the system.

2.3 1D Topological Superconductor

When a two-dimensional MTI thin film in the topological QAH phase is confined to a narrow geometry, the edge states localized on opposite boundaries strongly hybridize. In this regime—that we refer to as effective or quasi–one–dimensional limit—the Hall conductance ceases to be quantized, as the strong coupling between edge modes on opposite sides allows for electron backscattering, making the transport diffusive rather than ballistic in the presence of disorder. Nevertheless, when such a system is placed in proximity to a conventional s-wave superconductor, it can be driven into a 1D topological superconducting phase that supports MBSs at the wire ends [45–47, 84, 106, 107]. Indeed, when the width of the QAH system is comparable to the localization length of the edge states, the two chiral edge modes hybridize forming a single helical conducting channel. Inducing superconductivity in this helical channel, it is possible to realize an effective p-wave SC, whose physics is analogue to that of a proximitized Rashba semiconductor nanowire [76, 104, 105].

The topological properties of the system can be understood by analyzing the symmetry of the Hamiltonian within the framework of the classification scheme

introduced in Section 1.1.3. A quasi–one–dimensional nanoribbon of proximitized MTI can be described by the two-dimensional BdG Hamiltonian in Equation (2.19) discretized on a narrow transverse lattice along y with a width L_y comparable to the localization length of the QAH edge states. Following the procedure described in Appendix A.1, the Hamiltonian can be rewritten as

$$\tilde{h}_{\mathrm{2D}}^{\mathrm{BdG}}(k_x) = \sum_{n_y} \Psi_{k_x,n_y}^{\dagger} \left[h_0 \, \Psi_{k_x,n_y} + h_+ \, \Psi_{k_x,n_y+1} + h_- \, \Psi_{k_x,n_y-1} \right] \tag{2.28}$$

where

$$\Psi_{k_x,n_y} = \begin{bmatrix} \psi_{k_x,n_y} \\ \left(\psi_{-k_x,n_y}^{\dagger}\right)^T \end{bmatrix} , \tag{2.29}$$

is the Nambu basis introduced in Equation (2.2) and n_y is a discrete index labeling the N_y sites of the one-dimensional transverse lattice. The on-site energy is given by

$$\begin{aligned} h_0 = & \left[- \left(\mu + D \, \tilde{k}_x^2 \right) + \left(m_0 + m_1 \, \tilde{k}_x^2 \right) \lambda_x + \Lambda \sigma_z \right] \gamma_z - v_F k_x \sigma_y \lambda_z \gamma_z \\ & - \mathrm{Re} \, \left(\Delta_+ + \Delta_- \lambda_z \right) \sigma_y \gamma_y - \mathrm{Im} \, \left(\Delta_+ + \Delta_- \lambda_z \right) \sigma_y \gamma_x \, , \end{aligned} \tag{2.30}$$

while the hopping energies are defined as

$$h_{\pm} = \frac{1}{a^2} \left(D - m_1 \lambda_x \right) \gamma_z \mp \mathrm{i} \frac{v_F}{2a} \sigma_z \lambda_z \, , \tag{2.31}$$

where a is the lattice spacing and $\tilde{k}_x^2 \equiv k_x^2 + 2/a^2$.

While the physical time-reversal symmetry in Equation (1.27) is explicitly broken by the magnetization term $\Lambda \sigma_z$, the discretized Hamiltonian in Equation (2.28) still exhibits a time-reversal-like symmetry [46]. This antiunitary transformation is given by

$$\mathcal{T}' = \mathcal{U} \mathcal{K} \, , \qquad \mathcal{T}'^2 = +1 \, , \tag{2.32}$$

where the operator $\mathcal{U}$ reverses the sites on the discrete lattice, and can be represented in real space as the $N_y \times N_y$ anti–diagonal matrix

$$\mathcal{U}_{ij} = \delta_{\, i+j, \, N_y+1} \, , \tag{2.33}$$

which exchanges site j with its mirror partner $N_y + 1 - j$. The time-reversal-like symmetry in Equation (2.32) imposes the following condition on the Hamiltonian

$$\mathcal{T}'^{-1} \, \tilde{h}_{\mathrm{2D}}^{\mathrm{BdG}}(-k_x) \, \mathcal{T}' = \tilde{h}_{2D}^{\mathrm{BdG}}(k_x) \, . \tag{2.34}$$

By construction, the discretized BdG Hamiltonian $\tilde{h}_{\mathrm{2D}}^{\mathrm{BdG}}$ possesses the intrinsic particle–hole symmetry $\mathcal{P}$ introduced in Equation (2.9). Together with the time-reversal-like symmetry $\mathcal{T}'$, this gives rise to a unitary chiral symmetry,

$$\mathcal{S} = \mathcal{T}' \, \mathcal{P} = \gamma_x \sigma_z \, , \qquad \mathcal{S}^2 = +1 \, , \tag{2.35}$$

under which the Hamiltonian satisfies

$$\mathcal{S}^{-1} \, \tilde{h}_{\mathrm{2D}}^{\mathrm{BdG}}(k_x) \, \mathcal{S} = - \tilde{h}_{\mathrm{2D}}^{\mathrm{BdG}}(k_x) \, . \tag{2.36}$$

The simultaneous presence of time-reversal-like, particle–hole, and chiral symmetries, together with their squared properties, places the discretized Hamiltonian in Equation (2.28) in the BDI symmetry class of the periodic classification introduced in Table 1.1. Therefore, in an effective one-dimensional system ($d = 1$), the band topology of the Hamiltonian is characterized by an integer invariant $N_{\mathrm{BDI}} \in \mathbb{Z}$, which counts the number of zero-energy MBSs localized at the ends of the nanowire [46, 69, 70].

With respect to the physical time-reversal symmetry, which is broken by the Zeeman coupling, the Hamiltonian belongs to the symmetry class D. In one dimension, this class is characterized by a $\mathbb{Z}_2$ topological invariant ν, which encodes the parity of the MBSs localized at the ends of the proximitized nanowire [45, 70, 71]. The topological invariant of the symmetry class D can be obtained from the integer invariant N_{BDI} of the symmetry class BDI through the relation $\nu = (-1)^{N_{\mathrm{BDI}}}$, meaning that only the parity of the number of Majorana zero modes remains topologically protected once the time-reversal symmetry is broken [69, 108].

The value of the topological invariant N_{BDI} in the proximitized system is related to the number of energy bands crossing the Fermi energy in the non-proximitized case. In the effective 1D system, each subband that crosses the Fermi energy constitutes an available one-dimensional conducting helical channel. In the presence of induced pairing, each of these channels realizes an effective p-wave SC and host a Majorana zero mode at the wire ends. The BDI invariant N_{BDI} precisely counts the number of such Majorana modes protected by the combined particle–hole and chiral symmetries [46, 106]. The phase diagram in the (Λ, μ) parameter space for a proximitized quasi–one–dimensional nanowire is shown in Figure 2.5. The different regions were identified by discretizing the Hamiltonian in Equation (2.19) on a finite lattice along the y direction and periodic boundary conditions along x, and counting the number of bands crossing the Fermi level in the normal state.

For vanishing magnetization ($\Lambda = 0$), the Hamiltonian retains the physical time-reversal symmetry of Equation (1.27), which enforces the twofold Kramers degeneracy. In this regime the Fermi level can intersect only an even number of subbands. A finite Zeeman field Λ lifts the degeneracy and splits each band into two distinct branches, so that the Fermi energy may cross an odd number of subbands. Whenever n subbands are partially filled, the system realizes a phase with $N_{\mathrm{BDI}} = n$, which support n zero-energy MBSs at *each* end of the nanowire, protected by the coexistence of particle–hole and chiral symmetries. It should be emphasized that in the presence of disorder the chiral symmetry is broken, and the MBSs are protected by PHS alone. Under these conditions, two Majorana modes localized at the same end of the nanowire hybridize into a trivial fermionic state, meaning that only phases with an *odd* value of N_{BDI} remain topologically nontrivial [47, 98, 106, 109].

2.3.1 Majorana Bound States

An intuitive connection between the topological invariant N_{BDI} and the number n of subbands intersecting the Fermi level in the normal state, can be gained by examining how the energy spectrum of a quasi–one–dimensional QAH system evolves under the effect of magnetization and proximity-induced pairing. The energy spectrum of an effective one-dimensional MTI described by Equation (1.58) and Equation (2.19)

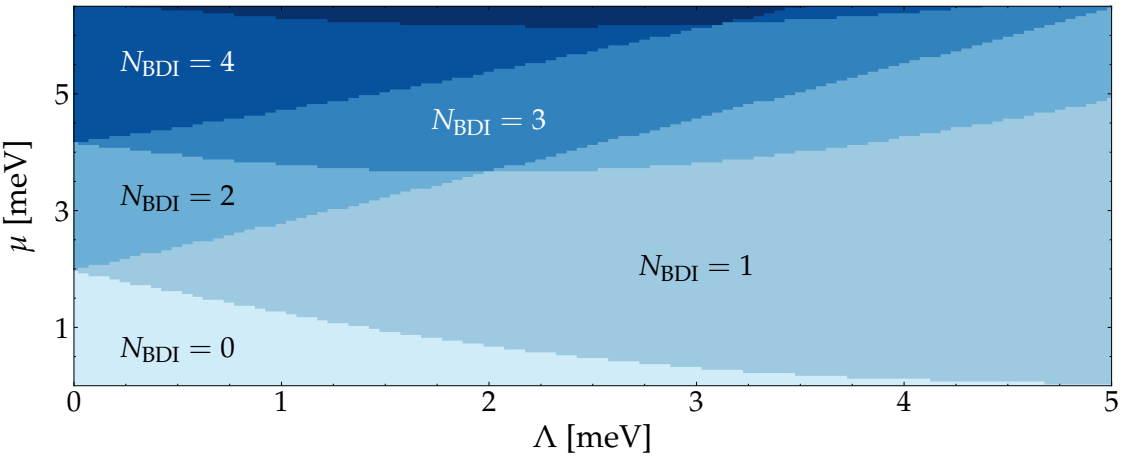

Figure 2.5: Phase diagram of the quasi–one–dimensional MTI in the presence of proximity-induced superconducting pairing. The topological invariant N_{BDI} corresponds to the number of subbands crossing the Fermi level in the non-proximitized limit. The diagram is obtained by discretizing the normal-state Hamiltonian of Equation (1.58) on a finite lattice of width $L_y = 300$ nm and by counting the number of bands at zero energy. The other parameters are $m_0 = 1$ meV, $m_1 = 0.001$ meVμm^2, $v_F = 0.26$ meVμm, and $D = 0$.

in the absence and presence of SC induced pairing, respectively, is shown in Figure 2.6.

The spectra are obtained by discretization of the Hamiltonians in Equations (1.58) and (2.19) on a finite lattice along y and imposing periodic boundary conditions along x. We assume a width $L_y = 300$ nm, comparable to the localization length of the edge states in the QAH phase. Panel (a) shows the energy spectrum of the MTI nanowire in the trivial insulating regime, characterized by a trivial gap at $k_x = 0$ with $\Lambda < m_0$. Upon increasing the magnetization, the system enters the QAH phase shown in panel (b) for $\Lambda > m_0$. Due to the confinement in a narrow geometry, the chiral edge channels strongly hybridize, resulting in the opening of a finite gap in the edge states.

Panel (c) shows the same spectrum obtained within the BdG framework with $\Delta = 0$ and $\mu = 2$ meV. The energy bands are doubled in electron (red branches) and hole (blue branches) states due to the degeneracy of the Nambu basis: in the presence of finite chemical potential, the former are shifted upward, while the latter downward. Introducing a finite pairing $\Delta \neq 0$ opens a superconducting gap around $E = 0$, and the nontrivial topology of the system is highlighted by a band inversion at $k_x = 0$, where the normal order of electron and hole branches is reversed.

It is worth emphasizing that the realization of a one-dimensional TSC does not strictly require starting from a MTI thin film in the QAH phase. If the system is in the trivial insulating regime, the low-energy states correspond to surface states delocalized across the entire transverse section rather than chiral edge-localized modes [47, 98, 106]. Nevertheless, in a quasi–one–dimensional geometry, these states still combine into a helical conducting channel, which, upon proximity coupling to a superconductor, gives rise to an effective p-wave SC supporting zero-energy MBSs at

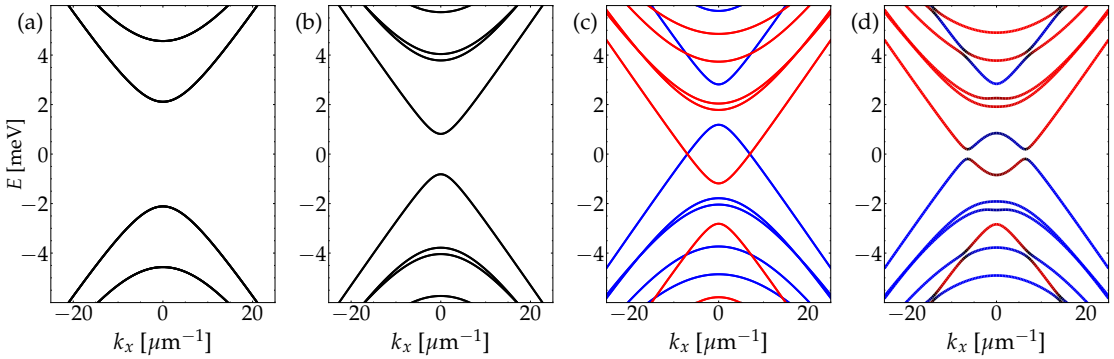

Figure 2.6: Evolution of the spectrum of a MTI nanoribbon with magnetization and induced pairing. The band structure is obtained by discretizing the Hamiltonian in Equation (2.19) on an effective one-dimensional geometry of width $L_y = 300$ nm, with periodic boundary conditions along the x direction. Panels (a) and (b) show the electron states of the spectrum of a non-proximitized system with $\mu = 0$, and for $\Lambda = 0$ and $\Lambda = 2$ meV, respectively. Panel (c) illustrates the full BdG spectrum of the MTI nanoribbon with $\Lambda = 2$ meV and $\mu = 2$ meV. Panel (d) displays the effect of an induced pairing with $\Delta_1 = 1$ meV and $\Delta_2 = 0$. The model parameters are $m_0 = 1$ meV, $m_1 = 0.001$ meVμm^2, $v_F = 0.26$ meVμm, and $D = 0$. Red and blue colors denote electron- and hole-like states, respectively, as obtained from Equation (2.27).

the wire ends [76, 104, 105]. Figure 2.7 compares the spectra of a non-proximitized MTI nanowire in the trivial and QAH regimes, both in the regime where a single band crosses the Fermi level. The green shaded region highlights the energy window where the normal-state system hosts a single Fermi crossing.

Despite both cases lead to a $N_{\mathrm{BDI}} = 1$ topological SC state with unpaired MBSs localized at the ends of the effective 1D nanowire, the QAH phase provides a more favorable platform for engineering robust topological superconductivity [46, 106]. In panel (a), the MTI is in a trivial insulating phase, and the two lowest bands lie close in energy, resulting in a narrow range of chemical potentials where the proximity effect yields a $N_{\mathrm{BDI}} = 1$ phase. By contrast, in panel (b) the system is in the QAH state, and the lowest band, corresponding to the topological chiral edge channel, is well separated from the second-lowest one originating from the discretization of the surface Dirac cones on a lattice with finite width. The energy gap at $k_x = 0$ in the edge dispersion arises from the strong hybridization of the chiral edge modes in the quasi–one–dimensional limit. As a result, the topological region corresponding to $N_{\mathrm{BDI}} = 1$ is significantly broader, making it more robust against fluctuations in the chemical potential [47, 98, 106]. Reducing the system width increases the transverse confinement, pushing the surface states to higher energies, and thereby isolating the single helical channel that originates from the strongly hybridized QAH chiral edge modes [46].

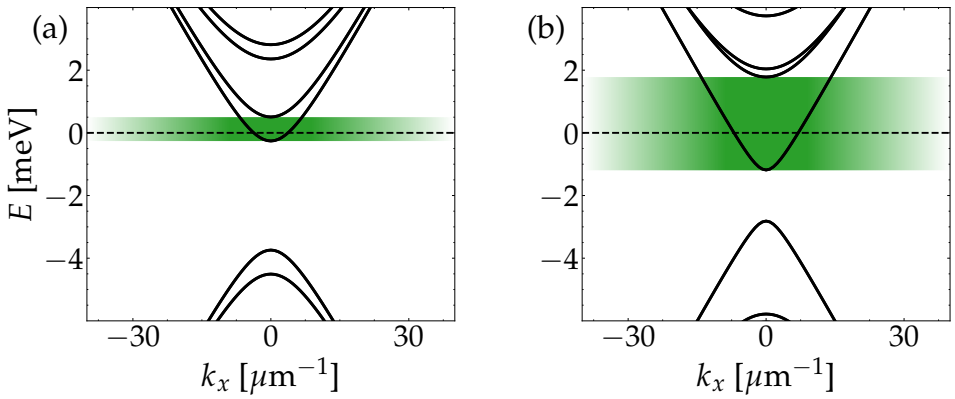

Figure 2.7: Comparison between the spectrum of a (a) normal and (b) QAH phase in a narrow quasi–one–dimensional film of non-proximitized MTI. The spectra are obtained discretizing the Hamiltonian in Equation (1.58) in a finite lattice along y with width $L_y = 300$ nm and periodic boundary conditions along x, with (a) $\Lambda = 0.5$ meV and (b) $\Lambda = 2$ meV. The other parameters are $m_0 = 1$ meV, $m_1 = 0.001$ meVμm^2, $v_F = 0.26$ meVμm, $\mu = 2$ meV and $D = 0$.

Summary

In this chapter, we introduced the BdG formalism as a framework to describe proximitized systems, emphasizing the role of particle–hole symmetry and its fundamental connection to the emergence of Majorana quasiparticles. Within this approach, we constructed effective three- and two-dimensional BdG Hamiltonians for proximitized MTIs, building on the low-energy models outlined in Section 1.2.

We showed that in the two-dimensional case, a proximitized MTI can host topological superconducting phases, whose topology is classified by the BdG Chern number $\mathcal{N}$. Depending on the interplay between the induced pairing amplitude and the magnetization, the system can realize different phases that support gapless chiral states propagating along the edges.

Moreover, we illustrated that, in the quasi–one–dimensional limit, a confined MTI film with narrow width can be engineered into a one-dimensional topological superconducting phase. In this regime, the topology is characterized by a nonzero integer invariant N_{BDI}, which determines the number of MBSs localized at the ends of finite-length nanowires.

These results establish proximitized MTIs as a versatile platform for realizing topological superconductivity in both two- and one-dimensional geometries, hosting either propagating Majorana modes or localized bound states. The next chapter is devoted to the study of transport properties in junctions based on such hybrid heterostructures, with the goal of identifying electrical signatures of the topological phases discussed here.

Part II

Transport Properties

Chapter 3

Transport in NSN Junctions

Overview

In the previous chapter, we established how proximitized MTIs provide a versatile platform for realizing topological superconductivity, supporting propagating MCPSs in two dimensions and localized MBSs in one dimension. Despite these theoretical proposals, however, the experimental observation of Majorana quasiparticles has remained inconclusive, as trivial mechanisms can mimic the transport signatures expected from topological superconducting phases. In this chapter, we investigate the transport properties of junctions composed of normal (N) and proximitized (S) thin films of MTIs, with the aim of identifying electric signatures associated with the emergence of zero-energy Majorana modes. Although such signatures are not strictly unique, we focus on transport observables that provide strong indications of Majorana physics in both one- and two-dimensional geometries.

The remainder of this chapter is organized as follows. In Section 3.1, we introduce the theoretical framework employed to describe quasiparticle transport across NS and SNS junctions. The analysis is based on a complex band-structure approach, under the assumption that each section of the junction is homogeneous along the transport direction. This framework allows us to compute the probability amplitudes of the elementary scattering processes and compute the differential conductance within the Blonder–Tinkham–Klapwijk (BTK) formalism.

In Section 3.2, we examine the conductance profiles of the one- and two-dimensional TSC phases induced in MTIs, for small voltage biases below the surface gap of the topological insulator, ensuring that the system remains within the linear-response regime. Special attention is devoted to the antisymmetric profile of the conductance, which directly reflects the emergence of Majorana quasiparticles in the proximitized region under asymmetric bias applied to the two normal leads.

Finally, in Section 3.3, we discuss interference patterns and conductance oscillations characteristic of the $\mathcal{N} = 1$ topological SC phase when the applied bias exceeds the surface gap. In this regime, three distinct transport behaviors can be identified depending on the quasiparticle energy. The intermediate one is particularly notable, as it exhibits characteristic current oscillations arising from the interference of a pair of propagating edge states associated with the emergence of the chiral TSC.

The results presented in this chapter are based on Refs. [100, 102].

3.1 Blonder–Tinkham–Klapwijk Formalism

The topological superconducting phases introduced in Chapter 2 can be probed through their characteristic conductance signatures, which reflect the presence of distinct edge and bound states in the central superconducting sector of an NSN junction made by normal (N) and proximitized (S) thin films of MTIs. From a theoretical perspective, the quasiparticle transport occurring at the interface between a normal and a superconducting system can be described by the BTK theory and its generalization in an NSN double junction [110–112]. The investigated device is schematically shown in Figure 3.1.

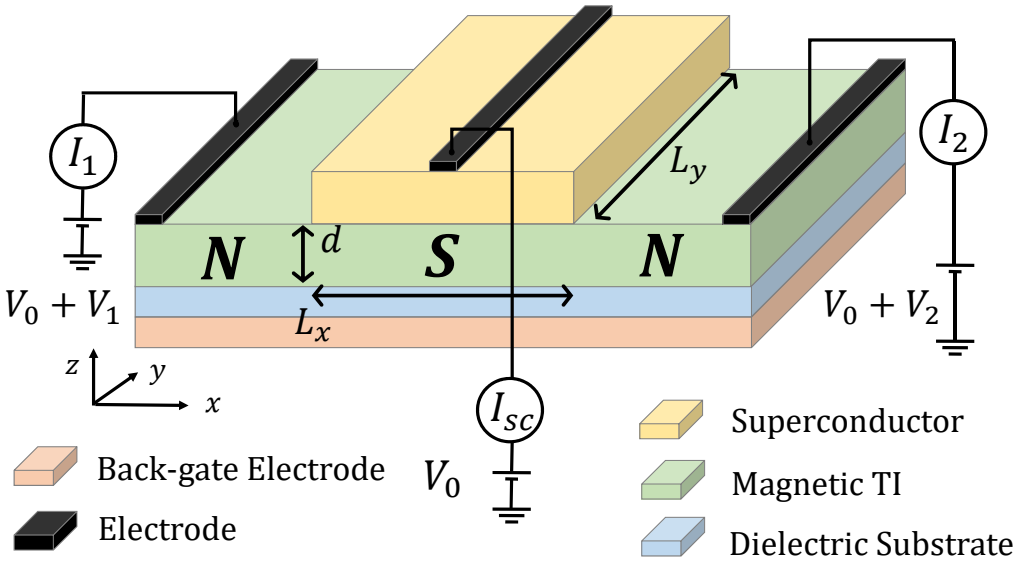

Figure 3.1: Schematic illustration of the NSN junction used for the modeling of the quasiparticle transport in the proximitized MTI thin film. The electrostatic potential $V_0 = -e\mu$ is controlled by the back-gate electrode, which tunes the chemical potential of the system. The central proximitized sector is grounded, while different voltage drops V_1 and V_2 are applied on the normal leads. Adapted from Ref. [100].

The system consists of two normal MTI leads, assumed to be semi-infinite along the longitudinal direction of propagation, and a central superconducting region of finite length, where a nonvanishing pairing potential is induced via proximity to a conventional s-wave spin-singlet SC placed on top of the topological insulator. The superconductor is grounded, making the device an effective three-terminal junction. The full structure extends over a width L_y along the transverse direction y, while the central superconducting section has a length L_x along the longitudinal propagation axis x, with the normal leads assumed to be translationally invariant. The thickness is assumed to be much smaller than the in-plane dimensions $d \ll L_{x,y}$. We assume that the central region is grounded, and that different voltage drops V_1 and V_2 are applied to the left and right terminals.

Both the normal and superconducting regions can be described within the BdG formalism introduced in Section 2.1. In the normal leads, the single-particle excitations are doubled into decoupled electron and hole states, whereas in the superconducting region they couple due to the nonzero pairing potential. Moreover, in the proximitized region, the electric current can also be sustained by a supercurrent of Cooper pairs. Consequently, the transport across the junction results from the competition between normal scattering processes and Andreev reflections, the latter originating from the interaction between the individual quasiparticles and the Cooper pair condensate.

In particular, when an electron is incident on a normal–superconductor (NS) interface, it may be reflected either as an electron (normal reflection) or as a hole, with the simultaneous creation of a Cooper pair into the superconductor (Andreev reflection). In the Andreev reflection process, both spin and momentum are conserved across the interface, with the missing charge and spin being absorbed by the superconducting condensate through the formation of a Cooper pair [113–116]. A sketch of the transport processes at the normal–superconductor interface is shown in Figure 3.2.

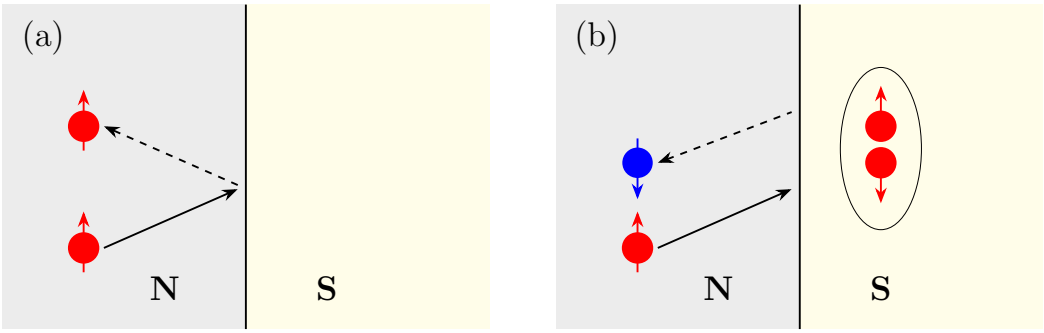

Figure 3.2: Schematic illustration of the reflection processes at the NS interface between a normal and a superconducting region. Panel (a) shows normal reflection, where an incoming electron (red circle) is reflected back as an electron, while panel (b) depicts Andreev reflection, where the incoming electron is retroreflected as a hole (blue circle). The missing spin and momentum are absorbed by the Cooper pair formed in the superconducting condensate.

In addition to local reflection processes, in a NSN double junction an incoming electron injected from one normal lead can induce the emission of a hole in the opposite terminal, a mechanism known as Andreev transmission or crossed Andreev reflection (CAR) [116, 117]. Since the emission of a hole from the SC is physically equivalent to the absorption of an electron into the Cooper pair condensate, the process effectively transfers two electrons—one from each normal lead—into the superconducting region, where they bind to form a Cooper pair. A sketch of the CAR process in the NSN junction is shown in Figure 3.3.

Local normal and Andreev reflections, together with the nonlocal CAR, constitute all the possible subgap transport processes that can occur in the NSN junction. It should be noted, however, that when the injected quasiparticles have energies above the superconducting gap, or when edge or boundary states emerge below the

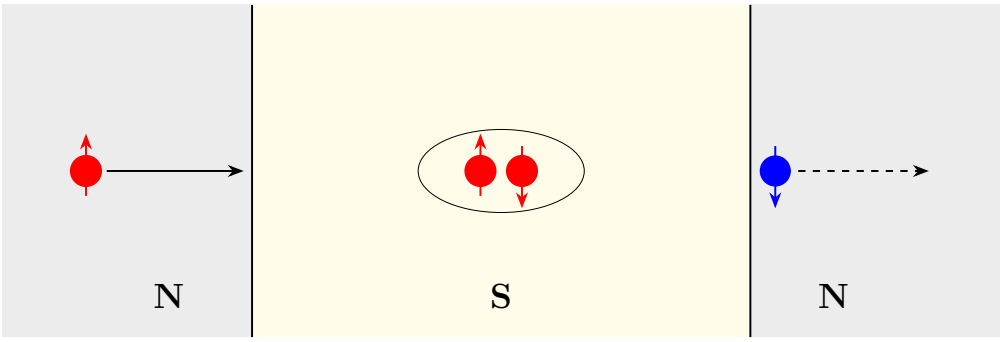

Figure 3.3: Schematic illustration of the CAR process in the NSN junction. An electron is injected in the superconducting sector from the left lead, and a hole is emitted in the right one, with simultaneous creation of a Cooper pair in the condensate.

gap due to a nontrivial bulk band topology in the proximitized region, the transmission of *single* quasiparticles across the junction becomes possible. In such cases, normal transmission can also occur, where electrons and holes propagate across the superconducting region while retaining their character.

In the following, we denote the probability amplitudes for these scattering processes as P_{ij}^{ab}, representing the probability for an incoming quasiparticle of type b in terminal j to scatter into a quasiparticle of type a in terminal i, with $i, j \in \{1, 2\}$ labeling the normal leads of the junction and $a, b \in \{\mathrm{e}, \mathrm{h}\}$ distinguishing electrons and holes states. In this language, reflection processes correspond to $i = j$, while transmission processes correspond to $i \neq j$, encompassing both normal and Andreev scattering events.

3.1.1 Scattering Amplitudes

The probability amplitudes P_{ij}^{ab} for all the possible transport processes in the NSN double junction can be obtained by solving the corresponding scattering problem. To this end, we employ a complex band structure approach, where each region of the junction is treated as homogeneous along the longitudinal propagation direction x, while complex momenta are used to describe boundary states localized at the interfaces of the proximitized sector [118–122]. We illustrate the method in the case of a two-dimensional system, where the continuum Hamiltonian $h_{\mathrm{BdG}}(k_x, k_y)$ is discretized on a finite lattice along the transverse direction y according to the procedure described in Appendix A.1, while the longitudinal direction x is treated with the approach outlined below. The extension to the three-dimensional case, where the z direction is also discretized on a lattice, follows straightforwardly.

In each homogeneous region of the junction labeled by $s \in \{N_1, N_2, S\}$, the wavefunction at fixed energy can be written as [100, 118, 119]

$$\Psi^{(s)}(x, y) = \sum_k c_k^{(s)} \, \mathrm{e}^{\mathrm{i}k^{(s)}x} \, \tilde{\Psi}_k^{(s)}(y) \,, \tag{3.1}$$

where $k \equiv k_x$ denotes the longitudinal momentum, and $\tilde{\Psi}_k^{(s)}(y)$ is the transverse wavefunction discretized on the lattice and expressed in the Nambu basis. The

momenta $k = k_r + \mathrm{i}k_i$ are, in general, complex and include both propagating modes, corresponding to real wavenumbers, and evanescent states, characterized by a finite imaginary part $k_i \neq 0$, according to

$$\mathrm{e}^{\mathrm{i}kx} = \mathrm{e}^{\mathrm{i}k_r x}\, \mathrm{e}^{-k_i x}\,. \tag{3.2}$$

In an infinitely long system, only propagating modes with real momentum $k \in \mathbb{R}$ are physical, while exponentially growing solutions must be discarded. In contrast, in finite or semi-infinite geometries, complex momenta associated with exponentially decaying solutions that satisfy $\int \mathrm{d}x\, |\Psi(x,y)|^2 < +\infty$ are also admissible, as they describe boundary states localized near the interfaces [119].

The set of complex wavenumbers and associated transverse modes $\{k^{(s)},\, \tilde{\Psi}_k^{(s)}\}$ can be obtained by solving the momentum eigenvalue problem for the k-dependent translational invariant Hamiltonian in each region of the junction. In fact, the usual energy eigenvalue problem of the Schrödinger equation can be recast into a non-Hermitian momentum eigenvalue equation at fixed energy, as discussed in details in Appendix A.2. Due to numerical truncation, only a finite set of wavenumbers and transverse modes is obtained at a given energy. This discrete basis then enables the construction of the wavefunction through Equation (3.1).

In the semi-infinite leads of the NSN junction, the modes are classified as incoming or outgoing, while exponentially divergent states are discarded as unphysical. The classification of input and output channels is determined by the sign of the quasiparticle probability flux, which for propagating states with real momentum is given by [100, 118]

$$I_k = \langle \tilde{\Psi}_k |\, \frac{\partial h_{\mathrm{BdG}}}{\partial k}\, |\tilde{\Psi}_k\rangle\,. \tag{3.3}$$

For the left terminal ($i = 1$), input modes correspond to states with real momentum that propagate toward the superconducting region with positive flux ($I_k > 0$). Output modes, instead, correspond to states with real momentum and negative quasiparticle flux ($I_k < 0$), as well as evanescent modes with complex momentum that decay away from the interface. The signs of the quasiparticle flux are reversed on the right lead ($i = 2$), so that input states correspond to propagating modes with $I_k < 0$, while the output ones are associated with $I_k > 0$. In contrast, in the superconducting region, all complex and real modes are physically admissible, and they correspond to output channels.

We denote the coefficients of the incoming (outgoing) modes in the wavefunction superposition as $\{a_k^{(s)}\}$ ($\{b_k^{(s)}\}$), so that Equation (3.1) can be rewritten as

$$\Psi^{(s)}(x,y) = \sum_{k\in s,\mathrm{inp}} a_k^{(s)}\, \mathrm{e}^{\mathrm{i}kx}\, \tilde{\Psi}_k^{(s)}(y) + \sum_{k\in s,\mathrm{out}} b_k^{(s)}\, \mathrm{e}^{\mathrm{i}kx}\, \tilde{\Psi}_k^{(s)}(y)\,. \tag{3.4}$$

While the input coefficients $a_k^{(s)}$ are fixed by the choice of the incoming scattering state, the outgoing ones $b_k^{(s)}$ must be determined by solving the scattering problem and constructing the full wavefunction across the junction. Due to truncation, the total number of unknowns is finite and their values must be fixed by imposing continuity of the wave function and its x-derivative at the normal–superconductor interfaces, ensuring conservation of the quasiparticle current across the boundary. In

practice, those equations are projected onto the total discrete set of complex modes by means of the overlap matrices [118, 119]

$$\mathcal{M}_{k'k}^{s's} = \int \mathrm{d}y \, \left[\tilde{\Psi}_{k'}^{(s')}(y)\right]^{\dagger} \, \tilde{\Psi}_{k}^{(s)}(y) \, . \tag{3.5}$$

Further details on the derivation of the linear system of equations for the boundary conditions at the interfaces of the junction are provided in Appendix A.3.

By solving the linear system imposed by the boundary conditions at the two interfaces, the scattering problem is fully determined and the complete wavefunction across the junction can be obtained. Assuming a single propagating incoming channel with $a_k^{(s)} = 1$ in one of the normal region s, while all the other incoming states are set to zero, one can finally obtain the scattering probabilities as

$$p_{k'k}^{s's} = \left| b_{k'}^{s'} \right|^2 , \tag{3.6}$$

which quantify the probability for a quasiparticle in the state k of lead s to be scattered into the state k' of lead s'. In the non-superconducting leads, the electron and hole degrees of freedom are decoupled in the absence of pairing, making it possible to discriminate between the two particle types. By summing the contributions in Equation (3.6) over all output channels, discriminating their particle type and lead, one obtains the total scattering probabilities as [100, 118, 119]

$$P_{ij}^{\mathrm{he}} = \sum_{k_h, k_e} p_{k_h k_e}^{ij} \, , \tag{3.7}$$

which quantify, for instance, the probability for an electron incident from lead j to be transmitted as a hole into lead i. The following procedure applies exclusively to non-proximitized leads, where electron and hole states can be unambiguously distinguished.

3.1.2 Differential Conductance

The probability amplitudes P_{ij}^{ab} for the different quasiparticle processes in the junction provide the fundamental ingredients to compute the differential conductance within the BTK formalism. In general, the electric currents flowing in the two normal terminals are not identical. It is therefore convenient to define two distinct differential conductances measured separately on each terminal:

$$G_i(E) = \frac{\partial I_i}{\partial V} \, , \tag{3.8}$$

where I_i denotes the current in the terminal i and $V \equiv V_1 - V_2$ is the total bias applied across the junction.

The current in each normal lead can be expressed in terms of the incoming and outgoing quasiparticle fluxes as [110, 112, 123]

$$I_i = \int_0^{+\infty} \mathrm{d}E \, \sum_a a \left[J_i^a(E) - K_i^a(E) \right] \, , \tag{3.9}$$

where $a = e, h = \pm$ denotes the particle type and

$$J_i^a(E) = \frac{e}{h} N_i^a(E) f_i^a(E)\,, \qquad K_i^a(E) = \frac{e}{h} \sum_{jb} P_{ij}^{ab}(E) f_j^b(E)\,. \tag{3.10}$$

Here, e denotes the elementary charge and h the Planck constant, $N_i^a(E)$ is the number of propagating modes of type a in terminal i, $f_i^a(E)$ is the corresponding Fermi distribution function, and $P_{ij}^{ab}(E)$ are the probability amplitudes defined above. Physically, $J_i^a(E)$ represents the flux of quasiparticles of type a injected from lead i, whereas $K_i^a(E)$ accounts for the corresponding outgoing flux after scattering, obtained by weighting the incoming distributions in all leads with the appropriate scattering probabilities $P_{ij}^{ab}(E)$. The Fermi distributions for electron and hole states are given by [112, 124]

$$f_i^a(E) = \begin{cases} \dfrac{1}{1 + \mathrm{e}^{(E - eV_i)/k_B T}} & \text{for } a = \mathrm{e}\,, \\ \dfrac{1}{1 + \mathrm{e}^{(E + eV_i)/k_B T}} & \text{for } a = \mathrm{h}\,, \end{cases} \tag{3.11}$$

where V_i is the bias applied to the normal lead i with respect to the grounded SC region. It is worth noting that, unlike in the original BTK model [110, 111], we do not include a δ-function potential to model the tunneling at the interface. In our setup, the NS interface is not a physical barrier but rather the transition between a normal and a proximitized film of MTI. Therefore, the transport properties are fully determined by the microscopic Hamiltonian without an additional interfacial potential.

By making use of Equation (3.10), the electric current in Equation (3.9) can be rewritten as

$$\begin{aligned} I_i &= \frac{e}{h} \int_0^{+\infty} \mathrm{d}E \, \left[J_i^e - K_i^e - J_i^h + K_i^h \right] = \\ &= \frac{e}{h} \int_0^{+\infty} \mathrm{d}E \, \left[N_i^e f_i^e - \sum_j \left(P_{ij}^{\mathrm{ee}} f_j^e + P_{ij}^{\mathrm{eh}} f_j^h \right) - N_i^h f_i^h + \sum_j \left(P_{ij}^{\mathrm{he}} f_j^e + P_{ij}^{\mathrm{hh}} f_j^h \right) \right], \end{aligned} \tag{3.12}$$

where for simplicity we omitted the energy dependence. Expanding the sum over j, the expression for the electric current in the normal terminal $i = 1$ becomes

$$\begin{aligned} I_1 = \frac{e}{h} \int_0^{+\infty} \mathrm{d}E \Big\{ &\left[N_1^{\mathrm{e}} - P_{11}^{\mathrm{ee}} + P_{11}^{\mathrm{he}} \right] f_1^e + \left[-N_1^h - P_{11}^{\mathrm{eh}} + P_{11}^{\mathrm{hh}} \right] f_1^h + \\ &+ \left[P_{12}^{\mathrm{he}} - P_{12}^{\mathrm{ee}} \right] f_2^e + \left[P_{12}^{\mathrm{hh}} - P_{12}^{\mathrm{eh}} \right] f_2^h \Big\}, \end{aligned} \tag{3.13}$$

and, similarly, for the terminal $i = 2$ we have

$$\begin{aligned} I_2 = \frac{e}{h} \int_0^{+\infty} \mathrm{d}E \Big\{ &\left[N_2^e - P_{22}^{\mathrm{ee}} + P_{22}^{\mathrm{he}} \right] f_2^e + \left[-N_2^h - P_{22}^{\mathrm{eh}} + P_{22}^{\mathrm{hh}} \right] f_2^h + \\ &+ \left[P_{21}^{\mathrm{he}} - P_{21}^{\mathrm{ee}} \right] f_1^e + \left[P_{21}^{\mathrm{hh}} - P_{21}^{\mathrm{eh}} \right] f_1^h \Big\}. \end{aligned} \tag{3.14}$$

To proceed, we explicitly consider the case in which the total bias across the junction is distributed *asymmetrically* between the two normal leads. We parametrize the voltages as $V_1 = \alpha V$ and $V_2 = -\beta V$, with $0 \leq \alpha \leq 1$ and $\alpha + \beta = 1$, so that the total voltage drop across the junction remains fixed to $V \equiv V_1 - V_2$. In the zero-temperature limit, the Fermi distributions reduce to step functions,

$$f_i^{\mathrm{e,h}} = \frac{1}{1 + \mathrm{e}^{(E \mp eV_i)/k_B T}} \xrightarrow[T \to 0]{} \Theta\left(\pm eV_i - E\right) , \tag{3.15}$$

where the + sign corresponds to electrons, while the − sign corresponds to holes. The expressions for the electric currents in the two normal terminals thus simplify to

$$I_1 = \frac{e}{h} \int_0^{\alpha eV} \mathrm{d}E \left[N_1^{\mathrm{e}} - P_{11}^{\mathrm{ee}} + P_{11}^{\mathrm{he}} \right] + \frac{e}{h} \int_0^{\beta eV} \mathrm{d}E \left[P_{12}^{\mathrm{hh}} - P_{12}^{\mathrm{eh}} \right] , \tag{3.16}$$

$$I_2 = \frac{e}{h} \int_0^{\beta eV} \mathrm{d}E \left[-N_2^{h} - P_{22}^{\mathrm{eh}} + P_{22}^{\mathrm{hh}} \right] + \frac{e}{h} \int_0^{\alpha eV} \mathrm{d}E \left[P_{21}^{\mathrm{he}} - P_{21}^{\mathrm{ee}} \right] . \tag{3.17}$$

By taking the derivative with respect to the total bias V, the differential conductance G_i in Equation (3.8) can be explicitly evaluated as

$$G_1(V) = \alpha \left[N_1^{\mathrm{e}}(\alpha eV) - P_{11}^{\mathrm{ee}}(\alpha eV) + P_{11}^{\mathrm{he}}(\alpha eV) \right] + \beta \left[P_{12}^{\mathrm{hh}}(\beta eV) - P_{12}^{\mathrm{eh}}(\beta eV) \right] , \tag{3.18}$$

$$G_2(V) = \beta \left[-N_2^{h}(\beta eV) - P_{22}^{\mathrm{eh}}(\beta eV) + P_{22}^{\mathrm{hh}}(\beta eV) \right] + \alpha \left[P_{21}^{\mathrm{he}}(\alpha eV) - P_{21}^{\mathrm{ee}}(\alpha eV) \right] , \tag{3.19}$$

expressed in units of e^2/h.

The differential conductance $G_1(V)$ measured at the left terminal is governed by the balance between the number of incoming electrons N_1^{e} and the scattering processes they undergo in the junction. The first term accounts for electrons injected from lead 1: normal reflections P_{11}^{ee} reduce the conductance, whereas Andreev reflections P_{11}^{he} yield a positive contribution. The second term corresponds to holes incoming from lead 2: normal transmission P_{12}^{hh} increases the conductance in lead 1, while crossed Andreev transmission P_{12}^{eh} contributes negatively. The expression for the conductance in lead 2 follows analogously by exchanging the role of electrons and holes in the corresponding processes.

3.2 Conductance Antisymmetry

In the following section, we investigate the electronic transport properties of the NSN junction formed by a two-dimensional or quasi–one–dimensional MTI thin film with a proximitized central sector under an asymmetric bias applied to the left and right leads. In this setup, the conductance is determined by the topological superconducting phase realized in the central SC region. The presence of topologically protected Majorana modes manifests itself through an antisymmetric conductance profile with respect to the point of equally-split bias. We analyze this behavior by means of theoretical arguments and numerical simulations, which, following Ref. [100], are carried out using the three-dimensional BdG Hamiltonian given in Equation (2.17).

3.2.1 Asymmetric Bias Splitting

When the proximitized MTI slab is in a two-dimensional thin-film configuration, it effectively reproduces the physics of a 2D superconductor and can host the topological phases discussed in Section 2.2: a trivial superconductor with $\mathcal{N} = 0$ and no edge states, a topological superconductor with $\mathcal{N} = 1$ characterized by a single unpaired MCPS on each edge, and a topological superconductor with $\mathcal{N} = 2$, equivalent to a proximitized QAH state, which supports a pair of particle–hole symmetric edge states on each side. If the system is sufficiently wide, the edge states localized on opposite sides do not hybridize and therefore remain gapless. In this limit, the energy spectra of the different phases resemble those shown in Figure 2.3, and the scattering amplitudes can be directly inferred from the connectivity of the edge modes across the different sectors of the junction [42, 43, 125]. The various scattering processes are illustrated schematically in Figure 3.4.

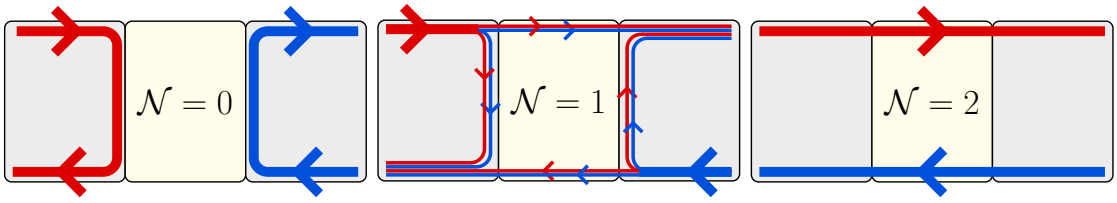

Figure 3.4: Schematic illustration of the scattering processes in an NSN junction composed of normal and proximitized MTIs in the film geometry. The normal leads are in the QAH state, while the central sector is assumed to realize a two-dimensional topological SC with $\mathcal{N} = 0, 1$, or 2. Red (blue) arrows represent the propagation of electron (hole) quasiparticles.

If the normal leads are held in a QAH state, a pair of zero-energy chiral modes propagate along the edges, reflecting the particle–hole degeneracy of the BdG Hamiltonian at $\Delta = 0$. When $\mathcal{N} = 2$, the superconducting sector is topologically equivalent to the QAH insulator in the normal terminals [41]. In this case, the chiral states run uninterruptedly through the normal and proximitized regions, and the edge current is perfectly transmitted [43, 126]. Conversely, the $\mathcal{N} = 0$ trivial superconductor is topologically different with respect to the QAH insulator in the normal terminals, and the bulk–boundary correspondence enforces the appearance of a gapless chiral state along the NS interface between normal and proximitized regions. This interface mode causes complete backscattering of the edge current flowing toward the superconductor [43, 126]. Finally, when $\mathcal{N} = 1$, the proximitized region hosts a single unpaired Majorana mode localized at each edge and along the junction interfaces. In this regime, the incoming chiral modes from the QAH leads split into two MCPSs at the junction interfaces: one is perfectly transmitted, while the other is completely reflected. For a bias below the SC gap, transmission and reflection occur with equal probability for normal and Andreev processes, as the chiral Majorana mode is an equal superposition of electron and hole states.

A similar framework applies to a MTI thin film in a quasi–one–dimensional geometry. When the slab width is smaller than the localization length of the edge modes, the QAH edge states hybridize into a single conducting channel, effectively

realizing a spinless 1D metallic phase where electrons can propagate in both directions. In the presence of induced pairing, the proximitized sector effectively realizes a one-dimensional p-wave superconductor [46]. Consequently, the interfaces between the normal and superconducting regions of the MTI reproduce the physics of a conventional NS junction between a normal metal and a p-wave superconductor [127]. The resulting transport processes, which depend on the topology of the proximitized sector, are illustrated schematically in Figure 3.5.

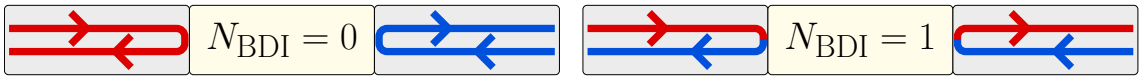

Figure 3.5: Schematic illustration of the scattering processes in an NSN junction composed of normal and proximitized MTIs in the wire geometry. Metallic helical propagating channels are active in the normal leads, while the central sector is assumed to realize a one-dimensional topological SC with $N_{\mathrm{BDI}} = 0, 1$. Red (blue) arrows represent the propagation of electron (hole) quasiparticles.

As discussed in Section 2.3, the central sector can be either a trivial superconductor with $N_{\mathrm{BDI}} = 0$ or a topological one with $N_{\mathrm{BDI}} = 1$, hosting unpaired MBSs in finite-length systems. In the topological phase, end-localized MBSs give rise to perfect Andreev reflection for biases below the superconducting gap [128–130]. Conversely, in the trivial phase, the conductance vanishes in the low-bias limit, as transport is dominated by normal reflection [127]. Higher-order states with $N_{\mathrm{BDI}} \geq 2$ are neglected here, since in the presence of disorder only the parity of the MBSs is a robust topological quantity, and their transport properties reduce to those of the $N_{\mathrm{BDI}} = 0, 1$ cases.

Choosing appropriate values for the transmission probabilities P_{ij}^{ab} to recover the scenarios above, the conductances at the two terminals of the junction can be directly obtained from Equations (3.18) and (3.19) in the different regimes discussed above. The scattering amplitudes and the resulting conductances $G_{1,2}$ are summarized in Tables 3.1 and 3.2, assuming an asymmetric bias configuration with $V_1 = \alpha V$ and $V_2 = (\alpha - 1)V$, where V is the total bias applied across the junction.

S-Phase	N_1^e	P_{11}^{ee}	P_{11}^{he}	P_{12}^{hh}	P_{12}^{eh}
$N_{BDI} = 0$	1	1	0	0	0
$N_{BDI} = 1$ (MBSs)	1	0	1	0	0
$\mathcal{N} = 0$	1	1	0	0	0
$\mathcal{N} = 1$ (MCPSs)	1	0.25	0.25	0.25	0.25
$\mathcal{N} = 2$ (QAH)	1	0	0	1	0

Table 3.1: Transmission amplitudes of the scattering processes at the $i = 1$ terminal of the junction. Results are displayed for all possible topological phases of the central superconducting region. Analogous results are obtained for the lead with $i = 2$.

Only in the presence of Majorana states—either one-dimensional MCPSs or end-localized MBSs—does the conductance depend on how the bias is distributed across

S-Phase	G_1	G_2	G_t
$N_{BDI} = 0$	0	0	0
$N_{BDI} = 1$ (MBSs)	$2\alpha e^2/h$	$2(\alpha - 1)e^2/h$	$2(2\alpha - 1)e^2/h$
$\mathcal{N} = 0$	0	0	0
$\mathcal{N} = 1$ (MCPSs)	$\alpha e^2/h$	$(\alpha - 1)e^2/h$	$(2\alpha - 1)e^2/h$
$\mathcal{N} = 2$ (QAH)	e^2/h	$-e^2/h$	0

Table 3.2: Conductances G_1 and G_2, together with their sum $G_t = G_1 + G_2$, evaluated from Equations (3.18) and (3.19) using the transmission probabilities listed in Table 3.1. The total conductance G_t is nonzero only in the presence of topologically protected Majorana modes, and its value allows one to distinguish between end-localized MBSs and dispersive MCPSs.

the junction. Indeed, when the central region is in a trivial superconducting phase or in a $\mathcal{N} = 2$ TSC, only normal reflection or transmission processes are expected to occur, making the conductance independent on the bias split. In contrast, in presence of Majorana states, the injected quasiparticles interact with the superconducting condensate, such that Cooper pairs are created or annihilated when Andreev reflection takes place at the interfaces [42, 128]. This coupling renders the transport sensitive to the bias partition: if the voltage drops applied to the two sides of the junction are unequal, the creation and annihilation of Cooper pairs at the two interfaces occur at different rates, resulting in a net Cooper-pair current flowing from the proximitized region to ground. Such a current is directly associated with a finite total conductance $G_t = G_1 + G_2$, which signals the presence of Majorana modes under an asymmetric bias splitting, $\alpha \neq 0$.

3.2.2 Symmetry Discussion

It is important to note that $G_t \neq 0$ is not, by itself, an unambiguous signature of Majorana states [131–133]. In the presence of disorder, a trivial Andreev bound state (ABS)—a discrete quasiparticle excitation localized at a normal–superconductor interface formed by successive Andreev reflections of electrons and holes—can give rise to a similar conductance whenever Andreev processes (reflection or transmission) occur at the two interfaces with different rates [134]. In this situation, the currents in the two leads may differ, $I_1 \neq I_2$, giving rise to a nonzero total conductance G_t. The latter corresponds to a net electric current that is emitted from, or absorbed by, the superconducting condensate and flows to ground. However, topologically protected Majorana modes are characterized by the *antisymmetry* of the total conductance with respect to the equally split bias point $\alpha = 0.5$ (see Table 3.2), reflecting identical scattering amplitudes for the Andreev processes at the two interfaces [100].

Analyzing the total conductance G_t as a function of the bias-splitting parameter α provides a practical criterion to identify transport features arising from trivial Andreev processes. While not a definitive proof, an antisymmetric profile of $G_t(\alpha)$ around $\alpha = 0.5$ is indicative of Majorana modes, since trivial Andreev bound states

are not generally constrained to display such behavior. In fact, trivial ABSs can give rise to a wide variety of $G_t(\alpha)$ dependencies, determined by the relative coupling strengths of the bound state to the two interfaces. For instance, if a trivial ABS couples exclusively to the left lead, the total conductance acquires an antisymmetric profile centered at $\alpha = 0$ (completely unbalanced bias). By contrast, in topological phases hosting Majorana modes, the identical scattering amplitudes at the two interfaces enforce an antisymmetric dependence of $G_t(\alpha)$ around $\alpha = 0.5$ (symmetric bias splitting) [100].

Moreover, despite sharing the same antisymmetric profile, the ratio G_t/G_0, where $G_0 \equiv e^2/h$ is the conductance quantum, distinguishes between the two types of Majorana modes that can appear in the superconductor. For a MCPS, one finds $G_t/G_0 = (2\alpha - 1)$, reflecting the fact that all scattering processes in Equations (3.18) and (3.19) occur with the same probability. In contrast, in the presence of end-localized MBSs, the relation $G_t/G_0 = 2(2\alpha - 1)$ signals perfect Andreev reflection at both ends of the proximitized region. Although similar antisymmetric profiles could in principle originate from trivial ABSs, their realization would require finely tuned and perfectly symmetric couplings to the two junction interfaces.

Experimentally, the total conductance G_t can be probed through the current I_{SC} flowing out of the proximitized region (see Figure 3.1). This current directly reflects the transport through the two normal leads while retaining the correlations between the scattering processes at the two interfaces of the junction. Within our simplified model, the only contribution to the current in the *s*-wave superconductor arises from Cooper pairs generated in the proximitized MTI or topological modes below the surface gap. We also neglect direct scattering between the normal leads and the *s*-wave superconductor, as the presence of a *physical* interface between distinct materials strongly reduces such processes compared to the dominant scattering within the MTI slab.

Conductance Matrix

The antisymmetric relation involving the total conductance G_t can be expressed in the equivalent language of the conductance matrix. By considering two-terminal transport between the normal leads of our three-terminal device, the current-voltage relation can be written as

$$\begin{pmatrix} I_1 \\ I_2 \end{pmatrix} = \begin{pmatrix} g_{11} & g_{12} \\ g_{21} & g_{22} \end{pmatrix} \begin{pmatrix} V_1 \\ V_2 \end{pmatrix} . \tag{3.20}$$

The conductance matrix elements are defined as $g_{ij} = \partial I_i / \partial V_j$ and can be distinguished into local ($i = j$) and nonlocal ($i \neq j$) components. The conductance G_i for the current in the $i = 1, 2$ terminal with asymmetric bias splitting takes the form

$$G_1 = \alpha\, g_{11} + (\alpha - 1)\, g_{12} , \qquad G_2 = \alpha\, g_{21} + (\alpha - 1)\, g_{22} , \tag{3.21}$$

and the total conductance can be written as

$$G_t = G_1 + G_2 = -(g_{12} + g_{22}) + \alpha(g_{11} + g_{12} + g_{21} + g_{22}) . \tag{3.22}$$

Therefore, in terms of local g_{ii} and nonlocal g_{ij} matrix elements the antisymmetric condition around $\alpha = 0.5$ can be written explicitly as

$$g_{11} - g_{22} = g_{12} - g_{21} \,, \tag{3.23}$$

meaning that the difference between local conductances must be equal to the difference between the nonlocal ones.

3.2.3 Numerical Results

To investigate the antisymmetric profile of the conductance with respect to the bias-splitting parameter α, we simulated a NSN junction composed of normal and proximitized MTI slabs, employing the complex band structure approach introduced in Section 3.1.1. The modeling is based on the effective three-dimensional BdG Hamiltonian defined in Equation (2.17). In what follows, we consider an MTI with thickness $d = 4$ nm (corresponding to approximately four QLs) and two representative values of the lateral width:

(i) $L_y = 160$ nm, corresponding to an effective two-dimensional film-like geometry;

(ii) $L_y = 20$ nm, corresponding to a quasi–one–dimensional wire-like geometry.

The first configuration reproduces the physics of the two-dimensional TSC described in Section 2.2, whereas the second one emulates the one-dimensional limit discussed in Section 2.3.

Since an asymmetric pairing between the top and bottom surfaces is required to realize topological superconductivity [41, 42, 45, 46], we assume a constant pairing field along the transverse direction y, and we restrict the proximity effect to the upper half of the system through

$$\Delta(y, z) = \Delta_0 \, \theta(z - d/2) \,, \tag{3.24}$$

where θ denotes the Heaviside step function. All numerical results presented below are obtained with $\Delta_0 = 10$ meV for the film geometry, and $\Delta_0 = 5$ meV for the wire case. Although these values are considerably larger than those typically accessible in experiments, they are convenient for numerical purposes: qualitatively similar results can be achieved for smaller pairings and rescaled system sizes. In particular, employing a large pairing amplitude Δ reduces the computational cost by enabling simulations of smaller systems, while at the same time enhancing the MBS energy gap and widening the parameter regime that hosts MCPSs, which are the main focus of our analysis.

Figure 3.6 shows the total conductance G_t as a function of the magnetization Λ and the bias-splitting parameter α. In the effective two-dimensional geometry, the normal leads are maintained in the QAH phase, which guarantees ballistic propagation of electron and hole quasiparticles toward the junction under a finite bias. By contrast, in the quasi–one–dimensional limit the non-proximitized part of the junction is maintained in a metallic-like state, where—in the presence of disorder—quasiparticles undergo diffusive transport through helical conducting channels arising from the discretization of the Dirac-cone surface states in the wire geometry. In

both cases, the occurrence of regions with $G_t \neq 0$ signals the presence of topological SC phases hosting zero-energy Majorana modes.

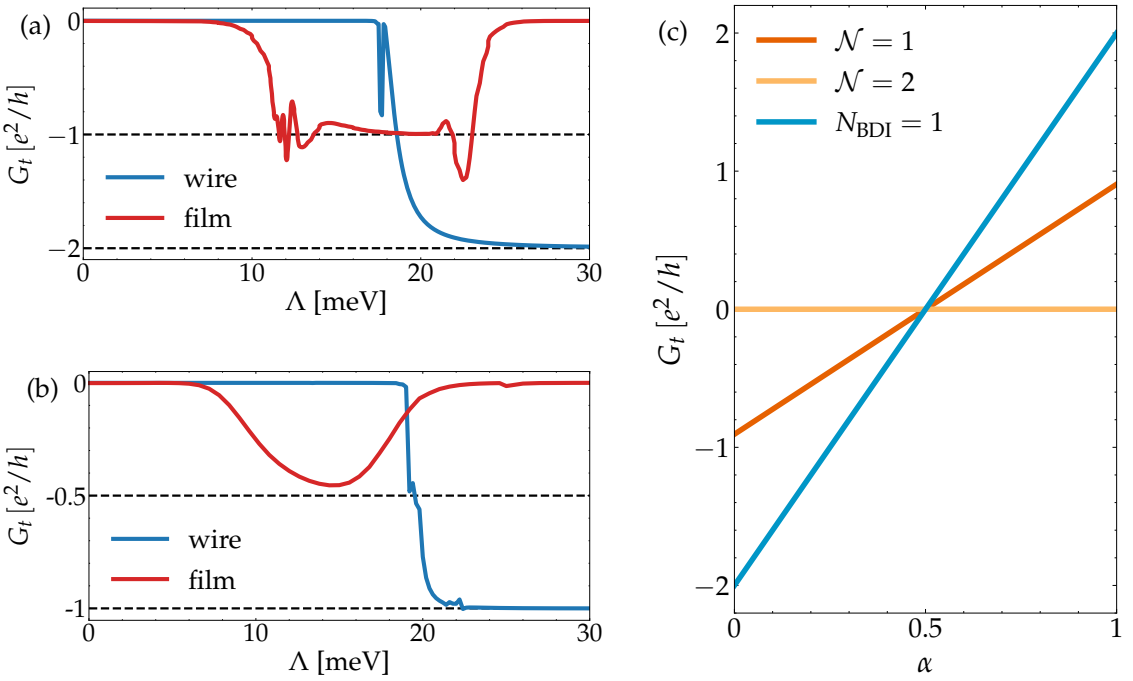

Figure 3.6: Total conductance $G_t = G_1 + G_2$ of the NSN junction under asymmetric bias splitting. (a)–(b) Dependence of G_t on the magnetization Λ for the quasi–one–dimensional wire (blue) and two-dimensional film (red) geometries with (a) $\alpha = 0$ and (b) $\alpha = 0.25$. (c) Conductance as a function of the bias-splitting parameter α for a junction with the proximitized central region in the $\mathcal{N} = 2$ (yellow), $\mathcal{N} = 1$ (orange), and $N_{\rm BDI} = 1$ (green) topological SC phases. In all panels, the total bias across the junction is fixed at $V = 0.1$ meV. Adapted from Ref. [100].

Panels (a) and (b) illustrate the case of an asymmetric voltage drop with (a) $\alpha = 0$ and (b) $\alpha = 0.25$. In the thin-film geometry (red line), the $\mathcal{N} = 1$ chiral TSC is clearly separated from the trivial $\mathcal{N} = 0$ superconductor and the $\mathcal{N} = 2$ proximitized QAH state, where $G_t = 0$ reflects equal and opposite terminal currents independent of how the bias is split. The $\mathcal{N} = 1$ phase yields $G_t = -e^2/2h$ at $\alpha = 0.25$ and $G_t = -e^2/h$ at $\alpha = 0$, in qualitative agreement with our theoretical analysis (see Table 3.2). An analogous behavior is found in the wire geometry (blue line), where the $N_{\rm BDI} = 1$ phase gives $G_t = -e^2/h$ and $-2e^2/2h$ for $\alpha = 0$ and $\alpha = 0.25$, respectively, while the $N_{\rm BDI} = 0$ phase is characterized by $G_t = 0$, corresponding to perfect normal reflection.

In panel (c), the total conductance G_t is shown as a function of the bias-splitting parameter α. The magnetization is fixed to realize the $\mathcal{N} = 1$ phase with MCPSs and the $\mathcal{N} = 2$ state in the film geometry, and the $N_{\rm BDI} = 1$ topological phase hosting MBSs in the wire geometry. The numerical results are in excellent agreement with the predictions summarized in Table 3.2. It is important to note that a symmetric bias configuration ($\alpha = 0.5$) cannot discriminate a TSC from either the trivial superconductor or the proximitized QAH phase, since all yield $G_t = 0$. Our

framework thus extends the analysis of electrical conductance in the NSN double junction with Majorana modes previously reported in Refs. [42–44].

Figure 3.7 shows the probability amplitudes associated with the scattering processes at the left interface of the junction, namely normal reflection P_{11}^{ee}, Andreev reflection P_{11}^{he}, normal transmission P_{21}^{ee}, and Andreev transmission P_{21}^{he}. Panel (a) corresponds to a one-dimensional $\mathcal{N} = 1$ topological superconducting thin film hosting MCPSs, while panel (b) refers to a two-dimensional $N_{\mathrm{BDI}} = 1$ topological superconducting wire with unpaired MBSs.

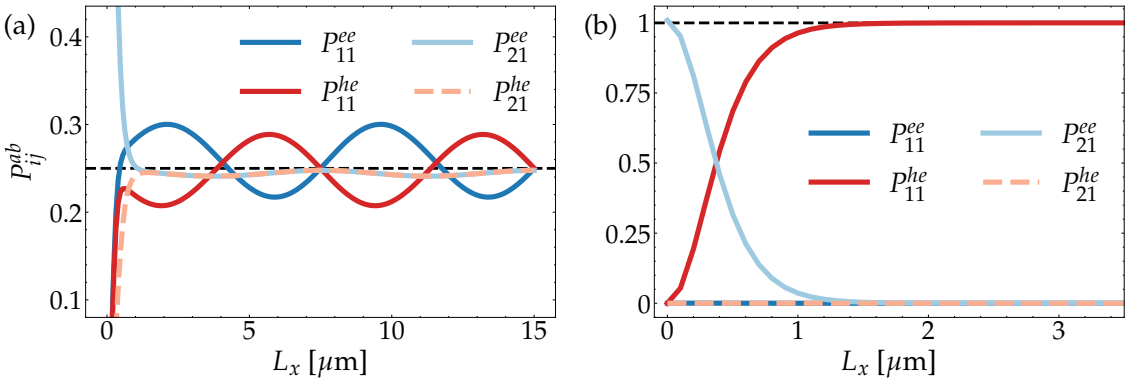

Figure 3.7: Scattering probability amplitudes at terminal $i = 1$ of the NSN junction as a function of the central region length L_x, for (a) the film geometry and (b) the wire geometry. The total bias across the junction is fixed at $V = 0.1$ meV. Blue (red) lines denote (normal) Andreev processes. Adapted from Ref. [100].

In the two-dimensional film geometry, normal and Andreev transmission and reflection occur with equal probability, $P_{j1}^{ae} = 0.25$ for $j = 1, 2$ and $a = \mathrm{e}, \mathrm{h}$. The small oscillations around this plateau originate from the interference between backscattered chiral modes at the two interfaces of the double junction, giving rise to an interferometric behaviour [44]. In the quasi–one–dimensional limit, provided the junction is sufficiently long to suppress transmission through evanescent modes, the injected electron undergoes perfect Andreev reflection with $P_{11}^{he} = 1$ in the presence of MBSs. The numerical results show excellent agreement with the theoretical predictions summarized in Table 3.1. In all cases, the total bias across the junction is fixed to $V = 0.1$ meV, well below the surface energy gap. This choice ensures that bulk modes are not activated in the proximitized region and that the injected quasiparticles interact with the condensate exclusively through the topologically protected Majorana boundary states.

3.3 Bias-Dependent Transport Regimes

In the previous section, we analyzed the antisymmetric profile of the total electric conductance G_t as a function of the bias-splitting parameter α, for small total biases below the surface gap of the proximitized MTI, in both one- and two-dimensional geometries. In this chapter, we turn our attention to the physics of MCPSs under symmetric bias conditions $V_1 = -V_2$ applied to the two sides of the junction, and

we investigate the dependence of the electric conductance on the total bias V. The central goal is to identify additional transport signatures characteristic of the $\mathcal{N} = 1$ chiral superconducting phase.

Due to the interplay of normal and Andreev reflection and transmission processes, the presence of zero-energy MCPSs gives rise to a half-quantized conductance plateau $G_1 = -G_2 = e^2/2h$, for a small voltage bias below the SC gap. Although this half-integer conductance plateau was originally proposed as a hallmark of proximitized QAH systems, subsequent works have demonstrated that it does not constitute an unambiguous signature of MCPSs [101, 135–137]. To address this limitation, we numerically simulate the conductance in the symmetric-bias configuration, where $G_1 = -G_2$, and analyze the emergence of three distinct transport regimes as the total bias V is increased. The simulations are performed within the framework of the three-dimensional BdG Hamiltonian introduced in Equation (2.17), following the methodology of Ref. [100].

3.3.1 Edge Spectrum

To gain insight into the emergence of the three distinct transport regimes in the NSN junction, we analyze the energy spectrum of a two-dimensional MTI thin film subject to a proximity-induced pairing applied to the upper interfaces. In particular, we study the evolution of the spectrum as the pairing amplitude is gradually increased, starting from a $\mathcal{N} = 2$ phase with $\Lambda > m_0$. The induced pairing plays a role analogous to that of the magnetization discussed in Section 2.2, driving the phase transition from the proximitized QAH state to the $\mathcal{N} = 1$ chiral TSC [41, 42]. This evolution is illustrated in Figure 3.8, which shows the energy spectrum of the MTI thin film as superconducting correlations are progressively introduced on its upper surface.

The edge or bulk character of the states, represented by the color scale in Figure 3.8, is quantified by the expectation value of the transverse coordinate, computed from the energy eigenstates $\psi_{n,k_x}(y)$ of the discretized Hamiltonian. For an energy state with band index n and longitudinal momentum k_x, the average transverse position is defined as

$$\langle y \rangle_{n,k_x} = \sum_i y_i \left|\psi_{n,k_x}(y_i)\right|^2 , \qquad \sum_i \left|\psi_{n,k_x}(y_i)\right|^2 = 1 , \tag{3.25}$$

where y_i denotes the coordinate of the i-th site in the finite transverse lattice.

In the absence of pairing $\Delta_1 = 0$ and for $\Lambda < m_0$, the MTI thin film is in the QAH phase. Within the Nambu formalism, the doubling of the degrees of freedom yields $\mathcal{N} = 2$ particle–hole symmetric, degenerate edge modes on each side of the system. Introducing a finite pairing amplitude $\Delta_1 \neq 0$ lifts this degeneracy: a gap opens at one of the two crossings, and the corresponding edge states are pushed into the bulk. As a consequence, only a single unpaired MCPS remains on each side below the gap, realizing the $\mathcal{N} = 1$ chiral SC phase [30, 41, 42]. In this regime, the boundary modes are strongly hybridized around $k_x = 0$, but they retain a well-defined edge character away from the Dirac point. Therefore, at slightly higher energies, a *pair* of chiral modes with different momenta k_1 and k_2 coexist on each side of the system, as shown in Figure 3.8 (b). Upon further increasing the pairing strength, these edge

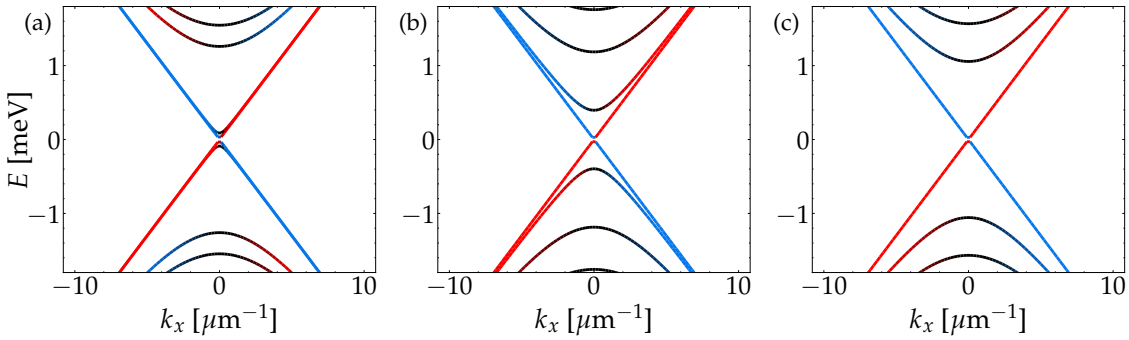

Figure 3.8: Evolution of the energy spectrum of a proximitized MTI thin film with increasing superconducting pairing on the top surface. The spectra are obtained by discretizing the Hamiltonian in eq. (2.19) on a finite lattice along the y direction with width $L_y = 1$ μm and imposing periodic boundary conditions along x. We assumed an induced pairing (a) $\Delta_1 = 0.5$ meV, (b) $\Delta_1 = 1.5$ meV, and (c) $\Delta_1 = 2.5$ meV and $\Delta_2 = 0$. The remaining parameters are fixed to $m_0 = 1$ meV, $m_1 = 0.001$ meVμm^2, $v_F = 0.26$ meVμm, $\mu = 0$, $D = 0$ and $\Lambda = 2$ meV. The color scale represents the average transverse position on the lattice, computed according to Equation (3.25), with red (blue) corresponding to $\langle y \rangle = +0.5$ μm ($\langle y \rangle = -0.5$ μm). In panel (a), the energy-degenerate bands are slightly displaced for clarity of visualization.

modes are progressively pushed toward the bulk until they delocalize completely and merge with the surface-state continuum.

In the intermediate regime, where $\Lambda - m_0 < \Delta_1 < \Lambda + m_0$ drives the system into the $\mathcal{N} = 1$ phase, three distinct transport regimes can be clearly identified at different energies:

(i) a low-energy regime, characterized by a *single* MCPS on each side;

(ii) an intermediate-energy regime, featuring a *pair* of linear edge-localized modes with different momenta;

(iii) a high-energy regime, with several propagating channels delocalized across the entire section of the film, and metallic-like transport properties.

These three distinct regimes are a characteristic feature of the spectrum of a chiral TSC, and their transport signatures provide a means to identify the $\mathcal{N} = 1$ topological phase hosting MCPSs. In particular, for a fixed energy in the intermediate-energy regime, the two edge channels occur at different wavenumbers k_1 and k_2. The finite momentum separation between these modes induces spatial interference, leading to characteristic oscillations in the electric current as a function of the quasiparticle energy when transport occurs along the edge of the proximitized MTI [102].

3.3.2 Quasiparticle Interference

The oscillations of the edge current in the intermediate-energy regime can be intuitively understood through a simple toy model, which predicts an oscillatory dependence of both normal and Andreev transmission probabilities. Let us consider a

proximitized one-dimensional spinless system that, at a given energy E, hosts two chiral propagating modes with longitudinal momenta k_1 and k_2. These modes are assumed to be equal superpositions of electron and hole states in the Nambu basis, and can be written as

$$|\psi_1\rangle = \tfrac{1}{\sqrt{2}}\left(|e\rangle + |h\rangle\right) , \qquad |\psi_2\rangle = \tfrac{1}{\sqrt{2}}\left(|e\rangle - |h\rangle\right) . \tag{3.26}$$

This toy model captures the essential edge physics of the two-mode regime of the chiral TSC, where, in the limiting case $\mu = 0$, the two states are equal superpositions of particle and hole components.

An incoming electron propagating into this proximitized region can be expressed as a coherent superposition of the two chiral modes through

$$|\psi\rangle = \frac{1}{\sqrt{2}}\left(\mathrm{e}^{\mathrm{i}k_1 x}\,|\psi_1\rangle + \mathrm{e}^{\mathrm{i}k_2 x}\,|\psi_2\rangle\right) , \tag{3.27}$$

where x denotes the distance traveled. The probability that an electron is perfectly transmitted across the junction is thus given by

$$P_e = |\langle e|\psi\rangle|^2 = \frac{1}{2}\left[1 + \cos\left(\delta_k\, L\right)\right] , \tag{3.28}$$

while the probability of converting an electron into a hole is

$$P_h = |\langle h|\psi\rangle|^2 = \frac{1}{2}\left[1 - \cos\left(\delta_k\, L\right)\right] , \tag{3.29}$$

where $\delta_k \equiv k_1 - k_2$ such that $\delta_k\, L$ is the phase difference acquired along the propagation length L. Analogous expressions can be found for an incoming hole.

When two edge modes with different momenta coexist at the boundary of an MTI thin film in the intermediate-energy regime of the chiral TSC, the resulting edge transport reflects the physics of the toy model discussed above. The probabilities of normal and Andreev transmission display out-of-phase oscillations as a function of the accumulated phase $\delta_k L$, and the differential conductance across the NSN junction exhibits characteristic oscillations in the intermediate-energy regime [102]. Figure 3.9 shows the differential conductance $G \equiv G_1 = -G_2$, computed from Equation (3.18) as a function of the symmetric bias $V_1 = -V_2 = V/2$, with the normal leads maintained in a QAH state.

The three distinct bias-dependent regimes can be clearly distinguished:

(i) a low-bias regime with a conductance plateau at $G = e^2/2h$, with small oscillations induced by the finite transverse width L_y;

(ii) an intermediate-bias regime, where large oscillations occur with $0 < G < e^2/h$;

(iii) a high-bias regime, exhibiting a metallic-like behavior with quasiparticle transport becoming difffusive rather than ballistic.

In the low-bias regime $E \approx 0$, a single MCPS is present within the surface gap of the $\mathcal{N} = 1$ topological superconductor and the conductance is half-quantized at the value $G = e^2/2h$. Oscillations around this plateau arise from the finite-size hybridization of edge modes located at opposite sides [44]. As the bias increases, but

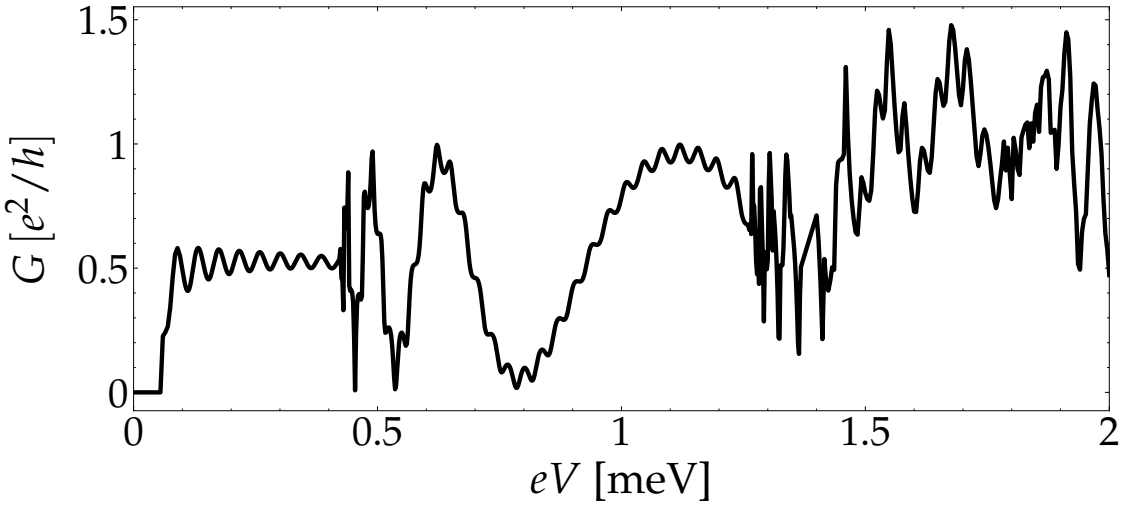

Figure 3.9: Differential conductance G of a NSN junction composed by normal and proximitized MTI thin films, plotted as a function of the applied bias voltage eV. The calculation is performed using the two-dimensional Hamiltonian in Equation (2.19), discretized on a finite lattice of width $L_y = 1$ μm along the y direction. We assume an induced SC pairing on the top surface, only with $\Delta_1 = 1.5$ meV and $\Delta_2 = 0$. The remaining parameters are $m_0 = 1$ meV, $m_1 = 0.001$ meVμm^2, $v_F = 0.26$ meVμm, $\mu = 0$, and $D = 0$. Replotted from Ref. [102].

still remains below the surface gap, the normal leads stay in the QAH regime, while the proximitized region hosts a pair of chiral edge modes with different wavenumbers. In this situation, the quasiparticle propagation is influenced by spatial interference, as the accumulated phase difference over the junction length L_x determines an oscillatory conductance ranging between $G = 0$ (perfect crossed Andreev reflection) and $G = e^2/h$ (perfect normal transmission). At even higher biases, additional delocalized states become active, and the system enters a metallic-like regime. Transport in the proximitized regions becomes diffusive rather than ballistic, and the conductance is expected to be strongly sensitive to disorder.

3.3.3 Current Density Distribution

The three different regimes can be distinguished not only in terms of two-terminal conductance, but also in terms of current density along the transverse section of the junction. We emphasize that the transverse current distribution is relevant information for the experimental characterization of proximitized TI thin films, and can be measured through superconducting quantum interference devices [138–140]. Resolving the full spatial profile of the current density offers valuable insight into the quasiparticle transport processes occurring in the junction. In contrast, conductance measurements alone have so far proven insufficient to yield an unambiguous signature of MCPSs in proximitized QAH films [101, 135–137].

The longitudinal component of the electric current density is given by [102, 118]

$$j_x(x,y) = -e\,\mathrm{Re}\left[\Psi^\dagger(x,y)\,v_x\gamma_z\,\Psi(x,y)\right], \tag{3.30}$$

where $\Psi(x, y)$ denotes the real-space wavefunction in Nambu basis, and the velocity operator in the longitudinal direction x takes the form ($\hbar = 1$)

$$v_x = \frac{\partial}{\partial k_x}\left[h_{\mathrm{2D}}^{\mathrm{BdG}}(k_x)\right] = 2k_x\left(D + m_1\lambda_x\right)\gamma_z - v_F\sigma_y\lambda_z\gamma_z\,. \tag{3.31}$$

Once the real-space wavefunction $\Psi(x, y)$ across the entire junction has been obtained following the procedure outlined in Appendices A.2 and A.3, the current density defined in Equation (3.30) can be directly evaluated.

The longitudinal current in the two *normal* leads of the NSN junction is shown in Figure 3.10 as a function of the transverse coordinate y for different values of the bias V applied across the junction. In the numerical simulations, the current density was evaluated at $x = \pm 15$ μm, assuming a central proximitized region of length $L_x = 20$ μm with $x = 0$ defined at its midpoint. The width of the transverse lattice was fixed to $L_y = 1$ μm. As long as the normal regions remain in the QAH phase, the resulting current profile is independent of the precise longitudinal position at which it is extracted.

Panels (a)–(b) show the electric current-density profiles for the low-bias regime $eV \in [0.1, 0.3]$ meV, where a single unpaired MCPSs is found on each side of the proximitized region. As long as the normal sectors of the MTI thin film are in the QAH phase, the current is strongly confined to the edges. The maxima in the current-density distribution correspond to quasiparticles injected toward the proximitized region: electrons propagate along the upper edge at $y = 0.5$ μm (blue column), while holes travel in the opposite direction along the lower edge at $y = -0.5$ μm (red column). In the presence of a single MCPS, electrons and holes are equally split between reflection and transmission at the junction interfaces [43]. Apart from negligible finite-size effects, no net electric current is transmitted or reflected through the superconducting region, as evidenced by $j_x = 0$ in the normal lead opposite to the one carrying the injected edge current.

A different physics is illustrated in Figure 3.10 (c)–(d), where the current-density profiles are shown for the intermediate-bias regime $eV \in [0.6, 0.8]$ meV. As in the previous case, the non-proximitized regions remain in the QAH phase, so that the current is confined to the edges and the transport is ballistic. However, as discussed in Section 3.3.2, the superconducting region hosts a pair of degenerate edge modes with different momenta. As a consequence, an injected quasiparticle traversing the central sector exhibits an oscillatory probability of undergoing normal or Andreev transmission, resulting in a modulated current density on the lead where the particle is transmitted. The spatial current distribution is highly sensitive to small variations in the applied bias, since the transmission amplitudes depend on the momentum mismatch δ_k between the edge channels, which in turn is determined by the quasiparticle energy.

Finally, Figure 3.10 (e)–(f) illustrate the metallic-like regime corresponding to the hig-bias regime $eV \in [1.7, 1.9]$ meV, exceeding the surface gap. In this case, the quasiparticles propagate through delocalized bulk modes in both the normal leads and the proximitized region, rendering the transport diffusive rather than ballistic. Although some maxima remain visible near the system boundaries, the current is transmitted across the entire transverse section of the junction, and disorder effects are therefore expected to play a significant role in the overall transport properties.

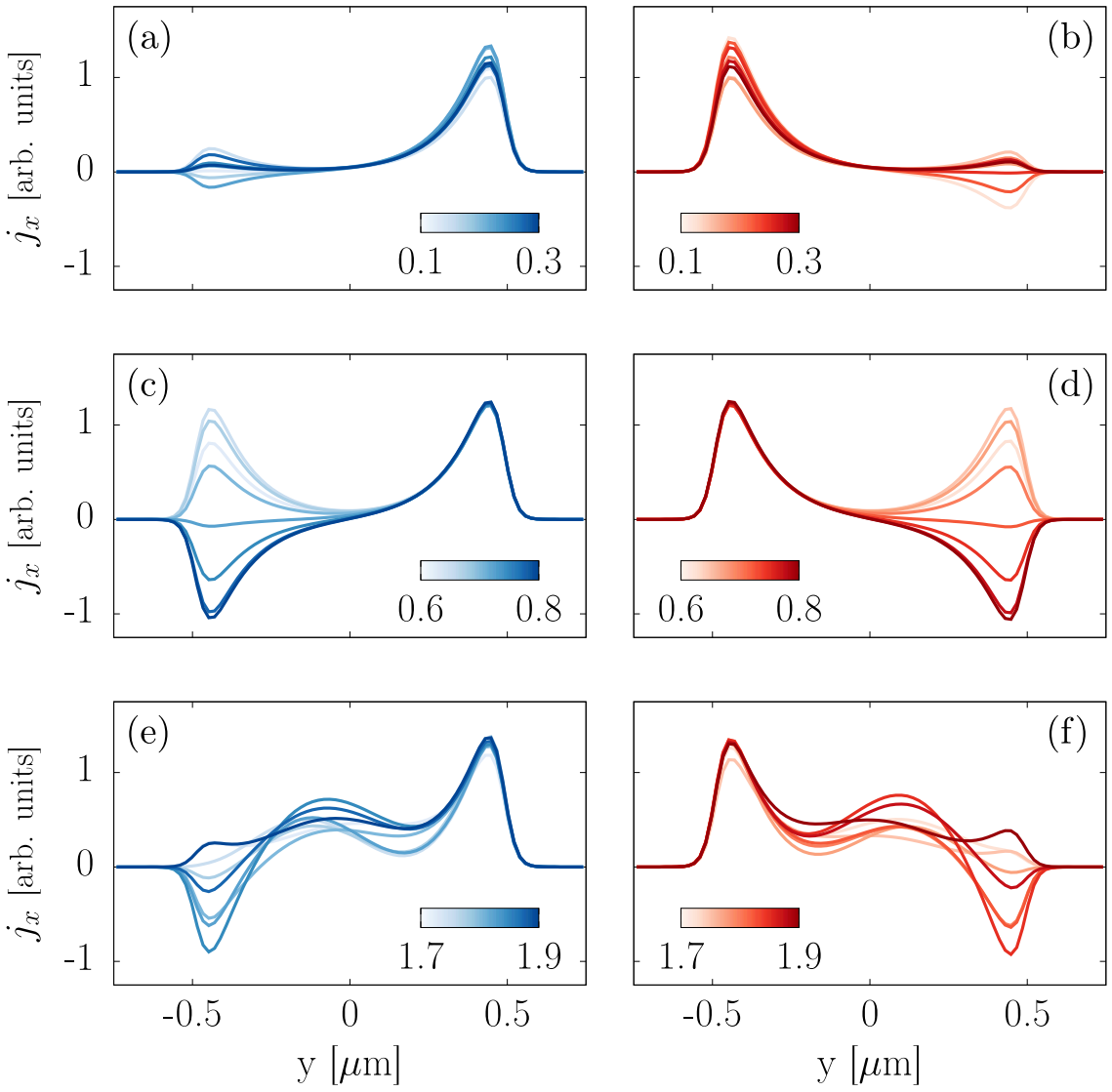

Figure 3.10: Longitudinal current density j_x across the transverse section of a NSN junction composed of normal and proximitized MTIs thin films, shown for different voltage biases. The current is evaluated along the transverse section of the junction in the left (right) normal lead and is plotted in red (blue). Results are presented for a $\mathcal{N} = 1$ topological superconductor in the three distinct regimes discussed in the main text: (a)-(b) low-bias regime with unpaired MCPSs, (c)–(d) intermediate-bias regime with two edge states at different momenta, and (e)–(f) high-bias regime with metallic-like states. The color scale denotes the quasiparticle injection energy eV in meV, corresponding to the applied bias across the junction. The system size and Hamiltonian parameters are chosen consistently with Figure 3.9. Reproduced from Ref. [102].

An analogous analysis of the transverse current density can be performed within the proximitized region of the TI thin film by evaluating the average current j_x in the central sector of the junction. In the present discussion, however, we have restricted our attention to the current distribution in the normal leads, where the entire electric current is carried by quasiparticles. In contrast, within the superconducting region, the quasiparticle contribution is screened by the Cooper pair condensate, which is not captured by our formalism. Nevertheless, qualitatively similar behavior is expected for the characteristic oscillations in the two-mode regime.

We emphasize that the oscillatory transport behavior relies on the fact that quasiparticle excitations in the superconducting region are coherent superpositions of electron and hole states. This condition is always satisfied in the limit of vanishing chemical potential, $\mu = 0$, where the Fermi energy coincides with the Dirac point of the topological surface states. Although such fine-tuned conditions represent a limitation of our analysis, the band structure of topological insulators of the Bi_2Se_3 family can be engineered, manipulating the Dirac surface states without affecting the bulk properties of the crystal [141, 142].

Summary

In this chapter, we investigated direct-current transport in NSN junctions based on proximitized MTIs, combining the Landauer–Büttiker framework with the BTK formalism to account for Andreev reflection. Using the complex band-structure approach, we modeled both propagating and evanescent modes at the NS interfaces of the junction, with the aim of identifying transport signatures of Majorana states and distinguishing them from trivial ABSs.

Our first main result concerns the low-bias linear-response regime, where only subgap quasiparticles or Andreev processes contribute to transport. We demonstrated that, in presence of asymmetric bias splitting, the occurrence of Andreev reflection can lead to an imbalance between the partial conductances G_1 and G_2 at the two normal leads, compensated by a Cooper-pair current that flows to ground from the superconductor. The presence of zero-energy Majorana modes, however, enforces identical scattering amplitudes at both interfaces, resulting in a robust *antisymmetric* profile of the total conductance as a function of the bias-splitting parameter. This distinctive feature was shown to occur in both quasi–one–dimensional nanowires and two-dimensional thin films.

Our second main result relates to the transport properties of the $\mathcal{N} = 1$ TSC phase, where Majorana chiral states propagate along the edges of the proximitized region. While a half-quantized conductance plateau is a well-known hallmark of this state, we demonstrated that increasing the voltage drop across the junction reveals two additional transport regimes, with the half-quantized plateau representing only the lowest-bias case. In particular, in the symmetric-bias configuration, we identified a regime of large oscillations in the differential conductance, arising from the interference of two co-propagating chiral modes along the same edge and directly linked to the emergence of the topological phase hosting MCPSs.

Overall, our analysis shows that electric transport experiments could reveal topological superconducting states with Majorana quasiparticles, with the antisymmetric

conductance profile and high-bias oscillations providing signatures that go beyond the conventional conductance-quantization plateaus. At the same time, the lack of an unambiguous zero-bias feature highlights the limitations of transport probes and the need for complementary observables.

The numerical analysis in this chapter were carried out by introducing a phenomenological pairing term in the BdG Hamiltonian to describe the proximitized MTIs. The final part of this thesis is devoted to developing a perturbative framework for evaluating in a more realistic way the induced superconducting correlations, explicitly accounting for the tunneling processes between the two materials at the interface of the heterostructure.

Part III

Induced Superconductivity

Chapter 4

Perturbation Theory

Overview

In the previous chapters, we analyzed proximitized MTIs within an effective first-quantization framework, where superconductivity was introduced phenomenologically by adding an external pairing term to the BdG Hamiltonian. While this approach provides a convenient low-energy description, it treats the induced pairing as an input parameter and therefore does not allow for a self-consistent evaluation of the proximity effect. This limitation motivates the development of a second-quantized formalism, in which superconducting correlations emerge naturally from tunneling across the MTI–SC interface and are captured by the anomalous components of the Green's function. In this framework, the tunneling interaction is treated as a perturbation on the ground states of the decoupled materials. This allows us to derive the corrections to the normal and anomalous Green's functions of the MTI, expressed in terms of the unperturbed propagators of the isolated systems.

The remainder of this chapter is organized as follows. In Section 4.1, we introduce the second-quantized Hamiltonian for the MTI–SC heterostructure, modeling the magnetic topological insulator as a thin film with translational invariance along x and y, and finite thickness d along z. The SC is assumed to be a conventional spin-singlet s-wave bulk superconductor. In Section 4.2 we outline the many-body Green's function formalism, which provides the natural framework to describe superconducting correlations and proximity-induced effects. Finally, in Section 4.3, we derive the lowest-order corrections to the MTI Green's functions in the interaction picture, treating the tunneling Hamiltonian as a perturbation on the unperturbed ground states of the decoupled materials.

4.1 Second-Quantized Model

The proximity effect in an MTI–SC heterostructure can be described within the framework of second quantization, where Green's functions provide a natural description of the system. In this approach, the normal and anomalous Green's functions describe the propagation amplitudes of single and correlated pairs of quasiparticles, respectively. The latter reflects the presence of the Cooper-pair condensate induced by the proximity effect.

In an otherwise non-superconducting MTI, the induced pairing arises from the *proximity effect*, where electrons from the Cooper-pair condensate tunnel into the topological surface states of the MTI, and, conversely, electrons in the MTI tunnel into the SC to form Cooper pairs. This process gives rise to an effective superconducting pairing in the topological insulator, and can be modeled by a Hamiltonian of the form

$$H = H_{\mathrm{MTI}} + H_{\mathrm{SC}} + H_{\mathrm{int}} \,. \tag{4.1}$$

In the following, we focus on a system that is translationally invariant along the in-plane directions x and y. The MTI thin film is taken to have a finite thickness d along the out-of-plane direction z, spanning the region $0 \leq z \leq d$, while the superconductor occupies the semi-infinite region $z < 0$. The SC is approximated as a bulk system, neglecting confinement effects, since the interface does not significantly alter the electronic wavefunctions within the condensate.

4.1.1 MTI Hamiltonian

In order to compute the perturbative correction to the normal and anomalous Green's functions in the MTI, we need to express the heterostructure Hamiltonian in the second quantization form using real-space field operators. We start by introducing the creation (annihilation) field operators $\psi^\dagger_{\sigma\tau}(\mathbf{r})$ ($\psi_{\sigma\tau}(\mathbf{r})$) in the MTI, which creates (annihilates) an electron at position $\mathbf{r}$ with spin $\sigma =\uparrow,\downarrow$ and orbital index $\tau = \pm$ [143, 144]. The field operators satisfy the fermionic anticommutation relations

$$\begin{aligned} \{\psi_{\sigma\tau}(\mathbf{r}), \psi^\dagger_{\sigma'\tau'}(\mathbf{r}')\} &= \delta_{\sigma\sigma'}\,\delta_{\tau\tau'}\,\delta(\mathbf{r}-\mathbf{r}')\,, \\ \{\psi_{\sigma\tau}(\mathbf{r}), \psi_{\sigma'\tau'}(\mathbf{r}')\} &= \{\psi^\dagger_{\sigma\tau}(\mathbf{r}), \psi^\dagger_{\sigma'\tau'}(\mathbf{r}')\} = 0\,. \end{aligned} \tag{4.2}$$

We consider a complete and orthonormal basis of single-particle eigenstates $|n\rangle$ of the MTI Hamiltonian h_{MTI}, satisfying

$$h_{\mathrm{MTI}}\,|n\rangle = \varepsilon_n\,|n\rangle\ , \tag{4.3}$$

with the orthonormality and completeness relations

$$\langle n|m\rangle = \delta_{nm}\,, \qquad \sum_n |n\rangle\,\langle n| = \hat{1}\,. \tag{4.4}$$

The corresponding first-quantized wavefunction in the spin–orbital basis $|\sigma\tau\mathbf{r}\rangle$ is defined as

$$\varphi_{n,\sigma\tau}(\mathbf{r}) = \langle \sigma\tau\mathbf{r}\,|\,n\rangle\ , \tag{4.5}$$

and the field operators can be expanded in terms of the eigenstates $|n\rangle$ as

$$\psi_{\sigma\tau}(\mathbf{r}) = \sum_n \varphi_{n,\sigma\tau}(\mathbf{r})\,c_n\,, \qquad \psi^\dagger_{\sigma\tau}(\mathbf{r}) = \sum_n \varphi^*_{n,\sigma\tau}(\mathbf{r})\,c^\dagger_n\,, \tag{4.6}$$

where $c^\dagger_n$ (c_n) creates (annihilates) an electron in the single-particle eigenstate $|n\rangle$, acting on the Fock space. Reversing Equation (4.6), the creation and annihilation operators c_n, $c^\dagger_n$ can be expressed in terms of the real-space field operators as

$$c_n = \sum_{\sigma\tau}\int \mathrm{d}\mathbf{r}\,\varphi^*_{n,\sigma\tau}(\mathbf{r})\psi_{\sigma\tau}(\mathbf{r})\,, \qquad c^\dagger_n = \sum_{\sigma\tau}\int \mathrm{d}\mathbf{r}\,\varphi_{n,\sigma\tau}(\mathbf{r})\psi^\dagger_{\sigma\tau}(\mathbf{r})\,. \tag{4.7}$$

As single-particle Hamiltonian h_{MTI} we adopt the 3D low-energy effective model for topological insulators of the Bi_2Se_3 family introduced in Equation (1.48). Using the second quantization formalism, the MTI Hamiltonian can be written in terms of real-space field operators as [143, 144]

$$H_{\mathrm{MTI}} = \sum_{\sigma\sigma'} \sum_{\tau\tau'} \int \mathrm{d}\mathbf{r}\, \psi^{\dagger}_{\sigma\tau}(\mathbf{r})\, h_{\sigma\tau,\sigma'\tau'}(-\mathrm{i}\nabla)\, \psi_{\sigma'\tau'}(\mathbf{r})\,, \tag{4.8}$$

where the matrix elements $h_{\sigma\tau,\sigma'\tau'}$ are defined as

$$h_{\sigma\tau,\sigma'\tau'}(-\mathrm{i}\nabla) = \langle \sigma\tau, \mathbf{r}|\ h_{\mathrm{MTI}}(-\mathrm{i}\nabla)\ |\sigma'\tau', \mathbf{r}\rangle\ , \tag{4.9}$$

and the real-space representation of the first-quantized Hamiltonian h_{MTI} is obtained by performing the usual substitution $\mathbf{k} \to -\mathrm{i}\nabla$ in Equation (1.48). In this representation, the differential operator acts on the spatial coordinate of the wave function to its right, $|\sigma'\tau', \mathbf{r}\rangle$. Since we are ultimately interested in a thin film of MTI with translational invariance along the x and y directions, we perform a Fourier transform of Equation (4.8) with respect to the in-plane coordinates. This yields a Hamiltonian that is diagonal in the corresponding momenta k_x and k_y, and depends explicitly only on the out-of-plane coordinate z

$$H_{\mathrm{MTI}} = \sum_{\sigma\sigma'} \sum_{\tau\tau'} \int \mathrm{d}z\, \psi^{\dagger}_{\sigma\tau}(z)\, h_{\sigma\tau,\sigma'\tau'}(-i\partial_z)\, \psi_{\sigma'\tau'}(z)\,. \tag{4.10}$$

For simplicity, here we have omitted the indices for the in-plane momenta k_x and k_y. The field operators in this mixed representation are defined as

$$\begin{aligned} \psi_{\sigma\tau}(z) \equiv \psi_{\sigma\tau}(k_{\parallel}, z) &= \int \mathrm{d}x\, \mathrm{d}y\, \mathrm{e}^{-\mathrm{i}(k_x x + k_y y)}\, \psi_{\sigma\tau}(x, y, z)\,, \\ \psi^{\dagger}_{\sigma\tau}(z) \equiv \psi^{\dagger}_{\sigma\tau}(k_{\parallel}, z) &= \int \mathrm{d}x\, \mathrm{d}y\, \mathrm{e}^{\mathrm{i}(k_x x + k_y y)}\, \psi^{\dagger}_{\sigma\tau}(x, y, z)\,. \end{aligned} \tag{4.11}$$

4.1.2 Superconductor Hamiltonian

In the same way as was done for the MTI, we introduce the real-space field operator $\phi^{\dagger}_{\sigma}(\mathbf{r})$ ($\phi_{\sigma}(\mathbf{r})$) which creates (annihilates) an electron in the SC at position $\mathbf{r}$ with spin $\sigma = \uparrow, \downarrow$ and satisfy the fermionic anticommutation relation [143, 144]

$$\begin{aligned} \{\phi_{\sigma}(\mathbf{r}), \phi^{\dagger}_{\sigma'}(\mathbf{r}')\} &= \delta_{\sigma\sigma'}\, \delta(\mathbf{r} - \mathbf{r}')\,, \\ \{\phi_{\sigma}(\mathbf{r}), \phi_{\sigma'}(\mathbf{r}')\} &= \{\phi^{\dagger}_{\sigma}(\mathbf{r}), \phi^{\dagger}_{\sigma'}(\mathbf{r}')\} = 0\,. \end{aligned} \tag{4.12}$$

Despite the presence of the physical interface with the MTI that we assume to be at $z = 0$, for the superconductor we assume periodic boundary conditions in all spatial direction, exploiting a full 3D *bulk* model which neglects confinement effects. To describe a conventional spin-singlet s-wave superconductor, we adopt the BCS Hamiltonian, which can be written as the sum of a single-particle kinetic term and a two-particle interaction $H_{\mathrm{SC}} = H_{\mathrm{kin}} + V_{\mathrm{SC}}$. The kinetic term can be written in second quantization as ($\hbar = 1$)

$$H_{\mathrm{kin}} = \sum_{\sigma} \int \mathrm{d}\mathbf{r}\, \phi^{\dagger}_{\sigma}(\mathbf{r}) \left(-\frac{\nabla^2}{2m} - \mu \right) \phi_{\sigma}(\mathbf{r})\,, \tag{4.13}$$

where m is the effective mass of the electrons in the superconductor and μ is the Fermi energy. Similarly, the two-particle interaction can be expressed as

$$V_{\mathrm{SC}} = \sum_{\sigma\sigma'} \int \mathrm{d}\mathbf{r}\, \mathrm{d}\mathbf{r}'\, \phi^\dagger_{\sigma'}(\mathbf{r}')\phi^\dagger_{\sigma}(\mathbf{r}) V_{\mathrm{int}}(\mathbf{r}-\mathbf{r}')\phi_{\sigma'}(\mathbf{r}')\phi_{\sigma}(\mathbf{r})\,, \tag{4.14}$$

where $V_{\mathrm{int}}(\mathbf{r}-\mathbf{r}')$ is the two-particle interaction potential. Following the usual Bardeen–Cooper–Schrieffer (BCS) prescription, we can apply a mean-field approximation to the interaction term [88–90]

$$V_{\mathrm{SC}} = \sum_{\sigma\sigma'} \int \mathrm{d}\mathbf{r}\, \mathrm{d}\mathbf{r}'\, \left[\phi^\dagger_{\sigma}(\mathbf{r})\Delta_{\sigma\sigma'}(\mathbf{r},\mathbf{r}')\phi^\dagger_{\sigma'}(\mathbf{r}') + \phi_{\sigma'}(\mathbf{r}')\Delta^*_{\sigma\sigma'}(\mathbf{r},\mathbf{r}')\phi_{\sigma}(\mathbf{r})\right]\,, \tag{4.15}$$

where the superconducting pairing potential is given by

$$\Delta_{\sigma\sigma'}(\mathbf{r},\mathbf{r}') = -V_{\mathrm{int}}(\mathbf{r},\mathbf{r}')\,\langle\phi_{\sigma}(\mathbf{r})\phi_{\sigma'}(\mathbf{r}')\rangle\,, \tag{4.16}$$

with $\langle\dots\rangle$ denoting a ground state average. Because any intrinsic pairing considered in the following will be of the conventional BCS form, we assume a local contact interaction

$$V_{\mathrm{int}}(\mathbf{r},\mathbf{r}') = \lambda(\mathbf{r})\delta(\mathbf{r}-\mathbf{r}')\,, \tag{4.17}$$

where $\lambda(\mathbf{r}) < 0$ is the coupling constant describing a phonon-mediated attractive electron-electron interaction. Inserting Equations (4.16) and (4.17) into Equation (4.15), the two-particle interaction can be written as

$$V_{\mathrm{SC}} = \sum_{\sigma\sigma'} \int \mathrm{d}\mathbf{r}\, \left[\phi^\dagger_{\sigma}(\mathbf{r})\Delta_{\sigma\sigma'}(\mathbf{r})\phi^\dagger_{\sigma'}(\mathbf{r}) + \phi_{\sigma'}(\mathbf{r}')\Delta^*_{\sigma\sigma'}(\mathbf{r})\phi_{\sigma}(\mathbf{r})\right]\,. \tag{4.18}$$

It is worth noting that the pairing potential is antisymmetric upon exchange of the field operators [88]

$$\Delta_{\sigma\sigma'}(\mathbf{r}) = -\lambda(\mathbf{r})\,\langle\phi_{\sigma}(\mathbf{r})\phi_{\sigma'}(\mathbf{r})\rangle = \lambda(\mathbf{r})\,\langle\phi_{\sigma'}(\mathbf{r})\phi_{\sigma}(\mathbf{r})\rangle = -\Delta_{\sigma'\sigma}(\mathbf{r})\,, \tag{4.19}$$

reflecting the antisymmetry of the fermionic wavefunction, which enforces the vanishing of the diagonal spin components, $\Delta_{\uparrow\uparrow}(\mathbf{r}) = \Delta_{\downarrow\downarrow}(\mathbf{r}) = 0$. Applying the mean-field approximation, the real-space BCS Hamiltonian can thus be written as

$$\begin{aligned} H_{\mathrm{SC}} = &\sum_{\sigma} \int \mathrm{d}\mathbf{r}\, \phi^\dagger_{\sigma}(\mathbf{r}) \left(-\frac{\nabla^2}{2m} - \mu\right) \phi_{\sigma}(\mathbf{r}) + \\ &+ \sum_{\sigma\sigma'} \int \mathrm{d}\mathbf{r}\, \left[\phi^\dagger_{\sigma}(\mathbf{r})\Delta_{\sigma\sigma'}(\mathbf{r})\phi^\dagger_{\sigma'}(\mathbf{r}) + \phi_{\sigma'}(\mathbf{r})\Delta^*_{\sigma\sigma'}(\mathbf{r})\phi_{\sigma}(\mathbf{r})\right]\,. \end{aligned} \tag{4.20}$$

Since the system is assumed to be perfectly translationally invariant in all spatial directions, we can perform a Fourier transform of Equation (4.20) to momentum space, where the Hamiltonian is diagonal in $\mathbf{k}$. The single-particle term becomes

$$H_{\mathrm{kin}} = \sum_{\sigma} \int \mathrm{d}\mathbf{k}\, \varepsilon_k\, \phi^\dagger_{\mathbf{k}\,\sigma}\, \phi_{\mathbf{k}\,\sigma}\,, \tag{4.21}$$

where $\varepsilon_k \equiv k^2/2m - \mu$ denotes the single-particle energy spectrum, and $k^2 = k_x^2 + k_y^2 + k_z^2$ is the modulus squared of the three-dimensional electron crystal momentum. The field operators in momentum space are defined as

$$\phi_{\mathbf{k}\,\sigma} = \int \mathrm{d}^3\mathbf{r}\, \mathrm{e}^{-\mathrm{i}\mathbf{k}\cdot\mathbf{r}}\, \phi_\sigma(\mathbf{r})\,, \qquad \phi^\dagger_{\mathbf{k}\,\sigma} = \int \mathrm{d}^3\mathbf{r}\, \mathrm{e}^{\mathrm{i}\mathbf{k}\cdot\mathbf{r}}\, \phi^\dagger_\sigma(\mathbf{r})\,. \tag{4.22}$$

Assuming a spatially uniform pairing potential $\Delta_{\sigma\sigma'}(\mathbf{r}) \equiv \Delta_{\sigma\sigma'}$, the interaction term in Equation (4.18) can be Fourier transformed as

$$V_{\mathrm{SC}} = \sum_{\sigma\sigma'} \int \mathrm{d}\mathbf{k}\, \left[\phi^\dagger_{\mathbf{k}\,\sigma}\Delta_{\sigma\sigma'}\phi^\dagger_{-\mathbf{k}\,\sigma'} + \phi_{-\mathbf{k}\,\sigma'}\Delta^*_{\sigma\sigma'}\phi_{\mathbf{k}\,\sigma}\right]\,, \tag{4.23}$$

and the full Hamiltonian reads as

$$H_{\mathrm{SC}} = \sum_{\sigma} \int d\mathbf{k}\, \varepsilon_k\, \phi^\dagger_{\mathbf{k}\,\sigma}\phi_{\mathbf{k}\,\sigma} + \sum_{\sigma\sigma'} \int \mathrm{d}\mathbf{k}\, \left[\phi^\dagger_{\mathbf{k}\,\sigma}\Delta_{\sigma\sigma'}\phi^\dagger_{-\mathbf{k}\,\sigma'} + \phi_{-\mathbf{k}\,\sigma'}\Delta^*_{\sigma\sigma'}\phi_{\mathbf{k}\,\sigma}\right]\,, \tag{4.24}$$

recovering the usuals BCS prescription. It is worth noting that, in order to comply with Equation (4.19), the pairing operator must be antisymmetric in spin space, meaning that $\Delta_{\uparrow\downarrow} = -\Delta_{\downarrow\uparrow}$ and $\Delta_{\uparrow\uparrow} = \Delta_{\downarrow\downarrow} = 0$.

4.1.3 Tunneling Hamiltonian

Due to tunneling of electrons from one material to the other, the SC can induce effective superconducting correlations into the MTI. The coupling Hamiltonian between the two materials can be expressed as

$$H_{\mathrm{int}} = \mathcal{T} + \mathcal{T}^\dagger\,, \tag{4.25}$$

where $\mathcal{T}$ represents the tunneling of electrons from the superconductor to the magnetic topological insulator, and $\mathcal{T}^\dagger$ is the opposite process. In second quantization, the real-space tunneling term can be written as

$$\mathcal{T} = \sum_{\sigma\sigma'}\sum_{\tau} \int \mathrm{d}\mathbf{r}\, \mathrm{d}\mathbf{r}'\, \psi^\dagger_{\sigma\tau}(\mathbf{r})\gamma_{\sigma\tau,\,\sigma'}(\mathbf{r},\mathbf{r}')\phi_{\sigma'}(\mathbf{r}')\,, \tag{4.26}$$

where $\gamma_{\sigma\tau,\,\sigma'}(\mathbf{r},\mathbf{r}')$ represents the probability that an electron at a position $\mathbf{r}'$ with spin σ' in the SC tunnels into the MTI at position $\mathbf{r}$ in the MTI with spin σ and parity τ. The opposite tunneling process can be explicitly written as

$$\mathcal{T}^\dagger = \sum_{\sigma\sigma'}\sum_{\tau} \int \mathrm{d}\mathbf{r}\, \mathrm{d}\mathbf{r}'\, \phi^\dagger_{\sigma'}(\mathbf{r}')\gamma^*_{\sigma\tau,\,\sigma'}(\mathbf{r},\mathbf{r}')\psi_{\sigma\tau}(\mathbf{r})\,. \tag{4.27}$$

Keeping the real-space dependence only along the out-of-plane coordinate z, and Fourier transforming along the in-plane x and y directions we obtain

$$H_{\mathrm{int}} = \mathcal{T} + \mathcal{T}^\dagger = \sum_{\sigma\sigma'}\sum_{\tau} \int \mathrm{d}z\, \mathrm{d}z'\, \left[\psi^\dagger_{\sigma\tau}(z)\gamma_{\sigma\tau,\,\sigma'}(z,z')\phi_{\sigma'}(z') + \mathrm{h.c.}\right]\,, \tag{4.28}$$

where we assumed the tunneling to be independent on the x, y coordinates and omitted the indices for the in-plane momenta k_x and k_y.

4.2 Green's Function

To describe a proximitized system in which a superconducting pairing is induced in a normal system by proximity with a SC, it is essential to work within the framework of Green's functions (also called propagators). In many-body theory, Green's functions encode the amplitude for a single particle, or for a correlated pair of particles, to propagate between two space-time points in an interacting quantum system.

4.2.1 Time-ordered Green's Functions

The time-ordered or causal normal Green's function for an MTI with translational invariance along the in plane directions x and y, is defined as [143–145]

$$\mathcal{G}_{\sigma\tau,\sigma'\tau'}(k_\parallel; zt, z't') = -\mathrm{i}\left\langle T_t\, \hat{\psi}_{\sigma\tau}(k_\parallel, z, t)\hat{\psi}^\dagger_{\sigma'\tau'}(k_\parallel, z', t')\right\rangle , \tag{4.29}$$

where $k_\parallel = (k_x, k_y)$ is the in-plane momentum, and $\hat{\psi}_{\sigma\tau}(k_\parallel, z, t)$ and $\hat{\psi}^\dagger_{\sigma\tau}(k_\parallel, z, t)$ denote the time-evolution in the Heisenberg picture of the annihilation and creation field operators introduced in Equation (4.11). The ground-state expectation value at zero temperature is denoted by $\langle \dots \rangle$, and T_t is the time-ordering operator, whose action is defined as

$$T_t\, A(t)B(t') = \begin{cases} A(t)B(t') & \text{if } \ t \geq t' , \\ -B(t')A(t) & \text{if } \ t < t' , \end{cases} \tag{4.30}$$

where A and B are fermionic operators. The normal Green's function, defined in Equation (4.29), describes the amplitude for a particle propagating within the MTI with in-plane momentum $k_\parallel$, being created at the spacetime point (z', t') and annihilated at (z, t). The time-ordering operator ensures the correct fermionic sign structure and preserves causality in the propagation of excitations.

In superconducting systems, the ground state is a condensate of Cooper pairs in which the total particle number is not conserved. As a result, anomalous correlations emerge, reflecting the coherent propagation of paired particles rather than individual quasiparticles. These are captured by the time-ordered anomalous Green's function, which in the infinite MTI slab is defined as [143–145]

$$\mathcal{F}^\dagger_{\sigma\tau,\sigma'\tau'}(k_\parallel; zt, z't') = -\mathrm{i}\left\langle T_t\, \hat{\psi}^\dagger_{\sigma\tau}(-k_\parallel, z, t)\hat{\psi}^\dagger_{\sigma'\tau'}(k_\parallel, z', t')\right\rangle . \tag{4.31}$$

This function vanishes in the normal phase but becomes nonzero in the superconducting state, where particle number is no longer conserved.

4.2.2 Gor'kov Green's Function

To describe superconductivity in a unified formalism, it is convenient to introduce the Nambu spinor notation, as introduced in Equation (2.2)

$$\Psi(k_\parallel, z, t) = \begin{pmatrix} \psi(k_\parallel, z, t) \\ \left[\psi^\dagger(-k_\parallel, z, t)\right]^T \end{pmatrix} , \qquad \Psi^\dagger(k_\parallel, z, t) = \begin{pmatrix} \psi^\dagger(k_\parallel, z', t') & \left[\psi(-k_\parallel, z, t)\right]^T \end{pmatrix} , \tag{4.32}$$

where $\psi^\dagger \equiv \psi^\dagger(k_\parallel, z, t)$ and $\psi \equiv \psi(k_\parallel, z, t)$ are four-component spinors, grouping the creation and annihilation field operators as a row and a column vector, respectively. In the basis of states $\{|\uparrow +\rangle, |\uparrow -\rangle, |\downarrow +\rangle, |\downarrow -\rangle\}$, we have explicitly

$$\psi = \begin{pmatrix} \hat{\psi}_{\uparrow+} & \hat{\psi}_{\uparrow-} & \hat{\psi}_{\downarrow+} & \hat{\psi}_{\downarrow-} \end{pmatrix}^T , \qquad \psi^\dagger = \begin{pmatrix} \hat{\psi}^\dagger_{\uparrow+} & \hat{\psi}^\dagger_{\uparrow-} & \hat{\psi}^\dagger_{\downarrow+} & \hat{\psi}^\dagger_{\downarrow-} \end{pmatrix} , \tag{4.33}$$

where we omitted the indices for in-plane momentum, real-space coordinate z and time t. The Gor'kov Green's function is then defined as the time-ordered correlator in Nambu space [145]

$$G(k_\parallel; zt, z't') = -\mathrm{i} \left\langle T_t \, \Psi(k_\parallel, z, t) \, \Psi^\dagger(k_\parallel, z', t') \right\rangle , \tag{4.34}$$

which encodes both normal and anomalous propagators

$$G(k_\parallel; zt, z't') = \begin{pmatrix} \mathcal{G}(k_\parallel; zt, z't') & \mathcal{F}(k_\parallel; zt, z't') \\ \mathcal{F}^\dagger(k_\parallel; zt, z't') & \overline{\mathcal{G}}(k_\parallel; zt, z't') \end{pmatrix} . \tag{4.35}$$

Normal and anomalous propagators recover the definition given in Equations (4.29) and (4.31), while their Hermitian conjugates are given by

$$\begin{aligned} \overline{\mathcal{G}}_{\sigma\tau,\sigma'\tau'}(k_\parallel; zt, z't') &= -\mathrm{i} \left\langle T_t \, \hat{\psi}^\dagger_{\sigma\tau}(-k_\parallel, z, t) \, \hat{\psi}_{\sigma'\tau'}(-k_\parallel, z', t') \right\rangle \\ \mathcal{F}_{\sigma\tau,\sigma'\tau'}(k_\parallel; zt, z't') &= -\mathrm{i} \left\langle T_t \, \hat{\psi}_{\sigma\tau}(k_\parallel, z, t) \, \hat{\psi}_{\sigma'\tau'}(-k_\parallel, z', t') \right\rangle . \end{aligned} \tag{4.36}$$

The former captures the amplitude for a hole that propagates through the system with in-plane momentum $k_\parallel$, as it describes an electron being removed (i.e., a hole created) at point (z, t) and subsequently re-inserted at point (z', t'). The latter describes the amplitude for destroying a Cooper pair, that is, removing two correlated particles at positions (z, t) and (z', t'), and thus capturing the presence of pairing correlations in a superconducting system.

4.3 Perturbative Expansion

In order to develop a perturbative theory of the proximity effect induced in the MTI due to the proximity with the SC, we work within the interaction picture and separate the Hamiltonian as

$$H = H_0 + H_{\mathrm{int}} , \tag{4.37}$$

where $H_0 = H_{\mathrm{MTI}} + H_{\mathrm{SC}}$ is the unperturbed Hamiltonian for the uncoupled MTI and superconductor, while the interaction H_{int} corresponds to the tunneling term in Equation (4.28). In the following, we use the following notation to distinguish between the different representations of an operator:

- the bare letter O is used for the time evolution in the *interaction* picture;
- the hat symbol $\hat{O}$ is used for the time evolution in the *Heisenberg* picture;
- the check symbol $\check{O}$ is used for the time-independent operators in the *Schrödinger* picture.

In the interaction picture, the time evolution of an operator is determined only by the unperturbed Hamiltonian while the evolution of a state depends on the interaction [146]

$$O(t) = \mathrm{e}^{\mathrm{i}H_0 t}\check{O}\mathrm{e}^{-\mathrm{i}H_0 t}\,, \qquad \Psi(t) = \mathrm{e}^{\mathrm{i}H_0 t}\mathrm{e}^{-\mathrm{i}Ht}\Psi(0)\,. \tag{4.38}$$

In contrast, the time-dependence of an operator in the Heisenberg representation is defined as

$$\hat{O}(t) = \mathrm{e}^{\mathrm{i}Ht}\check{O}\mathrm{e}^{-\mathrm{i}Ht}\,, \tag{4.39}$$

while the states are constant. Reversing Equation (4.38), and plugging it into Equation (4.39) we obtain

$$\hat{O}(t) = \mathrm{e}^{\mathrm{i}Ht}\mathrm{e}^{-\mathrm{i}H_0 t}O(t)\mathrm{e}^{\mathrm{i}H_0 t}\mathrm{e}^{-\mathrm{i}Ht} = U^\dagger(t)O(t)U(t)\,, \tag{4.40}$$

where we introduced the unitary operator $U(t) \equiv \mathrm{e}^{\mathrm{i}H_0 t}\mathrm{e}^{-\mathrm{i}Ht}$ that determines the time-evolution of a state in interaction picture

$$\Psi(t) = \mathrm{e}^{\mathrm{i}H_0 t}\mathrm{e}^{-\mathrm{i}Ht}\Psi(0) = U(t)\Psi(0)\,. \tag{4.41}$$

It is also possible to introduce an operator $S(t,t')$ that transforms the operator $\Psi(t')$ into $\Psi(t)$ as

$$\Psi(t) = S(t,t')\Psi(t')\,, \qquad U(t)\Psi(0) = S(t,t')U(t')\Psi(0)\,, \tag{4.42}$$

which implies $S(t,t') \equiv U(t)U^\dagger(t')$.

To proceed further we need to make a couple of assumptions. The first one is the Gell-Man and Low theorem, stating that the ground state ϕ_0 of the unperturbed Hamiltonian H_0 and the $t = 0$ ground state $\Psi(0)$ of the full Hamiltonian H are related by [143, 145, 147]

$$\Psi(0) = S(0,-\infty)\phi_0\,. \tag{4.43}$$

If we consider $t = 0$ and $t' = t$ in Equation (4.42), we have that

$$\Psi(0) = S(0,t)\Psi(t)\,, \tag{4.44}$$

and taking the limit $t \to -\infty$ we obtain

$$\Psi(0) = S(0,-\infty)\Psi(-\infty)\,. \tag{4.45}$$

By comparison between Equations (4.43) and (4.45), we can understand the Gell-Man and Low theorem as $\Psi(-\infty) = \phi_0$, meaning that starting in a remote past with a wavefunction ϕ_0 which does not contain any effect of the interaction H_{int}, the operator $S(0,-\infty)$ recovers adiabatically the ground state $\Psi(0)$ of the full interacting Hamiltonian $H = H_0 + H_{\mathrm{int}}$.

The second assumption is that the ground state at $t \to +\infty$

$$\Psi(+\infty) = S(+\infty,0)\Psi(0)\,, \tag{4.46}$$

is equal to the unperturbed one up to a phase factor $\mathrm{e}^{\mathrm{i}L}$ [143, 145]

$$\Psi(+\infty) = S(+\infty,0)\Psi(0) = S(+\infty,0)S(0,-\infty)\phi_0 = S(+\infty,-\infty)\phi_0 = \mathrm{e}^{\mathrm{i}L}\phi_0\,, \tag{4.47}$$

where $\mathrm{e}^{\mathrm{i}L} \equiv \langle\phi_0|\, S(+\infty,-\infty)\,|\phi_0\rangle$.

In order to express the Green's functions in the interaction picture, we replace the Heisenberg representation of the field operators with the corresponding interaction one. Recalling Equation (4.40), the normal Green's function defined in Equation (4.29) becomes

$$\begin{aligned}\mathcal{G}_{\sigma\tau,\sigma'\tau'}(zt,z't') &= -\mathrm{i}\left\langle T_t\,\hat{\psi}_{\sigma\tau}(zt)\hat{\psi}^{\dagger}_{\sigma'\tau'}(z't')\right\rangle = \\ &= -\mathrm{i}\left\langle T_t\,S(0,t)\psi_{\sigma\tau}(zt)S(t,t')\psi^{\dagger}_{\sigma\tau}(z't')S(t',0)\right\rangle\,,\end{aligned} \tag{4.48}$$

where we omitted the in-plane momentum. Using the previous assumption $\Psi(-\infty)=\phi_0$, it is possible to show that

$$\langle\Psi(0)| = \langle\phi_0|\, S(-\infty,0) = \mathrm{e}^{-\mathrm{i}L}\,\langle\phi_0|\, S(+\infty,0)\,, \tag{4.49}$$

and with some straightforward manipulation we finally obtain

$$\mathcal{G}_{\sigma\tau,\sigma'\tau'}(zt,z't') = -\mathrm{i}\frac{\langle\phi_0|\, T_t\,\psi_{\sigma\tau}(zt)\psi^{\dagger}_{\sigma\tau}(z't')S(+\infty,-\infty)\,|\phi_0\rangle}{\langle\phi_0|\, S(+\infty,-\infty)\,|\phi_0\rangle}\,. \tag{4.50}$$

Similarly, we can obtain an equivalent expression for the anomalous Green's function

$$\mathcal{F}^{\dagger}_{\sigma\tau,\sigma'\tau'}(zt,z't') = -\mathrm{i}\frac{\langle\phi_0|\, T_t\,\psi^{\dagger}_{\sigma\tau}(zt)\psi^{\dagger}_{\sigma\tau}(z't')S(+\infty,-\infty)\,|\phi_0\rangle}{\langle\phi_0|\, S(+\infty,-\infty)\,|\phi_0\rangle}\,. \tag{4.51}$$

4.3.1 Exponential Series

Recalling that $U(t) = \mathrm{e}^{\mathrm{i}H_0 t}\mathrm{e}^{-\mathrm{i}Ht}$, the matrix $S(t,t') = U(t)U^{\dagger}(t')$ can be easily expressed as a time-ordered operator

$$\frac{\partial}{\partial t}S(t,t') = -\mathrm{i}V(t)S(t,t')\,. \tag{4.52}$$

where $V \equiv H_{\mathrm{int}}$ denotes the interacting Hamiltonian. Equation (4.52) has the formal solution

$$S(t,t') = T_t\,\exp\left[-\mathrm{i}\int_{t'}^{t}\mathrm{d}t_1\,V(t_1)\right]\,, \tag{4.53}$$

and therefore it can be expanded in an exponential series as [143, 145, 147]

$$S(t,t') = 1 + \sum_{n=1}^{+\infty}\frac{(-\mathrm{i})^n}{n!}\int_{t'}^{t}\mathrm{d}t_1\cdots\int_{t'}^{t}\mathrm{d}t_n\,T_t\left[V(t_1)\ldots V(t_n)\right]\,. \tag{4.54}$$

Plugging Equation (4.54) into Equation (4.50), we can evaluate the normal Green's function perturbatively as

$$\begin{aligned}\mathcal{G}_{\sigma\tau,\sigma'\tau'}(zt,z't') = \sum_{n=0}^{+\infty}\frac{(-\mathrm{i})^{n+1}}{n!}\int_{-\infty}^{+\infty}\mathrm{d}t_1\cdots\int_{-\infty}^{+\infty}\mathrm{d}t_n \\ \frac{\langle\phi_0|\, T_t\,\psi_{\sigma\tau}(zt)V(t_1)\ldots V(t_n)\psi^{\dagger}_{\sigma'\tau'}(z't')\,|\phi_0\rangle}{\langle\phi_0|\, S(+\infty,-\infty)\,|\phi_0\rangle}\,.\end{aligned} \tag{4.55}$$

Let us neglect the phase factor e^{iL} in the denominator, since its only effect is to generate terms that cancel the disconnected contributions originating from the numerator. Up to the second-order in the interaction V, we can expand the Green's function in series as:

(i) unperturbed

$$\mathcal{G}^{(0)}_{\sigma\tau,\sigma'\tau'}(zt, z't') = -i \left\langle T_t\, \psi_{\sigma\tau}(zt)\psi^\dagger_{\sigma'\tau'}(z't') \right\rangle_0 ; \tag{4.56}$$

(ii) first-order

$$\mathcal{G}^{(1)}_{\sigma\tau,\sigma'\tau'}(zt, z't') = -\int_{-\infty}^{+\infty} dt_1 \left\langle T_t\, \psi_{\sigma\tau}(zt)V(t_1)\psi^\dagger_{\sigma'\tau'}(z't') \right\rangle_0 ; \tag{4.57}$$

(iii) second-order

$$\mathcal{G}^{(2)}_{\sigma\tau,\sigma'\tau'}(zt, z't') = \frac{i}{2}\int_{-\infty}^{+\infty} dt_1 \int_{-\infty}^{+\infty} dt_2 \left\langle T_t\, \psi_{\sigma\tau}(zt)V(t_1)V(t_2)\psi^\dagger_{\sigma'\tau'}(z't') \right\rangle_0 . \tag{4.58}$$

Here $\langle \dots \rangle_0 \equiv \langle \phi_0 | \dots | \phi_0 \rangle$ indicates the average on the unperturbed ground state ϕ_0.

Proceeding in analogous way, we can obtain a perturbative correction to the anomalous Green's function. Plugging Equation (4.54) into Equation (4.51) the series expansion for the anomalous propagator is explicitly given by

$$\begin{aligned}\mathcal{F}^\dagger_{\sigma\tau,\sigma'\tau'}(zt, z't') = &\sum_{n=0}^{+\infty} \frac{(-i)^{n+1}}{n!} \int_{-\infty}^{+\infty} dt_1 \cdots \int_{-\infty}^{+\infty} dt_n \\ &\frac{\langle \phi_0 |\, T_t\, \psi^\dagger_{\sigma\tau}(zt)V(t_1)\dots V(t_n)\psi^\dagger_{\sigma'\tau'}(z't') \,|\phi_0\rangle}{\langle \phi_0 |\, S(+\infty, -\infty) \,|\phi_0\rangle} .\end{aligned} \tag{4.59}$$

Neglecting the phase factor e^{iL} in the denominator, the perturbative expansion of the propagator yields the following corrections up to second order in the tunneling Hamiltonian:

(i) unperturbed

$$\mathcal{F}^{\dagger\,(0)}_{\sigma\tau,\sigma'\tau'}(zt, z't') = -i \left\langle T_t\, \psi^\dagger_{\sigma\tau}(zt)\psi^\dagger_{\sigma'\tau'}(z't') \right\rangle_0 ; \tag{4.60}$$

(ii) first-order

$$\mathcal{F}^{\dagger\,(1)}_{\sigma\tau,\sigma'\tau'}(zt, z't') = -\int_{-\infty}^{+\infty} dt_1 \left\langle T_t\, \psi^\dagger_{\sigma\tau}(zt)V(t_1)\psi^\dagger_{\sigma'\tau'}(z't') \right\rangle_0 ; \tag{4.61}$$

(iii) second-order

$$\mathcal{F}^{\dagger\,(2)}_{\sigma\tau,\sigma'\tau'}(zt, z't') = \frac{i}{2}\int_{-\infty}^{+\infty} dt_1 \int_{-\infty}^{+\infty} dt_2 \left\langle T_t\, \psi^\dagger_{\sigma\tau}(zt)V(t_1)V(t_2)\psi^\dagger_{\sigma'\tau'}(z't') \right\rangle_0 . \tag{4.62}$$

It is straightforward to verify that all odd-order contributions in the perturbative series of Equations (4.55) and (4.59) vanish. Consequently, the leading corrections to both the normal and anomalous components of the Green's function correspond to the second order terms in the series expansion. The detailed evaluation of the first- and second-order corrections is presented in Appendix B, while here we report only the final expressions for the second-order terms.

4.3.2 Second-Order Corrections

Normal Green's Function

The leading correction to the normal Green's function can be obtained by evaluating the time-ordered expectation value in Equation (4.58)

$$\left\langle T_t\, \psi_{\sigma\tau}(zt)\, V(t_1)\, V(t_2)\, \psi^\dagger_{\sigma'\tau'}(z't') \right\rangle_0 , \tag{4.63}$$

where only those terms containing an equal number of creation $\psi^\dagger$ and annihilation ψ field operators in the product $V(t_1)V(t_2)$ give a nonvanishing contribution in the unperturbed ground state. Up to overall constants, the time-ordered bracket can be written explicitly as [143, 145]

$$\begin{aligned} &\left\langle T_t\ \psi(\xi)\, \psi^\dagger(1)\, \phi(1')\, \phi^\dagger(2')\, \psi(2)\, \psi^\dagger(\xi') \right\rangle_0 = \\ &\left\langle T_t\ \psi(\xi)\, \psi^\dagger(1)\, \psi(2)\, \psi^\dagger(\xi') \right\rangle_0 \left\langle T_t\ \phi(1')\, \phi^\dagger(2') \right\rangle_0 , \end{aligned} \tag{4.64}$$

where we introduced a compact notation $\xi \equiv (z, t, \sigma, \tau)$ to denote the complete set of spatial, temporal, spin, and orbital indices associated with each field operator. For the *integrated* variables, we adopt the following convention

$$i \equiv (z_i, t_i, \sigma_i, \tau_i) , \qquad i' \equiv (z'_i, t_i, \sigma'_i, \tau'_i) , \tag{4.65}$$

where the time coordinate of a primed index is the same of the corresponding unprimed one. Here, we have separated the MTI and SC contributions, since the corresponding field operators commute and factorize in the unperturbed ground state.

The two brackets in Equation (4.64) can be evaluated through Wick's theorem expanding them into all possible nonvanishing contractions, which correspond to the normal and anomalous Green's functions evaluated in the unperturbed ground states of the two materials [143, 145, 148]. Assuming the tunneling term to be local in space, i.e. that it couples only electrons at the same position

$$\gamma_{\sigma\tau,\sigma'}(z) \equiv \gamma_{\sigma\tau,\sigma'}(z)\, \delta(z - z') , \tag{4.66}$$

the second-order correction in Equation (4.58) can be evaluated in the frequency domain as (see Appendix B.1.2)

$$\begin{aligned} \mathcal{G}^{(2)}_{\mathrm{MTI}}(z, z'; \omega) = \int \mathrm{d}z_1\, \mathrm{d}z_2 \Big\{ &\mathcal{G}^{(0)}_{\mathrm{MTI}}(z, z_1; \omega)\, \Gamma(z_1)\, \mathcal{G}^{(0)}_{\mathrm{SC}}(z_1, z_2; \omega)\, \Gamma^\dagger(z_2)\, \mathcal{G}^{(0)}_{\mathrm{MTI}}(z_2, z'; \omega) \\ &- \mathcal{G}^{(0)}_{\mathrm{MTI}}(z, z'; \omega)\, \Gamma(z_1)\, \mathcal{G}^{(0)}_{\mathrm{SC}}(z_1, z_2; \omega)\, \Gamma^\dagger(z_2)\, \mathcal{G}^{(0)}_{\mathrm{MTI}}(z_2, z_1; \omega) \Big\} , \end{aligned} \tag{4.67}$$

where $\mathcal{G}^{(0)}_{\mathrm{MTI}}$ ($\mathcal{G}^{(0)}_{\mathrm{SC}}$) denotes the unperturbed normal Green's function matrix of dimension 4×4 (2×2) in the MTI (SC), and Γ is the 4×2 tunneling matrix whose elements are the tunneling amplitudes $\gamma_{\sigma\tau,\sigma'}(z)$ defined in Equation (4.66). The corresponding Feynman diagrams are illustrated in Figure 4.1. The first term describes the tunneling of an electron between the MTI and the SC, representing a back-and-forth tunneling process. The second term corresponds to a disconnected diagram, which cancels with the denominator $\langle\phi_0|S(-\infty, +\infty)|\phi_0\rangle$ of the perturbative expansion and can therefore be neglected.

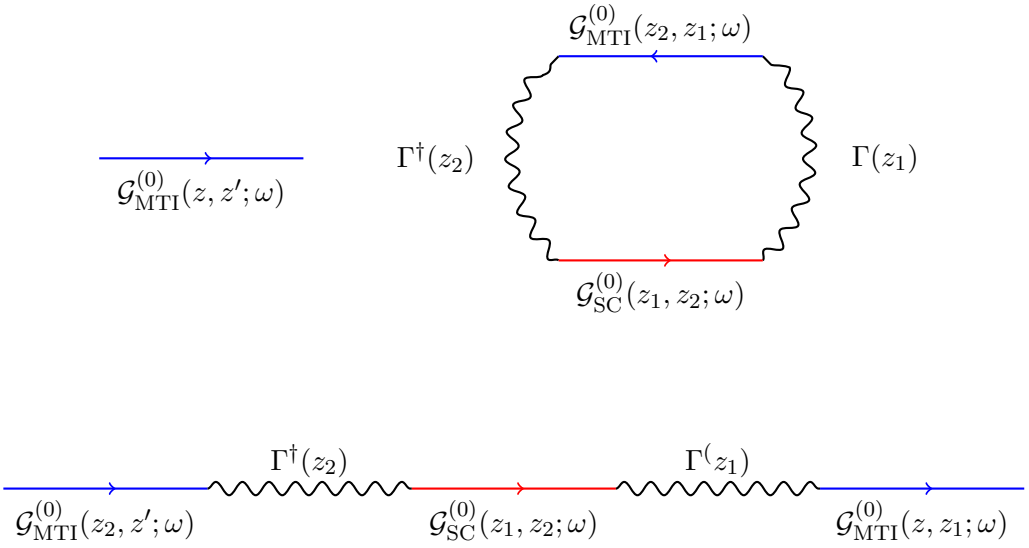

Figure 4.1: Feynman diagrams corresponding to the second-order correction to the normal MTI Green's function in Equation (4.67). The blue (red) arrows represent the unperturbed normal Green's function in the MTI (SC), while the wiggly line stand for the tunneling interaction.

Anomalous Green's Function

Similarly, in order to evaluate the second-order correction to the anomalous MTI Green's function in Equation (4.62), we need to compute the time-ordered bracket

$$\left\langle T_t\, \psi^\dagger_{\sigma\tau}(zt) V(t_1) V(t_2) \psi^\dagger_{\sigma'\tau'}(z't') \right\rangle_0 . \tag{4.68}$$

Neglecting the terms that vanish due to an unequal number of creation $\psi^\dagger$ and annihilation ψ operators, the time-ordered bracket reduces to

$$\begin{aligned} &\left\langle T_t\, \psi^\dagger(\xi)\phi^\dagger(1')\psi(1)\phi^\dagger(2')\psi(2)\psi^\dagger(\xi') \right\rangle_0 = \\ &-\left\langle T_t\, \psi^\dagger(\xi)\psi(1)\psi(2)\psi^\dagger(\xi') \right\rangle_0 \left\langle T_t\, \phi^\dagger(1')\phi^\dagger(2') \right\rangle_0 , \end{aligned} \tag{4.69}$$

where we employed the compact notation introduced in Equation (4.65).

Equation (4.69) can be evaluated through Wick's theorem [143, 145, 148]. For a local tunneling as in Equation (4.66), the second-order correction to the anomalous MTI Green's function in the frequency domain is (see Appendix B.2.1)

$$\begin{aligned} \mathcal{F}^{\dagger\,(2)}_{\mathrm{MTI}}(z, z'; \omega) &= \int \mathrm{d}z_1\, \mathrm{d}z_2 \times \\ \times \left[\mathcal{G}^{(0)}_{\mathrm{MTI}}(z_1, z; -\omega)\right]^T \Gamma^*(z_1)\, &\mathcal{F}^{\dagger\,(0)}_{\mathrm{SC}}(z_2, z_1; \omega)\, \Gamma^\dagger(z_2)\, \mathcal{G}^{(0)}_{\mathrm{MTI}}(z_2, z'; \omega) , \end{aligned} \tag{4.70}$$

where $\mathcal{F}^{\dagger\,(0)}_{\mathrm{SC}}$ is the 2×2 anomalous Green's function in the unperturbed SC. The corresponding Feynman diagram is sketched in Figure 4.2. Physically, it corresponds to an Andreev reflection process [113, 115]: an electron tunnels from the MTI into

the SC and is back-reflected as a hole, while a Cooper pair is formed in the superconducting condensate (see Figure 3.2). It is worth noting that this result has general validity, as it applies to a broad class of normal–superconductor heterostructures where SC correlations arise from the proximity effect, under the assumption of local tunneling at the interface between the two materials.

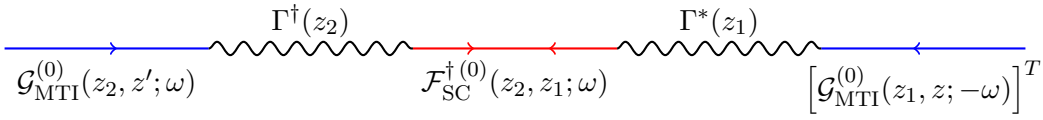

Figure 4.2: Feynman diagrams corresponding to the second-order correction to the anomalous MTI Green's function in Equation (4.70). The blue arrows represent the unperturbed normal Green's function in the MTI, the red double arrow stands for the unperturbed anomalous Green's function in the SC, and the wiggly lines stand for the tunneling interaction.

The above equation provides the final expression for the perturbative correction to the anomalous Green's function, characterizing the induced superconducting pairing in the magnetically doped TI system. In the following chapters, we first evaluate the unperturbed Green's functions in the two materials in the decoupled limit ($V = 0$), and subsequently employ Equation (4.70) to model the proximity-induced pairing in the proximitized MTI.

Summary

In this chapter, we developed a second-quantized formalism to describe the pairing amplitude induced in MTIs by proximity to a conventional superconductor. After introducing the second-quantized Hamiltonian of the MTI–SC heterostructure, we outline the normal and anomalous Green's functions, which encode the propagation amplitude of individual and coherent pairs of quasiparticles within the MTI. By treating the tunneling interaction as a perturbation on the ground states of the uncoupled materials, we derived the corrections to the Green's functions in the interaction picture.

A key result of this analysis is that all odd-order contributions to the MTI Green's functions vanish, so that the lowest nonvanishing correction arises at *second order* in the tunneling amplitude. We obtained explicit analytical expressions for these second-order terms, together with their Feynman-diagram representation. In particular, the correction to the anomalous Green's function can be physically interpreted as an Andreev process, in which an electron tunnels into the superconductor and is reflected as a hole, creating a Cooper pair. These results establish the microscopic origin of the proximity effect and provide the foundation for the quantitative evaluation of the induced pairing: building on this framework, in the next chapter we evaluate the unperturbed Green's functions of the two decoupled materials, which provide the essential input for the perturbative expansion developed here.

Chapter 5

Unperturbed Materials

Overview

In the previous chapter, we developed a perturbative framework to describe the correlations induced in MTI thin films by proximity to a conventional superconductor, and showed that the lowest nonvanishing correction to the Green's functions arises at second order in the tunneling amplitude. Building on this result, the aim of the present chapter is to evaluate the unperturbed Green's functions in the two decoupled materials, which will serve as the input for the perturbative expansion enabling the quantitative analysis of the induced pairing.

The remainder of this chapter is organized as follows. In Section 5.1, we derive and solve the Gor'kov equations for a conventional spin-singlet s-wave bulk superconductor with full translational invariance. The solution is obtained in momentum space and Fourier transformed along the out-of-plane direction z by evaluating the corresponding contour integral in the complex plane. In Section 5.2, we turn to the normal Green's function of an MTI thin film with translational invariance in the in-plane directions and finite thickness along z. The equation of motion reduces to a system of coupled second-order differential equations, from which we obtain a general momentum-dependent solution, as well as a closed-form expression valid in the limiting case of $k_x = k_y = 0$ and for surface-localized states decaying exponentially away from the interface.

5.1 Bulk Superconductor

The energy spectrum of a conventional bulk superconductor can be conveniently computed using the Nambu formalism introduced in Equation (2.2), where the BCS Hamiltonian Equation (4.24) acquires a quadratic form and can thus be diagonalized straightforwardly [88, 89]. Introducing the Nambu spinors

$$\Phi_{\mathbf{k}} = \begin{pmatrix} \phi_{\mathbf{k}\uparrow} \\ \phi^{\dagger}_{-\mathbf{k}\downarrow} \end{pmatrix}, \qquad \Phi^{\dagger}_{\mathbf{k}} = \begin{pmatrix} \phi^{\dagger}_{\mathbf{k}\uparrow} & \phi_{-\mathbf{k}\downarrow} \end{pmatrix}, \tag{5.1}$$

and exploiting the fermionic anticommutation relations of the field operators, the second-quantized Hamiltonian Equation (4.24) can be recast as

$$H_{\mathrm{SC}} = \frac{1}{2}\int \mathrm{d}\mathbf{k}\, \Phi_{\mathbf{k}}^{\dagger}\, h_{\mathrm{BdG}}(\mathbf{k})\, \Phi_{\mathbf{k}}\,. \tag{5.2}$$

The corresponding BdG Hamiltonian in momentum space reads

$$h_{\mathrm{BdG}}(\mathbf{k}) = \begin{pmatrix} \varepsilon_k & \Delta \\ \Delta^* & -\varepsilon_k \end{pmatrix}, \tag{5.3}$$

where $\varepsilon_k = (k_x^2 + k_y^2 + k_z^2)/2m - \mu$ denotes the free-electron dispersion and $\Delta \equiv \Delta_{\uparrow\downarrow} = -\Delta_{\downarrow\uparrow}$ is the superconducting pairing amplitude.

The energy spectrum of the bulk SC can thus be found straightforwardly by diagonalizing Equation (5.3), whose eigenstates and eigenvalues are given by

$$E_k = \pm\sqrt{\varepsilon_k^2 + |\Delta|^2}\,, \qquad \Phi_{\mathbf{k}} = \frac{|\Delta|}{\sqrt{2\varepsilon_k\,(\varepsilon_k \pm E_k)}} \begin{pmatrix} \frac{1}{\Delta^*}\Big(\varepsilon_k \pm E_k\Big) \\ 1 \end{pmatrix}. \tag{5.4}$$

The two components of the Nambu spinor $\Phi_k \equiv (u_k\ v_k)^T$ can be identified as the electron u_k and hole v_k amplitudes of the single quasiparticle excitations, and the particle-hole character can be computed as the expectation value

$$\langle \gamma_z \rangle = \Phi_{\mathbf{k}}^{\dagger}\, \gamma_z\, \Phi_{\mathbf{k}}\,, \tag{5.5}$$

where $\gamma_{x,y,z}$ is a set of Pauli matrices acting in the particle-hole subspace. The BdG spectrum for single particle excitations in a conventional bulk SC is shown in Figure 5.1 as a function of the crystalline momentum. The colors are used to represent the particle-hole character of the corresponding eigenstates.

5.1.1 Gor'kov Equations

The physics of a superconducting system is governed by the Gor'kov equations, which couple the normal and anomalous components of the Green's function. A detailed derivation for a conventional spin-singlet s-wave superconductor with full translational invariance is presented below. Unless otherwise specified, we express all equations in natural units, setting $\hbar = 1$, and fix the effective mass of the electrons in the superconductor by assuming $\frac{1}{2m} = 1$.

For a conventional BCS superconductor described by the Hamiltonian in Equation (4.24), the unperturbed time-ordered Green's functions in momentum space, defined in Equations (4.56) and (4.60), take the form

$$\begin{aligned} \mathcal{G}^{(0)}_{\sigma\sigma'}(\mathbf{k}; t, t') &= -\mathrm{i}\left\langle T_t\, \phi_{\mathbf{k}\,\sigma}(t) \phi^{\dagger}_{\mathbf{k}\,\sigma'}(t') \right\rangle_0\,, \\ \mathcal{F}^{\dagger\,(0)}_{\sigma\sigma'}(\mathbf{k}; t, t') &= -\mathrm{i}\left\langle T_t\, \phi^{\dagger}_{-\mathbf{k}\,\sigma}(t) \phi^{\dagger}_{\mathbf{k}\,\sigma'}(t') \right\rangle_0\,, \end{aligned} \tag{5.6}$$

where $\phi^{\dagger}_{\mathbf{k}\,\sigma}(t)$ and $\phi_{\mathbf{k}\,\sigma}(t)$) are the time-evolved SC field operators defined in Equation (4.22). It is worth noting that in the absence of a perturbation $V = 0$, the

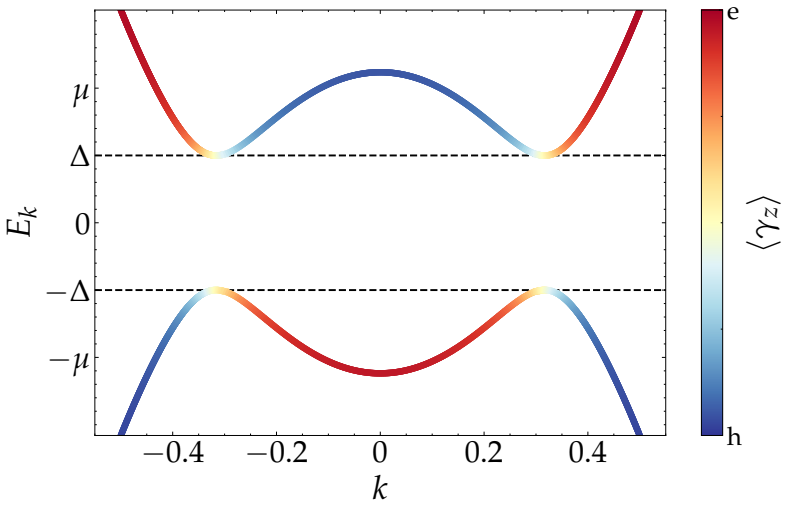

Figure 5.1: Single-particle energy spectrum of the BCS superconductor as a function of the modulus squared of the crystal momentum $k^2 = k_x^2 + k_y^2 + k_z^2$. The colors represent the particle-hole character of the eigenstates obtained through Equation (5.5).

time-evolution in the Heisenberg representation Equation (4.39) is equal to the time-evolution in the interacting one Equation (4.38). Making explicitly the action of the time-ordering operator, the normal Green's function becomes

$$\mathcal{G}^{(0)}_{\sigma\sigma'}(\mathbf{k};t,t') = -\mathrm{i}\theta(t-t')\left\langle \phi_{\mathbf{k}\,\sigma}(t)\phi^\dagger_{\mathbf{k}\,\sigma'}(t')\right\rangle_0 + \mathrm{i}\theta(t'-t)\left\langle \phi^\dagger_{\mathbf{k}\,\sigma'}(t')\phi_{\mathbf{k}\,\sigma}(t)\right\rangle_0 , \tag{5.7}$$

and the time derivative can be evaluated as

$$\begin{aligned}\partial_t \mathcal{G}^{(0)}_{\sigma\sigma'}(\mathbf{k};t,t') &= -\mathrm{i}\delta(t-t')\left\langle \left\{\phi_{\mathbf{k}\,\sigma}(t),\phi^\dagger_{\mathbf{k}\,\sigma'}(t')\right\}\right\rangle_0 - \mathrm{i}\left\langle T_t\,\partial_t\phi_{\mathbf{k}\,\sigma}(t)\phi^\dagger_{\mathbf{k}\,\sigma'}(t')\right\rangle_0 = \\ &= -\mathrm{i}\delta_{\sigma\sigma'}\delta(t-t') - \mathrm{i}\left\langle T_t\,\partial_t\phi_{\mathbf{k}\,\sigma}(t)\phi^\dagger_{\mathbf{k}\,\sigma'}(t')\right\rangle_0 ,\end{aligned} \tag{5.8}$$

where we took advantage of the anticommutation relation

$$\left\{\phi_{\mathbf{k}\,\sigma}(t),\phi^\dagger_{\mathbf{k}\,\sigma'}(t)\right\} = \delta_{\sigma\sigma'} , \tag{5.9}$$

since the field operators act at the same instant of time $t = t'$. Similarly, for the anomalous Green's function we have that

$$\partial_t \mathcal{F}^{\dagger\,(0)}_{\sigma\sigma'}(\mathbf{k};t,t') = -\mathrm{i}\left\langle T_t\,\partial_t\phi^\dagger_{-\mathbf{k}\,\sigma}(t)\phi^\dagger_{\mathbf{k}\,\sigma'}(t')\right\rangle_0 , \tag{5.10}$$

since the anticommutator of two creation field operators is always vanishing. The time-derivative of an operator $O(t)$ can be evaluated as [143, 146]

$$\partial_t O(t) = \mathrm{i}\,[H,O(t)] = \mathrm{i}\,\mathrm{e}^{\mathrm{i}Ht}\,[H,O]\,\mathrm{e}^{-\mathrm{i}Ht} , \tag{5.11}$$

and for the SC Hamiltonian in Equation (4.24) we obtain

$$\begin{aligned}\mathrm{i}\partial_t\phi_{\mathbf{k}\,\sigma}(t) &= \varepsilon_k\phi_{\mathbf{k}\,\sigma}(t) + \sum_{\sigma'}\Delta_{\sigma\sigma'}\phi^\dagger_{-\mathbf{k}\,\sigma'}(t) , \\ \mathrm{i}\partial_t\phi^\dagger_{\mathbf{k}\,\sigma}(t) &= -\varepsilon_k\phi^\dagger_{\mathbf{k}\,\sigma}(t) + \sum_{\sigma'}\Delta^*_{\sigma\sigma'}\phi_{-\mathbf{k}\,\sigma'}(t) .\end{aligned} \tag{5.12}$$

Plugging Equation (5.12) into Equations (5.8) and (5.10), we can obtain two paired equations coupling normal and anomalous Green's functions. For the normal one, we have

$$\begin{aligned}\partial_t \mathcal{G}^{(0)}_{\sigma\sigma'}(\mathbf{k};t,t') &= -\,\mathrm{i}\delta_{\sigma\sigma'}\delta(t-t') - \mathrm{i}\left\langle T_t\, \partial_t \phi_{\mathbf{k}\,\sigma}(t)\phi^\dagger_{\mathbf{k}\,\sigma'}(t')\right\rangle_0 = \\ &= -\,\mathrm{i}\delta_{\sigma\sigma'}\delta(t-t') - \varepsilon_k \left\langle T_t\, \phi_{\mathbf{k}\,\sigma}(t)\phi^\dagger_{\mathbf{k}\,\sigma'}(t')\right\rangle_0 - \\ &\quad - \sum_{\sigma''} \Delta_{\sigma\sigma''} \left\langle T_t\, \phi^\dagger_{-\mathbf{k}\,\sigma''}(t)\phi^\dagger_{\mathbf{k}\,\sigma'}(t')\right\rangle_0 = \\ &= -\,\mathrm{i}\delta_{\sigma\sigma'}\delta(t-t') - \mathrm{i}\varepsilon_k \mathcal{G}^{(0)}_{\sigma\sigma'}(\mathbf{k};t,t') - \mathrm{i}\sum_{\sigma''} \Delta_{\sigma\sigma''}\mathcal{F}^{\dagger\,(0)}_{\sigma''\sigma'}(\mathbf{k};t,t')\,.\end{aligned} \tag{5.13}$$

The previous equation can be rewritten in compact form using matrix notation

$$\partial_t \mathcal{G}^{(0)}_{\mathrm{SC}}(\mathbf{k};t,t') = -\mathrm{i}\delta(t-t') - \mathrm{i}\varepsilon_k\, \mathcal{G}^{(0)}_{\mathrm{SC}}(\mathbf{k};t,t') - \mathrm{i}\Delta\sigma_y\, \mathcal{F}^{\dagger\,(0)}_{\mathrm{SC}}(\mathbf{k};t,t')\,, \tag{5.14}$$

where $\Delta \equiv \Delta_{\uparrow\downarrow} = -\Delta_{\downarrow\uparrow}$, and σ_y denotes the Pauli matrix acting in the spin space of the superconductor. Here, we introduced the normal $\mathcal{G}_{\mathrm{SC}}$ and anomalous $\mathcal{F}^\dagger_{\mathrm{SC}}$ Green's functions matrices, which in the basis $\{|\uparrow\rangle, |\downarrow\rangle\}$ are explicitly given by

$$\mathcal{G}_{SC} = \begin{bmatrix} \mathcal{G}_{\uparrow\uparrow} & \mathcal{G}_{\uparrow\downarrow} \\ \mathcal{G}_{\downarrow\uparrow} & \mathcal{G}_{\downarrow\downarrow} \end{bmatrix}, \qquad \mathcal{F}^\dagger_{SC} = \begin{bmatrix} \mathcal{F}^\dagger_{\uparrow\uparrow} & \mathcal{F}^\dagger_{\uparrow\downarrow} \\ \mathcal{F}^\dagger_{\downarrow\uparrow} & \mathcal{F}^\dagger_{\downarrow\downarrow} \end{bmatrix}. \tag{5.15}$$

With some straightforward manipulation we finally obtain

$$(\mathrm{i}\partial_t - \varepsilon_k)\, \mathcal{G}^{(0)}_{\mathrm{SC}}(\mathbf{k};t,t') - \Delta\sigma_y\, \mathcal{F}^{\dagger\,(0)}_{\mathrm{SC}}(\mathbf{k};t,t') = \delta(t-t')\,, \tag{5.16}$$

Similarly, we can obtain a second equation for the anomalous propagator. Plugging Equation (5.12) into Equation (5.10), we have

$$\begin{aligned}\partial_t \mathcal{F}^{\dagger\,(0)}_{\sigma\sigma'}(\mathbf{k};t,t') &= -\mathrm{i}\left\langle T_t\, \partial_t \phi^\dagger_{-\mathbf{k}\,\sigma}(t)\phi^\dagger_{\mathbf{k}\,\sigma'}(t')\right\rangle_0 = \\ &= \varepsilon_k \left\langle T_t\, \phi^\dagger_{-\mathbf{k}\,\sigma}(t)\phi^\dagger_{\mathbf{k}\,\sigma'}(t')\right\rangle_0 - \sum_{\sigma''} \Delta^*_{\sigma\sigma''} \left\langle T_t\, \phi_{\mathbf{k}\,\sigma''}(t)\phi^\dagger_{\mathbf{k}\,\sigma'}(t')\right\rangle_0 = \\ &= \mathrm{i}\varepsilon_k\, \mathcal{F}^{\dagger\,(0)}_{\sigma\sigma'}(\mathbf{k};t,t') - \mathrm{i}\sum_{\sigma''} \Delta^*_{\sigma\sigma''}\mathcal{G}^{(0)}_{\sigma''\sigma'}(\mathbf{k};t,t')\,,\end{aligned} \tag{5.17}$$

which with the matrix notation introduced in Equation (5.15) becomes

$$\partial_t \mathcal{F}^{\dagger\,(0)}_{\mathrm{SC}}(\mathbf{k};t,t') = \mathrm{i}\varepsilon_k\, \mathcal{F}^{\dagger\,(0)}_{\mathrm{SC}}(\mathbf{k};t,t') - \mathrm{i}\Delta^*\sigma_y\, \mathcal{G}^{(0)}_{\mathrm{SC}}(\mathbf{k};t,t')\,. \tag{5.18}$$

With some algebraic manipulation, the above equation can be rewritten as

$$(\mathrm{i}\partial_t + \varepsilon_k)\, \mathcal{F}^{\dagger\,(0)}_{\mathrm{SC}}(\mathbf{k};t,t') - \Delta^*\sigma_y \mathcal{G}^{(0)}_{\mathrm{SC}}(\mathbf{k};t,t') = 0\,. \tag{5.19}$$

The Equations (5.16) and (5.19) that couple normal and anomalous Green's functions take the name of *Gor'kov equations*, and describe the physics of a conventional spin-singlet s-wave SC with an isotropic pairing $\Delta\sigma_y$ [143, 144].

Since the Hamiltonian in Equation (4.24) does not depend explicitly on time, the system is time-translational invariant. Fourier transforming the propagators to frequency space the time derivatives become algebraic, and Equations (5.16) and (5.19) can thus be rewritten as

$$\begin{aligned}(\omega + \mathrm{i}\eta\,\mathrm{sgn}\,\omega - \varepsilon_k)\,\mathcal{G}^{(0)}_{\mathrm{SC}}(\mathbf{k};\omega) - \Delta\sigma_y\,\mathcal{F}^{\dagger\,(0)}_{\mathrm{SC}}(\mathbf{k};\omega) = 1\,,\\ (\omega + \mathrm{i}\eta\,\mathrm{sgn}\,\omega + \varepsilon_k)\,\mathcal{F}^{\dagger\,(0)}_{\mathrm{SC}}(\mathbf{k};\omega) - \Delta^*\sigma_y\,\mathcal{G}^{(0)}_{\mathrm{SC}}(\mathbf{k};\omega) = 0\,,\end{aligned} \tag{5.20}$$

where $\eta > 0$ is an infinitesimal positive constant that displaces the poles of the Green's function from the real axis, enforcing the correct analytic continuation and ensuring the causal structure of the time-ordered propagator.

5.1.2 Momentum-Space Solution

The Gor'kov equations (5.20) in momentum and frequency space are algebraic and can be directly solved as [143, 144]

$$\mathcal{G}^{(0)}_{\mathrm{SC}}(\mathbf{k};\omega) = \frac{\omega + \varepsilon_k}{(\omega + \mathrm{i}\eta\,\mathrm{sgn}\,\omega)^2 - E_k^2}\,, \qquad \mathcal{F}^{\dagger\,(0)}_{\mathrm{SC}}(\mathbf{k};\omega) = \frac{\Delta^*}{(\omega + \mathrm{i}\eta\,\mathrm{sgn}\,\omega)^2 - E_k^2}\,\sigma_y\,, \tag{5.21}$$

where $E_k^2 \equiv \varepsilon_k^2 + |\Delta|^2$ denotes the squared Bogoliubov excitation spectrum. Consistently with the assumption of a conventional spin-singlet s-wave pairing, the off-diagonal (diagonal) part of the normal (anomalous) propagator vanishes

$$\mathcal{G}_{\uparrow\downarrow} = \mathcal{G}_{\downarrow\uparrow} = 0\,, \qquad \mathcal{F}^{\dagger}_{\uparrow\uparrow} = \mathcal{F}^{\dagger}_{\downarrow\downarrow} = 0\,, \tag{5.22}$$

while the nontrivial components are

$$\mathcal{G}_{\uparrow\uparrow} = \mathcal{G}_{\downarrow\downarrow} = \frac{\omega + \varepsilon_k}{(\omega + \mathrm{i}\eta\,\mathrm{sgn}\,\omega)^2 - E_k^2}\,, \qquad \mathcal{F}^{\dagger}_{\uparrow\downarrow} = -\mathcal{F}^{\dagger}_{\downarrow\uparrow} = -\frac{\mathrm{i}\Delta^*}{(\omega + \mathrm{i}\eta\,\mathrm{sgn}\,\omega)^2 - E_k^2}\,, \tag{5.23}$$

with the anomalous propagator being antisymmetric in spin space.

5.1.3 Real-Space Solution

Despite we assumed full translational invariance and derived and solved the Gor'kov equations for a bulk superconductor, to evaluate the perturbative corrections in Equations (4.67) and (4.70) we are ultimately interested in the real-space dependence along z of the Green's functions. For this purpose, we need to Fourier transform Equation (5.21) to real space along z and evaluate the following integrals

$$\mathcal{G}^{(0)}_{\mathrm{SC}}(k_\parallel, z, z';\omega) \equiv \mathcal{G}^{(0)}_{\mathrm{SC}}(k_\parallel, z - z';\omega) = \int \frac{\mathrm{d}k_z}{2\pi}\,\mathrm{e}^{\mathrm{i}k_z(z-z')}\mathcal{G}^{(0)}_{\mathrm{SC}}(\mathbf{k};\omega)\,, \tag{5.24}$$

$$\mathcal{F}^{\dagger\,(0)}_{\mathrm{SC}}(k_\parallel, z, z';\omega) \equiv \mathcal{F}^{\dagger\,(0)}_{\mathrm{SC}}(k_\parallel, z - z';\omega) = \int \frac{\mathrm{d}k_z}{2\pi}\,\mathrm{e}^{\mathrm{i}k_z(z-z')}\mathcal{F}^{\dagger\,(0)}_{\mathrm{SC}}(\mathbf{k};\omega)\,. \tag{5.25}$$

Extending the momentum from the real axis to the complex plane $k_z \to k_r + ik_i$, the integrals in Equations (5.24) and (5.25) can be evaluated in the complex plane if the exponential factor

$$\mathrm{e}^{\mathrm{i}k_z(z-z')} = \mathrm{e}^{\mathrm{i}k_r(z-z')}\mathrm{e}^{-k_i(z-z')}\,, \tag{5.26}$$

converges in the limit of large imaginary part k_i. For $k_i > 0$, we have

$$\lim_{k_i \to +\infty} \mathrm{e}^{-k_i(z-z')} = \begin{cases} 0 & \text{if} \quad z - z' > 0\,, \\ +\infty & \text{if} \quad z - z' < 0\,, \end{cases} \tag{5.27}$$

and conversely for $k_i < 0$

$$\lim_{k_i \to -\infty} \mathrm{e}^{-k_i(z-z')} = \begin{cases} +\infty & \text{if} \quad z - z' > 0\,, \\ 0 & \text{if} \quad z - z' < 0\,, \end{cases} \tag{5.28}$$

meaning that to ensure the convergence of the integrals we need to choose a closed path in the upper (lower) half of the complex plane when $z - z' \geq 0$ ($z - z' < 0$).

In general, the integral of a complex-valued function $f(k_z)$ over a closed contour γ in the complex plane can be evaluated using the residue theorem as [149, 150]

$$\oint_\gamma f(k_z)\,\mathrm{d}k_z = 2\pi\mathrm{i} \sum_j I(\gamma, k_j)\,\mathrm{Res}(f, k_j)\,, \tag{5.29}$$

where k_j are the poles enclosed by γ, $\mathrm{Res}(f, k_j)$ denotes the residue of f at k_j, and $I(\gamma, k_j)$ is the winding number of the contour γ around the pole k_j, whose sign is positive (negative) for an anticlockwise (clockwise) loop. If we choose as closed path γ the semicircle C_R of radius R with the diameter along the real axis, the contour integral can be decomposed as

$$\oint_\gamma f(k_z)\,\mathrm{d}k_z = \int_{-R}^{R} f(k_z)\,\mathrm{d}k_z + \int_{C_R} f(k_z)\,\mathrm{d}k_z\,. \tag{5.30}$$

In the limit of large $|k_z|$, if the integrand function decays at least as $|f(k_z)| \sim 1/|k_z|^a$ for $a > 1$, by Jordan's lemma we have that [149, 150]

$$\lim_{R \to +\infty} \int_{C_R} f(k_z)\,\mathrm{d}k_z = 0\,, \tag{5.31}$$

and taking the limit $R \to +\infty$ in Equation (5.30) we obtain

$$\oint_\gamma f(k_z)\,\mathrm{d}k_z \;=\; \lim_{R \to \infty} \left[\int_{-R}^{R} f(k_z)\,\mathrm{d}k_z + \int_{C_R} f(k_z)\,\mathrm{d}k_z \right] = \int_{-\infty}^{+\infty} f(k_z)\,\mathrm{d}k_z\,. \tag{5.32}$$

Therefore, by means of Equation (5.29), the integral on the real axis can be computed as the sum of the residues enclosed by the path γ

$$\int_{-\infty}^{+\infty} \frac{\mathrm{d}k_z}{2\pi}\, f(k_z) = \oint_\gamma \frac{\mathrm{d}k_z}{2\pi}\, f(k_z) = \pm\mathrm{i} \sum_j \mathrm{Res}(f, k_j)\,, \tag{5.33}$$

where the positive (negative) sign is for the loop closed in the upper (lower) half-plane. The integrals in Equations (5.24) and (5.25) can be computed in the complex plane along the paths shown in Figure 5.2 taking the limit $R \to +\infty$.

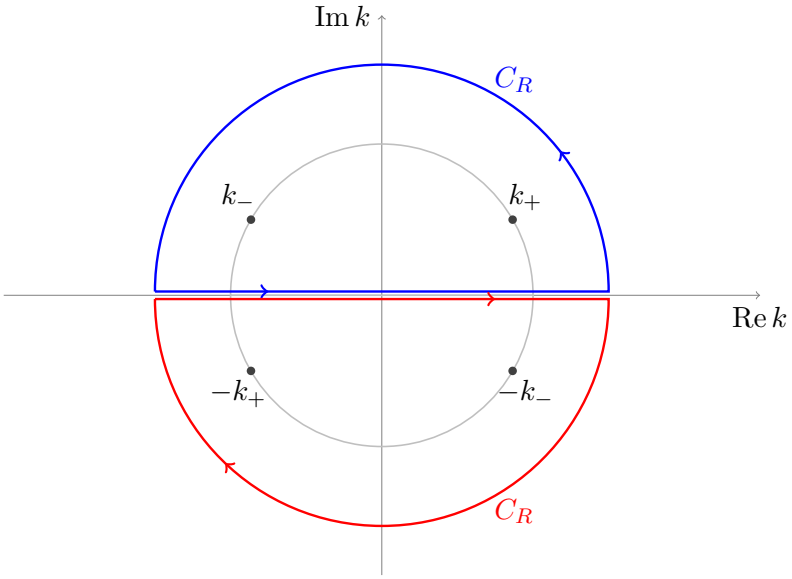

Figure 5.2: The closed paths in the upper (lower) half of the complex plane used to evaluate the integrals in Equations (5.24) and (5.25) are shown as blue (red) lines. The black dots represent the poles of the Green's functions, located along a circle of radius $|k_p|$ centered at the origin.

Complex Poles

To Fourier transform the propagators into real space, we first need to find the poles of the Green's functions in Equation (5.21), corresponding to the zeros of Bogoliubov quasiparticle spectrum $\omega^2 - E_k^2 = 0$. With some straightforward algebra, the four poles can be found as

$$k_p = \pm \mathrm{i}\sqrt{\frac{1}{t}(\varepsilon_0 \pm \omega_0)}\,, \tag{5.34}$$

where $t \equiv 1/2m$, $\varepsilon_0 \equiv t(k_x^2 + k_y^2) - \mu$, $\omega_0 = \sqrt{\omega^2 - |\Delta|^2}$ and we neglected the infinitesimal imaginary part η for the sake of simplicity. Since we are interested in the proximity effect, we restrict our analysis to $-|\Delta| < \omega < |\Delta|$. In this limit we have that

$$\omega_0 = \mathrm{i}\sqrt{|\Delta|^2 - \omega^2}\,, \tag{5.35}$$

is always a purely imaginary number, and the four poles in Equation (5.34) can be evaluated explicitly as $k_p = \pm k_\pm$ with $k_\pm \equiv \pm\kappa_r + \mathrm{i}\kappa_i$ where real and imaginary parts are given by

$$\kappa_r = \sqrt{\frac{1}{2t}\left(\sqrt{E_0^2 - \omega^2} - \varepsilon_0\right)}\,, \qquad \kappa_i = \sqrt{\frac{1}{2t}\left(\sqrt{E_0^2 - \omega^2} + \varepsilon_0\right)}\,, \tag{5.36}$$

and $E_0 \equiv \sqrt{\varepsilon_0^2 + |\Delta|^2}$. For energies below the superconducting gap, the poles always possess finite real and imaginary parts and lie on a circle of radius

$$|k_p| = \frac{1}{2t}\sqrt{E_0^2 - \omega^2}\,, \tag{5.37}$$

centered at the origin, and they become purely real or imaginary only for $\omega = |\Delta|$.

Normal Green's Function

For the normal Green's function, the integrand function in Equation (5.24) is explicitly given by

$$g(k_z) \equiv \frac{\omega + \varepsilon_k}{(\omega + \mathrm{i}\eta\,\mathrm{sgn}\,\omega)^2 - E_k^2}\,\mathrm{e}^{\mathrm{i}k_z(z-z')}\,. \tag{5.38}$$

For $z-z' \geq 0$, the integration contour can be closed in the upper half-plane, enclosing the poles $k_\pm$ as illustrated in Figure 5.2. The integral in Equation (5.24) can thus be evaluated as

$$\int \frac{\mathrm{d}k_z}{2\pi}\, g(k_z) = \mathrm{i}\Big[\mathrm{Res}(g, k_+) + \mathrm{Res}(g, k_-)\Big]\,. \tag{5.39}$$

Since both the poles are simple, the residues can be computed as

$$\mathrm{Res}(g, k_p) = \lim_{k_z \to k_p} (k_z - k_p) g(k_z)\,, \tag{5.40}$$

yielding

$$\mathrm{Res}(g, k_\pm) = \pm \frac{\omega \mp \omega_0}{4t\omega_0} \frac{1}{k_\pm} \mathrm{e}^{\mathrm{i}k_\pm(z-z')} \tag{5.41}$$

Skipping some straightforward algebra, the integral can be evaluated as

$$\int \frac{\mathrm{d}k_z}{2\pi}\, g(k_z) = \mathrm{i}\Big[\mathrm{Res}(g, k_+) + \mathrm{Res}(g, k_-)\Big] = \frac{\mathrm{i}}{4t\omega_0}\left[\frac{\Omega_-}{k_+}\mathrm{e}^{\mathrm{i}k_+(z-z')} - \frac{\Omega_+}{k_-}\mathrm{e}^{\mathrm{i}k_-(z-z')}\right], \tag{5.42}$$

where $\Omega_\pm \equiv \omega \pm \omega_0$. Since the poles in the upper and lower half–planes are related by inversion symmetry, an analogous expression follows for $z - z' < 0$. Recalling that the unperturbed normal Green's function in the bulk SC is proportional to identity in spin space, the real-space propagator can be finally written as

$$\mathcal{G}^{(0)}_{\mathrm{SC}}(k_\parallel, z - z'; \omega) = \frac{\mathrm{i}}{4t\omega_0}\left[\frac{\Omega_-}{k_+}\mathrm{e}^{\mathrm{i}k_+|z-z'|} - \frac{\Omega_+}{k_-}\mathrm{e}^{\mathrm{i}k_-|z-z'|}\right]\mathbf{1}\,. \tag{5.43}$$

The diagonal nonvanishing component of the normal SC Green's function is shown in Figure 5.3, plotted as a function of the spatial coordinate difference $z - z'$ and the energy ω below the gap.

Anomalous Green's Function

For the anomalous Green's function, the integrand function in Equation (5.25) is explicitly given by

$$f(k_z) \equiv \frac{\mathrm{i}\Delta^*}{(\omega + \mathrm{i}\eta\,\mathrm{sgn}\,\omega)^2 - E_k^2}\,\mathrm{e}^{\mathrm{i}k_z(z-z')}\,, \tag{5.44}$$

and we recall that the off-diagonal components are related by a sign change. We treat explicitly only the case of $z - z' \geq 0$, which can be integrated in the upper half-plane enclosing the poles $k_\pm$ as illustrated in Figure 5.2. The case $z - z' < 0$ yields an analogous result. The integral in Equation (5.25) can thus be evaluated as

$$\int \frac{\mathrm{d}k_z}{2\pi}\, f(k_z) = \mathrm{i}\Big[\mathrm{Res}(f, k_+) + \mathrm{Res}(f, k_-)\Big]\,, \tag{5.45}$$

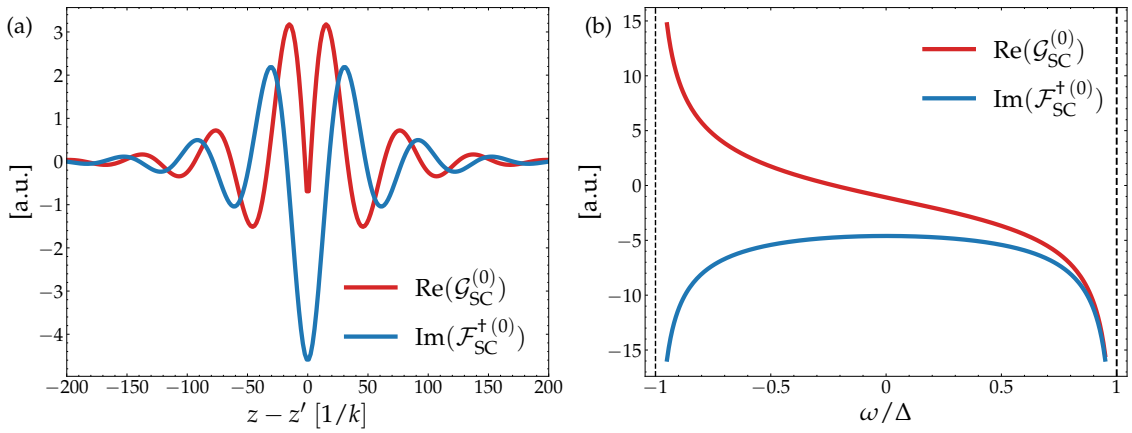

Figure 5.3: Unperturbed normal and anomalous Green's functions of a BCS superconductor, plotted as a function of (a) the real-space coordinate difference $z - z'$ at zero energy $\omega = 0$, and (b) the frequency ω below the gap at fixed position $z = z'$. The red curve shows the real part of the normal Green's function computed in Equation (5.43), while the blue curve shows the imaginary part of the anomalous Green's function in Equation (5.48). The plot was obtained for $k_x = k_y = 0$, $\Delta = 5$ meV and $\mu = 10$ meV.

where the residues can be computed through Equation (5.40) since the poles are simple. With some straightforward algebra, it is possible to obtain

$$\mathrm{Res}(f, k_\pm) = \pm \frac{\mathrm{i}\Delta^*}{4t\omega_0} \frac{1}{k_\pm} \mathrm{e}^{\mathrm{i}k_\pm (z - z')} \,, \tag{5.46}$$

and the integral is thus given by

$$\int \frac{\mathrm{d}k_z}{2\pi} f(k) = \mathrm{i}\Big[\mathrm{Res}(f, k_+) + \mathrm{Res}(f, k_-)\Big] = -\frac{\Delta^*}{4t\omega_0}\left[\frac{\mathrm{e}^{\mathrm{i}k_+(z-z')}}{k_+} - \frac{\mathrm{e}^{\mathrm{i}k_-(z-z')}}{k_-}\right]. \tag{5.47}$$

Taking into account the analogous result that can be obtained for $z - z' < 0$ with the opposite poles, and recalling that $\mathcal{F}^{(0)\,\dagger} \propto \sigma_y$ in spin space, we can finally write the real-space anomalous Green's function in the superconductor as

$$\mathcal{F}^{\dagger\,(0)}_{\mathrm{SC}}(k_\parallel, z - z'; \omega) = -\frac{\Delta^*}{4t\omega_0}\left[\frac{\mathrm{e}^{\mathrm{i}k_+|z-z'|}}{k_+} - \frac{\mathrm{e}^{\mathrm{i}k_-|z-z'|}}{k_-}\right]\sigma_y \,. \tag{5.48}$$

The off-diagonal nonvanishing components of the anomalous SC Green's function is shown in Figure 5.3, plotted as a function of the spatial coordinate difference $z - z'$ and the energy ω below the gap.

5.2 Unperturbed MTI

5.2.1 Equation of Motion

In the absence of the tunneling term, the unperturbed normal and anomalous Green's functions in the MTI can be computed exactly solving the corresponding equations of motion, which in real space take the form of a system of coupled

second-order linear differential equations. Recalling Equations (4.56) and (4.60), the unperturbed time-ordered propagators in the interaction picture are given by

$$\begin{aligned}\mathcal{G}^{(0)}_{\sigma\tau,\sigma'\tau'}(zt,z't') &= -\mathrm{i}\left\langle T_t\,\psi_{\sigma\tau}(zt)\psi^\dagger_{\sigma'\tau'}(z't')\right\rangle_0\,,\\ \mathcal{F}^{\dagger\,(0)}_{\sigma\tau,\sigma'\tau'}(zt,z't') &= -\mathrm{i}\left\langle T_t\,\psi^\dagger_{\sigma\tau}(zt)\psi^\dagger_{\sigma'\tau'}(z't')\right\rangle_0\,,\end{aligned} \tag{5.49}$$

where we omitted the in-plane momenta k_x and k_y for the translational invariant directions x and y. We emphasize that in the absence of a perturbation $V = 0$, the time evolution of the field operators in the interacting representation Equation (4.38) is equal to the Heisenberg one Equation (4.39). Making explicitly the action of the time-ordering operator, the normal Green's function becomes [144]

$$\mathcal{G}^{(0)}_{\sigma\tau,\sigma'\tau'}(zt,z't') = -\mathrm{i}\theta(t-t')\left\langle\psi_{\sigma\tau}(zt)\psi^\dagger_{\sigma'\tau'}(z't')\right\rangle_0 + \mathrm{i}\theta(t'-t)\left\langle\psi^\dagger_{\sigma'\tau'}(z't')\psi_{\sigma\tau}(zt)\right\rangle_0\,, \tag{5.50}$$

and its time derivative can be easily evaluated as

$$\begin{aligned}\partial_t\mathcal{G}^{(0)}_{\sigma\tau,\sigma'\tau'}(zt,z't') &= -\mathrm{i}\delta(t-t')\left\langle\left\{\psi_{\sigma\tau}(zt),\psi^\dagger_{\sigma'\tau'}(z't')\right\}\right\rangle_0 - \mathrm{i}\left\langle T_t\,\partial_t\psi_{\sigma\tau}(zt)\psi^\dagger_{\sigma'\tau'}(z't')\right\rangle_0\\ &= -\mathrm{i}\delta_{\sigma\sigma'}\delta_{\tau\tau'}\delta(z-z')\delta(t-t') - \mathrm{i}\left\langle T_t\,\partial_t\psi_{\sigma\tau}(zt)\psi^\dagger_{\sigma'\tau'}(z't')\right\rangle_0\,,\end{aligned} \tag{5.51}$$

where we have used the canonical fermionic anticommutation relation at $t = t'$

$$\left\{\psi_{\sigma\tau}(zt),\psi^\dagger_{\sigma'\tau'}(z't)\right\} = \delta_{\sigma\sigma'}\delta_{\tau\tau'}\delta(z-z')\,. \tag{5.52}$$

For the anomalous Green's function we can obtain an analogous result

$$\partial_t\mathcal{F}^{\dagger\,(0)}_{\sigma\tau,\sigma'\tau'}(zt,z't') = -\mathrm{i}\left\langle T_t\,\partial_t\psi^\dagger_{\sigma\tau}(zt)\psi^\dagger_{\sigma'\tau'}(z't')\right\rangle_0\,, \tag{5.53}$$

taking into account that the anticommutator between two fermionic creation field operators vanishes identically.

The time-derivative of the field operators $\psi_{\sigma\tau}(zt)$ and $\psi^\dagger_{\sigma\tau}(zt)$ on the unperturbed ground state is given by [144, 146]

$$\begin{aligned}\partial_t\psi_{\sigma\tau}(zt) &= \mathrm{i}\mathrm{e}^{\mathrm{i}Ht}\left[H,\psi_{\sigma\tau}(z)\right]\mathrm{e}^{-\mathrm{i}Ht} = -\mathrm{i}\sum_{\sigma'\tau'}h_{\sigma\tau,\sigma'\tau'}\psi_{\sigma\tau}(zt)\,,\\ \partial_t\psi^\dagger_{\sigma\tau}(zt) &= \mathrm{i}\mathrm{e}^{\mathrm{i}Ht}\left[H,\psi^\dagger_{\sigma\tau}(z)\right]\mathrm{e}^{-\mathrm{i}Ht} = \mathrm{i}\sum_{\sigma'\tau'}h_{\sigma\tau,\sigma'\tau'}\psi^\dagger_{\sigma\tau}(z)\,,\end{aligned} \tag{5.54}$$

where we used the Hamiltonian $H = H_{\mathrm{MTI}}$ for a non-proximitized thin film of MTI in Equation (4.10), whose matrix elements $h_{\sigma\tau,\sigma'\tau'}$ are defined in Equation (4.9). Plugging Equation (5.54) into Equation (5.49), the time-derivative of the normal and anomalous Green's functions can be obtained. The normal one becomes

$$\begin{aligned}\partial_t\mathcal{G}^{(0)}_{\sigma\tau,\sigma'\tau'}(zt,z't') =& -\mathrm{i}\delta_{\sigma\sigma'}\delta_{\tau\tau'}\delta(z-z')\delta(t-t') - \mathrm{i}\left\langle T_t\,\partial_t\psi_{\sigma\tau}(zt)\psi^\dagger_{\sigma'\tau'}(z't')\right\rangle_0 =\\ =& -\mathrm{i}\delta_{\sigma\sigma'}\delta_{\tau\tau'}\delta(z-z')\delta(t-t') -\\ &-\sum_{\sigma''\tau''}h_{\sigma\tau,\sigma''\tau''}\left\langle T_t\,\psi_{\sigma''\lambda''}(zt)\psi^\dagger_{\sigma'\tau'}(z't')\right\rangle_0 =\\ =& -\mathrm{i}\delta_{\sigma\sigma'}\delta_{\tau\tau'}\delta(z-z')\delta(t-t') - \mathrm{i}\sum_{\sigma''\tau''}h_{\sigma\tau,\sigma''\tau''}\mathcal{G}^{(0)}_{\sigma''\lambda'',\sigma'\tau'}(zt,z't')\,.\end{aligned} \tag{5.55}$$

Equivalently, one may write

$$-\sum_{\sigma''\tau''}\Big(\delta_{\sigma\sigma''}\delta_{\tau\tau''}\,\partial_t+\mathrm{i}\,h_{\sigma\tau,\sigma''\tau''}\Big)\mathcal{G}^{(0)}_{\sigma''\lambda'',\sigma'\tau'}(zt,z't')=\mathrm{i}\delta_{\sigma\sigma'}\delta_{\tau\tau'}\delta(z-z')\delta(t-t')\,, \tag{5.56}$$

which can be recast in matrix form as

$$\Big(\partial_t+\mathrm{i}\,h_{\mathrm{MTI}}\Big)\mathcal{G}^{(0)}_{\mathrm{MTI}}(zt,z't')=\mathrm{i}\delta_{\sigma\sigma'}\delta_{\tau\tau'}\delta(z-z')\delta(t-t')\,, \tag{5.57}$$

In analogous way, for the anomalous propagator we obtain [144]

$$\begin{aligned}\partial_t\mathcal{F}^{\dagger\,(0)}_{\sigma\tau,\sigma'\tau'}(zt,z't')&=-\mathrm{i}\left\langle T_t\,\partial_t\psi^\dagger_{\sigma\tau}(zt)\psi^\dagger_{\sigma'\tau'}(z't')\right\rangle_0=\\&=\sum_{\sigma''\tau''}h_{\sigma\tau,\sigma''\tau''}\left\langle T_t\,\psi^\dagger_{\sigma''\lambda''}(z)\psi^\dagger_{\sigma'\tau'}(z't')\right\rangle_0=\\&=\mathrm{i}\sum_{\sigma''\tau''}h_{\sigma\tau,\sigma''\tau''}\mathcal{F}^{\dagger\,(0)}_{\sigma''\lambda'',\sigma'\tau'}(zt,z't')\,,\end{aligned} \tag{5.58}$$

which can be rewritten as

$$\sum_{\sigma''\lambda''}\Big(\delta_{\sigma\sigma''}\delta_{\tau\tau''}\,\partial_t-\mathrm{i}\,h_{\sigma\tau,\sigma''\tau''}\Big)\mathcal{F}^{\dagger\,(0)}_{\sigma''\lambda'',\sigma'\tau'}(zt,z't')=0\,. \tag{5.59}$$

and using matrix notation finally becomes

$$\Big(\partial_t-\mathrm{i}\,h_{\mathrm{MTI}}(-i\partial_z)\Big)\mathcal{F}^{\dagger\,(0)}_{\mathrm{MTI}}(zt,z't')=0\,. \tag{5.60}$$

Equations (5.57) and (5.59) are the equations of motion for the normal and anomalous Green's functions in a non-proximitized thin film of MTI with translational invariance along the in-plane directions x and y and finite thickness along z. In the absence of proximity effect, the two equations become decoupled and can be solved independently, reflecting the absence of induced superconducting correlations in the system.

Since the Hamiltonian in Equation (4.10) does not depend explicitly on time, the system is time-translational invariant. Fourier transforming the Green's functions to frequency space the time derivatives become algebraic, such that Equations (5.57) and (5.59) become

$$\begin{aligned}\Big(\omega-h_{\mathrm{MTI}}(-i\partial_z)\Big)\mathcal{G}^{(0)}_{\mathrm{MTI}}(z,z';\omega)&=\delta(z-z')\,,\\\Big(\omega+h_{\mathrm{MTI}}(-i\partial_z)\Big)\mathcal{F}^{\dagger\,(0)}_{\mathrm{MTI}}(z,z';\omega)&=0\,.\end{aligned} \tag{5.61}$$

5.2.2 General Solution

To solve Equation (5.61) we must first solve the corresponding homogeneous equation valid for $z\neq z'$ and then find the particular solution applying boundary and matching conditions.

Homogeneous Solution

We begin by determining the general solution of the associated homogeneous system of equations. Since the anomalous Green's function vanishes identically in the absence of superconducting proximity-induced pairing, we deal with the normal propagator only, whose corresponding homogeneous equation reads

$$\Big(\omega - h_{\mathrm{MTI}}(-i\partial_z)\Big)\mathcal{G}^{(0)}_{\mathrm{MTI}}(z,z';\omega) = 0\,. \tag{5.62}$$

In the spin-orbital basis of states $\{|\uparrow +\rangle, |\uparrow -\rangle, |\downarrow +\rangle, |\downarrow -\rangle\}$, the differential equations take the explicit form

$$\begin{aligned}(B_1 - tD_1)\,\partial_z^2\, g_{\sigma\tau,\sigma'\tau'} = &-\left[t\,(e_0 + s\Lambda - \omega) + m_0\right] g_{\sigma\tau,\sigma'\tau'} - \\ &- A_2 t\,(k_x - \mathrm{i}sk_y)\, g_{\bar\sigma\bar\tau,\sigma'\tau'} + \\ &+ \mathrm{i}tsA_1\,\partial_z\, g_{\sigma\bar\tau,\sigma'\tau'}\,,\end{aligned} \tag{5.63}$$

where $g_{\sigma\tau,\sigma'\tau'}$ denote the matrix elements of the normal Green's function $\mathcal{G}^{(0)}_{\mathrm{MTI}}$, and the barred indices $\bar\sigma$ and $\bar\tau$ indicate the opposite spin and orbital states, respectively. We introduced the abbreviations $e_0 \equiv C_0 + D_2k^2$, $m_0 \equiv M_0 - B_2k^2$, and $k^2 \equiv k_x^2 + k_y^2$, while the spin and orbital indices are encoded through

$$s = \begin{cases} +1 & \text{if } \sigma = \uparrow \\ -1 & \text{if } \sigma = \downarrow \end{cases}, \qquad t = \begin{cases} +1 & \text{if } \tau = + \\ -1 & \text{if } \tau = - \end{cases}. \tag{5.64}$$

Equation (5.63) constitutes a system of four coupled second-order linear differential equations—one for each spin-orbital combination $\sigma\tau$. Importantly, since the right-hand side does not depend on $\sigma'\tau'$, the homogeneous solution is identical across all columns of the Green's function matrix.

To simplify the system, Equation (5.63) can be rewritten in a compact matrix form as

$$\partial_z^2\, g_{\sigma\tau} = [\mathsf{C}]_{\sigma\tau,\sigma\tau}\; g_{\sigma\tau} + [\mathsf{C}]_{\sigma\tau,\bar\sigma\bar\tau}\; g_{\bar\sigma\bar\tau} + [\mathsf{D}]_{\sigma\tau,\sigma\bar\tau}\; \partial_z g_{\sigma\bar\tau}\,, \tag{5.65}$$

where C and D are 4×4 matrices defined by comparison with Equation (5.62), that in the chosen basis are explicitly given by

$$\mathsf{C} = \begin{bmatrix} -\frac{e_0+m_0+\Lambda-\omega}{B1-D1} & 0 & 0 & -\frac{A_2(k_x-\mathrm{i}k_y)}{B1-D1} \\ 0 & -\frac{e_0+m_0-\Lambda-\omega}{B1-D1} & -\frac{A_2(k_x+\mathrm{i}k_y)}{B1-D1} & 0 \\ 0 & \frac{A_2(k_x-\mathrm{i}k_y)}{B1+D1} & \frac{e_0-m_0+\Lambda-\omega}{B1+D1} & 0 \\ \frac{A_2(k_x+\mathrm{i}k_y)}{B1+D1} & 0 & 0 & \frac{e_0-m_0-\Lambda-\omega}{B1+D1} \end{bmatrix}, \tag{5.66}$$

and

$$\mathsf{D} = \mathrm{i}A_1 \begin{bmatrix} 0 & 0 & \frac{1}{B1-D1} & 0 \\ 0 & 0 & 0 & -\frac{1}{B1-D1} \\ -\frac{1}{B1+D1} & 0 & 0 & 0 \\ 0 & \frac{1}{B1+D1} & 0 & 0 \end{bmatrix}. \tag{5.67}$$

Enlarging the space of unknowns and adding a set of four new equations in the unknowns $g_{\sigma\tau,\sigma'\tau'}$, Equation (5.62) can be reduced to a closed system of first-order differential equations [151, 152]. Indeed, Equation (5.65) can be rearranged as

$$\partial_z^2\, g_{\sigma\tau} = [\mathsf{C}]_{\sigma\tau,\sigma\tau}\; g_{\sigma\tau} + [\mathsf{C}]_{\sigma\tau,\bar{\sigma}\bar{\tau}}\; g_{\bar{\sigma}\bar{\tau}} + [\mathsf{D}]_{\sigma\tau,\sigma\bar{\tau}}\; \partial_z g_{\sigma\bar{\tau}}\,, \tag{5.68}$$

and taking into account also the trivial identity, it can be seen as a system of eight *first-order* differential equations in the unknowns $g_{\sigma\tau}$ and $\partial_z g_{\sigma\tau}$. Introducing the eight-component vector of unknowns

$$\mathbf{X} = \begin{pmatrix} g_{\uparrow+} & g_{\uparrow-} & g_{\downarrow+} & g_{\downarrow-} & \partial_z g_{\uparrow+} & \partial_z g_{\uparrow-} & \partial_z g_{\downarrow+} & \partial_z g_{\downarrow-} \end{pmatrix}, \tag{5.69}$$

Equation (5.68) can be written in matrix form as [153]

$$\partial_z \mathbf{X}(z,z') = \mathbf{M}\,\mathbf{X}(z,z')\,, \tag{5.70}$$

where

$$\mathbf{M} = \begin{bmatrix} 0 & 1 \\ \mathsf{C} & \mathsf{D} \end{bmatrix}, \tag{5.71}$$

and 0 and 1 are the 4×4 zero and identity matrices, respectively. The general solution to Equation (5.70) can be formally expressed via matrix exponentiation as [151, 152]

$$\mathbf{X}(z,z') = \mathrm{e}^{\mathbf{M}z}\,\mathbf{X}_0(z')\,, \tag{5.72}$$

where $\mathbf{X}_0(z')$ is an eight-components vector-valued function to be fixed by appropriate boundary or matching conditions.

To obtain the general solution of the homogeneous system of equations Equation (5.62) is thus sufficient to compute the exponential of the matrix $\mathbf{M}$. Explicitly, the general homogeneous solution in Equation (5.70) can be written as a linear combination of the matrix elements in the first four rows of the matrix $\mathbf{M}$

$$g_{\sigma\tau}(z,z') = \sum_j \left[\mathrm{e}^{\mathbf{M}z}\right]_{\sigma\tau,j} \mathbf{X}_{0,j}(z')\,, \tag{5.73}$$

where $\mathbf{X}_{0,j}$ for $j=1,\ldots,8$ are the components of the vector $\mathbf{X}_0$. Real and imaginary parts of the matrix elements in the first four rows of $\mathrm{e}^{\mathbf{M}z}$ are shown in Figures 5.4 and 5.5 as a function of the out-of-plane coordinate z.

Particular Solution

To find the full solution to Equation (5.62) we need to apply boundary conditions at the extremities of the MTI thin film and determine the particular solution for $\mathbf{X}_0(z')$. By including the inhomogeneous Dirac delta term, Equation (5.63) takes the following form

$$\begin{aligned} &(B_1 - tD_1)\,\partial_z^2\, g_{\sigma\tau,\sigma'\tau'} + \left[t\,(e_0 + s\Lambda - \omega) + m_0\right] g_{\sigma\tau,\sigma'\tau'} \\ &+A_2 t\,(k_x - \mathrm{i}sk_y)\, g_{\bar{\sigma}\bar{\tau},\sigma'\tau'} - \mathrm{i}tsA_1\,\partial_z\, g_{\sigma\bar{\tau},\sigma'\tau'} = \delta_{\sigma\sigma'}\delta_{\tau\tau'}\delta(z-z')\,, \end{aligned} \tag{5.74}$$

which depends also on $\sigma'\tau'$, meaning that the particular solution is different for each column of the Green's function matrix.

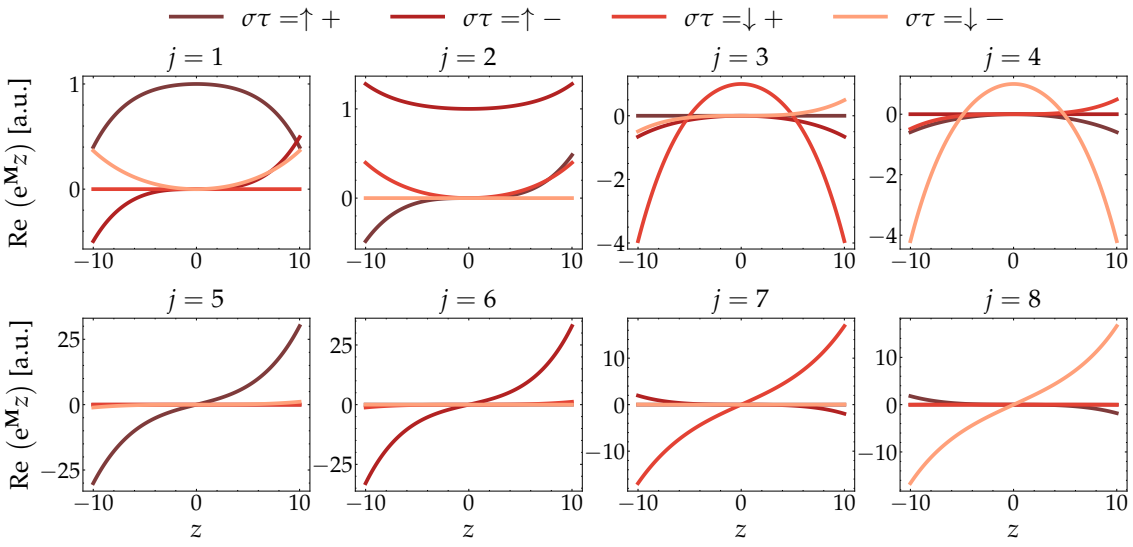

Figure 5.4: Real parts of the matrix elements in the first four rows of $e^{\mathbf{M}z}$—which constitute the components of the general homogeneous solution described in Equation (5.73)—plotted as a function of the out-of-plane coordinate z. The calculation is performed assuming $k_x = k_y = 0.01\ \text{Å}^{-1}$, $\Lambda = 20$ meV, and $\omega = 5$ meV, using the Bi_2Se_3 Hamiltonian parameters listed in Table 1.2.

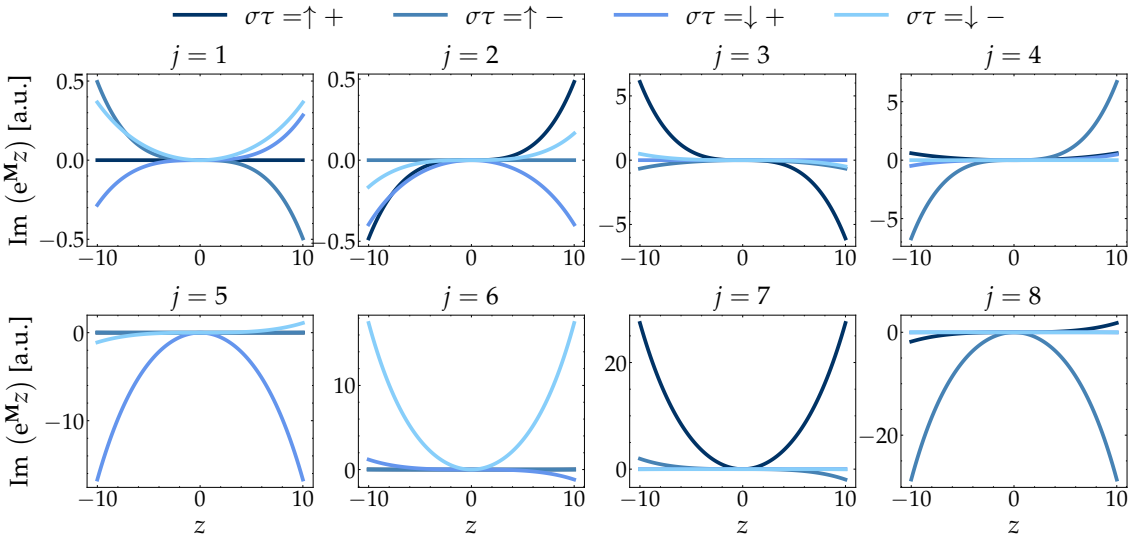

Figure 5.5: Imaginary parts of the matrix elements in the first four rows of $e^{\mathbf{M}z}$—which constitute the components of the general homogeneous solution described in Equation (5.73)—plotted as a function of the out-of-plane coordinate z. All the parameters are the same as those used in Figure 5.4.

For $z \neq z'$, the delta function vanishes, and Equation (5.74) reduces to the homogeneous one in Equation (5.63), whose general solution has already been derived. In principle, the solutions on either side of $z = z'$ may differ, and without loss of generality they can be expressed as

$$\mathbf{X}(z, z') = \begin{cases} \mathrm{e}^{\mathbf{M}z}\, \mathbf{X}_0^L(z') & \text{for } z < z' \,, \\ \mathrm{e}^{\mathbf{M}z}\, \mathbf{X}_0^R(z') & \text{for } z > z' \,, \end{cases} \tag{5.75}$$

where $\mathbf{X}_0^L(z')$ and $\mathbf{X}_0^R(z')$ are the corresponding coefficient vectors for the left and right branches, respectively. The components in the first four rows of the vector in Equation (5.75) correspond to the solutions for the normal MTI Green's function and we denote them as $g^L_{\sigma\tau,\sigma'\tau'}$ and $g^R_{\sigma\tau,\sigma'\tau'}$, respectively.

At the boundaries of the MTI thin film, $z = 0$ and $z = d$, we impose Neumann boundary conditions to ensure that the Green's function remains finite and does not vanish at the interfaces:

$$\partial_z\, g^L_{\sigma\tau,\sigma'\tau'}(z, z')\Big|_{z=0} = 0 \,, \tag{5.76}$$

$$\partial_z\, g^R_{\sigma\tau,\sigma'\tau'}(z, z')\Big|_{z=d} = 0 \,. \tag{5.77}$$

While this choice is not the only possible one, it is the most convenient for the computation of the induced pairing since allows us to assume that the tunneling $\Gamma(z) \propto \delta(z)$ occurs sharply at the MTI-SC interface at $z = 0$ without the need to evaluate the real-space integrals in Equation (4.70). Furthermore, this assumption is physically justified because it enforces the quasiparticle current normal to the surfaces of the MTI film to vanish, ensuring that no current flows out of the sample.

In addition, we impose continuity of the Green's function at $z = z'$,

$$g^L_{\sigma\tau,\sigma'\tau'}(z = z', z') = g^R_{\sigma\tau,\sigma'\tau'}(z = z', z') \,, \tag{5.78}$$

ensuring that no discontinuity arises in the propagator itself. Finally, in order to account for the singular source term $\delta(z - z')$, we integrate Equation (5.74) over an infinitesimal interval around $z = z'$. Making use of the continuity condition (5.78), this yields a discontinuity in the first derivative:

$$\Big[\partial_z\, g^R_{\sigma\tau,\sigma'\tau'}(z, z') - \partial_z\, g^L_{\sigma\tau,\sigma'\tau'}(z, z')\Big]_{z=z'} = \frac{\delta_{\sigma\sigma'}\delta_{\tau\tau'}}{B_1 - tD_1} \,. \tag{5.79}$$

For each fixed pair $\sigma'\tau'$, the boundary conditions (5.76)–(5.77), together with the continuity (5.78) and derivative jump condition (5.79), form a closed system of 16 linear equations for the 16 unknown coefficients $g^R_{\sigma\tau,\sigma'\tau'}$ and $g^L_{\sigma\tau,\sigma'\tau'}$ appearing in the general solution Equation (5.75). Being linear, such a system can be straightforwardly solved with matrix techniques. The particular solution for the normal Green's function in a non-proximitized thin film of Bi_2Se_3 with thickness $d = 100\,\text{Å}$ are shown in Figures 5.6 and 5.7 for $z' = d/2$.

5.2.3 Analytical Solution

While the general solution derived above is formally exact, it relies on the numerical evaluation of the matrix exponential and the subsequent solution of a boundary

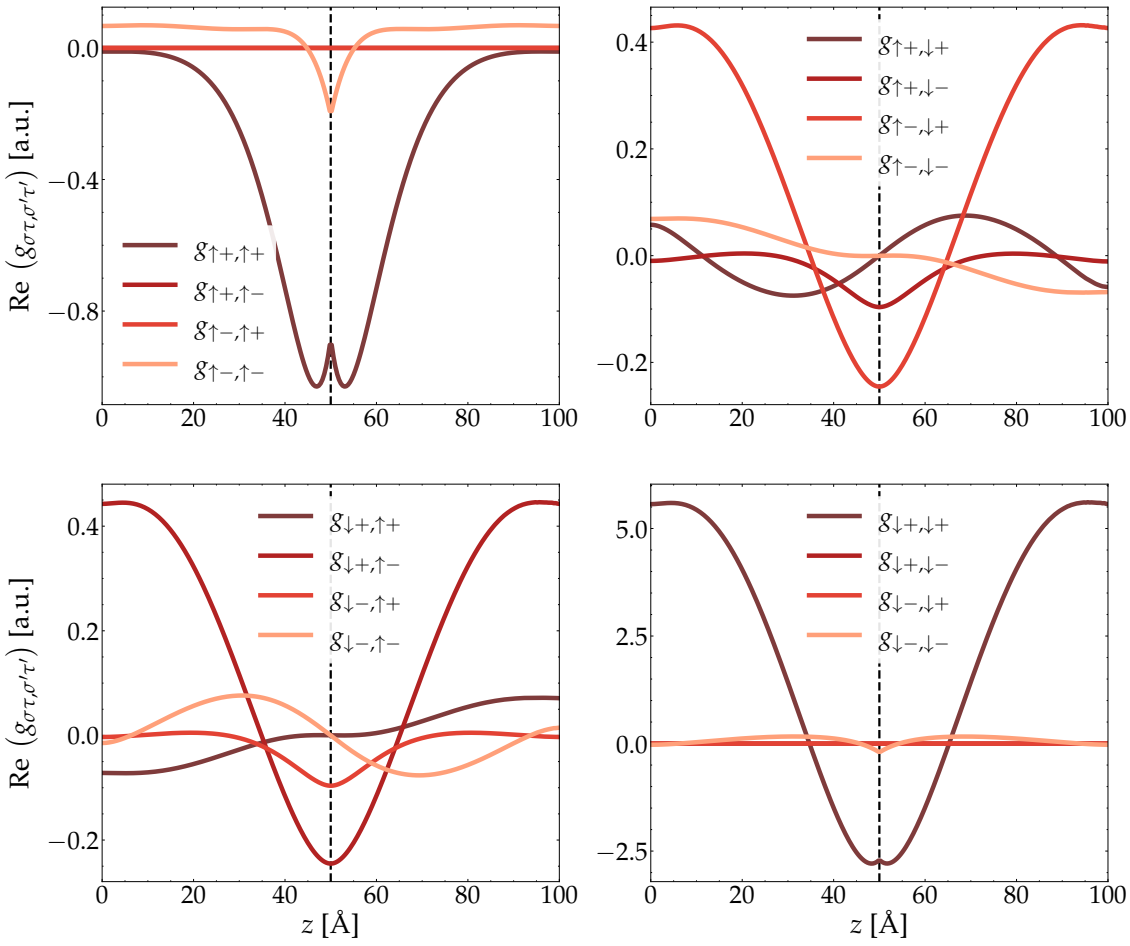

Figure 5.6: Real part of the matrix elements of the normal Green's function $g_{\sigma\tau,\sigma'\tau'}(z, z')$ in a non-proximitized MTI thin film with thickness $d = 100\,\text{Å}$, evaluated at $z' = d/2$. The vertical dashed line is drawn at $z' = 50\,\text{Å}$. All the parameters are the same as those used in Figure 5.4.

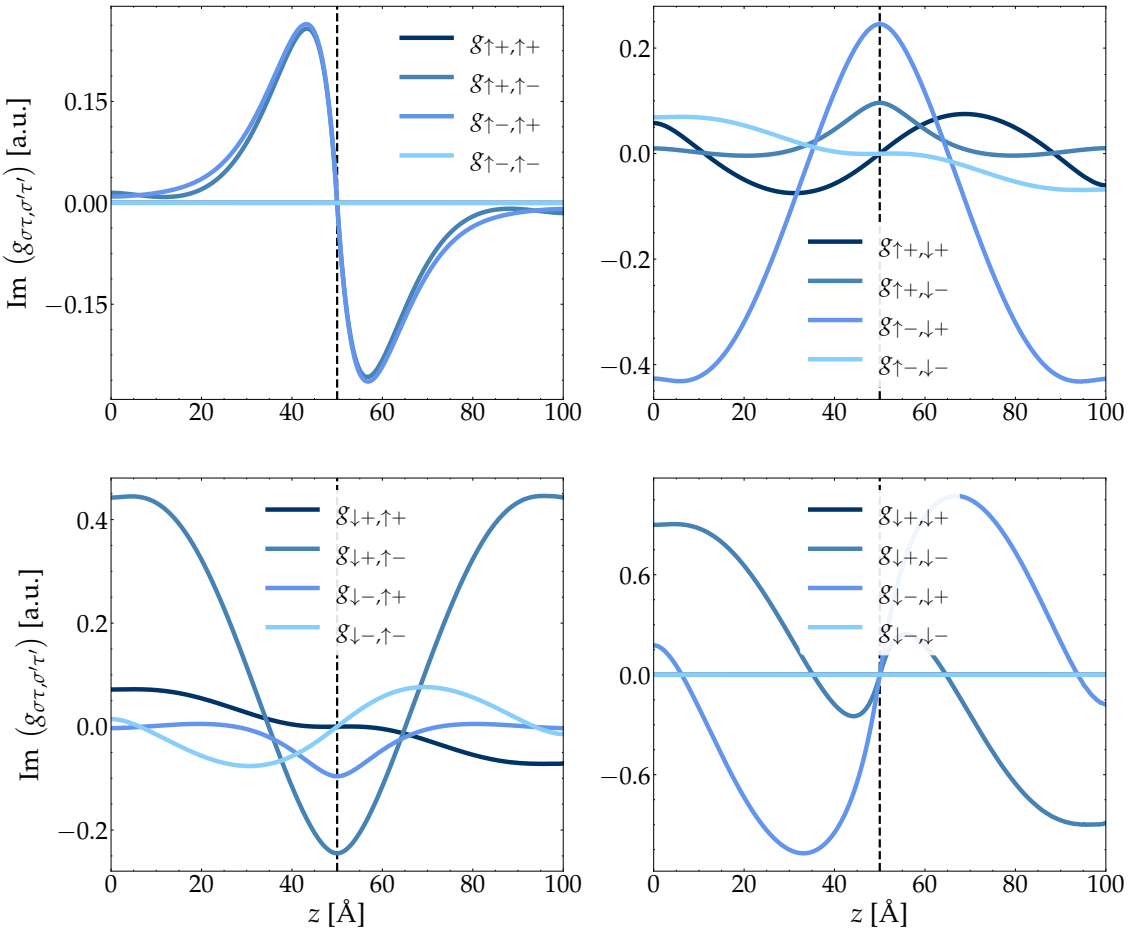

Figure 5.7: Imaginary part of the matrix elements of the normal Green's function $g_{\sigma\tau,\sigma'\tau'}(z, z')$ in a non-proximitized MTI thin film with thickness $d = 100$ Å, evaluated at $z' = d/2$. The vertical dashed line is drawn at $z' = 50$ Å. All the parameters are the same as those used in Figure 5.4.

value problem involving 16 coupled linear equations. Although this approach is necessary for full generality, it can conceal the underlying physical structure and limit analytical interpretation. To gain deeper insight, we now restrict our attention to surface-localized states that decay exponentially away from the interface at $z = 0$. Moreover, we focus on the limit of vanishing in-plane momentum $k_x = k_y = 0$, for which the MTI normal Green's function admits a closed-form analytical solution [153].

At the $\overline{\Gamma} = (0, 0)$ point in the surface BZ, spin-momentum locking becomes ineffective due to the vanishing of the spin-orbit coupling terms, and the spin species effectively decouple [35, 80]. This symmetry simplifies the problem substantially: the normal Green's function becomes diagonal in spin space, and the full system reduces to a pair of coupled second-order differential equations for each spin component. Specifically, the homogeneous system of Equation (5.62) reduces to:

$$\begin{aligned} (B_1 - D_1)\,\partial_z^2\, g_{\sigma+} &= -\left(M_0 + \tilde{C}_0\right) g_{\sigma+} + \mathrm{i}\, s\, A_1\, \partial_z\, g_{\sigma-}\,, \\ (B_1 + D_1)\,\partial_z^2\, g_{\sigma-} &= -\left(M_0 - \tilde{C}_0\right) g_{\sigma-} - \mathrm{i}\, s\, A_1\, \partial_z\, g_{\sigma+}\,, \end{aligned} \tag{5.80}$$

where $\tilde{C}_0 \equiv C_0 + s\Lambda - \omega$ and, for notational simplicity, we have omitted the indices $\sigma' = \sigma$ and τ'. The index $s = \pm 1$ denotes the spin projection as in Equation (5.64).

By differentiating and substituting between the two equations, one obtains a decoupled fourth-order differential equation for $g_{\sigma+}$ and a third-order differential equation for $g_{\sigma-}$

$$\begin{aligned} \partial_z^4\, g_{\sigma+} - \mathbf{a}\,\partial_z^2\, g_{\sigma+} + \mathbf{b}\, g_{\sigma+} &= 0\,, \\ g_{\sigma-} &= \mathbf{c}\,\partial_z^3\, g_{\sigma+} + \mathbf{d}\,\partial_z\, g_{\sigma+}\,, \end{aligned} \tag{5.81}$$

where the coefficients are defined as

$$\begin{aligned} \mathbf{a} &= \frac{1}{B_1^2 - D_1^2}\left(A_1^2 - 2D_1\tilde{C}_0 - 2B_1 M_0\right), & \mathbf{b} &= \frac{1}{B_1^2 - D_1^2}\left(M_0^2 - \tilde{C}_0^2\right), \\ \mathbf{c} &= \mathrm{i}s\,\frac{B_1^2 - D_1^2}{A_1\left(M_0 - \tilde{C}_0\right)}, & \mathbf{d} &= \mathrm{i}s\,\frac{A_1 - (B_1^2 - D_1^2)\left(M_0 + \tilde{C}_0\right)}{A_1\left(M_0 - \tilde{C}_0\right)}\,. \end{aligned} \tag{5.82}$$

The general solution to this system takes the form [151]

$$\begin{aligned} g_{\sigma+}(z, z') &= g_1\, e^{\lambda_1 z} + g_2\, e^{-\lambda_1 z} + g_3\, e^{\lambda_2 z} + g_4\, e^{-\lambda_2 z}\,, \\ g_{\sigma-}(z, z') &= \eta_1\left(g_1\, e^{\lambda_1 z} - g_2\, e^{-\lambda_1 z}\right) + \eta_2\left(g_3\, e^{\lambda_2 z} - g_4\, e^{-\lambda_2 z}\right)\,, \end{aligned} \tag{5.83}$$

where the functions $g_i \equiv g_i(z')$ are fixed by boundary and matching conditions. The characteristic exponents λ_i and the coefficients η_i are given by

$$\lambda_{1,2} = \frac{1}{\sqrt{2}}\sqrt{\mathbf{a} \pm \sqrt{\mathbf{a}^2 - 4\mathbf{b}}}\,, \qquad \eta_i = \lambda_i\left(\mathbf{c}\lambda_i^2 - \mathbf{d}\right)\,. \tag{5.84}$$

We emphasize that $\lambda_{1,2} \equiv \lambda_{1,2}^{\sigma}(\omega)$ depend explicitly on the spin index σ and the energy ω. However, the corresponding indices are omitted throughout for notational simplicity.

To further simplify the analytical structure of the found solution, we now consider a physically motivated limiting case. Specifically, we make the following assumptions:

(i) neglect electron–hole asymmetry by setting $D_1 = 0$;

(ii) remove the constant energy offset by setting $C_0 = 0$ in the effective Hamiltonian of Equation (1.46);

(iii) assume a low-energy, weak-magnetization regime where $\omega, \Lambda \ll M_0$.

Within this regime, the structure of the general solution in Equation (5.83) remains intact, but the characteristic exponents simplify considerably.

For $A_1^2 - 4M_0B_1 < 0$, we can approximate [153]

$$\lambda_{1,2} \approx \frac{1}{\sqrt{2}B_1}\sqrt{A_1^2 - 2M_0B_1 \pm A_1\sqrt{A_1^2 - 4M_0B_1}}\,, \tag{5.85}$$

where the inner square root becomes imaginary, yielding complex-conjugate pairs. In these conditions, we can define

$$\lambda_1 = \lambda + \mathrm{i}\kappa\,, \qquad \lambda_2 = \lambda - \mathrm{i}\kappa\,, \tag{5.86}$$

which represent decaying and oscillatory modes. In the limiting case where $\omega = 0$ and $\Lambda \ll M_0$, the real and imaginary parts can be obtained from Equation (5.85) as

$$\lambda \approx \frac{A_1}{2B_1}\,, \qquad \kappa \approx \frac{1}{2B_1}\sqrt{4M_0B_1 - A_1^2}\,. \tag{5.87}$$

These quantities are real and positive for $A_1, B_1 > 0$, ensuring physically acceptable solutions that decay away from the surface. While the specific expressions in Equation (5.87) were obtained by setting $\omega = \Lambda = 0$, the structure of Equation (5.86) remains valid more generally as long as $\omega, \Lambda \ll M_0$ and particle–hole asymmetry is negligible.

Particular Solution

To construct the particular solution for the normal Green's function, we follow the strategy outlined in the previous section, now restricting the possible solutions to surface-localized states of topological origin. In this context, we seek solutions that *decay exponentially* away from the surface at $z = 0$, which is consistent with the physical expectation for topologically protected states confined near the boundary of a finite system. These states are characterized by their localization at the interfaces of the thin film and their suppression into the bulk, making them particularly relevant in the analysis of surface transport and proximity effects.

We consider again the homogeneous solution derived in Equation (5.83), which can be in principle different in the two regions created by the singular point $z = z'$. Specifically, for $z \leq z'$, we assume a general solution of the form:

$$\begin{aligned} g^L_{\sigma+,\sigma\tau'}(z,z') &= l_1\,\mathrm{e}^{\lambda_1 z} + l_2\,\mathrm{e}^{-\lambda_1 z} + l_3\,\mathrm{e}^{\lambda_2 z} + l_4\,\mathrm{e}^{-\lambda_2 z}\,, \\ g^L_{\sigma-,\sigma\tau'}(z,z') &= \eta_1\left(l_1\,\mathrm{e}^{\lambda_1 z} - l_2\,\mathrm{e}^{-\lambda_1 z}\right) + \eta_2\left(l_3\,\mathrm{e}^{\lambda_2 z} - l_4\,\mathrm{e}^{-\lambda_2 z}\right)\,, \end{aligned} \tag{5.88}$$

where the coefficients $l_i \equiv l_i(z')$ are undetermined functions of the source coordinate z' that will be fixed by boundary and matching conditions.

For $z > z'$, we impose that the Green's function remains bounded in the limit $z \to +\infty$, which in the present case corresponds to requiring that no exponentially growing modes are present. Physically, this condition eliminates bulk-like delocalized solutions and ensures that the response remains localized near the interface at $z = 0$. Accordingly, we discard the growing terms proportional to $\mathrm{e}^{\lambda z}$ by setting $r_1 = r_4 = 0$ in Equation (5.83) to obtain

$$\begin{aligned} g^R_{\sigma+,\sigma\tau'}(z,z') &= r_2\,\mathrm{e}^{-\lambda_1 z} + r_3\,\mathrm{e}^{-\lambda_2 z}\,, \\ g^R_{\sigma-,\sigma\tau'}(z,z') &= -\eta_1\,r_2\,\mathrm{e}^{-\lambda_1 z} - \eta_2\,r_3\,\mathrm{e}^{-\lambda_2 z}\,, \end{aligned} \tag{5.89}$$

where $r_2 \equiv r_2(z')$ and $r_3 \equiv r_3(z')$ are again functions to be determined by boundary and matching conditions. This construction reflects a physically motivated ansatz: we retain only the components of the Green's function that decay away from the interface at $z = 0$, consistently with the assumption that the MTI thin film is in a topological phase with Dirac-cone surface states localized on the interfaces and within a large bulk gap [35, 36, 80]. States that penetrate into the bulk are thus excluded from the possible solutions.

To fully determine the particular solution, we impose the same boundary and matching conditions introduced previously in Equations (5.76), (5.78) and (5.79). We recall that these conditions include Neumann boundary condition at $z = 0$, continuity of the Green's function at $z = z'$, and the discontinuity of the first derivative at $z = z'$ determined by the inhomogeneous delta-function source. Together, these yield a linear system of six equations for the six unknown functions $l_i(z')$ and $r_i(z')$, which fully determine the particular solution for a given spin σ and orbital channel τ, τ'.

After solving this system, we obtain the Green's function in a closed analytical form. In particular, at the interface $z = 0$, the solution simplifies to [153]

$$g_{\sigma\tau,\sigma\tau'}(z=0,z') = \mathrm{e}^{-\lambda z'}\left[\alpha^\sigma_{\tau\tau'}\cos(\kappa z') + \beta^\sigma_{\tau\tau'}\sin(\kappa z')\right], \tag{5.90}$$

where $\lambda \equiv \lambda_\sigma(\omega)$ and $\kappa \equiv \kappa_\sigma(\omega)$ are the real and imaginary parts of the complex characteristic exponents introduced in Equation (5.86). Both quantities depend on the spin index σ and the energy ω, and encode the decay length and oscillation frequency of the surface states, respectively. The coefficients $\alpha^\sigma_{\tau\tau'}$ and $\beta^\sigma_{\tau\tau'}$ contain the full dependence on the orbital indices and boundary geometry and are derived explicitly in Appendix C. The analytical solution given in Equation (5.90), evaluated for a Bi_2Se_3 thin film with thickness $d = 100\,\text{Å}$ for vanishing in-plane momentum and at the $z = 0$ interface, is shown in Figure 5.8 as a function of the out-of-plane coordinate z'. Only the Green's function components with non-vanishing real or imaginary parts are displayed.

These expressions provide an analytically tractable description of the Green's function near the interface, capturing the essential features of surface-state propagation in the MTI thin film geometry. Importantly, this analytical result illustrates the emergence of exponentially damped oscillations characteristic of systems with a nontrivial topological mass term. The interplay between the decay length $1/\lambda$ and

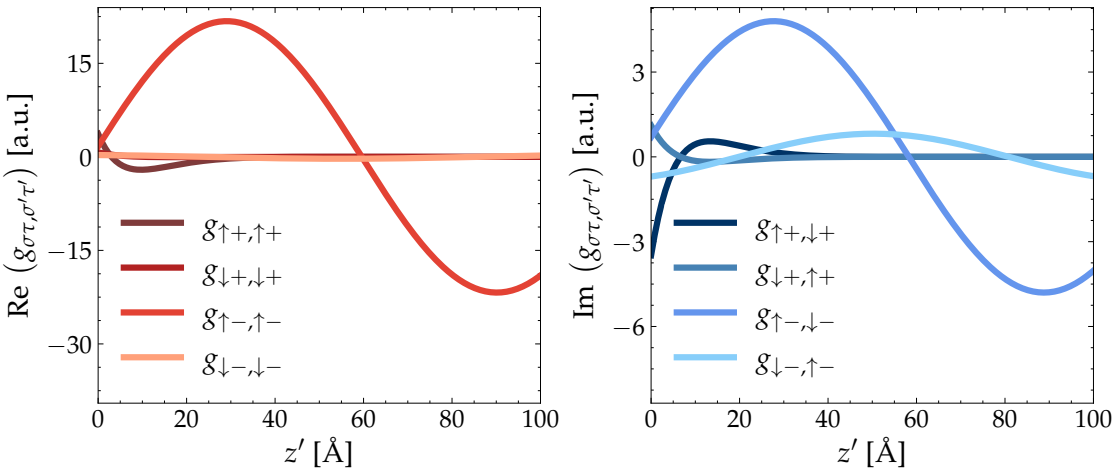

Figure 5.8: Real (left) and imaginary (right) parts of the normal Green's function $g_{\sigma\tau,\sigma'\tau'}$ at the $\overline{\Gamma}$ point, obtained from the analytical solution at $z = 0$ in Equation (5.90). Only components with a nonvanishing real or imaginary part are displayed, plotted as functions of the out-of-plane coordinate z'. All the parameters are chosen consistently with those used in Figure 5.4.

oscillation frequency κ is a direct consequence of the band inversion present in the bulk MTI and reflects the hybridization between spin and orbital degrees of freedom near the surface.

Summary

In this chapter, we evaluated the unperturbed Green's functions of the two decoupled materials forming the MTI–SC heterostructure, and providing the essential ingredients for the perturbative theory developed in Chapter 4.

For the bulk superconductor, we derived and solved the Gor'kov equations in momentum space, which couple normal and anomalous propagator. We then performed a Fourier transform along the out-of-plane direction z, obtaining closed-form expressions for both the normal and anomalous Green's functions in real space.

We then turned to the magnetic topological insulator, deriving the equation of motion for the unperturbed normal propagator. By solving the resulting system of second-order linear differential equations, we obtained the real-space Green's function in two different ways. First, we derived a general solution valid for arbitrary in-plane momentum near the high-symmetry point $\overline{\Gamma}$ of the two-dimensional Brillouin zone and for generic Hamiltonian parameters. Second, we obtained an analytical closed-form expression in the limiting case $k_x = k_y = 0$, restricting the solution to surface-localized states that decay exponentially away from the interface. Together, these results provide both a general description of quasiparticle propagation in MTI thin films, and a tractable analytical limit useful for further analysis.

The unperturbed Green's functions derived in this chapter provide the ingredients for evaluating the second–order corrections to the anomalous propagator in proximitized MTIs, which will be the focus of the last chapter.

Chapter 6

Induced Pairing

Overview

In Chapters 4 and 5, we developed a perturbative framework to describe superconductivity induced in proximitized MTIs, and solved the equations of motion for both the bulk SC and the thin film of topological insulator, obtaining the unperturbed normal and anomalous Green's functions of the two isolated materials. These results provide the building blocks necessary to evaluate the perturbative correction to the anomalous MTI propagator, which encodes the effective superconducting pairing induced by proximity to the conventional SC. Following Chapter 5, we consider a bulk superconductor, translationally invariant in all directions, coupled to a MTI thin film of thickness d and with in-plane translational symmetry. The induced pairing is evaluated using both the general solution of the unperturbed MTI propagator and the analytical one valid at the $\overline{\Gamma}$ point, discussed in the previous chapter.

The study of the induced pairing correlations serves a dual purpose. First, it provides a microscopic description of how superconductivity penetrates into the proximitized surface states of the MTI, allowing us to characterize the spatial profile of the induced correlations and to extract their decay length away from the interface. Second, it reveals how the interplay between topology and magnetization shapes the structure of the superconducting order parameter, influencing its symmetry properties in both spin and momentum space. In this sense, the present discussion complements the analysis of topological superconductivity in proximitized MTIs outlined in the first part of this thesis.

The chapter is organized as follows. In Section 6.1, we refine the assumptions on the tunneling Hamiltonian and evaluate the induced pairing, focusing on its spatial dependence along z and deriving an explicit expression for the decay length in the analytically tractable limit. In Section 6.2, we analyze the spin structure of the anomalous propagator, decomposing it into singlet and triplet components and examining how these are affected by the magnetization of the MTI thin film. In Section 6.3, we turn to the symmetry of the induced correlations in momentum space, studying the evolution of the even- and odd-parity components under the Zeeman field and expanding the superconducting order parameter in circular harmonics to resolve the contributions with different out-of-plane angular momentum. Finally, we connect the momentum-space structure of the induced pairing to the physics of the two-dimensional topological superconductor, relating the circular harmonics

with nonvanishing angular momentum to nontrivial phases hosting chiral Majorana modes.

6.1 Real–Space Pairing Profile

The anomalous Green's function in the MTI can be evaluated from the perturbative expansion introduced in Section 4.3, making use of the unperturbed propagators derived in Sections 5.1 and 5.2 for the two materials.

In the previous analysis, the tunneling process was assumed to be strictly local in space, i.e., coupling only electrons at the same position $z = z'$, as expressed in Equation (4.66). We now refine this assumption by restricting the tunneling to occur sharply at the MTI–SC interface, which we place at $z_0 = 0$:

$$\gamma_{\sigma\tau,\sigma'}(z) \equiv \gamma_{\sigma\tau,\sigma'}\,\delta(z - z_0)\,. \tag{6.1}$$

Alternative spatial profiles centered at z_0 could in principle be chosen, but the delta function form is particularly convenient as it eliminates the real-space integral. With this assumption, the second-order anomalous propagator of Equation (4.70) reduces to the following matrix product [153]

$$\mathcal{F}^{\dagger\,(2)}_{\mathrm{MTI}}(z, z'; \omega) = \left[\mathcal{G}^{(0)}_{\mathrm{MTI}}(0, z; -\omega)\right]^{T}\,\Gamma^{*}\,\mathcal{F}^{\dagger\,(0)}_{\mathrm{SC}}(0; \omega)\,\Gamma^{\dagger}\,\mathcal{G}^{(0)}_{\mathrm{MTI}}(0, z'; \omega)\,, \tag{6.2}$$

where the in-plane momentum $k_{\parallel} = (k_x, k_y)$ has been omitted for simplicity, and Γ denotes the 4×2 tunneling matrix with elements $\gamma_{\sigma\tau,\sigma'}$, which are now position independent. In the following, we restrict to orbital-independent, spin-conserving tunneling, specified by $\gamma_{\sigma\tau,\sigma'} = \gamma\,\delta_{\sigma\sigma'}$, where $\gamma \in \mathbb{C}$ denotes the tunneling amplitude. In practice, Equation (6.2) can be evaluated in two alternative ways:

(i) using the general momentum-dependent solution of $\mathcal{G}^{(0)}_{\mathrm{MTI}}$ presented in Section 5.2.2 and valid for generic magnetization and all Hamiltonian parameters;

(ii) employing the analytical expression of $\mathcal{G}^{(0)}_{\mathrm{MTI}}$ derived in Section 5.2.3, which applies at the $\overline{\Gamma}$ point under the conditions $C_0 = 0$ and $D_1 = 0$. This solution is valid in the limit of weak magnetization and for surface states that decay exponentially away from the interface at $z = 0$.

Since low-energy transport and topological properties are governed by quasiparticles near the Fermi surface, it is sufficient to characterize the induced pairing at the Fermi level [89, 144]. Accordingly, we restrict the analysis to $\omega = 0$, which probes the static, long–time limit of the anomalous correlations. In the following, we refer to the local Green's function at coincident coordinates $z = z'$ evaluated at the Fermi level, as the "induced pairing"

$$\mathcal{F}^{\dagger}(k_{\parallel}, z) \equiv \mathcal{F}^{\dagger\,(2)}_{\mathrm{MTI}}(k_{\parallel}; z, z; \omega = 0)\,. \tag{6.3}$$

Moreover, we quantify the magnitude of the induced pairing through the Frobenius norm of the corresponding 4×4 matrix, defined as [152, 154]

$$\|\mathcal{F}^{\dagger}(k_{\parallel}, z)\|^2 \equiv \sum_{\sigma,\sigma'}\sum_{\tau,\tau'}\left|\mathcal{F}^{\dagger}_{\sigma\tau,\sigma'\tau'}(k_{\parallel}, z)\right|^2\,, \tag{6.4}$$

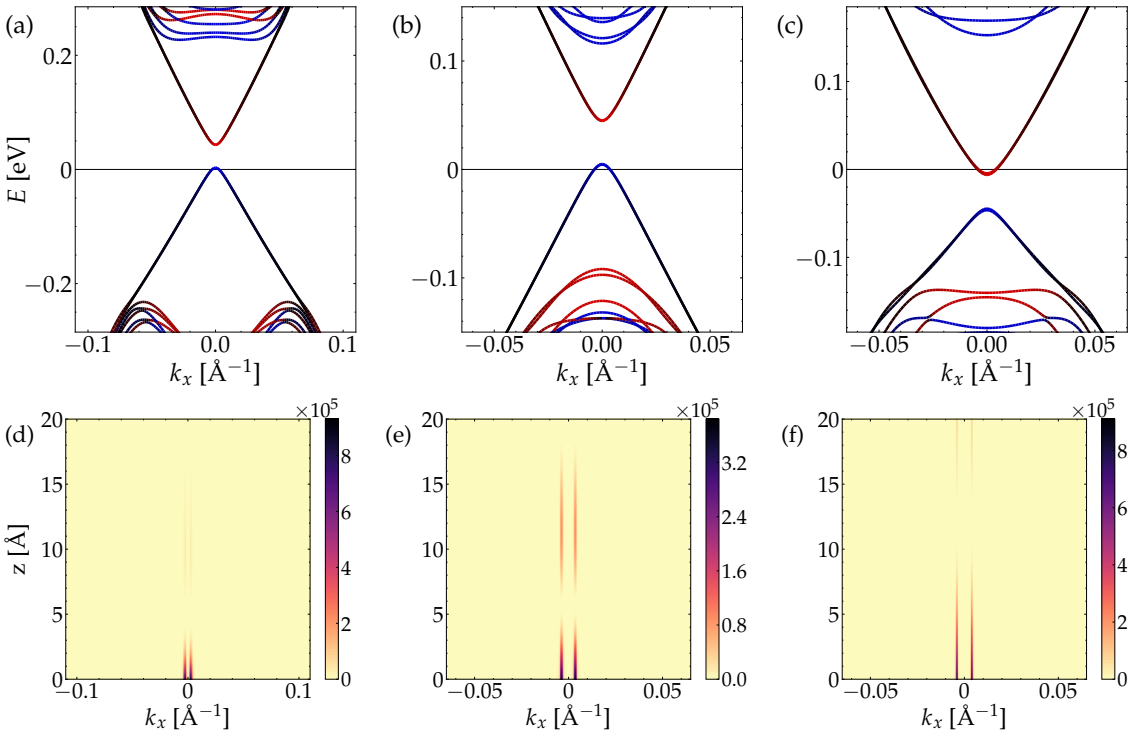

Figure 6.1: Band structure and induced pairing in the (k_x, z) plane for the materials of the Bi_2Se_3 family at $k_y = 0$. Panels (a,d) correspond to Bi_2Se_3, (b,e) to Bi_2Te_3, and (c,f) to Sb_2Te_3. The top row displays the band dispersion along k_x, obtained by discretizing Equation (1.48), with the color scale indicating the spin polarization $\langle \sigma_z \rangle$ of the corresponding states. The bottom row displays the magnitude of the induced pairing obtained from Equation (6.4), and expressed in units of $|\gamma|^2$. The calculations assume a MTI thin film of thickness $d = 10$ nm with magnetization $\Lambda = 20$ meV, proximitized by a SC with $\mu = 10$ meV and $\Delta = 5$ meV. The remaining parameters are taken from Table 1.2, setting $C_0 = -50$ meV in Bi_2Se_3, $C_0 = -68$ meV in Bi_2Te_3, and $C_0 = 45$ meV in Sb_2Te_3, in order to proximitize states near the $\overline{\Gamma}$ point.

where σ, σ' and τ, τ' denote the usual spin and orbital degrees of freedom. The magnitude of the induced pairing, obtained from Equation (6.4), is shown in Figure 6.1.

Panels (a,d) correspond to Bi_2Se_3, panels (b,e) to Bi_2Te_3, and panels (c,f) to Sb_2Te_3. The upper row displays the energy spectra of proximitized MTI thin films composed of the three compounds of the Bi_2Se_3 family, with red (blue) color indicating spin-up (spin-down) polarization, as obtained from Equation (1.59). The spectra are shifted by setting $C_0 = -50$ meV in Bi_2Se_3, $C_0 = -68$ meV in Bi_2Te_3, and $C_0 = 45$ meV in Sb_2Te_3, in order to induce superconductivity into the states near the $\overline{\Gamma}$ point. The lower row shows the corresponding induced pairing amplitude in the (k_x, z) plane at $k_y = 0$, as obtained from the full momentum-dependent solution of the normal propagator.

For the chosen set of parameters, the proximity effect in all three materials is induced into the gapped Dirac-cone surface states at $E = 0$—indicated by the horizontal line in the energy spectra—which thereby acquire a finite pairing amplitude [28, 30]. Accordingly, the induced superconductivity is maximized at those values

of k_x where the low-energy modes of the MTI are present, while remains negligible elsewhere. As expected, the anomalous Green's function is maximal at the interface and decays into the bulk. This decay is exponential but modulated, with oscillations that can be related to the real-space profile of the probability density of the proximitized surface states. The dependence of the induced pairing amplitude on the out-of-plane coordinate z is shown in Figure 6.2, as obtained from the analytical solution at the $\overline{\Gamma}$ point.

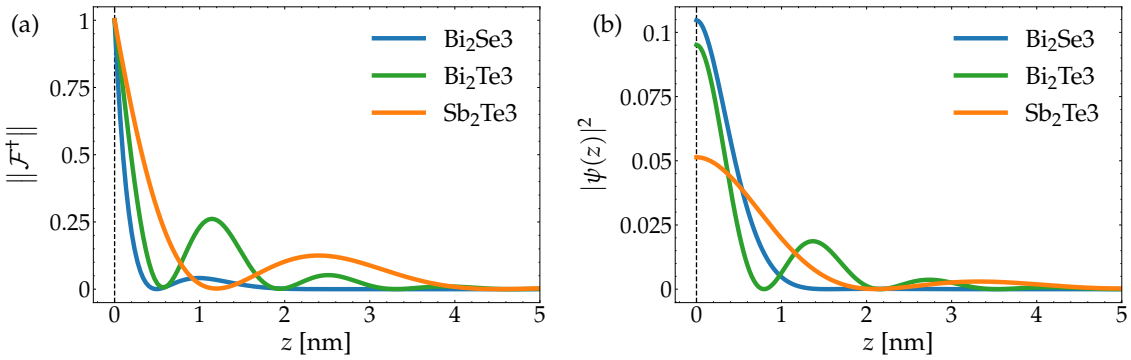

Figure 6.2: Real-space profiles of the superconducting proximity effect in the compounds of the Bi_2Se_3 family. Panel (a) displays the magnitude of the induced pairing at the $\overline{\Gamma}$ point, obtained from the analytical solution, and normalized to its value at the interface $z = 0$. Panel (b) depicts the probability density $|\psi(z)|^2$ of the lowest-energy surface state, obtained from the discretization of Equation (1.48) on a finite lattice with thickness $d = 10$ nm. For the MTI, we assumed a magnetization $\Lambda = 20$ meV, neglected the trivial energy shift setting $C_0 = 0$, and removed the particle–hole asymmetry of the Dirac spectrum imposing $D_1 = 0$. For the SC, we take a chemical potential $\mu = 10$ meV and a superconducting gap $\Delta = 5$ meV. All the remaining parameters are taken from Table 1.2.

The figure compares the spatial dependence of the induced pairing magnitude, shown in panel (a), with the probability density of the lowest-energy surface state, displayed in panel (b), for the three materials of the Bi_2Se_3 family. In all cases, the decay of the induced pairing is mainly determined by the penetration depth of the proximitized surface states, both exhibiting qualitatively similar spatial profiles and comparable oscillatory behavior.

The results above were obtained at the high-symmetry point $k_x = k_y = 0$ in momentum space. To characterize how the total magnitude of the induced pairing evolves with magnetization, it is useful to evaluate a momentum-averaged amplitude of the anomalous Green's function across the BZ. However, since the induced correlations are strongly peaked around the Fermi surface of the normal state (see Figure 6.1), we evaluate the order parameter at the Fermi momentum, which in the Dirac limit of proximitized surface states can be approximated as

$$k_F \approx \frac{1}{A_2}\sqrt{C_0^2 - \Lambda^2}\,. \tag{6.5}$$

Expressing the Green's function in polar coordinates as $\mathcal{F}^\dagger(k_\parallel, z) = \mathcal{F}^\dagger(k, \theta; z)$, where $k = |k_\parallel|$ is the modulus of the in-plane momentum and $\theta = \arctan(k_y/k_x)$ its

polar angle, we define the angularly averaged magnitude as

$$\left\|\overline{\mathcal{F}^{\dagger}}(k_F, z)\right\| \equiv \frac{1}{2\pi}\int_0^{2\pi} \mathrm{d}\theta \left\|\mathcal{F}^{\dagger}(k_F, \theta; z)\right\|. \tag{6.6}$$

The amplitudes of the superconducting correlations evaluated at the Fermi momentum and averaged over the polar angle θ are shown in Figure 6.3 as a function of the magnetization in the proximitized MTI thin film, for the different compounds of the Bi_2Se_3 family.

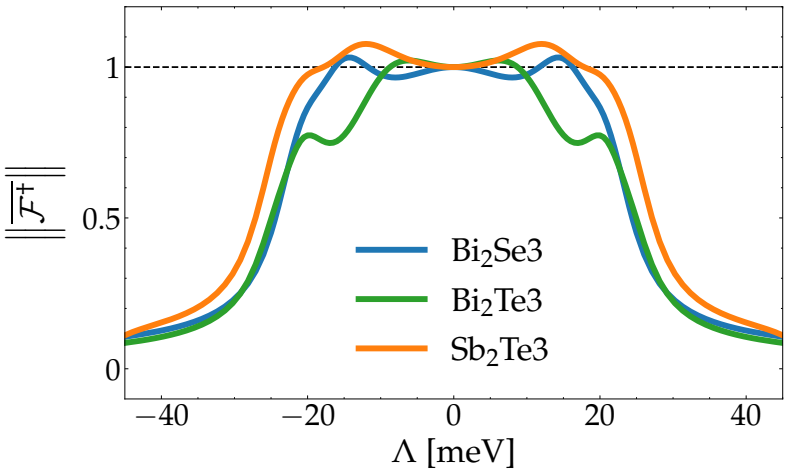

Figure 6.3: Dependence of the induced pairing amplitude at the $z = 0$ interface on the magnetization Λ for the three compounds of the Bi_2Se_3 family. The curves are obtained by taking the angular average of the Frobenius norm of the anomalous Green's function evaluated at the Fermi momentum k_F, as defined in Equation (6.6), and are normalized to their value at $\Lambda = 0$. The film thickness and all the Hamiltonian parameters are chosen consistently with those used in Figure 6.2.

The figure illustrates how the induced superconducting correlations evolve with increasing the exchange field. For a weak magnetization, $|\Lambda| \lesssim 20$ meV, the total induced pairing remains qualitatively unchanged. For larger exchange fields, however, the superconducting amplitude is progressively suppressed and eventually vanishes. In particular, for the selected values of C_0, an exchange field of $\Lambda \approx 25$ meV opens a magnetic gap at $\bar{\Gamma}$ large enough to eliminate the zero-energy electronic states in the MTI film, thereby suppressing the proximity effect. This result demonstrates that induced superconductivity can coexist with the magnetization of the topological insulator, provided that low-energy states remain available for the proximity effect.

6.1.1 Decay Length

An explicit expression for the decay length of the anomalous Green's function into the bulk of the MTI thin film can be derived at the $\overline{\Gamma}$ point using the analytical solution. According to Equation (6.2), the real-space dependence of the induced correlations is entirely governed by the unperturbed normal MTI propagators, whose

matrix elements in the analytical limit decay exponentially from the interface as

$$g_{\sigma\tau,\sigma\tau'}(0,z) \propto \mathrm{e}^{-\lambda_\sigma z}\,, \tag{6.7}$$

as derived in Equation (5.90). Here, λ_σ denotes the real part of the coefficients introduced in Equation (5.86), which physically capture the characteristic decay length of the surface states localized near the $z = 0$ interface. In the limit of vanishing excitation energy and weak magnetization $\Lambda \ll M_0$, the characteristic lengths $\lambda_\uparrow$ and $\lambda_\downarrow$ become degenerate and reduce to the approximation $\lambda \approx A_1/2B_1$ given in Equation (5.85). Evaluating the matrix product in Equation (6.2), the exponential factors $\mathrm{e}^{-\lambda_\sigma z}$ that describe electron and hole propagating toward the interface can be factorized. As a result, the spatial profile of the anomalous Green's function at the $\overline{\Gamma}$ point is governed by an overall exponential modulation $\mathrm{e}^{-z/\xi_{\mathrm{ind}}}$, with a characteristic decay length [153]

$$\xi_{\mathrm{ind}} = \frac{1}{\lambda_\uparrow + \lambda_\downarrow}\,. \tag{6.8}$$

The decay length ξ_{ind} of the superconducting correlations is shown in Figure 6.4 as a function of the Zeeman field for the compounds of the Bi_2Se_3 family, evaluated in the analytically tractable limit of $k_x = k_y = 0$ and small magnetization. The figure illustrates that the induced decay length ξ_{ind} depends only weakly on the magnetization of the proximitized MTI thin film, with variations of at most about 2% over the range of Zeeman field considered. This demonstrates that the spatial extent of the induced superconducting correlations is largely insensitive to Λ.

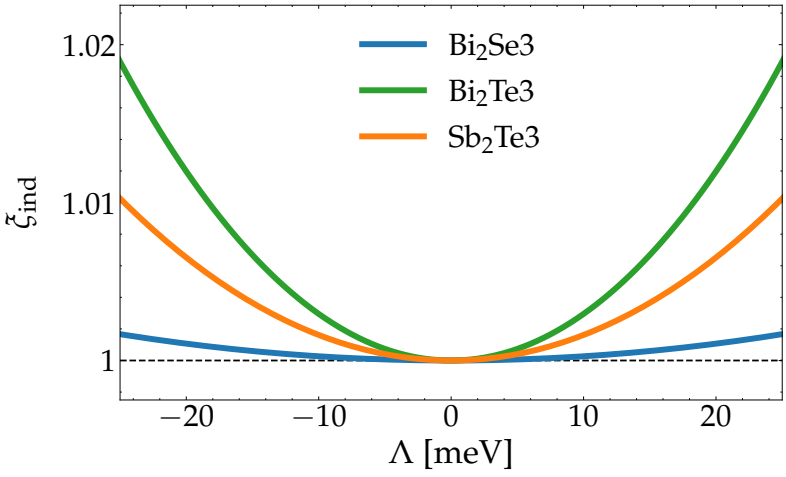

Figure 6.4: Dependence of the decay length defined in Equation (6.8) on the magnetization Λ for the three compounds of the Bi_2Se_3 family. The decay length is obtained in the analytically tractable limit by evaluating λ_σ from Equations (5.85) and (5.86) and is normalized to its value at $\Lambda = 0$. All parameters are chosen consistently with those used in Figure 6.2.

6.2 Spin Symmetry

To analyze the influence of magnetization on the superconducting order parameter, we examine the symmetry properties of the induced correlations in spin and momentum space. The anomalous Green's function is constrained by the Pauli exclusion principle, which enforces antisymmetry under the exchange of the two electrons [89, 144, 146]:

$$\mathcal{F}^{\dagger}_{\alpha\beta}(k_x, k_y; z, z'; \omega) = -\mathcal{F}^{\dagger}_{\beta\alpha}(-k_x, -k_y; z', z; -\omega)\,. \tag{6.9}$$

At the Fermi level $\omega = 0$, the propagator must be *odd* under the exchange of at least one set of quantum numbers: spin, momentum, or orbital. Since the orbital degree of freedom is not directly accessible in experiments, our analysis focuses only on the symmetry structure of the pairing in spin and momentum space.

To systematically classify the different pairing channels, it is convenient to expand the anomalous propagator $\mathcal{F}^{\dagger}(k_{\parallel}, z)$ over a complete basis $\{B_a\}$ of 16 orthonormal matrices that span the entire 4×4 space. With respect to the Hilbert–Schmidt inner product [152, 155]

$$\langle A, B \rangle = \mathrm{Tr}\,\left(A^{\dagger} B\right)\,, \tag{6.10}$$

orthonormality is defined as

$$\langle B_\alpha, B_\beta \rangle = \mathrm{Tr}\,\left(B^{\dagger}_{\alpha} B_\beta\right) = \delta_{\alpha\beta}\,. \tag{6.11}$$

Any 4×4 matrix M acting in this space can then be written as a linear combination of the basis elements as [152, 155]

$$M = \sum_a f_a\, B_a\,, \tag{6.12}$$

where the coefficients

$$f_a = \mathrm{Tr}\,\left(B^{\dagger}_{a} M\right) \tag{6.13}$$

quantify the weight of the matrix M in the channel a.

A convenient orthonormal basis for the space spanned by spin and orbital degrees of freedom is provided by the tensor products

$$\left\{ \frac{1}{2}\,\sigma_\mu \otimes \tau_\eta \;\middle|\; \mu, \eta \in \{0, x, y, z\} \right\}, \tag{6.14}$$

where σ_μ denote the Pauli matrices acting in spin space, and τ_η denote the Pauli matrices acting in orbital space, both including the identity. This set of 16 matrices forms a complete basis of the 4×4 space, allowing one to expand

$$\mathcal{F}^{\dagger}(k_{\parallel}; z) = \sum_{\mu,\eta} f_{\mu\eta}(k_{\parallel}, z)\; \sigma_\mu \otimes \tau_\eta\,, \tag{6.15}$$

where the complex coefficients $f_{\mu\eta}(k_{\parallel}, z)$ encode the entire spin–orbital structure of the anomalous Green's function.

In principle, one could analyze the full symmetry of the anomalous propagator by decomposing it into all 16 spin–orbital channels $\{\sigma_\mu \otimes \tau_\eta\}$. However, since the orbital degrees of freedom cannot be resolved experimentally, we restrict our analysis to the spin structure only. Accordingly, we regard the anomalous propagator $\mathcal{F}^{\dagger}(k_{\parallel}, z)$ as

a 2×2 matrix in spin space, where each entry is itself a 2×2 block in orbital space. The Green's function can then be decomposed in the spin basis alone as

$$\mathcal{F}^\dagger(k_\parallel, z) = \frac{1}{\sqrt{2}} \sum_\mu \sigma_\mu \otimes f_\mu(k_\parallel, z)\,, \tag{6.16}$$

where the prefactor $1/\sqrt{2}$ arises from the normalization of the Pauli basis, and the projection onto the spin channels is obtained by tracing over the spin indices only

$$f_\mu(k_\parallel, z) = \mathrm{Tr}_{\mathrm{spin}}\Big[\left(\sigma_\mu^\dagger \otimes \tau_0\right) \mathcal{F}^\dagger(k_\parallel, z)\Big]\,. \tag{6.17}$$

The coefficients of the expansion $f_\mu(k_\parallel, z)$ are 2×2 matrices in orbital space and encode the orbital structure of the pairing within each spin channel.

6.2.1 Singlet and Triplet Decomposition

The Pauli basis σ_μ naturally distinguishes between the antisymmetric and symmetric components of the spin structure: the spin-singlet contribution is associated with the antisymmetric matrix $\sigma_y^T = -\sigma_y$, while the symmetric spin-triplet contributions are spanned by the symmetric matrices σ_0, σ_x, and σ_z. However, to recover the standard singlet–triplet decomposition and make explicit the physical correspondence with the spin projection S_z, it is convenient to introduce the orthonormal basis

$$s_{\mathrm{s}} = \tfrac{\mathrm{i}}{\sqrt{2}}\sigma_y\,, \qquad s_{\mathrm{t}}^{(0)} = \tfrac{1}{\sqrt{2}}\sigma_x\,, \qquad s_{\mathrm{t}}^{(+1)} = \tfrac{1}{2}\left(\sigma_0 + \sigma_z\right)\,, \qquad s_{\mathrm{t}}^{(-1)} = \tfrac{1}{2}\left(\sigma_0 - \sigma_z\right)\,, \tag{6.18}$$

where s_{s} projects onto the spin-singlet channel, while $s_{\mathrm{t}}^{(0)}$ and $s_{\mathrm{t}}^{(\pm1)}$ select the three spin-triplet components with $S_z = 0, \pm 1$, respectively. In terms of this basis, the anomalous Green's function can be expanded as

$$\mathcal{F}^\dagger(k_\parallel, z) = s_{\mathrm{s}} \otimes f_{\mathrm{s}}(k_\parallel, z) \;+ \sum_{S_z=0,\pm1} s_{\mathrm{t}}^{(S_z)} \otimes f_{\mathrm{t}}^{(S_z)}(k_\parallel, z)\,, \tag{6.19}$$

with f_{s} and $f_{\mathrm{t}}^{(S_z)}$ obtained from Equation (6.17), replacing the Pauli matrices with the basis defined in Equation (6.18).

By writing explicitly the anomalous propagator in the spin basis $\{|\uparrow\rangle, |\downarrow\rangle\}$,

$$\mathcal{F}^\dagger = \begin{bmatrix} \mathcal{F}^\dagger_{\uparrow\uparrow} & \mathcal{F}^\dagger_{\uparrow\downarrow} \\ \mathcal{F}^\dagger_{\downarrow\uparrow} & \mathcal{F}^\dagger_{\downarrow\downarrow} \end{bmatrix}\,, \tag{6.20}$$

one verifies that the coefficients in Equation (6.19) reduce to the standard singlet and triplet combinations [156–158]. The singlet component, associated with s_{s}, is given by [153]

$$f_{\mathrm{s}} = \frac{1}{\sqrt{2}}\left(\mathcal{F}^\dagger_{\uparrow\downarrow} - \mathcal{F}^\dagger_{\downarrow\uparrow}\right)\,, \tag{6.21}$$

while the triplet components, associated with $s_{\mathrm{t}}^{(S_z)}$, are [153]

$$f_{\mathrm{t}}^{(0)} = \frac{1}{\sqrt{2}}\left(\mathcal{F}^\dagger_{\uparrow\downarrow} + \mathcal{F}^\dagger_{\downarrow\uparrow}\right), \qquad f_{\mathrm{t}}^{(+1)} = \mathcal{F}^\dagger_{\uparrow\uparrow}, \qquad f_{\mathrm{t}}^{(-1)} = \mathcal{F}^\dagger_{\downarrow\downarrow}. \tag{6.22}$$

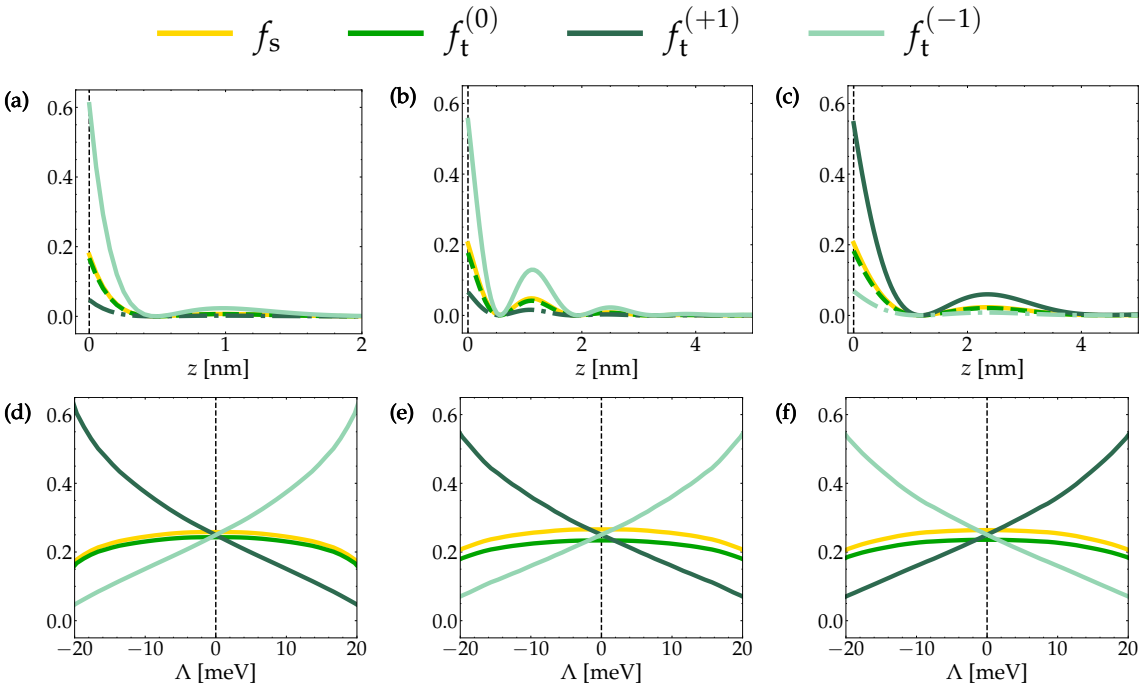

Figure 6.5: Magnitude of the spin-singlet and spin-triplet components as functions of the real-space coordinate z and the magnetization Λ for the compounds of the Bi_2Se_3 family. The plots are obtained by taking the Frobenius norm of Equations (6.21) and (6.22) and averaging over the two-dimensional BZ. Panels (a,d) correspond to Bi_2Se_3, panels (b,e) to Bi_2Te_3, and panels (c,f) to Sb_2Te_3. In the first row, each component is evaluated at $\Lambda = 20$ meV, with their sum normalized to unity at the interface $z = 0$. In the second row, the components are evaluated at $z = 0$, and their sum is normalized to unity for any Λ. All parameters are chosen consistently with those used in Figure 6.1.

The magnitude of the spin-singlet and spin-triplet components defined in Equations (6.21) and (6.22) and averaged over the two-dimensional BZ, is shown in Figure 6.5 for the different materials of the Bi_2Se_3 family.

Panels (a–c) show the spatial profiles of the spin components as a function of the distance from the MTI–SC interface at $z = 0$. For each material under consideration, all spin components share the same spatial dependence, corresponding to the modulated exponential decay of the induced pairing, and differ only by their overall weight. Panels (d–f) illustrate the influence of magnetization on the superconducting correlations evaluated at the interface $z = 0$. As discussed in Section 1.2, the Zeeman field breaks time-reversal symmetry, opening a gap in the Dirac cones and polarizing the surface states near the $\overline{\Gamma}$ point [37–39]. The spin structure of the proximity-induced pairing reflects this behavior. Although the total weight of singlet and triplet channels remains mainly unaffected by the breaking of time-reversal symmetry, the relative weights of the individual triplet components follow the changes in the underlying band structure. In particular, the induced pairing acquires a predominantly spin-polarized character, with the $S_z = \pm 1$ triplet channels becoming dominant, according to the polarization of the proximitized surface states

(see Figure 6.1).

It is worth noting that, even in the absence of magnetization ($\Lambda = 0$), the anomalous Green's function contains both spin-singlet and spin-triplet components. In a bulk SC, the anomalous Green's function is even under both frequency and momentum inversion, and the antisymmetry condition of Equation (6.9) is satisfied entirely in the spin sector, meaning that only the singlet channel is nonvanishing [144, 156, 158]. In contrast, for a thin film of topological insulator, spin–orbit coupling breaks the spin-rotational symmetry, and translational invariance is lost along the out-of-plane direction z. As a consequence, spin and parity cease to be good quantum numbers, and the single-particle eigenstates become mixed. Upon introducing a superconducting pairing, this mixing gives rise to a coexistence of even- and odd-parity channels, as well as singlet and triplet components with equal weights [156, 159, 160]. The presence of magnetization lifts the balance between spin components with different S_z projections: since the proximitized surface states become spin-polarized, the weight of the corresponding $\mathcal{F}_{\uparrow\uparrow}$ and $\mathcal{F}_{\downarrow\downarrow}$ channels is enhanced.

6.3 Momentum Symmetry

To analyze the symmetry properties of the induced pairing in momentum space, we decompose the anomalous MTI Green's function $\mathcal{F}^\dagger(k_\parallel, z)$ into its symmetric and antisymmetric components under the inversion of the in-plane momentum:

$$\begin{aligned} \mathcal{F}^\dagger_{\text{odd}}(k_\parallel, z) &= \frac{1}{2}\Big[\mathcal{F}^\dagger(k_\parallel, z) - \mathcal{F}^\dagger(-k_\parallel, z)\Big], \\ \mathcal{F}^\dagger_{\text{even}}(k_\parallel, z) &= \frac{1}{2}\Big[\mathcal{F}^\dagger(k_\parallel, z) + \mathcal{F}^\dagger(-k_\parallel, z)\Big]. \end{aligned} \tag{6.23}$$

This decomposition reflects the spatial parity of the superconducting order parameter in the x–y plane: inversion in momentum space corresponds, via Fourier transform, to inversion in real space. Therefore, the symmetric component corresponds to even-parity pairing, such as s-wave or d-wave, while the antisymmetric component is related to odd-parity terms, such as p-wave or f-wave [88, 156, 158]. The magnitude of the even- and odd-parity components, averaged over the two-dimensional BZ, is shown in Figure 6.6 for the different materials of the Bi_2Se_3 family.

Panels (a–c) show the spatial profiles of the momentum components away from the MTI–SC interface at $z = 0$. As in the spin-resolved case, their spatial dependence simply follows the exponential decay of the induced pairing, with even- and odd-parity components sharing the same profile up to an overall constant. Panels (d–f) illustrate the role of magnetization: in the absence of a Zeeman field ($\Lambda = 0$), the averaged magnitude of even- and odd-parity components is the same, whereas a finite magnetization ($\Lambda \neq 0$) breaks this balance and enhances the weight of the unconventional antisymmetric terms, which at lowest order correspond to p- and f-wave symmetries [156, 159, 160].

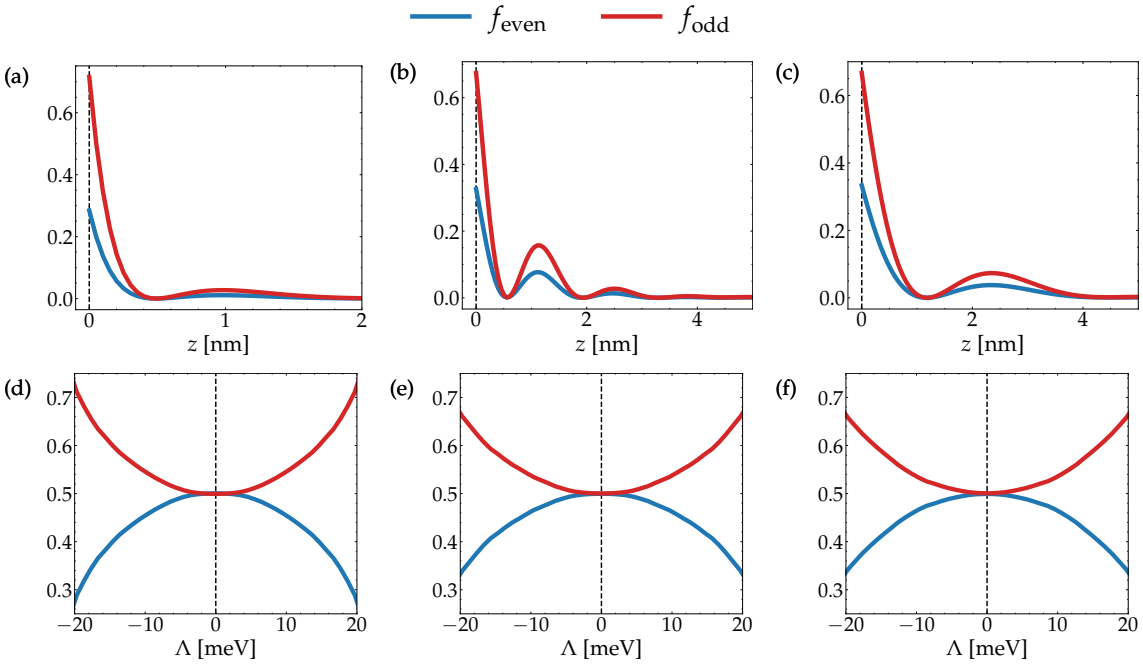

Figure 6.6: Magnitude of the even and odd components in momentum space as functions of the real-space coordinate z and the magnetization Λ for the compounds of the Bi_2Se_3 family. The plots are obtained by taking the Frobenius norm of Equation (6.23) and averaging over the two-dimensional BZ. Panels (a,d) correspond to Bi_2Se_3, panels (b,e) to Bi_2Te_3, and panels (c,f) to Sb_2Te_3. In the first row, each component is evaluated at $\Lambda = 20$ meV, with their sum normalized to unity at the interface $z = 0$. In the second row, the components are evaluated at $z = 0$, and their sum is normalized to unity for any Λ. All parameters are chosen consistently with those used in Figure 6.1.

6.3.1 Circular Harmonics

The above decomposition illustrates how the symmetric and antisymmetric momentum components of the induced superconducting order parameter are affected by the magnetization in thin films of MTI materials of the Bi_2Se_3 family. A more systematic analysis can be carried out by expanding the momentum-dependent pairing in circular harmonics [158, 161, 162], which form a complete basis for integrable functions defined over the two-dimensional BZ. In practice, this involves first separating the different components $f_{\mu\eta}(k_\parallel, z)$ according to the spin–orbital decomposition provided in Equation (6.15), and then classifying each channel by its momentum symmetry.

Using polar coordinates, the coefficient quantifying the weight of the anomalous Green's function in each channel can be expressed as $f_{\mu\eta}(k_\parallel, z) = f_{\mu\eta}(k, \theta, z)$, where $k = |k_\parallel|$ denotes the modulus of the in-plane momentum and $\theta = \arctan(k_x/k_y)$ its polar angle. Any square-integrable function $f_{\mu\eta}(k, \theta, z)$ can then be expanded in terms of circular harmonics as [153, 161, 162]

$$f_{\mu\eta}(k, \theta, z) = \sum_{m=-\infty}^{+\infty} \alpha_m^{(\mu\eta)}(k, z)\, \mathrm{e}^{\mathrm{i}m\theta}\,, \tag{6.24}$$

where

$$\alpha_m^{(\mu\eta)}(k,z) = \frac{1}{2\pi}\int_0^{2\pi} \mathrm{d}\theta\, f_{\mu\eta}(k,\theta,z)\,\mathrm{e}^{-\mathrm{i}m\theta}\,, \tag{6.25}$$

specifies the weight of the m-th angular component of the pairing in the selected spin–orbital channel, and $m \in \mathbb{Z}$ labels the out-of-plane angular momentum. The physical meaning of these circular harmonics can be understood by noting that, in a translationally invariant two-dimensional system, the out-of-plane angular momentum operator is defined as [146]

$$\hat{L}_z = -\mathrm{i}\frac{\partial}{\partial\theta}\,, \tag{6.26}$$

and its action on the circular harmonics is given by

$$\hat{L}_z\left[\alpha_m(k,z)\mathrm{e}^{\mathrm{i}m\theta}\right] = m\,\alpha_m(k,z)\mathrm{e}^{\mathrm{i}m\theta}\,, \tag{6.27}$$

meaning that $\alpha_m(k,z)\,\mathrm{e}^{\mathrm{i}m\theta}$ is an eigenstate of $\hat{L}_z$ with eigenvalue m.

Upon Fourier transforming the circular harmonics $g_m(k,\theta,z) \equiv \alpha_m(k,z)\,\mathrm{e}^{\mathrm{i}m\theta}$ to real space, the out-of-plane angular momentum m is conserved. Using polar coordinates in both momentum and real space, the Fourier transform reads

$$\tilde{g}_m(r,\phi,z) = \int_0^\infty k\,\mathrm{d}k\,\alpha_m(k,z)\int_0^{2\pi}\mathrm{d}\theta\,\mathrm{e}^{\mathrm{i}m\theta}\mathrm{e}^{\mathrm{i}kr\cos(\theta-\phi)}\,. \tag{6.28}$$

Expanding the complex exponential with the Jacobi–Anger identity and performing the angular integral yields [161, 163]

$$\tilde{g}_m(r,\phi,z) = \tilde{\alpha}_m(r,z)\,\mathrm{e}^{\mathrm{i}m\phi}\,, \tag{6.29}$$

with the radial part being

$$\tilde{\alpha}_m(r,z) = 2\pi(-\mathrm{i})^m\int_0^\infty k\,\mathrm{d}k\,\alpha_m(k,z)J_{-m}(kr)\,, \tag{6.30}$$

where J_m is the m-th Bessel function of the first kind. Equation (6.29) shows that the out-of-plane angular momentum m is conserved in real space.

The physical meaning of the circular harmonics, and their usefulness for classifying the pairing symmetry, follows from their rotational properties. Under a rotation $\theta \to \theta + \varphi$, the real-space harmonics transform as

$$\tilde{\alpha}_m(r,z)\,\mathrm{e}^{\mathrm{i}m\theta} \;\longrightarrow\; \tilde{\alpha}_m(r,z)\,\mathrm{e}^{\mathrm{i}m(\theta+\varphi)} = \tilde{\alpha}_m(r,z)\,\mathrm{e}^{\mathrm{i}m\phi}\,\mathrm{e}^{\mathrm{i}m\theta}\,, \tag{6.31}$$

acquiring a phase factor $\mathrm{e}^{\mathrm{i}m\varphi}$ determined by the angular momentum m. In other words, for any $m \neq 0$, the circular harmonics change sign under a rotation of angle π/m, giving rise to characteristic nodal structures. These rotational properties are connected to the conventional classification of superconducting pairing: $m = 0$ corresponds to the fully isotropic s-wave, $|m| = 1$ to the twofold p-wave, $|m| = 2$ to the fourfold d-wave, $|m| = 3$ to the sixfold f-wave, and so on [88, 156, 158]. Illustrative examples of two-dimensional functions constructed from the lowest harmonics are displayed in Figure 6.7.

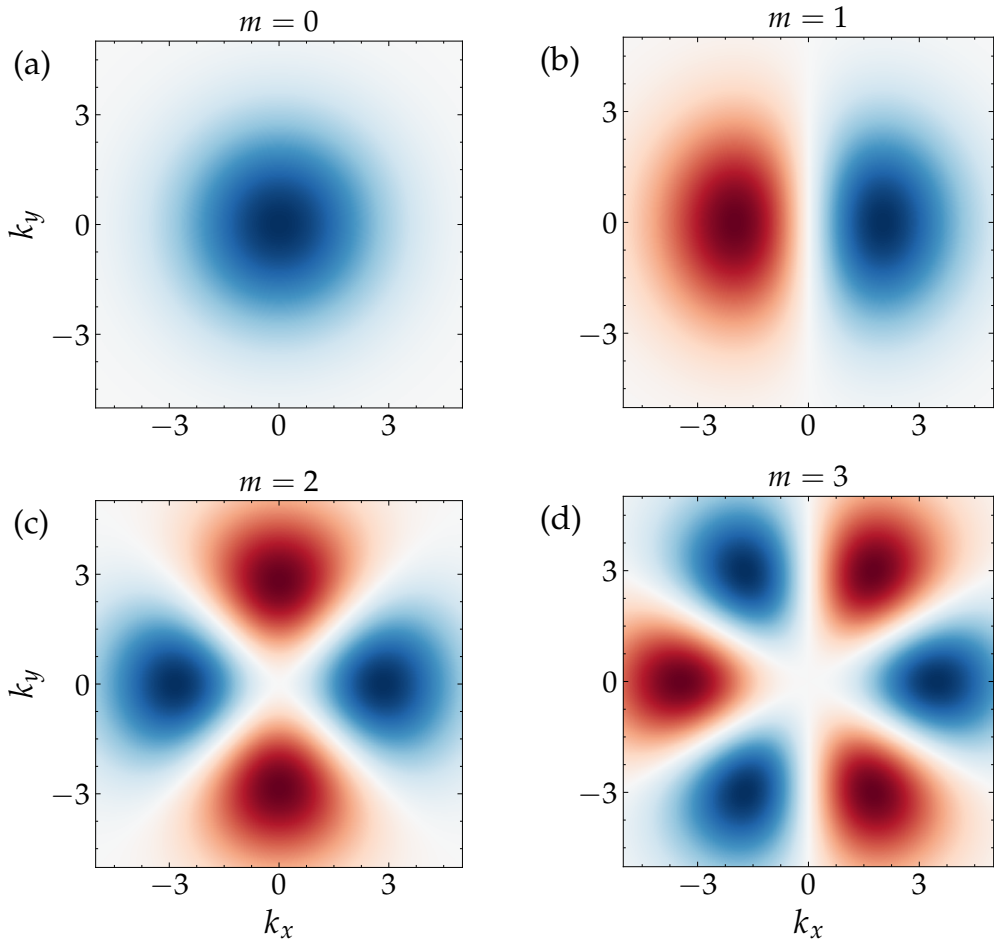

Figure 6.7: Illustrative examples of two-dimensional functions in momentum space with different angular symmetries, constructed from the lowest circular harmonics. Panel (a) shows the isotropic $m = 0$ component, while panels (b,c,d) correspond to $m = 1, 2, 3$, respectively. The radial dependence is modeled as the convolution of a Gaussian centered at $k = 0$ with the monomial $k^{|m|}$. Red (blue) regions indicate the positive (negative) lobes of the functions, normalized to the range $[-1, 1]$. In all cases only the real part is shown.

In the following, we exploit the expansion in circular harmonics to distinguish explicitly the different angular momentum components of the anomalous Green's function and to quantify how their relative weights depend on the magnetization of the MTI. Since momentum symmetry is well defined only within each pairing channel, we introduce an overall weight proceeding as follows. First, we expand each channel in the basis of circular harmonics, and extract the coefficients $\alpha_m^{(\mu\eta)}(k, z)$ according to Equation (6.25). We then average over the radial component k of the in-plane momentum by evaluating the integral

$$w_m^{(\mu\eta)}(z) = \int k \, \mathrm{d}k \left| \alpha_m^{(\mu\eta)}(k, z) \right|^2 , \tag{6.32}$$

where $w_m^{(\mu\eta)}(z)$ denotes the weight of the harmonic with angular momentum m in the μ, η channel. Finally, the total weight of the m-th component is obtained by

summing over all pairing channels [153]

$$w_m(z) = \sum_{\mu,\eta} w_m^{(\mu\eta)}(z)\,. \tag{6.33}$$

The weights obtained from the decomposition of the anomalous Green's function are shown in Figure 6.8 for the lowest angular momentum harmonics, $m = 0$ and $m = \pm 1$. The higher-order components are not displayed, as their overall weight is negligible.

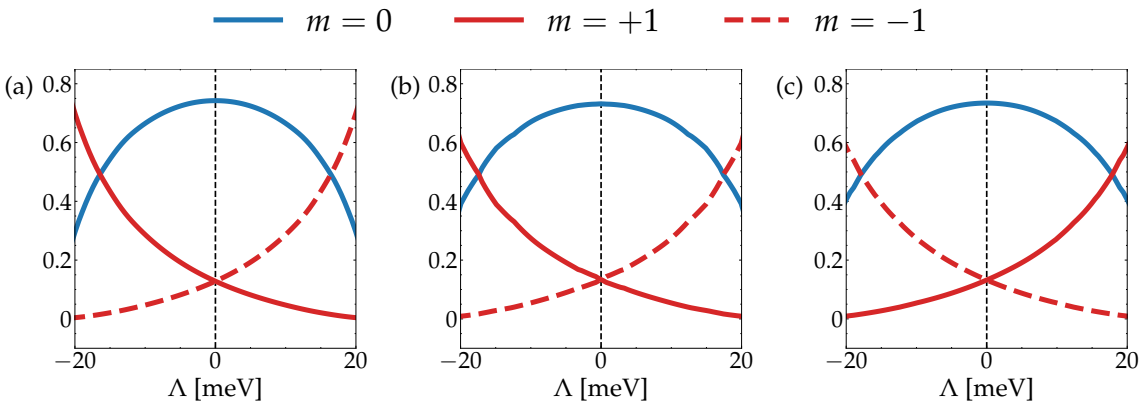

Figure 6.8: Relative weights of the circular-harmonic components of the induced pairing amplitude as a function of the magnetization Λ for (a) Bi_2Se_3, (b) Bi_2Te_3, and (c) Sb_2Te_3. The weights are evaluated at the interface $z = 0$ using Equation (6.33), and they are normalized such that the sum of the components with $|m| \leq 3$ equals unity. All parameters are chosen consistently with those used in Figure 6.1.

Consistent with the magnetic profile of the even- and odd-momentum components, the symmetric $m = 0$ term is maximal at $\Lambda = 0$ and decreases with increasing the Zeeman field. In contrast, the antisymmetric components vary monotonically with Λ, with the $m = 1$ ($m = -1$) contribution maximized when the proximitized states exhibit a net spin-up (spin-down) polarization (see Figure 6.1). It is worth stressing that, although the two analyses are in qualitative agreement, the relative weight of the symmetric s-wave term ($m = 0$) and of the combined p-wave components ($m = \pm 1$) does not match exactly the average magnitude of the even- and odd-parity contributions shown in Figure 6.6. This discrepancy can be mainly attributed to two factors. First, the expansion in Equation (6.24) is truncated to the lowest out-of-plane angular momenta $|m| \leq 3$. Second, the definition of the overall weights w_m is not strictly equivalent to the norm of the even and odd components averaged over the BZ. However, the qualitative behavior remains the same: finite magnetization suppresses the isotropic $m = 0$ component, while enhancing either the $m = 1$ or $m = -1$ channel, depending on the spin polarization of the proximitized surface states [156, 159, 160].

The results discussed above were obtained in the canonical basis of Equation (1.35), where the spin is quantized along the out–of–plane $\hat{z}$ axis. To facilitate a direct comparison with previous analyses of proximity–induced superconductivity in non–magnetic topological insulators [164, 165], it is instructive to express the

anomalous Green's function in a basis that captures the helical nature of the surface states. For each orbital sector τ, we therefore introduce the spin–helical basis [153]

$$\frac{1}{\sqrt{2}}\Big(|\uparrow\,\tau\rangle \pm \mathrm{e}^{\mathrm{i}\theta}\,|\downarrow\,\tau\rangle\Big)\,. \tag{6.34}$$

In the time–reversal–invariant limit $\Lambda = 0$, these states exhibit a perfect in-plane helical spin texture, having expectation values

$$\langle\boldsymbol{\sigma}\rangle = \left(\pm\frac{k_x}{k},\ \pm\frac{k_y}{k},\ 0\right)\,, \tag{6.35}$$

which coincide with the characteristic spin–momentum–locked texture of the topological surface states. This correspondence makes the basis of Equation (6.34) particularly well suited for analyzing the induced pairing in the Dirac spectrum of the MTI thin film, where the in–plane spin texture matches that of the helical eigenstates [24, 30]. Within this representation, the BdG Hamiltonian for the proximitized surface states of a non–magnetic TI assumes the block–diagonal structure characteristic of a helical superconductor, with two decoupled subsectors that effectively realize $p + \mathrm{i}p$ pairing structures of opposite chirality [164, 165]. The evolution of the induced correlations in the helical basis of Equation (6.34) is illustrated in Fig. 6.9, displaying the relative weights of the lowest angular–momentum components of the anomalous propagator as functions of the magnetization of the MTI film.

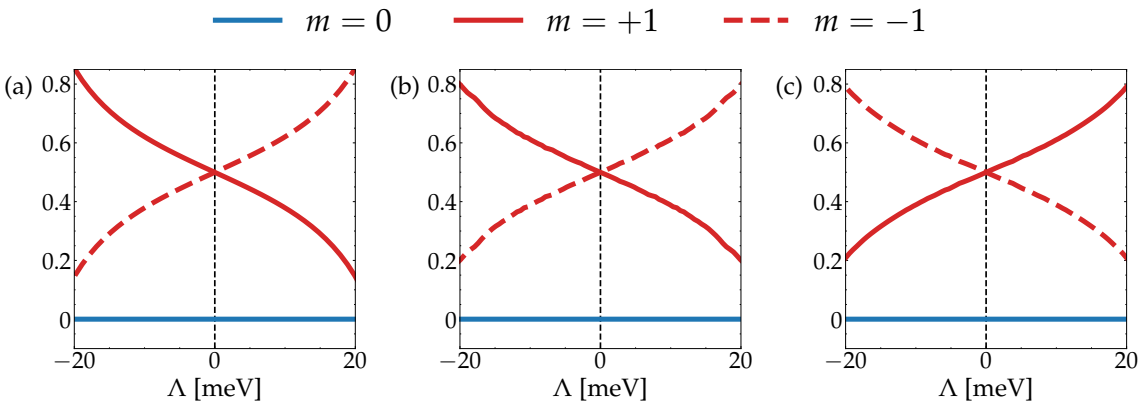

Figure 6.9: Relative weights of the circular–harmonic components of the induced pairing amplitude, evaluated in the helical basis defined in Equation (6.34), and plotted as functions of the magnetization Λ for (a) Bi_2Se_3, (b) Bi_2Te_3, and (c) Sb_2Te_3. The weights are evaluated at the interface $z = 0$ using Equation (6.33), and they are normalized such that the sum of the components with $|m| \leq 3$ equals unity. All parameters are chosen consistently with those used in Figure 6.1.

In the spin–helical representation of Equation (6.34), the s-wave component of the induced pairing with $m = 0$ remains negligible for all magnetizations when the proximity effect acts within the Dirac surface spectrum. In the time–reversal–invariant limit ($\Lambda = 0$), the angular–momentum components with $m = +1$ and $m = -1$ exhibit identical weights, indicating that the induced pairing decomposes into two subsectors of opposite chirality. Taken together, these two subsectors form

a helical superconducting phase [28, 30, 164, 165]. A finite magnetization breaks the balance between the two chiral sectors and selects a preferred chirality, enhancing the corresponding component of the induced pairing and yielding an order parameter dominated by either the $m = +1$ or the $m = -1$ harmonic [157, 166].

It is worth noting that the shape of the induced superconducting pairing in the BZ is directly linked to the spin polarization of the proximitized surface states. According to the spectra shown in Figure 6.1, a spin-up (spin-down) polarization corresponds to an $m = +1$ ($m = -1$) phase dependence. We emphasize, however, that the detailed phase structure of the order parameter depends on the chosen representation of the Hilbert space, and generally changes when evaluated in a momentum–dependent basis. For superconductivity induced in Dirac surface states, our findings remain fully consistent with previous analyses [164, 165].

6.3.2 Topological Implications

The expansion in circular harmonics discussed above not only classifies explicitly the symmetry of the induced pairing in momentum space but also establishes a direct connection to the topology of the effective two-dimensional superconducting system. Indeed, the integer index m specifies the out-of-plane angular momentum associated with the in-plane rotation of the induced Cooper pairs, and determines the nodal structure of the pairing function in both momentum and real space. At the same time, it reflects the Chern number of the BdG Hamiltonian, carrying the relevant information for the topological classification of the two-dimensional superconducting phase [167–170].

To illustrate this connection, let us consider the simple case of a spinless two-dimensional superconductor described by the BdG Hamiltonian (see Equation (2.3))

$$h_{\mathrm{BdG}}(\mathbf{k}) = \begin{pmatrix} \varepsilon_{\mathbf{k}} & \Delta_{\mathbf{k}} \\ \Delta_{\mathbf{k}}^{*} & -\varepsilon_{\mathbf{k}} \end{pmatrix} , \tag{6.36}$$

with quasiparticle spectrum

$$E_{\mathbf{k}} = \pm\sqrt{\varepsilon_{\mathbf{k}}^{2} + |\Delta_{\mathbf{k}}|^{2}} , \tag{6.37}$$

where $\mathbf{k} \equiv (k_x, k_y)$ is the two-dimensional momentum, $\varepsilon_{\mathbf{k}}$ denotes the single-particle parabolic dispersion in $\mathbf{k}$ and $\Delta_{\mathbf{k}} \equiv |\Delta_{\mathbf{k}}|\, \mathrm{e}^{\mathrm{i}\theta_{\mathbf{k}}}$ is the superconducting pairing. At the Fermi surface, the energy gap is controlled by the modulus of the order parameter, $E_{\mathrm{gap}} = 2|\Delta_{\mathbf{k}}|$, while its phase $\theta_{\mathbf{k}}$ carries the topological information, determining how the superconducting order parameter winds in real and momentum space.

The relation between the phase of the pairing and the topology of the superconducting band structure can be made explicit by computing the Chern invariant of the system. The eigenstates of the Hamiltonian in Equation (6.36) are given by

$$u_{\mathbf{k}}^{(\pm)} = \tfrac{1}{\sqrt{2}} \begin{pmatrix} \pm\, \mathrm{e}^{\mathrm{i}\theta_{\mathbf{k}}} & 1 \end{pmatrix}^{T} , \tag{6.38}$$

with the minus (plus) sign denoting the negative (positive) energy branch of the Bogoliubov spectrum. For the lowest state, the Berry connection defined in Equation (1.17) reads

$$\mathcal{A}(\mathbf{k}) = \mathrm{i}\, \langle u_{\mathbf{k}}^{(-)} | \nabla_{\mathbf{k}} u_{\mathbf{k}}^{(-)} \rangle = -\tfrac{1}{2} \nabla_{\mathbf{k}} \theta_{\mathbf{k}} \, . \tag{6.39}$$

The associated Berry phase accumulated by adiabatic transport along a closed loop on the Fermi surface is

$$\gamma = \oint_{\mathrm{FS}} \mathcal{A}(\mathbf{k}) \cdot \mathrm{d}\mathbf{k} = -\tfrac{1}{2} \oint_{\mathrm{FS}} \nabla_{\mathbf{k}} \theta_{\mathbf{k}} \cdot \mathrm{d}\mathbf{k} = -\pi n \,, \tag{6.40}$$

where FS denotes the one-dimensional Fermi contour in the two-dimensional Brillouin zone. To preserve the single-valuedness of the order parameter, the variation of the phase along a closed loop is restricted to multiples of 2π: the integer n thus quantifies the winding of the superconducting phase $\theta_{\mathbf{k}}$ around the Fermi surface. Recalling Equation (1.20), the BdG Chern number can be computed as [169, 170]

$$\mathcal{N} = \frac{1}{2\pi} \oint_{\mathrm{FS}} \mathcal{A}(\mathbf{k}) \cdot \mathrm{d}\mathbf{k} = -\tfrac{1}{2} n \,, \tag{6.41}$$

which makes explicit the correspondence between the winding number n of the superconducting phase $\theta_{\mathbf{k}}$ and the BdG topological invariant $\mathcal{N}$. The prefactor $\frac{1}{2}$ arises from the unphysical nature of the spinless model, and the correct relation $\mathcal{N} = n$ is recovered once the electron spin is properly taken into account

It is now clear that Equation (6.41) establishes a direct correspondence between the symmetry of the pairing in momentum space and the topology of the superconducting band structure. Within the circular-harmonics expansion, the winding of the superconducting phase is set by the out-of-plane angular momentum: the order parameter changes sign upon a rotation of an angle π/m, resulting in m windings around the Fermi surface (see Figure 6.7). Consequently, the isotropic s-wave component with $m = 0$ corresponds to a topologically trivial superconducting phase with $\mathcal{N} = 0$. In contrast, the p-wave components with $m = \pm 1$ give rise to a chiral TSC characterized by $\mathcal{N} = \pm 1$, which supports Majorana modes along the edges. Higher-order harmonics with angular momentum $|m| > 1$ correspond to higher Chern-number states [169, 170].

We emphasize that the presence of nonvanishing pairing components with $m = \pm 1$ is not by itself sufficient to guarantee the emergence of a topologically nontrivial phase. Within the decomposition in circular harmonics introduced in Equation (6.24), the induced pairing $\Delta_{\mathbf{k}}^{(m)}$ in channel m exhibits the characteristic dependence $\mathrm{e}^{\mathrm{i}m\theta}$. Using polar coordinates $k_x = k\cos\theta$ and $k_y = k\sin\theta$, one finds

$$\Delta_{\mathbf{k}}^{(m)} = |\Delta_{\mathbf{k}}^{(m)}|\, e^{im\theta} \propto \frac{1}{k^{|m|}} \left[k_x + \mathrm{i}\,\mathrm{sgn}(m)\, k_y\right]^{|m|} \,. \tag{6.42}$$

which for the first harmonics reduces to $\Delta_{\mathbf{k}}^{(\pm 1)} \propto k_x \pm \mathrm{i}k_y$. A linear combination of the two $m = \pm 1$ components yields

$$\Delta_{\mathbf{k}} \propto \alpha(k_x + \mathrm{i}k_y) + \beta(k_x - \mathrm{i}k_y) \,, \qquad \text{for} \quad \alpha, \beta \in \mathbb{C} \,, \tag{6.43}$$

so that the superconducting gap becomes proportional to

$$|\Delta_{\mathbf{k}}|^2 \propto |ak_x + bk_y|^2 = |a|^2 k_x^2 + |b|^2 k_y^2 + (ab^* + a^* b) k_x k_y \,, \tag{6.44}$$

where we identified $a \equiv \alpha + \beta$ and $b \equiv \mathrm{i}(\alpha - \beta)$. For $a, b \neq 0$, Equation (6.44) is nonvanishing everywhere except at $k_x = k_y = 0$, which does not belong to the

Fermi surface. However, if $a = 0$ or $b = 0$, the order parameter depends only on a single momentum component, and the superconducting state becomes gapless, with a nodal line along $k_y = 0$ or $k_x = 0$, respectively. The condition for realizing a fully gapped chiral TSC is therefore $\alpha \neq \pm\beta$, implying that the two angular momentum components with $m = \pm 1$ must enter the linear combination of Equation (6.43) with *different* weights.

This simplified picture illustrates how the topology of the proximitized MTI thin film can be inferred from the harmonic decomposition in Figure 6.8. For small Λ, the isotropic $m = 0$ component dominates, yielding a trivial s-wave state. For large positive magnetization ($\Lambda \gtrsim 15$ meV), one of the p-wave channels with $m = \pm 1$ prevails, determining the chirality and driving the system into a $\mathcal{N} = \pm 1$ topological phase. Conversely, for large negative magnetization ($\Lambda \lesssim -15$ meV), the opposite channel dominates, selecting the opposite chirality and leading to a $\mathcal{N} = \mp 1$ phase [41, 42, 100, 102]. We stress once more that the dominant $m = \pm 1$ component reflects the spin polarization of the proximitized states in the MTI thin film (see Figure 6.1). These results are in qualitative agreement with the discussion of the two-dimensional topological superconductor in Section 2.2.

Summary

In this chapter, we presented a detailed analysis of the superconducting proximity effect in thin films of magnetic topological insulators. Using the solutions for the unperturbed propagators of the decoupled materials derived in Chapter 5, we evaluated the perturbative correction to the anomalous Green's function in the MTI, and examined its spatial profile, together with its evolution under the Zeeman field. In the analytically tractable limit at the $\overline{\Gamma}$ point, and for surface states localized near the interface, we derived a closed-form expression for the decay length of the induced pairing, showing that it is mainly determined by the spatial localization of the proximitized surface states.

Building on this, we analyzed the spin structure of the induced pairing, distinguishing singlet and triplet contributions and determining their evolution under finite magnetization. The momentum dependence of the superconducting order parameter was characterized in a similar way, separating symmetric and antisymmetric components under in-plane momentum exchange. A more systematic classification of the momentum structure was obtained by projecting onto circular harmonics, identifying the dominant angular momentum channels and their evolution with the Zeeman field. Finally, we connected these symmetry analyses to the topology of the two-dimensional system, showing how the prevalence of $m = \pm 1$ components under strong magnetization drives the system into a chiral topological superconducting phase.

The results presented in this chapter complement the discussion on the topological properties of the proximitized MTI thin film developed in the first part of the thesis. There, the system was analyzed within a first-quantized framework, where the superconducting pairing was introduced as an input parameter in the effective BdG Hamiltonian, whose energy spectrum revealed the phase transitions and the emergence of topologically protected boundary modes. Here, by contrast, we em-

ployed a second-quantized formalism in which the superconducting order parameter is obtained explicitly from the anomalous Green's function, providing direct access to its spatial, spin, and momentum structure. Taken together, these complementary approaches highlight how the interplay between magnetism, topology, and superconductivity gives rise to rich physical phenomena, leading to the emergence of exotic states of matter whose unique properties hold promise for applications in quantum technologies.

Conclusions and Outlook

Main Results

In this thesis, we investigated the physics of proximitized MTIs of the Bi_2Se_3 family of compounds, focusing on their potential to host nontrivial superconducting phases and emergent Majorana excitations. The analysis of these hybrid systems was carried out along two parallel and complementary routes. From a first-quantized perspective, we modeled the proximity effect within the BdG framework, where the induced pairing is introduced as an input parameter of the effective Hamiltonian. Within this approach, we examined how the topological properties of these materials depend on magnetization and pairing amplitude in confined geometries, and we studied electronic transport in double normal–superconductor junctions made of MTI thin films with a proximitized central region. From a second-quantized perspective, we employed a perturbative approach to describe the induced superconductivity, explicitly accounting for electron tunneling between the SC and the surface states of the topological insulating thin film. By deriving the full structure of the induced anomalous Green's function in real space, spin, and momentum, we characterized its symmetry properties and connected them to the topology of the system.

Two original results were presented in Chapter 3, building on Refs. [100, 102]. First, we showed that asymmetric voltage drops across a NSN junction in the linear-response regime lead to unequal currents on the two sides due to Andreev processes, yielding a net differential conductance related to the resulting current that flows to ground from the SC region. In the presence of topologically protected Majorana states, the scattering probabilities at the two interfaces become equal, enforcing an *antisymmetric* profile of this conductance as a function of the bias-splitting parameter.

Second, we investigated the transport signatures of the chiral TSC state in the NSN junction with symmetric bias configuration beyond the linear-response regime. In this setting, we identified three distinct bias-dependent transport regimes. In the intermediate one, the differential conductance exhibits pronounced oscillations, produced by the interference of two propagating modes with different momenta localized along the same edge of the system. This configuration directly reflects the emergence of the chiral TSC phase featured by MCPSs.

In the last part, we presented our main findings on the induced pairing in a MTI thin film proximitized by a conventional s-wave SC. By characterizing the spatial profile of the induced correlations, we derived an analytical expression for their decay length, showing that it is primarily governed by the decay of the underlying surface states. We further resolved the structure of the anomalous Green's function

in spin and momentum space, demonstrating that spin-polarized pairing channels dominate at large magnetization in accordance with the polarization of the proximitized surface states. Finally, we connected the momentum structure of the induced pairing to the topology of the effective two-dimensional superconductor, showing that increasing the exchange field drives the system into the chiral TSC phase.

Perspectives

From a theoretical perspective, hybrid MTI–SC structures provide a fertile ground for exploring the emergence of topological superconductivity [41, 45, 46]. The present thesis has combined effective Hamiltonian modeling, transport analysis, and many-body Green's function techniques to establish a coherent picture of how superconductivity manifests in proximitized MTIs and how it can give rise to zero-energy Majorana modes in different geometries. While these results capture the essential mechanisms, they rely on simplified models that neglect disorder, electron–electron interactions, and realistic device architectures. Addressing these limitations will be crucial to provide quantitative guidance for experimental realizations and to bridge the gap between idealized theoretical models and engineered devices. Beyond this, the theoretical framework developed here for the induced pairing can be naturally extended to more complex hybrid structures, such as superconductor–normal–superconductor and multiterminal Josephson junctions, enabling a systematic investigation of phase-coherent transport, nonlocal correlations, and topological Josephson effects in the presence of magnetic textures and spin–orbit coupling [171–173]. Further generalizations of this formalism could be extended to time-dependent or periodically driven systems, providing a framework to investigate Floquet-induced topological superconductivity and the non-equilibrium dynamics of Majorana modes [174–177].

On the experimental side, a major open challenge remains the unambiguous realization of a solid-state platform hosting topological Majorana quasiparticles. Despite extensive efforts in the fabrication and characterization of semiconductor nanowires and proximitized topological insulator films, the experimental evidence for the expected conductance quantization remains inconclusive [101, 131, 135, 136, 178]. The results presented in this thesis contribute to this ongoing search by identifying material regimes and device configurations under which proximity-induced superconductivity in MTIs can realize topological phases with spatially separated Majorana modes. In this sense, we hope that the theoretical predictions developed here will help interpret experimental observations and guide the design of optimized heterostructures and device geometries toward achieving robust Majorana signatures in topological insulating thin films and nanowires.

From an applied point of view, the most compelling long-term prospect of proximity-induced superconductivity in topological insulators lies in the potential use of Majorana quasiparticles as building blocks for topological quantum computation. The chiral and localized Majorana states discussed in this thesis embody non-Abelian excitations, whose braiding statistics form the basis for intrinsically fault-tolerant quantum operations [31–34, 74]. Realizing such a platform, however, will require substantial advances in material growth and device fabrication, together

with experimental probes capable of unambiguously distinguishing genuine topological Majorana modes from trivial Andreev bound states [101, 135–137]. In parallel, hybrid MTI–SC systems may also find application as topological spintronic elements or as platforms to explore magnetoelectric and thermoelectric responses of superconducting topological matter, thereby broadening their relevance beyond quantum computation. Indeed, the coexistence of magnetic order, spin–orbit coupling, and superconducting correlations in proximitized MTIs enables the emergence of spin-polarized triplet pairing and controllable spin supercurrents. These features allow for dissipationless spin transport and for nonreciprocal superconducting devices in which the supercurrent depends on the magnetization direction, as the spin-polarized Cooper pairs carry a finite net spin. In this context, proximity-induced triplet correlations could be exploited to design superconducting spin diodes or memory elements based on magnetization-controlled supercurrents, thereby contributing to the development of low-dissipation spin-based logic architectures [179–182].

In conclusion, while many challenges remain, the results presented in this work represent a step toward establishing proximitized MTIs as a versatile platform for topological superconductivity, providing insights into the role of magnetism in shaping the induced pairing symmetry, the mechanisms underlying the emergence of Majorana modes, and their observable signatures in transport experiments. The interplay between magnetism, topology, and superconductivity remains a central theme in condensed matter physics, driving both fundamental theoretical developments and the pursuit of practical implementations in topological quantum technologies. Future progress at the intersection between theoretical physics, materials science, and device engineering will determine how the concepts explored here will evolve into experimentally realizable architectures capable of harnessing the unique properties of Majorana quasiparticles.

Appendix A

Numerical Implementation

In this appendix, we summarize the numerical methods underlying our calculations. First, in Appendix A.1, we discuss the discretization of continuum Hamiltonians on a finite lattice with open boundary conditions. Second, in Appendices A.2 and A.3, we provide further details on the complex band-structure approach employed to analyze quasiparticle transport in junctions composed of homogeneous sectors.

A.1 Lattice Discretization

To obtain the energy spectrum of a momentum-dependent Hamiltonian in a confined geometry, we discretize the finite direction into a lattice of N sites and approximate the spatial derivatives by finite differences. For clarity, we consider a two-dimensional system in which the Hamiltonian depends on the momenta k_x, k_y. We impose periodic boundary conditions along the x direction, so that k_x remains a good quantum number, while the y direction is discretized under Dirichlet boundary conditions, corresponding to a vanishing wavefunction at the edges of the system. The generalization of this procedure to three-dimensional geometries is straightforward.

Consider a non–interacting single–particle quadratic Hamiltonian, which can be expressed in the continuum limit as

$$h(k_x, k_y) = A\, k_y^2 + B\, k_y + C\,, \tag{A.1}$$

where $A \equiv A(k_x)$, $B \equiv B(k_x)$ and $C \equiv C(k_x)$ are $n \times n$ matrices acting on the n-dimensional single-particle Hilbert space, defined by the tensor product of the internal degrees of freedom that characterize the system under consideration. Assuming a lattice of finite length L_y along y and imposing Dirichlet boundary conditions, the wavefunction is required to vanish at the edges of the system, $\psi(y = 0) = 0$ and $\psi(y = L) = 0$. In this case, the Schrödinger equation for the single-particle Hamiltonian h can be rewritten in real space as

$$h\left(k_x, -\mathrm{i}\,\partial_y\right)\, \psi_{k_x}(y) = -A\,\partial_y^2\,\psi_{k_x}(y) - \mathrm{i}B\,\partial_y\,\psi_{k_x}(y) + C\,\psi_{k_x}(y) = E_{k_x}\,\psi_{k_x}(y)\,, \tag{A.2}$$

where the momentum operator has been replaced by its real-space representation, $k_y \to -\mathrm{i}\,\partial_y$.

Using the finite difference approximation, the partial derivatives of the wavefunction can be approximated as [183]

$$\begin{aligned}\partial_y \psi_{k_x}(y) &\approx \frac{1}{2a}\left[\psi_{k_x}(y+a) - \psi_{k_x}(y-a)\right] ,\\ \partial_y^2 \psi_{k_x}(y) &\approx \frac{1}{a^2}\left[\psi_{k_x}(y+a) - 2\psi_{k_x}(y) + \psi_{k_x}(y-a)\right] ,\end{aligned} \tag{A.3}$$

where a is the lattice spacing. Plugging Equation (A.3) into Equation (A.2) we obtain

$$\begin{aligned} h\left(k_x, -\mathrm{i}\,\partial_y\right)\, \psi_{k_x}(y) \approx &- \frac{A}{a^2}\left[\,\psi_{k_x}(y+a) - 2\,\psi_{k_x}(y) + \,\psi_{k_x}(y-a)\right] + C\,\psi_{k_x}(y)\\ &- \mathrm{i}\frac{B}{2a}\left[\,\psi_{k_x}(y+a) - \,\psi_{k_x}(y-a)\right] =\\ = &- \left[\frac{A}{a^2} + \mathrm{i}\frac{B}{2a}\right]\,\psi_{k_x}(y) + \left[C + \frac{2A}{a^2}\right]\,\psi_{k_x}(y+a)\\ &- \left[\frac{A}{a^2} - \mathrm{i}\frac{B}{2a}\right]\,\psi_{k_x}(y-a)\,, \end{aligned} \tag{A.4}$$

and defining the on-site energy and hopping terms as

$$h_0 \equiv C + \frac{2A}{a^2}\,, \qquad h_\pm \equiv -\left[\frac{A}{a^2} - \mathrm{i}\frac{B}{2a}\right]\,, \tag{A.5}$$

Equation (A.4) can be rewritten as a tight-binding problem [184]

$$h_+\,\psi_{k_x}(y+a) + h_0\,\psi_{k_x}(y) + h_-\,\psi_{k_x}(y-a) = E_{k_x}\,\psi_{k_x}(y)\,, \tag{A.6}$$

where $y = ma$ denotes the position of the m-th lattice site with $m = 0, 1, \ldots, N$, and the length of the lattice is $L_y = (N+1)\,a$. The above equation in is valid in the bulk of the lattice, away from the boundaries. Imposing Dirichlet boundary conditions at $y = 0$ and $y = L_y$ yields the following additional constraints on the wavefunction:

$$\begin{aligned} h_+\,\psi_{k_x}(a) + h_0\,\psi_{k_x}(0) &= E_{k_x}\,\,\psi_{k_x}(0)\,,\\ h_0\,\psi_{k_x}(L_y) + h_-\,\psi_{k_x}(L_y - a) &= E_{k_x}\,\psi_{k_x}(L_y)\,. \end{aligned} \tag{A.7}$$

The bulk equation in Eq. (A.6), together with the open boundary conditions specified in Equation (A.7), constitutes a closed system that can be solved by introducing a transverse wavefunction of the form

$$\Psi_{k_x} = \begin{bmatrix}\psi_{k_x}(0) & \psi_{k_x}(a) & \ldots & \psi_{k_x}(Na)\end{bmatrix}^T\,, \tag{A.8}$$

which enables to recast the problem as a standard eigenvalue equation

$$h_{\mathrm{TB}}(k_x)\,\Psi_{k_x} = E_{k_x}\,\Psi_{k_x}\,. \tag{A.9}$$

Here, h_{TB} plays the role of a tight-binding Hamiltonian matrix, and in terms of the on-site and hopping energies it is given by

$$h_{\mathrm{TB}} = \begin{bmatrix} h_0 & h_+ & 0 & \dots & & 0 \\ h_- & h_0 & h_+ & \dots & & \vdots \\ 0 & h_- & h_0 & h_+ & & \\ \vdots & & & & & \\ 0 & \dots & & & 0 \; h_- & h_0 \end{bmatrix} . \tag{A.10}$$

The tight-binding matrix h_{TB} has dimension $(N+1)\,n \times (N+1)\,n$, where $N+1$ is the number of lattice sites and n is the dimension of the original single-particle Hamiltonian, determined by the internal degrees of freedom of the electron.

A.2 Momentum Eigenvalue Problem

To model quasiparticle transport in the NSN junction, the continuum Hamiltonian $h_{\mathrm{BdG}} \equiv h_{\mathrm{BdG}}(k_x, k_y)$ for each homogeneous region $s \in \{N_1, N_2, S\}$ of the system is discretized on a finite lattice along the transverse directions y and z. For the longitudinal direction x, along which quasiparticle transport occurs, we employ a complex band structure approach based on the complex momentum $k \equiv k_x$, obtained under the assumption of translational invariance. Propagating states with real momentum k can be obtained by solving the energy eigenvalue problem outlined in Appendix A.1

$$h_{\mathrm{BdG}}(k)\,\Psi_k = E\,\Psi_k\,, \tag{A.11}$$

whereas transport in non-translationally invariant systems, such as the NSN junction, additionally requires evanescent states characterized by complex values of k [118–122]. For simplicity, the transverse real-space coordinates y and z are omitted in the following.

We begin by rewriting the Hamiltonian in terms of its k-dependent contributions

$$h_{\mathrm{BdG}}(k) \equiv \mathcal{A} + \mathcal{B}\,k + \mathcal{C}\,k^2\,, \tag{A.12}$$

where $\mathcal{A}$, $\mathcal{B}$, and $\mathcal{C}$ are matrices acting in the Nambu space of the proximitized MTI system. The explicit expressions for $\mathcal{A}$, $\mathcal{B}$, and $\mathcal{C}$ can be obtained by comparison with the BdG Hamiltonians in Equations (2.17) and (2.19). Introducing the enlarged wavefunction

$$\Phi = \begin{bmatrix} \Psi_k \\ k\,\Psi_k \end{bmatrix}, \tag{A.13}$$

the energy eigenvalue problem in Equation (A.11) can be reformulated as a *momentum* eigenvalue problem at fixed energy [185]. After straightforward algebra, this yields

$$\mathbf{M}_E\,\Phi = k\,\Phi\,, \qquad \mathbf{M}_E = \begin{pmatrix} 0 & 1 \\ -\mathcal{C}^{-1}(\mathcal{A}-E) & -\mathcal{C}^{-1}\mathcal{B} \end{pmatrix}, \tag{A.14}$$

where 0 and 1 denote the zero and identity matrices, respectively.

It is worth noting that the momentum eigenvalue problem in Equation (A.14) is defined by a non-Hermitian, energy-dependent matrix $\mathbf{M}_E$, so that its eigenvalues k are, in general, complex and thus encompass both the propagating and the evanescent modes allowed at a given energy. In particular, if the system is in a topological phase, its boundary states are described by evanescent modes: while such solutions are unphysical in an infinite system, they acquire physical significance in the description of semi-infinite or finite geometries, such as the homogeneous sectors of the junction [118–122]. The first pair of complex momenta with the smallest absolute values, obtained as solutions of Equation (A.14) for the two-dimensional MTI Hamiltonian in Equation (1.58), are shown in Figure A.1 for different energies. The Hamiltonian is discretized on a finite transverse lattice of width $L_y = 1.5$ μm along y, with $k \equiv k_x$ denoting the momentum along the longitudinal propagation direction.

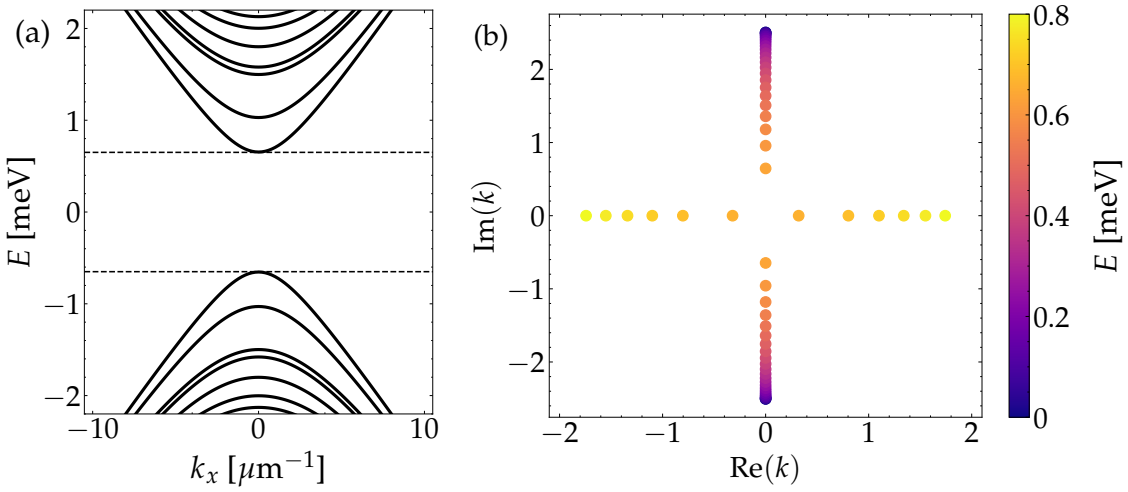

Figure A.1: (a) Energy spectrum of the two-dimensional Hamiltonian in Equation (1.58), discretized on a transverse lattice of width $L_y = 1.5$ μm with periodic boundary conditions along x. (b) Complex plane representation of the first two momentum solutions with the smallest absolute values, obtained from Equation (A.14) as a function of energy. The parameters were set to $m_0 = 1\,\text{meV}$, $m_1 = 0.001\,\text{meV}\mu\text{m}^2$, $v_F = 0.26\,\text{meV}\,\mu\text{m}$, $D = 0$, and $\Lambda = 0.5$ meV.

Panel (a) displays the energy spectrum of the system, which exhibits a gap around zero energy highlighted by the horizontal dashed lines. As shown in panel (b), for energies within this gap, $E < 0.65$ meV, only complex momenta are allowed, since no real propagating solutions exist. For energies above the gap, the momenta obtained from Equation (A.14) can be either real, corresponding to the propagating states, or complex, corresponding to evanescent modes which can emerge in systems with finite length.

A.3 Boundary Conditions at the Interfaces

In the following section, we provide additional details on the derivation of the linear system of equations that governs the boundary conditions at the interface of the NSN junction, as introduced in Section 3.1.1. The analysis builds upon the complex band-structure formalism developed in Refs. [118–122].

Within the complex band structure approach, the single particle wavefunction in each sector of the junction can be written as the superposition

$$\Psi^{(s)}(x,y) = \sum_k c_k(s)\, \mathrm{e}^{\mathrm{i}k^{(s)}x}\, \tilde{\Psi}_k^{(s)}(y)\,, \tag{A.15}$$

where the set of complex wavenumbers and associated transverse modes $\{k^{(s)},\, \tilde{\Psi}_k^{(s)}\}$ are solutions to the momentum eigenvalue problem in Equation (A.14). Denoting incoming (outgoing) modes as $\{a_k^{(s)}\}$ ($\{b_k^{(s)}\}$), Equation (A.15) can be expressed as

$$\Psi^{(s)}(x,y) = \sum_{k\in s,\mathrm{inp}} a_k^{(s)}\, \mathrm{e}^{\mathrm{i}kx}\, \tilde{\Psi}_k^{(s)}(y) + \sum_{k\in s,\mathrm{out}} b_k^{(s)}\, \mathrm{e}^{\mathrm{i}kx}\, \tilde{\Psi}_k^{(s)}(y)\,. \tag{A.16}$$

While the input coefficients $a_k^{(s)}$ are fixed by the choice of the incoming scattering state, the outgoing ones $b_k^{(s)}$ represent the unknowns of the scattering problem and must be determined by constructing the full wavefunction across the entire junction.

At the normal–superconductor interfaces located at $x = x_1$ and $x = x_2$, the boundary conditions are imposed by enforcing the continuity of both the wavefunction and its derivative with respect to x, ensuring quasiparticle current conservation across the interface [100, 118, 119]. Explicitly, one obtains

$$\Psi^{(N_i)}(x_i,y) = \Psi^{(S)}(x_i,y)\,, \qquad \left.\frac{\partial\Psi^{(N_i)}(x,y)}{\partial x}\right|_{x=x_i} = \left.\frac{\partial\Psi^{(S)}(x,y)}{\partial x}\right|_{x=x_i}. \tag{A.17}$$

Separating input and output modes, the boundary conditions for the continuity of the wavefunction at $x = x_1$ take the form

$$\sum_{k\in S} b_k^{(S)}\, \mathrm{e}^{\mathrm{i}kx_1}\, \tilde{\Psi}_k^{(N_1)}(y) - \sum_{k\in N_1,\mathrm{out}} b_k^{(N_1)}\, \mathrm{e}^{\mathrm{i}kx_1}\, \tilde{\Psi}_k^{(N_1)}(y) = \sum_{k\in N_1,\mathrm{inp}} a_k^{(N_1)}\, \mathrm{e}^{\mathrm{i}kx_1}\, \tilde{\Psi}_k^{(N_1)}(y)\,, \tag{A.18}$$

and the one for the conservation of the quasiparticle current is given by

$$\sum_{k\in S} b_k^{(S)}\, k\, \mathrm{e}^{\mathrm{i}kx_1}\, \tilde{\Psi}_k^{(S)}(y) - \sum_{k\in N_1,\mathrm{out}} b_k^{(N_1)}\, k\, \mathrm{e}^{\mathrm{i}kx_1}\, \tilde{\Psi}_k^{(N_1)}(y) = \sum_{k\in N_1,\mathrm{inp}} a_k^{(N_1)}\, k\, \mathrm{e}^{\mathrm{i}kx_1} \tilde{\Psi}_k^{(N_1)}(y)\,. \tag{A.19}$$

Analogous equations can be obtained for the interface at $x = x_2$.

To solve this system of equations, it is convenient to project the transverse wavefunctions $\tilde{\Psi}_k$ onto the complete discrete set of complex modes through the overlap matrices [100, 118, 119]

$$\mathcal{M}_{k'k}^{s's} = \int \mathrm{d}y\, \left[\tilde{\Psi}_{k'}^{(s')}(y)\right]^\dagger \tilde{\Psi}_k^{(s)}(y)\,, \tag{A.20}$$

in order to remove the explicit dependence on the transverse coordinate y of the lattice. In this way, Equations (A.18) and (A.19) become

$$\begin{aligned}
&\sum_{k\in S} \mathrm{e}^{\mathrm{i}kx_1}\, \mathcal{M}^{N_1 S}_{kk'}\, b^{(S)}_k - \sum_{k\in N_1,\mathrm{out}} \mathrm{e}^{\mathrm{i}kx_1}\, \mathcal{M}^{N_1 N_1}_{kk'}\, b^{(N_1)}_k = \sum_{k\in N_1,\mathrm{inp}} \mathrm{e}^{\mathrm{i}kx_1}\, \mathcal{M}^{N_1 N_1}_{kk'}\, a^{(N_1)}_k\,, \\
&\sum_{k\in S} k\, \mathrm{e}^{\mathrm{i}kx_1}\, \mathcal{M}^{SS}_{kk'}\, b^{(S)}_k - \sum_{k\in N_1,\mathrm{out}} k\, \mathrm{e}^{\mathrm{i}kx_1}\, \mathcal{M}^{SN_1}_{kk'}\, b^{(N_1)}_k = \sum_{k\in N_1,\mathrm{inp}} k\, \mathrm{e}^{\mathrm{i}kx_1}\, \mathcal{M}^{SN_1}_{kk'}\, a^{(N_1)}_k\,,
\end{aligned} \tag{A.21}$$

and an analogous set of equations can be derived for the interface at $x = x_2$.

Equation (A.21) is defined for each output mode k' in the normal leads $N_{1,2}$, including all possible scattering channels for a quasiparticle injected from lead $i = 1$. It is worth noting that the resulting system contains more equations than unknowns: once the second set of boundary conditions at the interface $x = x_2$ is taken into account, one obtains

$$N_{\mathrm{unk}} = N^{(N_1)}_{\mathrm{out}} + N^{(N_2)}_{\mathrm{out}}\,, \qquad N_{\mathrm{eq}} = 2N_{\mathrm{unk}}\,. \tag{A.22}$$

where $N^{(N_i)}_{\mathrm{out}}$ is the number of output modes in the normal terminal i. A solvable system is obtained by retaining only half of the equations: wavefunction continuity is imposed for output modes k' in lead 1, whereas derivative continuity is imposed for output modes k' in lead 2. Since the number of equations scales with the number of output modes considered, increasing the number of complex wavenumbers systematically improves the accuracy of the full wavefunction in the junction. Moreover, one can verify that if the basis of output modes and transverse wavefunctions is sufficiently large, both the continuity of the wavefunction and the continuity of its derivative are simultaneously satisfied.

Appendix B

Perturbative Expansion

In this appendix, we provide additional details on the evaluation of the first- and second-order corrections to the normal and anomalous Green's functions in the MTI, providing additional details to the discussion presented in Chapter 4.

B.1 Normal Green's Function

B.1.1 First Order

To compute the first-order term of the Green's function $\mathcal{G}^{(1)}(\xi, \xi')$, we evaluate the time-ordered expectation value

$$\left\langle T_t \; \psi(\xi)\, V(t_1)\, \psi^\dagger(\xi') \right\rangle_0 , \tag{B.1}$$

where $V = \mathcal{T} + \mathcal{T}^\dagger$ is the tunneling Hamiltonian defined in Equation (4.28), and $\xi \equiv (z, t, \sigma, \tau)$ denotes the complete set of spatial, temporal, spin, and orbital indices associated with each field operator. Up to overall constants, the contribution associated with $\mathcal{T}$ takes the explicit form

$$\left\langle T_t \; \psi(\xi)\, \psi^\dagger(1)\, \phi_s(1')\, \psi^\dagger(\xi') \right\rangle_0 = - \left\langle T_t \; \psi(\xi)\, \psi^\dagger(1)\, \psi^\dagger(\xi') \right\rangle_0 \left\langle T_t \; \phi(1') \right\rangle_0 = 0 , \tag{B.2}$$

where we separated the operators acting in the two materials, which commute by construction as they are independent on the unperturbed ground state, and adopted the conventions for the primed integration indices introduced in Equation (4.65). The above expression vanishes identically, as the superconducting correlator contains an unpaired annihilation operator ϕ, which yields zero when acting on the ground state. By the same reasoning, the contribution from $\mathcal{T}^\dagger$ also vanishes. Therefore, the first-order correction to the normal MTI Green's function is identically zero:

$$\mathcal{G}^{(1)}(\xi, \xi') = 0 . \tag{B.3}$$

For the same reason, all *odd* terms in the perturbative expansion of Equation (4.55) vanish.

B.1.2 Second Order

To compute the second-order correction to the normal Green's function in the MTI, we evaluate the time-ordered expectation value

$$\left\langle T_t\ \psi(\xi)\, V(t_1)\, V(t_2)\, \psi^\dagger(\xi') \right\rangle_0 . \tag{B.4}$$

Among the terms generated by the product $V(t_1)V(t_2)$, the only nonvanishing contributions are $\mathcal{T}\mathcal{T}^\dagger$ and its Hermitian conjugate $\mathcal{T}^\dagger\mathcal{T}$, since they contain an equal number of creation operators $\psi^\dagger$ and annihilation operators ψ. After permuting and relabeling the integration variables, these two contributions reduce to the same time-ordered bracket, which, up to some constants, can be expressed explicitly as

$$\begin{aligned} &\left\langle T_t\, \psi(\xi)\psi^\dagger(1)\phi(1')\phi^\dagger(2')\psi(2)\psi^\dagger(\xi') \right\rangle_0 = \\ &\left\langle T_t\, \psi(\xi)\psi^\dagger(1)\psi(2)\psi^\dagger(\xi') \right\rangle_0 \left\langle T_t\, \phi(1')\phi^\dagger(2') \right\rangle_0 . \end{aligned} \tag{B.5}$$

The first bracket can be evaluated through the Wick's theorem, expanding it into all possible non-vanishing contractions [143, 145, 148]

$$\begin{aligned} &\left\langle T_t\, \psi(\xi)\psi^\dagger(1)\psi(2)\psi^\dagger(\xi') \right\rangle_0 = \\ &= \left\langle T_t\, \psi(\xi)\psi^\dagger(1) \right\rangle_0 \left\langle T_t\, \psi(2)\psi^\dagger(\xi') \right\rangle_0 - \left\langle T_t\, \psi(\xi)\psi^\dagger(\xi') \right\rangle_0 \left\langle T_t\, \psi(2)\psi^\dagger(1) \right\rangle_0 = \\ &= -\mathcal{G}^{(0)}_{\mathrm{MTI}}(\xi,1)\mathcal{G}^{(0)}_{\mathrm{MTI}}(2,\xi') + \mathcal{G}^{(0)}_{\mathrm{MTI}}(\xi,\xi')\mathcal{G}^{(0)}_{\mathrm{MTI}}(2,1) , \end{aligned} \tag{B.6}$$

where the time-ordered brackets in the second and third rows can be recognized as different components of the unperturbed MTI Green's function. Here, we highlighted the possible contractions with blue (red) lines, corresponding to permutations which require an even (odd) number of exchanges to sort the fermionic operators in the desired order. In a similar way, the bracket between SC field operators corresponds to the unperturbed normal Green's function in the superconductor

$$\left\langle T_t\, \phi(1')\phi^\dagger(2') \right\rangle_0 = \mathrm{i}\mathcal{G}^{(0)}_{\mathrm{SC}}(1',2') , \tag{B.7}$$

and we can finally obtain

$$\begin{aligned} &\left\langle T_t\, \psi(\xi)\psi^\dagger(1)\psi(2)\psi^\dagger(\xi') \right\rangle_0 \left\langle T_t\, \phi(1')\phi^\dagger(2') \right\rangle_0 = \\ &= -\mathrm{i}\mathcal{G}^{(0)}_{\mathrm{MTI}}(\xi,1)\mathcal{G}^{(0)}_{\mathrm{SC}}(1',2')\mathcal{G}^{(0)}_{\mathrm{MTI}}(2,\xi') + \mathrm{i}\mathcal{G}^{(0)}_{\mathrm{MTI}}(\xi,\xi')\mathcal{G}^{(0)}_{\mathrm{SC}}(1',2')\mathcal{G}^{(0)}_{\mathrm{MTI}}(2,1) . \end{aligned} \tag{B.8}$$

Since the Hamiltonian does not depend explicitly on time, the Green's function depends only on the time difference, and it is convenient to Fourier transform to frequency space according to

$$\mathcal{G}^{(0)}(\omega) = \int \mathrm{d}(t-t')\, \mathrm{e}^{\mathrm{i}\omega(t-t')}\mathcal{G}^{(0)}(t-t') . \tag{B.9}$$

By means of Equations (B.8) and (B.9), the second-order correction to the normal MTI Green's function in Equation (4.58) can be expressed as

$$\mathcal{G}^{(2)}_{\mathrm{MTI}}(z,z';\omega) = \int \mathrm{d}z_1\,\mathrm{d}z_1'\,\mathrm{d}z_2\,\mathrm{d}z_2' \times \Big\{ \mathcal{G}^{(0)}_{\mathrm{MTI}}(z,z_1;\omega)\,\Gamma(z_1,z_1')\,\mathcal{G}^{(0)}_{\mathrm{SC}}(z_1',z_2';\omega)\,\Gamma^\dagger(z_2,z_2')\,\mathcal{G}^{(0)}_{\mathrm{MTI}}(z_2,z';\omega) - \mathcal{G}^{(0)}_{\mathrm{MTI}}(z,z';\omega)\,\Gamma(z_1,z_1')\,\mathcal{G}^{(0)}_{\mathrm{SC}}(z_1',z_2';\omega)\,\Gamma^\dagger(z_2,z_2')\,\mathcal{G}^{(0)}_{\mathrm{MTI}}(z_2,z_1;\omega) \Big\}, \tag{B.10}$$

where $\mathcal{G}^{(0)}_{\mathrm{MTI}}(z,z';\omega)$ $[\mathcal{G}^{(0)}_{\mathrm{SC}}(z,z';\omega)]$ denotes the 4×4 (2×2) unperturbed normal Green's function matrix of the MTI (SC), acting in the spin–orbital space. Assuming a local tunneling as in Equation (4.66), and neglecting the second term which correspond to a disconnected diagram, the above expression reduces to the compact result given in Section 4.3.2:

$$\mathcal{G}^{(2)}_{\mathrm{MTI}}(z,z';\omega) = \int \mathrm{d}z_1\,\mathrm{d}z_2\,\mathcal{G}^{(0)}_{\mathrm{MTI}}(z,z_1;\omega)\,\Gamma(z_1)\,\mathcal{G}^{(0)}_{\mathrm{SC}}(z_1,z_2;\omega)\,\Gamma^\dagger(z_2)\,\mathcal{G}^{(0)}_{\mathrm{MTI}}(z_2,z';\omega)\,. \tag{B.11}$$

B.2 Anomalous Green's Function

B.2.1 Second Order

The odd-order correction to the anomalous MTI Green's function vanishes for reasons analogous to those of the normal component. We therefore restrict the discussion to the second-order term only.

To evaluate the second-order correction to the anomalous propagator, we need to compute the time-ordered bracket

$$\Big\langle T_t\,\psi^\dagger(\xi)V(t_1)V(t_2)\psi^\dagger(\xi')\Big\rangle_0\,. \tag{B.12}$$

Among the terms generated by the product $V(t_1)V(t_2)$, the only nonvanishing contribution is $\mathcal{T}^\dagger\mathcal{T}^\dagger$, since this is the only term which ensures that the full correlator contains an equal number of creation operators $\psi^\dagger$ and annihilation operators ψ. The corresponding time-ordered expectation value reads

$$\begin{aligned} &\Big\langle T_t\,\psi^\dagger(\xi)\phi^\dagger(1')\psi(1)\phi^\dagger(2')\psi(2)\psi^\dagger(\xi')\Big\rangle_0 = \\ &= -\Big\langle T_t\,\psi^\dagger(\xi)\psi(1)\psi(2)\psi^\dagger(\xi')\Big\rangle_0 \Big\langle T_t\,\phi^\dagger(1')\phi^\dagger(2')\Big\rangle_0\,. \end{aligned} \tag{B.13}$$

The first term can be evaluated through Wick's theorem as [143, 145, 148]

$$\begin{aligned} &-\Big\langle T_t\,\psi^\dagger(\xi)\psi(1)\psi(2)\psi^\dagger(\xi')\Big\rangle_0 = \\ &\Big\langle T_t\,\psi(1)\psi^\dagger(\xi)\Big\rangle_0 \Big\langle T_t\,\psi(2)\psi^\dagger(\xi')\Big\rangle_0 - \Big\langle T_t\,\psi(2)\psi^\dagger(\xi)\Big\rangle_0 \Big\langle T_t\,\psi(1)\psi^\dagger(\xi')\Big\rangle_0 = \\ &= \mathcal{G}^{(0)}_{\mathrm{MTI}}(2,\xi)\mathcal{G}^{(0)}_{\mathrm{MTI}}(1,\xi') - \mathcal{G}^{(0)}_{\mathrm{MTI}}(1,\xi)\mathcal{G}^{(0)}_{\mathrm{MTI}}(2,\xi')\,, \end{aligned} \tag{B.14}$$

where the blue (red) lines indicate the pairings which require an even (odd) number of exchanges to sort the fermionic operators in the desired order. Similarly, the second bracket is proportional to the unperturbed anomalous Green's function in the superconductor

$$\left\langle T_t\, \phi^\dagger(1')\phi^\dagger(2') \right\rangle_0 = \mathrm{i}\mathcal{F}^{\dagger\,(0)}_{\mathrm{SC}}(1',2')\,. \tag{B.15}$$

yielding

$$\begin{aligned} -\left\langle T_t\, \psi^\dagger(\xi)\psi(1)\psi(2)\psi^\dagger(\xi') \right\rangle_0 \left\langle T_t\, \phi^\dagger(1')\phi^\dagger(2') \right\rangle_0 = \\ \mathrm{i}\mathcal{F}^{\dagger\,(0)}_{\mathrm{SC}}(z_1' t_1, z_2' t_2)\mathcal{G}^{(0)}_{\mathrm{MTI}}(2,\xi)\mathcal{G}^{(0)}_{\mathrm{MTI}}(1,\xi') - \mathrm{i}\mathcal{F}^{\dagger\,(0)}_{\mathrm{SC}}(1',2')\mathcal{G}^{(0)}_{\mathrm{MTI}}(1,\xi)\mathcal{G}^{(0)}_{\mathrm{MTI}}(2,\xi')\,. \end{aligned} \tag{B.16}$$

Taking advantage of the fermionic anticommutation relations,

$$\mathcal{F}^{\dagger\,(0)}_{\mathrm{SC}}(1,2) = -\mathcal{F}^{\dagger\,(0)}_{\mathrm{SC}}(2,1)\,, \tag{B.17}$$

and exchanging the integrated variables, it is straightforward to verify that the two contributions in the previous expression are equivalent. Substituting Equation (B.16) into Equation (4.62) and transforming to frequency space using Equation (B.9), the second-order correction to the anomalous MTI Green's function can be written as

$$\begin{aligned} \mathcal{F}^{\dagger\,(2)}_{\mathrm{MTI}}(z,z';\omega) = \int \mathrm{d}z_1\, \mathrm{d}z_1' \int \mathrm{d}z_2\, \mathrm{d}z_2' \\ \times \left[\mathcal{G}^{(0)}_{\mathrm{MTI}}(z_1,z;-\omega)\right]^T \Gamma^*(z_1,z_1')\, \mathcal{F}^{\dagger\,(0)}_{\mathrm{SC}}(z_2',z_1';\omega)\, \Gamma^\dagger(z_2,z_2')\, \mathcal{G}^{(0)}_{\mathrm{MTI}}(z_2,z';\omega)\,, \end{aligned} \tag{B.18}$$

where $\mathcal{F}^{(0)}_{\mathrm{SC}}(z,z';\omega)$ denotes the 2×2 unperturbed anomalous Green's function matrix acting in the spin space of the SC. Equation (B.18) represents the most general expression for the second-order perturbative correction to the anomalous MTI Green's function. Under the assumption of local tunneling, as in Equation (4.66), the above result simplifies to the compact form reported in Section 4.3.2:

$$\begin{aligned} \mathcal{F}^{\dagger\,(2)}_{\mathrm{MTI}}(z,z';\omega) = \int \mathrm{d}z_1\, \mathrm{d}z_2 \\ \times \left[\mathcal{G}^{(0)}_{\mathrm{MTI}}(z_1,z;-\omega)\right]^T \Gamma^*(z_1)\, \mathcal{F}^{\dagger\,(0)}_{\mathrm{SC}}(z_2,z_1;\omega)\, \Gamma^\dagger(z_2)\, \mathcal{G}^{(0)}_{\mathrm{MTI}}(z_2,z';\omega)\,. \end{aligned} \tag{B.19}$$

Appendix C

Analytical Solution

In this appendix, we provide further details on the derivation of the normal-state MTI Green's function in the analytical limit introduced in Section 5.2.3.

We set the trivial energy shift to zero ($C = 0$) and neglect the electron–hole asymmetry term ($D_1 = 0$). Furthermore, we focus on small excitation energies around the Fermi level and assume a weak magnetization compared to the bulk gap. The most general homogeneous solution of Equation (5.80) is given by the combination of complex exponentials given in Equation (5.83). Without loss of generality, for $z \leq z'$ we can assume

$$\begin{aligned} g^L_{\sigma+,\sigma\tau'}(z,z') &= \mathrm{e}^{\lambda_1 z} l_1 + \mathrm{e}^{-\lambda_1 z} l_2 + \mathrm{e}^{\lambda_2 z} l_3 + \mathrm{e}^{-\lambda_2 z} l_4 \,, \\ g^L_{\sigma-,\sigma\tau'}(z,z') &= \eta_1 \left(\mathrm{e}^{\lambda_1 z} l_1 - \mathrm{e}^{-\lambda_1 z} l_2\right) + \eta_2 \left(\mathrm{e}^{\lambda_2 z} l_3 - \mathrm{e}^{-\lambda_2 z} l_4\right) . \end{aligned} \tag{C.1}$$

For $z > z'$, instead, we assume that the homogeneous solution decay exponentially away from the $z = 0$ interface, thus restricting our analysis to surface-localized modes only. The solution then reads

$$\begin{aligned} g^R_{\sigma+,\sigma\tau'}(z,z') &= \mathrm{e}^{-\lambda_1 z} r_2 + \mathrm{e}^{-\lambda_2 z} r_4 \,, \\ g^R_{\sigma-,\sigma\tau'}(z,z') &= -\eta_1 \,\mathrm{e}^{-\lambda_1 z} r_2 - \eta_2 \,\mathrm{e}^{-\lambda_2 z} r_4 \,. \end{aligned} \tag{C.2}$$

We enforce Neumann boundary conditions at the interface $z = 0$ by requiring

$$\frac{\partial}{\partial z} g^L_{\sigma\pm,\sigma\tau'}(z,z')\Big|_{z=0} = 0 \,. \tag{C.3}$$

Explicitly, this condition yields

$$\begin{aligned} \lambda_1 l_1 - \lambda_1 l_2 + \lambda_2 l_3 - \lambda_2 l_4 &= 0 \,, \\ \eta_1 \lambda_1 l_1 + \eta_1 \lambda_1 l_2 + \eta_2 \lambda_2 l_3 + \eta_2 \lambda_2 l_4 &= 0 \,. \end{aligned} \tag{C.4}$$

Next, we impose continuity of the Green's function at $z = z'$,

$$g^L_{\sigma\pm,\sigma\tau'}(z = z', z') = g^R_{\sigma\pm,\sigma\tau'}(z = z', z') \,, \tag{C.5}$$

which explicitly gives

$$\begin{aligned} \mathrm{e}^{\lambda_1 z'} l_1 + \mathrm{e}^{-\lambda_1 z'} l_2 + \mathrm{e}^{\lambda_2 z'} l_3 + \mathrm{e}^{-\lambda_2 z'} l_4 &= \mathrm{e}^{-\lambda_1 z'} r_2 + \mathrm{e}^{-\lambda_2 z'} r_4 \,, \\ \eta_1 \mathrm{e}^{\lambda_1 z'} l_1 - \eta_1 \mathrm{e}^{-\lambda_1 z'} l_2 + \eta_2 \mathrm{e}^{\lambda_2 z'} l_3 - \eta_2 \mathrm{e}^{-\lambda_2 z'} l_4 &= -\eta_1 \mathrm{e}^{-\lambda_1 z'} r_2 - \eta_2 \mathrm{e}^{-\lambda_2 z'} r_4 \,. \end{aligned} \tag{C.6}$$

Finally, we impose the discontinuity of the first spatial derivative at $z = z'$,

$$\left[\partial_z\, g^R_{\sigma\tau,\sigma\tau'}(z,z') - \partial_z\, g^L_{\sigma\tau,\sigma\tau'}(z,z')\right]_{z=z'} = \frac{\delta_{\tau\tau'}}{B_1 - tD_1}\,, \tag{C.7}$$

which originates from the Dirac delta term in Equation (5.74). Explicitly, we obtain

$$\begin{aligned} &\lambda_1 \mathrm{e}^{\lambda_1 z'} l_1 - \lambda_1 \mathrm{e}^{-\lambda_1 z'} l_2 + \lambda_2 \mathrm{e}^{\lambda_2 z'} l_3 - \lambda_2 \mathrm{e}^{-\lambda_2 z'} l_4 \\ &\quad + \lambda_1 \mathrm{e}^{-\lambda_1 z'} r_2 + \lambda_2 \mathrm{e}^{-\lambda_2 z'} r_4 \;=\; -\frac{\delta_{\tau\tau'}}{B_1 - D_1}\,, \end{aligned} \tag{C.8}$$

$$\begin{aligned} &\eta_1\lambda_1 \mathrm{e}^{\lambda_1 z'} l_1 + \eta_1\lambda_1 \mathrm{e}^{-\lambda_1 z'} l_2 + \eta_2\lambda_2 \mathrm{e}^{\lambda_2 z'} l_3 + \eta_2\lambda_2 \mathrm{e}^{-\lambda_2 z'} l_4 \\ &\quad - \eta_1\lambda_1 \mathrm{e}^{-\lambda_1 z'} r_2 - \eta_2\lambda_2 \mathrm{e}^{-\lambda_2 z'} r_4 \;=\; -\frac{\delta_{\tau\tau'}}{B_1 + D_1}\,. \end{aligned} \tag{C.9}$$

Equations (C.4), (C.6), (C.8) and (C.9) represent a system of 6 linear equations in the 6 unknown functions l_i, r_i and can thus be solved straightforwardly using matrix techniques. By grouping the unknowns in the following vector

$$\mathbf{x} \equiv \begin{pmatrix} l_1 & l_2 & l_3 & l_4 & r_2 & r_4 \end{pmatrix}^T\,, \tag{C.10}$$

the system of linear equations can be easily rearranged in matrix form as

$$\mathbb{A}\mathbf{x} = \mathbf{y}_\pm\,, \tag{C.11}$$

where the matrix $\mathbb{A}$ is given by

$$\mathbb{A} \equiv \begin{bmatrix} \lambda_1 & -\lambda_1 & \lambda_2 & -\lambda_2 & 0 & 0 \\ \eta_1\lambda_1 & \eta_1\lambda_1 & \eta_2\lambda_2 & \eta_2\lambda_2 & 0 & 0 \\ e^{\lambda_1 z'} & e^{-\lambda_1 z'} & e^{\lambda_2 z'} & e^{-\lambda_2 z'} & -e^{-\lambda_1 z'} & -e^{-\lambda_2 z'} \\ \eta_1 e^{\lambda_1 z'} & -\eta_1 e^{-\lambda_1 z'} & \eta_2 e^{\lambda_2 z'} & -\eta_2 e^{-\lambda_2 z'} & \eta_1 e^{-\lambda_1 z'} & \eta_2 e^{-\lambda_2 z'} \\ \lambda_1 e^{\lambda_1 z'} & -\lambda_1 e^{-\lambda_1 z'} & \lambda_2 e^{\lambda_2 z'} & -\lambda_2 e^{-\lambda_2 z'} & \lambda_1 e^{-\lambda_1 z'} & \lambda_2 e^{-\lambda_2 z'} \\ \eta_1\lambda_1 e^{\lambda_1 z'} & \eta_1\lambda_1 e^{-\lambda_1 z'} & \eta_2\lambda_2 e^{\lambda_2 z'} & \eta_2\lambda_2 e^{-\lambda_2 z'} & -\eta_1\lambda_1 e^{-\lambda_1 z'} & -\eta_2\lambda_2 e^{-\lambda_2 z'} \end{bmatrix}. \tag{C.12}$$

and the non-homogeneous term is defined as

$$\mathbf{y}_\pm \equiv \begin{pmatrix} 0 & \dots & 0 & -\frac{\delta_{\tau\tau'}}{(B_1 \mp D_1)} & 0 \end{pmatrix}^T\,. \tag{C.13}$$

Solving Equation (C.11), we obtain explicit expressions for the coefficients $l_i \equiv l_i(z')$ and $r_i \equiv r_i(z')$, which determine the particular solution of the unperturbed MTI Green's function through Equations (C.1) and (C.2). Making use of the complex-conjugate relations of Equation (5.86), which hold in the regime of weak magnetization compared to the bulk gap of the topological insulator, the components of the normal propagator at the interface $z = 0$ can be expressed in the general form

$$g_{\sigma\tau,\sigma\tau'}(z=0,z') = \mathrm{e}^{-\lambda z'}\left[\alpha^\sigma_{\tau\tau'}\cos(\kappa z') + \beta^\sigma_{\tau\tau'}\sin(\kappa z')\right]. \tag{C.14}$$

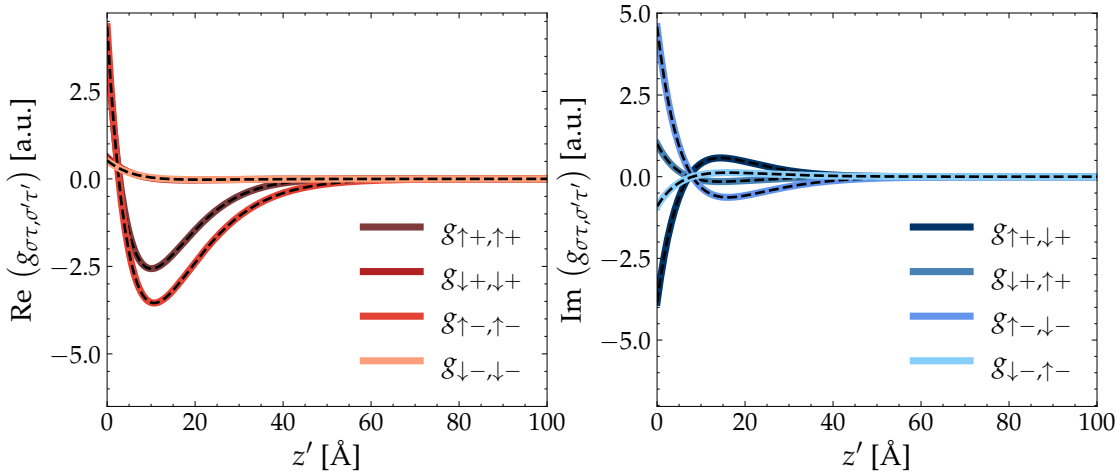

Figure C.1: Real (left) and imaginary (right) parts of the normal Green's function $g_{\sigma\tau,\sigma'\tau'}$ at the $\overline{\Gamma}$ point, evaluated at the interface $z = 0$. The colored solid lines correspond to the analytical solution in Equation (5.90), while the black dashed lines denotes the corresponding components extracted from the full solution discussed in Section 5.2.2. The calculations are performed assuming $\omega = 1$ mev and $\Lambda = 5$ meV, and the Bi_2Se_3 Hamiltonian parameters listed in Table 1.2.

For compactness, we omit the spin dependence of λ_i and η_i in what follows. The coefficients $\alpha_{\tau\tau'}$ and $\beta_{\tau\tau'}$ are given by

$$\alpha_{++} = \frac{1}{B_1 - D_1}\frac{\eta_1\lambda_1 - \eta_2\lambda_2}{\lambda_1\lambda_2\,(\eta_1 - \eta_2)}, \qquad \beta_{++} = -\frac{\mathrm{i}}{B_1 - D_1}\frac{(\eta_1\lambda_1 - \eta_2\lambda_2)(\eta_2\lambda_1 + \eta_1\lambda_2)}{\lambda_1\lambda_2\,(\eta_1 - \eta_2)(\eta_2\lambda_1 - \eta_1\lambda_2)};$$

$$\alpha_{+-} = -\frac{1}{B_1 + D_1}\frac{\lambda_1 - \lambda_2}{\lambda_1\lambda_2\,(\eta_1 - \eta_2)}, \qquad \beta_{+-} = \frac{\mathrm{i}}{B_1 + D_1}\frac{\lambda_1 + \lambda_2}{\lambda_1\lambda_2\,(\eta_1 - \eta_2)};$$

$$\alpha_{-+} = -\frac{1}{B_1 - D_1}\frac{\eta_1\eta_2\,(\lambda_1 - \lambda_2)}{\lambda_1\lambda_2\,(\eta_1 - \eta_2)}, \qquad \beta_{-+} = \frac{\mathrm{i}}{B_1 - D_1}\frac{\eta_1\eta_2\,(\lambda_1 + \lambda_2)}{\lambda_1\lambda_2\,(\eta_1 - \eta_2)};$$

$$\alpha_{--} = -\frac{1}{B_1 + D_1}\frac{\eta_1\lambda_2 - \eta_2\lambda_1}{\lambda_1\lambda_2\,(\eta_1 - \eta_2)}, \qquad \beta_{--} = \frac{\mathrm{i}}{B_1 + D_1}\frac{(\eta_1\lambda_2 - \eta_2\lambda_1)(\eta_1\lambda_1 + \eta_2\lambda_2)}{\lambda_1\lambda_2\,(\eta_1 - \eta_2)(\eta_1\lambda_1 - \eta_2\lambda_2)}.$$

The analytical solution at the $\overline{\Gamma}$ point, evaluated at the interface $z = 0$ and plotted as a function of the out-of-plane coordinate, is shown in Figure C.1. The colored solid lines represent the analytical expressions obtained from Equation (C.14), while the black dashed lines correspond to the same components extracted from the full numerical solution presented in Section 5.2.2. A direct comparison between the two makes it evident that, in the regime of small magnetization $\Lambda \ll M_0$ and energies close to the Fermi level $\omega \approx 0$, the analytical and numerical results coincide. This agreement is specifically robust when the film thickness is much larger than the characteristic decay length of the surface states. Under these conditions, the analytical solution faithfully reproduces the full behavior of the Green's function, demonstrating the validity of the closed-form analytical approximation.

Bibliography

[1] L. M. Lederman and C. T. Hill. *Symmetry and the beautiful universe*. Prometheus books, 2011.

[2] E. Noether. "Invariante variationsprobleme." In: *Gesammelte abhandlungen-collected papers*. Springer, 1983, pp. 231–239.

[3] Y. Kosmann-Schwarzbach. "The Noether theorems." In: *The Noether theorems: invariance and conservation laws in the twentieth century*. Springer, 2010, pp. 55–64.

[4] J. Hanc, S. Tuleja, and M. Hancova. Symmetries and conservation laws: consequences of noether's theorem. *American Journal of Physics* **72** (2004), pp. 428–435.

[5] C. Lanczos. *The variational principles of mechanics*. Courier Corporation, 2012.

[6] J. L. Kelley. *General topology*. Courier Dover Publications, 2017.

[7] M. Nakahara. *Geometry, topology and physics*. CRC press, 2018.

[8] A. P. Ramirez and B. Skinner. Dawn of the topological age? *Phys. Today* **73** (2020), pp. 30–36.

[9] K. v. Klitzing, G. Dorda, and M. Pepper. New method for high-accuracy determination of the fine-structure constant based on quantized Hall resistance. *Phys. Rev. Lett.* **45** (1980), pp. 494–497.

[10] K. Von Klitzing. The quantized Hall effect. *Rev. Mod. Phys.* **58** (1986), p. 519.

[11] K. von Klitzing et al. 40 Years of the quantum Hall effect. *Nat. Rev. Phys.* **2** (2020), pp. 397–401.

[12] Y. Hatsugai. Topological aspects of the quantum Hall effect. *J. Phys.: Condens. Matter* **9** (1997), p. 2507.

[13] Y. Hatsugai. Chern number and edge states in the integer quantum Hall effect. *Phys. Rev. Lett.* **71** (1993), pp. 3697–3700.

[14] F. D. M. Haldane. Model for a quantum Hall effect without Landau levels: condensed-matter realization of the "parity anomaly". *Phys. Rev. Lett.* **61** (1988), pp. 2015–2018.

[15] C.-Z. Chang, C.-X. Liu, and A. H. MacDonald. Colloquium: quantum anomalous Hall effect. *Rev. Mod. Phys.* **95** (2023), p. 011002.

[16] C.-X. Liu, S.-C. Zhang, and X.-L. Qi. The quantum anomalous Hall effect: theory and experiment. *Annual Review of Condensed Matter Physics* **7** (2016), pp. 301–321.

[17] B. A. Bernevig and S.-C. Zhang. Quantum spin Hall effect. *Phys. Rev. Lett.* **96** (2006), p. 106802.

[18] J. Maciejko, T. L. Hughes, and S.-C. Zhang. The quantum spin Hall effect. *Annu. Rev. Condens. Matter Phys.* **2** (2011), pp. 31–53.

[19] C. L. Kane and E. J. Mele. Quantum spin Hall effect in graphene. *Phys. Rev. Lett.* **95** (2005), p. 226801.

[20] M. Konig et al. Quantum spin Hall insulator state in HgTe quantum wells. *Science* **318** (2007), pp. 766–770.

[21] M. König et al. The quantum spin Hall effect: theory and experiment. *J. Phys. Soc. Jpn.* **77** (2008), p. 031007.

[22] C. L. Kane and E. J. Mele. Z_2 Topological order and the quantum spin Hall effect. *Phys. Rev. Lett.* **95** (2005), p. 146802.

[23] M. Z. Hasan and J. E. Moore. Three-dimensional topological insulators. *Annu. Rev. Condens. Matter Phys.* **2** (2011), pp. 55–78.

[24] M. Z. Hasan and C. L. Kane. Colloquium: topological insulators. *Rev. Mod. Phys.* **82** (2010), pp. 3045–3067.

[25] L. Fu, C. L. Kane, and E. J. Mele. Topological insulators in three dimensions. *Phys. Rev. Lett.* **98** (2007), p. 106803.

[26] L. Fu and C. L. Kane. Topological insulators with inversion symmetry. *Phys. Rev. B* **76** (2007), p. 045302.

[27] C. W. Beenakker. Search for Majorana fermions in superconductors. *Annu. Rev. Condens. Matter Phys.* **4** (2013), pp. 113–136.

[28] M. Sato and Y. Ando. Topological superconductors: a review. *Reports on Progress in Physics* **80** (2017), p. 076501.

[29] M. Leijnse and K. Flensberg. Introduction to topological superconductivity and Majorana fermions. *Semiconductor Science and Technology* **27** (2012), p. 124003.

[30] X.-L. Qi and S.-C. Zhang. Topological insulators and superconductors. *Rev. Mod. Phys.* **83** (2011), pp. 1057–1110.

[31] S. D. Sarma, M. Freedman, and C. Nayak. Majorana zero modes and topological quantum computation. *npj Quantum Information* **1** (2015), pp. 1–13.

[32] R. Aguado and L. P. Kouwenhoven. Majorana qubits for topological quantum computing. *Phys. Today* **73** (2020), pp. 44–50.

[33] J. Alicea et al. Non-abelian statistics and topological quantum information processing in 1d wire networks. *Nat. Phys.* **7** (2011), pp. 412–417.

[34] B. Lian et al. Topological quantum computation based on chiral Majorana fermions. *Proc. Natl. Acad. Sci. U.S.A.* **115** (2018), pp. 10938–10942.

[35] H. Zhang et al. Topological insulators in Bi_2Se_3, Bi_2Te_3 and Sb_2Te_3 with a single Dirac cone on the surface. *Nat. Phys.* **5** (2009), pp. 438–442.

[36] Y. Chen et al. Experimental realization of a three-dimensional topological insulator, Bi_2Te_3. *Science* **325** (2009), pp. 178–181.

[37] Y. Chen et al. Massive Dirac fermion on the surface of a magnetically doped topological insulator. *Science* **329** (2010), pp. 659–662.

[38] Y. Tokura, K. Yasuda, and A. Tsukazaki. Magnetic topological insulators. *Nat. Rev. Phys.* **1** (2019), pp. 126–143.

[39] R. Yu et al. Quantized anomalous Hall effect in magnetic topological insulators. *Science* **329** (2010), pp. 61–64.

[40] C.-Z. Chang et al. Experimental observation of the quantum anomalous Hall effect in a magnetic topological insulator. *Science* **340** (2013), pp. 167–170.

[41] X.-L. Qi, T. L. Hughes, and S.-C. Zhang. Chiral topological superconductor from the quantum Hall state. *Phys. Rev. B* **82** (2010), p. 184516.

[42] J. Wang et al. Chiral topological superconductor and half-integer conductance plateau from quantum anomalous Hall plateau transition. *Phys. Rev. B* **92** (2015), p. 064520.

[43] S. B. Chung et al. Conductance and noise signatures of Majorana backscattering. *Phys. Rev. B* **83** (2011), p. 100512.

[44] J. Osca and L. Serra. Conductance oscillations and speed of chiral Majorana mode in a quantum anomalous Hall two-dimensional strip. *Phys. Rev. B* **98** (2018), p. 121407.

[45] Y. Zeng et al. Quantum anomalous Hall Majorana platform. *Phys. Rev. B* **97** (2018), p. 081102.

[46] C.-Z. Chen et al. Quasi-one-dimensional quantum anomalous Hall systems as new platforms for scalable topological quantum computation. *Phys. Rev. B* **97** (2018), p. 104504.

[47] D. Burke et al. Robust Majorana bound states in magnetic topological insulator nanoribbons with fragile chiral edge channels. *Phys. Rev. B* **109** (2024), p. 045138.

[48] A. P. Mackenzie and Y. Maeno. The superconductivity of Sr_2RuO_4 and the physics of spin-triplet pairing. *Rev. Mod. Phys.* **75** (2003), pp. 657–712.

[49] F. Konschelle. Transport equations for superconductors in the presence of spin interaction. *Eur. Phys. J. B* **87** (2014), p. 119.

[50] M. W. Hirsch. *Differential topology*. Vol. 33. Springer Science & Business Media, 2012.

[51] I. Chavel. *Riemannian geometry: a modern introduction*. Cambridge university press, 1995.

[52] W. S. Massey. *A basic course in algebraic topology*. Springer Science & Business Media, 1991.

[53] F. Pollmann et al. Symmetry protection of topological phases in one-dimensional quantum spin systems. *Phys. Rev. B* **85** (2012), p. 075125.

[54] X.-G. Wen. Symmetry-protected topological invariants of symmetry-protected topological phases of interacting bosons and fermions. *Phys. Rev. B* **89** (2014), p. 035147.

[55] C. L. Kane. "Topological band theory and the $\mathbb{Z}_2$ invariant." In: *Contemporary concepts of condensed matter science*. Vol. 6. Elsevier, 2013, pp. 3–34.

[56] T. Fukui et al. Bulk-edge correspondence for Chern topological phases: a viewpoint from a generalized index theorem. *J. Phys. Soc. Jpn.* **81** (2012), p. 114602.

[57] R. S. Mong and V. Shivamoggi. Edge states and the bulk-boundary correspondence in Dirac Hamiltonians. *Phys. Rev. B* **83** (2011), p. 125109.

[58] D. Xiao, M.-C. Chang, and Q. Niu. Berry phase effects on electronic properties. *Rev. Mod. Phys.* **82** (2010), pp. 1959–2007.

[59] S. M. Girvin and K. Yang. *Modern condensed matter physics*. Cambridge University Press, 2019.

[60] D. Moore. The calculation of nonadiabatic Berry phases. *Physics reports* **210** (1991), pp. 1–43.

[61] J. W. Zwanziger, M. Koenig, and A. Pines. Berry's phase. *Annual review of physical chemistry* **41** (1990).

[62] M. V. Berry. Quantal phase factors accompanying adiabatic changes. *Proceedings of the Royal Society of London. A. Mathematical and Physical Sciences* **392** (1984), pp. 45–57.

[63] S.-S. Chern and J. Simons. Characteristic forms and geometric invariants. *Annals of Mathematics* **99** (1974), pp. 48–69.

[64] G. Sundaram and Q. Niu. Wave-packet dynamics in slowly perturbed crystals: gradient corrections and Berry-phase effects. *Phys. Rev. B* **59** (1999), p. 14915.

[65] D. J. Thouless et al. Quantized Hall conductance in a two-dimensional periodic potential. *Phys. Rev. Lett.* **49** (1982), p. 405.

[66] H. A. Kramers. Théorie générale de la rotation paramagnétique dans les cristaux. *Proc. Acad. Amst* **33** (1930).

[67] L. Fu. Time reversal polarization and a Z_2 adiabatic spin pump. *Phys. Rev. B* **74** (2006), p. 195312.

[68] J. E. Moore and L. Balents. Topological invariants of time-reversal-invariant band structures. *Phys. Rev. B* **75** (2007), p. 121306.

[69] A. P. Schnyder et al. Classification of topological insulators and superconductors in three spatial dimensions. *Phys. Rev. B* **78** (2008), p. 195125.

[70] C.-K. Chiu et al. Classification of topological quantum matter with symmetries. *Rev. Mod. Phys.* **88** (2016), p. 035005.

[71] S. Ryu et al. Topological insulators and superconductors: tenfold way and dimensional hierarchy. *New Journal of Physics* **12** (2010), p. 065010.

[72] A. Altland and M. R. Zirnbauer. Nonstandard symmetry classes in mesoscopic normal-superconducting hybrid structures. *Phys. Rev. B* **55** (1997), p. 1142.

[73] E. Majorana. Teoria simmetrica dell'elettrone e del positrone. *Il Nuovo Cimento (1924-1942)* **14** (1937), pp. 171–184.

[74] F. Wilczek. Majorana returns. *Nat. Phys.* **5** (2009), pp. 614–618.

[75] A. Y. Kitaev. Unpaired Majorana fermions in quantumwires. *Phys.-Usp.* **44** (2001), p. 131.

[76] R. M. Lutchyn, J. D. Sau, and S. Das Sarma. Majorana fermions and a topological phase transition in semiconductor-superconductor heterostructures. *Phys. Rev. Lett.* **105** (2010), p. 077001.

[77] M. Bahari et al. Helical topological superconducting pairing at finite excitation energies. *Phys. Rev. Lett.* **132** (2024), p. 266201.

[78] T. Karabassov et al. Hybrid helical state and superconducting diode effect in superconductor/ferromagnet/topological insulator heterostructures. *Phys. Rev. B* **106** (2022), p. 224509.

[79] B. A. Bernevig. *Topological insulators and topological superconductors*. Princeton university press, 2013.

[80] C.-X. Liu et al. Model Hamiltonian for topological insulators. *Phys. Rev. B* **82** (2010), p. 045122.

[81] E. Zsurka et al. Low-energy modeling of three-dimensional topological insulator nanostructures. *Phys. Rev.* **8** (2024), p. 084204.

[82] G. L. Bir and G. E. Pikus. *Symmetry and strain-induced effects in semiconductors*. New York: Wiley, 1974.

[83] R. Winkler. "Band structure of semiconductors." In: *Spin—orbit coupling effects in two-dimensional electron and hole systems*. Springer, 2003, pp. 9–21.

[84] J. Legendre et al. Topological properties of finite-size heterostructures of magnetic topological insulators and superconductors. *Phys. Rev. B* **110** (2024), p. 075426.

[85] K. Moors et al. Magnetotransport signatures of three-dimensional topological insulator nanostructures. *Phys. Rev. B* **97** (2018), p. 245429.

[86] B. A. Bernevig, T. L. Hughes, and S.-C. Zhang. Quantum spin Hall effect and topological phase transition in HgTe quantum wells. *Science* **314** (2006), pp. 1757–1761.

[87] C.-X. Liu et al. Oscillatory crossover from two-dimensional to three-dimensional topological insulators. *Phys. Rev. B* **81** (2010), p. 041307.

[88] M. Tinkham. *Introduction to superconductivity*. Courier Corporation, 2004.

[89] P.-G. De Gennes. *Superconductivity of metals and alloys*. CRC press, 2018.

[90] J. R. Schrieffer. *Theory of superconductivity*. CRC press, 2018.

[91] K. Fossheim and A. Sudbø. *Superconductivity: physics and applications*. John Wiley & Sons, 2004.

[92] N. N. Bogoljubov, V. V. Tolmachov, and D. Širkov. A new method in the theory of superconductivity. *Fortschr. Phys.* **6** (1958), pp. 605–682.

[93] N. Bogoliubov. On the theory of superfluidity. *J. Phys* **11** (1947), p. 23.

[94] M. R. Zirnbauer. Particle–hole symmetries in condensed matter. *J. Math. Phys.* **62** (2021).

[95] Y. Tanaka, S. Tamura, and J. Cayao. Theory of Majorana zero modes in unconventional superconductors. *Prog. Theor. Exp. Phys.* **2024** (2024), p. 08C105.

[96] P. Marra. Majorana nanowires for topological quantum computation. *J. Appl. Phys.* **132** (2022).

[97] X.-L. Qi, T. L. Hughes, and S.-C. Zhang. Topological invariants for the Fermi surface of a time-reversal-invariant superconductor. *Phys. Rev. B* **81** (2010), p. 134508.

[98] D. Heffels et al. Robust and fragile Majorana bound states in proximitized topological insulator nanoribbons. *Nanomaterials* **13** (2023), p. 723.

[99] F. de Juan, J. H. Bardarson, and R. Ilan. Conditions for fully gapped topological superconductivity in topological insulator nanowires. *SciPost Physics* **6** (2019), p. 060.

[100] D. Di Miceli et al. Conductance asymmetry in proximitized magnetic topological insulator junctions with Majorana modes. *Phys. Rev. B* **108** (2023), p. 035424.

[101] Q. L. He et al. Retracted: chiral Majorana fermion modes in a quantum anomalous Hall insulator–superconductor structure. *Science* **357** (2017), pp. 294–299.

[102] D. Di Miceli and L. Serra. Quantum-anomalous-Hall current patterns and interference in thin slabs of chiral topological superconductors. *Scientific Reports* **13** (2023), p. 19955.

[103] J. Hu et al. Chiral topological superconductivity in superconductor-obstructed atomic insulator-ferromagnetic insulator heterostructures. *Phys. Rev. Lett.* **132** (2024), p. 036601.

[104] Y. Oreg, G. Refael, and F. Von Oppen. Helical liquids and Majorana bound states in quantum wires. *Phys. Rev. Lett.* **105** (2010), p. 177002.

[105] J. Alicea. Majorana fermions in a tunable semiconductor device. *Phys. Rev. B* **81** (2010), p. 125318.

[106] E. Zsurka et al. Optimizing proximitized magnetic topological insulator nanoribbons for Majorana bound states. *Phys. Rev. B* **112** (2025), p. 094504.

[107] A. Cook and M. Franz. Majorana fermions in a topological-insulator nanowire proximity-coupled to an s-wave superconductor. *Phys. Rev. B* **84** (2011), p. 201105.

[108] S. Tewari and J. D. Sau. Topological invariants for spin-orbit coupled superconductor nanowires. *Phys. Rev. Lett.* **109** (2012), p. 150408.

[109] A. C. Potter and P. A. Lee. Multichannel generalization of Kitaev's Majorana end states and a practical route to realize them in thin films. *Phys. Rev. Lett.* **105** (2010), p. 227003.

[110] G. Blonder, m. M. Tinkham, and T. Klapwijk. Transition from metallic to tunneling regimes in superconducting microconstrictions: excess current, charge imbalance, and supercurrent conversion. *Phys. Rev. B* **25** (1982), p. 4515.

[111] M. Octavio et al. Subharmonic energy-gap structure in superconducting constrictions. *Phys. Rev. B* **27** (1983), p. 6739.

[112] C. Lambert, V. Hui, and S. Robinson. Multi-probe conductance formulae for mesoscopic superconductors. *J. Phys.: Condens. Matter* **5** (1993), p. 4187.

[113] A. F. Andreev. The thermal conductivity of the intermediate state in superconductors. *Sov. Phys. JETP* **19** (1964). Zh. Eksp. Teor. Fiz. 46, 1823 (1964), pp. 1228–1231.

[114] C. Beenakker. Colloquium: Andreev reflection and Klein tunneling in graphene. *Rev. Mod. Phys.* **80** (2008), pp. 1337–1354.

[115] C. Beenakker. "Why does a metal—superconductor junction have a resistance?" In: *Quantum mesoscopic phenomena and mesoscopic devices in microelectronics*. Springer, 2000, pp. 51–60.

[116] B. Pannetier and H. Courtois. Andreev reflection and proximity effect. *Journal of low temperature physics* **118** (2000), pp. 599–615.

[117] G. Deutscher. Crossed Andreev reflections. *J. Supercond.* **15** (2002), pp. 43–47.

[118] J. Osca and L. Serra. Complex band-structure analysis and topological physics of Majorana nanowires. *Eur. Phys. J. B* **92** (2019), p. 101.

[119] L. Serra. Majorana modes and complex band structure of quantum wires. *Phys. Rev. B* **87** (2013), p. 075440.

[120] J. Osca and L. Serra. Majorana states and magnetic orbital motion in planar hybrid nanowires. *Phys. Rev. B* **91** (2015), p. 235417.

[121] J. Osca and L. Serra. Current distributions in stripe Majorana junctions. *Eur. Phys. J. B* **90** (2017), p. 28.

[122] J. Osca and L. Serra. Topological suppression of magnetoconductance oscillations in normal–superconductor junctions. *Phys. Status Solidi B* **254** (2017), p. 1700135.

[123] J. S. Lim, R. Lopez, and L. Serra. Transport through Majorana nanowires attached to normal leads. *New Journal of Physics* **14** (2012), p. 083020.

[124] L. D. Landau and E. M. Lifshitz. *Statistical physics: volume 5*. Vol. 5. Elsevier, 2013.

[125] A. R. Akhmerov, J. Nilsson, and C. W. J. Beenakker. Electrically detected interferometry of Majorana fermions in a topological insulator. *Phys. Rev. Lett.* **102** (2009), p. 216404.

[126] B. Lian, J. Wang, and S.-C. Zhang. Edge-state-induced Andreev oscillation in quantum anomalous Hall insulator-superconductor junctions. *Phys. Rev. B* **93** (2016), p. 161401.

[127] F. Setiawan et al. Conductance spectroscopy of topological superconductor wire junctions. *Phys. Rev. B* **91** (2015), p. 214513.

[128] K. T. Law, P. A. Lee, and T. K. Ng. Majorana fermion induced resonant Andreev reflection. *Phys. Rev. Lett.* **103** (2009), p. 237001.

[129] K. Flensberg. Tunneling characteristics of a chain of Majorana bound states. *Phys. Rev. B* **82** (2010), p. 180516.

[130] E. Prada, P. San-Jose, and R. Aguado. Transport spectroscopy of NS nanowire junctions with Majorana fermions. *Phys. Rev. B* **86** (2012), p. 180503.

[131] H. Zhang et al. Retracted article: quantized Majorana conductance. *Nature* **556** (2018), pp. 74–79.

[132] D. Bagrets and A. Altland. Class *D* spectral peak in Majorana quantum wires. *Phys. Rev. Lett.* **109** (2012), p. 227005.

[133] J. Liu et al. Zero-bias peaks in the tunneling conductance of spin-orbit-coupled superconducting wires with and without Majorana end-states. *Phys. Rev. Lett.* **109** (2012), p. 267002.

[134] J. Sauls. *Andreev bound states and their signatures*. 2018.

[135] H. H. Thorp. Editorial retraction. *Science* **378** (2022), p. 718.

[136] M. Kayyalha et al. Absence of evidence for chiral Majorana modes in quantum anomalous hall-superconductor devices. *Science* **367** (2020), pp. 64–67.

[137] A. Uday et al. Non-majorana origin of the half-integer conductance quantization elucidated by multiterminal superconductor–quantum anomalous Hall insulator heterostructure. *Phys. Rev. B* **111** (2025), p. 035440.

[138] G. Ferguson et al. Direct visualization of electronic transport in a quantum anomalous Hall insulator. *Nat. Mater.* **22** (2023), pp. 1100–1105.

[139] K. C. Nowack et al. Imaging currents in HgTe quantum wells in the quantum spin Hall regime. *Nat. Mater.* **12** (2013), pp. 787–791.

[140] E. M. Spanton et al. Images of edge current in InAs/GaSb quantum wells. *Phys. Rev. Lett.* **113** (2014), p. 026804.

[141] J. Zhang et al. Band structure engineering in $(Bi_{1-x}Sb_x)_2Te_3$ ternary topological insulators. *Nat. Commun.* **2** (2011), p. 574.

[142] T. Arakane et al. Tunable Dirac cone in the topological insulator $Bi_{2-x}Sb_xTe_{3-y}Se_y$. *Nat. Commun.* **3** (2012), p. 636.

[143] G. D. Mahan. *Many-particle physics*. Springer Science & Business Media, 2013.

[144] T. Kita. *Statistical mechanics of superconductivity*. Springer, 2015.

[145] A. L. Fetter and J. D. Walecka. *Quantum theory of many-particle systems*. Courier Corporation, 2012.

[146] J. J. Sakurai and J. Napolitano. *Modern quantum mechanics*. Cambridge University Press, 2020.

[147] M. Gell-Mann and F. Low. Bound states in quantum field theory. *Phys. Rev.* **84** (1951), p. 350.

[148] G.-C. Wick. The evaluation of the collision matrix. *Phys. Rev.* **80** (1950), p. 268.

[149] G. B. Arfken, H. J. Weber, and F. E. Harris. *Mathematical methods for physicists: a comprehensive guide*. Academic press, 2011.

[150] E. T. Whittaker and G. N. Watson. *A course of modern analysis*. Courier Dover Publications, 2020.

[151] G. Strang. *Linear algebra and its applications*. 2012.

[152] R. A. Horn and C. R. Johnson. *Matrix analysis*. Cambridge university press, 2012.

[153] D. Di Miceli et al. Proximity-induced superconductivity in magnetic topological insulator films. *arXiv preprint arXiv:2512.03797* (2025).

[154] G. H. Golub and C. F. Van Loan. *Matrix computations*. JHU press, 2013.

[155] J. B. Conway. *A course in functional analysis*. Vol. 96. Springer, 2019.

[156] Y. Tanaka, M. Sato, and N. Nagaosa. Symmetry and topology in superconductors – odd-frequency pairing and edge states. *J. Phys. Soc. Jpn.* **81** (2011), p. 011013.

[157] K. Maeda et al. Classification of pair symmetries in superconductors with unconventional magnetism. *Phys. Rev. B* **111** (2025), p. 144508.

[158] M. Sigrist and K. Ueda. Phenomenological theory of unconventional superconductivity. *Rev. Mod. Phys.* **63** (1991), p. 239.

[159] P. Burset et al. Superconducting proximity effect in three-dimensional topological insulators in the presence of a magnetic field. *Phys. Rev. B* **92** (2015), p. 205424.

[160] Z. Faraei and S. Jafari. Superconducting proximity in three-dimensional Dirac materials: odd-frequency, pseudoscalar, pseudovector, and tensor-valued superconducting orders. *Phys. Rev. B* **96** (2017), p. 134516.

[161] Y. Katznelson. *An introduction to harmonic analysis*. Cambridge University Press, 2004.

[162] E. M. Stein and R. Shakarchi. *Fourier analysis: an introduction*. Vol. 1. Princeton University Press, 2011.

[163] M. Abramowitz and I. A. Stegun. *Handbook of mathematical functions with formulas, graphs, and mathematical tables*. Vol. 55. US Government printing office, 1948.

[164] L. Fu and C. L. Kane. Superconducting Proximity Effect and Majorana Fermions at the Surface of a Topological Insulator. *Phys. Rev. Lett.* **100** (2008), p. 096407.

[165] A. C. Potter and P. A. Lee. Engineering a $p+ip$ superconductor: Comparison of topological insulator and Rashba spin-orbit-coupled materials. *Phys. Rev. B* **83** (2011), p. 184520.

[166] C. Triola, E. Rossi, and A. V. Balatsky. Effect of a spin-active interface on proximity-induced superconductivity in topological insulators. *Phys. Rev. B* **89** (2014), p. 165309.

[167] L. Fu and E. Berg. Odd-parity topological superconductors: theory and application to $Cu_xBi_2Se_3$. *Phys. Rev. Lett.* **105** (2010), p. 097001.

[168] M. Sato. Topological odd-parity superconductors. *Phys. Rev. B* **81** (2010), p. 220504.

[169] N. Read and D. Green. Paired states of fermions in two dimensions with breaking of parity and time-reversal symmetries and the fractional quantum Hall effect. *Phys. Rev. B* **61** (2000), p. 10267.

[170] M. Sato. Topological properties of spin-triplet superconductors and Fermi surface topology in the normal state. *Phys. Rev. B* **79** (2009), p. 214526.

[171] A. Zazunov et al. Josephson effect in junctions of conventional and topological superconductors. *Beilstein J. Nanotechnol.* **9** (2018), pp. 1659–1676.

[172] A. C. Potter and L. Fu. Anomalous supercurrent from Majorana states in topological insulator Josephson junctions. *Phys. Rev. B* **88** (2013), p. 121109.

[173] K. Laubscher and J. D. Sau. Detection of Majorana zero modes bound to Josephson vortices in planar superconductor–topological insulator–superconductor junctions. *Phys. Rev. B* **111** (2025), p. 235442.

[174] T. Oka and S. Kitamura. Floquet engineering of quantum materials. *Annual Review of Condensed Matter Physics* **10** (2019), pp. 387–408.

[175] M. S. Rudner and N. H. Lindner. Band structure engineering and non-equilibrium dynamics in Floquet topological insulators. *Nature reviews physics* **2** (2020), pp. 229–244.

[176] L. Jiang et al. Majorana fermions in equilibrium and in driven cold-atom quantum wires. *Phys. Rev. Lett.* **106** (2011), p. 220402.

[177] G. Liu et al. Topological superfluid transition induced by a periodically driven optical lattice. *Phys. Rev. A* **86** (2012), p. 013639.

[178] E. Prada et al. From Andreev to Majorana bound states in hybrid superconductor–semiconductor nanowires. *Nature Reviews Physics* **2** (2020), pp. 575–594.

[179] F. S. Bergeret et al. Colloquium: nonequilibrium effects in superconductors with a spin-splitting field. *Rev. Mod. Phys.* **90** (2018), p. 041001.

[180] J. Linder and J. W. Robinson. Superconducting spintronics. *Nature Physics* **11** (2015), pp. 307–315.

[181] M. Eschrig. Spin-polarized supercurrents for spintronics: a review of current progress. *Reports on Progress in Physics* **78** (2015), p. 104501.

[182] J. Ma, R. Zhan, and X. Lin. Superconducting diode effects: mechanisms, materials and applications. *Advanced Physics Research* (2025), p. 2400180.

[183] L. M. Milne-Thomson. *The calculus of finite differences*. American Mathematical Soc., 2000.

[184] S. Datta. *Quantum transport: atom to transistor*. Cambridge university press, 2005.

[185] F. Tisseur and K. Meerbergen. The quadratic eigenvalue problem. *SIAM Rev.* **43** (2001), pp. 235–286.